



HAL
open science

Nanosources optiques excitées par courant tunnel inélastique

Delphine Pommier

► **To cite this version:**

Delphine Pommier. Nanosources optiques excitées par courant tunnel inélastique. Optics [physics.optics]. Université Paris-Saclay, 2021. English. NNT : 2021UPASP056 . tel-03741825

HAL Id: tel-03741825

<https://theses.hal.science/tel-03741825v1>

Submitted on 2 Aug 2022

HAL is a multi-disciplinary open access archive for the deposit and dissemination of scientific research documents, whether they are published or not. The documents may come from teaching and research institutions in France or abroad, or from public or private research centers.

L'archive ouverte pluridisciplinaire **HAL**, est destinée au dépôt et à la diffusion de documents scientifiques de niveau recherche, publiés ou non, émanant des établissements d'enseignement et de recherche français ou étrangers, des laboratoires publics ou privés.

Optical nanosources excited by inelastic tunneling current

Nanosources optiques excitées par courant tunnel inélastique

Thèse de doctorat de l'université Paris-Saclay

École doctorale n°572 Ondes et Matière (EDOM)

Spécialité de doctorat: Physique

Unité de recherche : Université Paris-Saclay, CNRS, Institut des
Sciences Moléculaires d'Orsay, 91405, Orsay, France

Référent : Faculté des sciences d'Orsay

Thèse présentée et soutenue à Paris-Saclay,
le 21 Juillet 2021, par

DELPHINE POMMIER

Composition du Jury :

Riad HAIDAR

Directeur de recherche, ONERA, Université Paris-Saclay

Président

Roland CORATGER

Professeur des universités, Toulouse 3 Paul Sabatier

Rapporteur & Examineur

Agnès MAÎTRE

Professeur des universités, Sorbonne-Université

Rapporteur & Examineur

Nicolas BONOD

Directeur de recherche, Institut Fresnel, Marseille

Examineur

Luiz Fernando ZAGONEL

Professeur des universités, Universidade Estadual de
Campinas, Brésil

Examineur

Direction de la thèse :

Elizabeth Boer-Duchemin

Maître de conférences, Université Paris-Saclay

Directeur de thèse

Eric LE MOAL

Chargé de recherche, Université Paris-Saclay

Invité

A ma famille, et à surtout ma mère, qui a été mon plus grand soutien.

Titre: Nanosources optiques excitées par courant tunnel inélastique

Mots clés : Résonance plasmonique de surface, Nanophotonique, Nanostructures, Semiconducteurs, Excitons, Microscopie à force atomique, Microscopie à effet tunnel, Microscopie en champ proche

Résumé: Dans cette thèse, deux types de nanosources de lumière différentes excitées par courant tunnel sont présentées: l'émission de lumière grâce aux plasmons et aux excitons. La première partie de cette thèse concerne des semiconducteurs 2D : les dichalcogénures de métaux de transition (TMD). Leurs propriétés optiques et électroniques ouvrent de nouvelles opportunités d'applications, par exemple dans le domaine du photovoltaïque. Ici, nous présentons une nouvelle méthode pour exciter électriquement des excitons dans une monocouche de TMD (MoSe₂ et WS₂) en utilisant un microscope à effet tunnel (STM), et étudions donc l'électroluminescence, le mécanisme d'excitation et les propriétés des excitons ainsi créés dans ces matériaux. Dans

une seconde partie, nous étudions l'excitation de plasmons de surface propagatifs par le courant tunnel inélastique. Les plasmons de surface propagatifs sont utilisés dans des applications variées, qui peuvent aller des détecteurs biologiques au domaine du photovoltaïque. Ils peuvent également être utilisés pour alimenter des circuits plasmoniques, qui pourraient être utilisés pour remplacer des circuits électroniques afin de gagner en bande passante. Pour cette application, il y a donc besoin d'avoir une nanosource de plasmons propagatifs excitée électriquement. Dans nos expériences, des nanoantennes sont utilisées pour créer une résonance dans le spectre des plasmons, et augmenter l'efficacité d'excitation des plasmons de surface propagatifs. Nous avons tout d'abord utilisé un STM pour exciter des plasmons de surface sur un film d'or avec des nanoantennes afin de comprendre l'impact de la présence d'une nanoantenne sur l'émission des plasmons de surface. Nous avons ensuite utilisé une jonction tunnel intégrée entre un nanocube d'or et un film d'or pour exciter des plasmons de surface propagatifs.

Title: Optical nanosources excited by inelastic tunneling current

Keywords : Surface plasmon resonance, Nanophotonic, Nanostructures, Semiconductors, Excitons, Atomic force microscopy, Scanning tunneling microscopy, Near-field microscopy

Abstract: In this thesis, plasmonic and excitonic nanosources of light, two different types of nanosources excited by tunneling current, are presented. The first part of this thesis concerns the 2D semiconductors known as transition metal dichalcogenides (TMDs). Their optical and electronic properties could lead to new opportunities for applications. Here, we demonstrate a new method to electrically excite excitons in a TMD monolayer (MoSe₂ and WS₂) using a scanning tunneling microscope (STM), and thus we study the electroluminescence, the excitation mechanism and the dif-

ferent excitons in these materials. In the second part of this thesis, we study the excitation of propagating surface plasmons using inelastic tunneling current. Propagating surface plasmons are used in a variety of applications, from biosensors to photovoltaics. They could also be used in plasmonic circuits, which could replace electronic circuits in order to obtain a gain in bandwidth. Thus, for such an application, there is a need for an electrically excited nanosource of plasmons. In our experiments, nanoantennas are used to induce a resonance in the plasmon spectrum and increase the propagating surface plasmon excitation efficiency. We first used an STM to excite surface plasmons on a gold film with nanoantennas to understand the impact of the presence of the antenna on the surface plasmon emission. Then we used an integrated tunneling junction between a gold nanocube and a gold film as a nanosource of propagating surface plasmons.

Synthèse

Dans cette thèse, deux types de nanosources optiques différentes, excitées par courant tunnel inélastique, sont présentées : une nanosource de plasmons de surface propagatifs et une nanosource excitonique dans un dichalcogénure de métal de transition (les TMDs, qui sont des semiconducteur en couche mince de moins d'un nanomètre d'épaisseur).

Le premier chapitre introduit la physique des quasi-particules excitées par les nanosources, tout d'abord en introduisant les plasmons de surface et leurs propriétés, puis en décrivant le courant tunnel inélastique qui est utilisé pour exciter les plasmons de surface ainsi que les excitons. Ces derniers sont ensuite introduits. En deuxième partie, ce chapitre présente les différents outils utilisés expérimentalement, en particulier le microscope à effet tunnel (Scanning Tunneling Microscope, STM) et le microscope à force atomique (Atomic Force Microscope, AFM), ainsi que le microscope optique utilisé pour détecter la lumière provenant de l'échantillon. En effet, les plasmons de surface peuvent se désexciter en photons lorsqu'ils se propagent sur un film mince en configuration de Kretschmann. De même, la recombinaison des excitons dans les TMDs peut être radiative, et la lumière ainsi émise peut être analysée spectralement, angulairement et spatialement.

Les chapitres suivants présentent trois expériences réalisées au cours de cette thèse.

Dans un premier temps, c'est l'excitation électrique par STM d'excitons dans une mono-couche de diséléniure de molybdène (MoSe_2) qui est étudiée dans le chapitre 2, grâce à l'analyse spectrale, spatiale et en efficacité de leur recombinaison radiative. Une étude du spectre et de l'émission angulaire de l'électroluminescence montre que la lumière émise provient bien de la recombinaison d'excitons: c'est donc la première excitation d'excitons dans un TMD en mono-couche par un STM. Après avoir observé le seuil en tension pour l'émission des photons et donc l'excitation d'excitons, le mécanisme d'excitation des excitons proposé est le transfert résonant d'énergie grâce au courant tunnel inélastique. Notre système expérimental est doté d'un objectif à huile, qui permet d'imager un grand champ de vision sur l'échantillon, et donc de visualiser la propagation des excitons: nous avons observé que les excitons peuvent se propager sur plusieurs microns dans une mono-couche de MoSe_2 avant de se recombinaison. En combinant la précision d'excitation du STM avec notre système de collection de la lumière, nous avons mesuré des "cartes de photons", qui nous permettent de comparer l'image STM de l'échantillon à une carte d'efficacité d'excitation. Ces mesures nous ont permis de mettre en avant la présence de défauts dans la topographie qui ont une efficacité d'excitation d'exciton plus élevée. Ces résultats ont fait l'objet d'une publication : Ref [1].

Dans un second temps, c'est un autre type de quasi-particule qui est étudié: les plasmons de surface. L'objectif de cette deuxième partie est de concevoir une nanosource de plasmons de surface propagatifs qui soit à la fois alimentée électriquement, efficace et de taille nanométrique. La solution retenue pour exciter les plasmons de façon électrique est d'utiliser le courant tunnel. Nous utilisons un échantillon avec une nanoantenne afin d'augmenter la densité d'états électromagnétique locale, la densité d'états électromagnétique radiatifs, et donc l'efficacité d'excitation des plasmons de surface.

Le troisième chapitre est donc consacré à l'étude de l'impact d'une antenne en or sur le spectre et l'efficacité d'émission des plasmons de surface, que l'on excite ici en utilisant le courant tunnel d'un STM. Nous présentons tout d'abord des simulations électromagnétique démontrant une augmentation importante de l'efficacité d'excitation électrique des plasmons en présence d'une antenne dont les dimensions ont été optimisées (par comparaison avec un substrat d'or sans antenne). Cependant, les dimensions idéales de l'antenne définies par ces simulations initiales étaient difficiles à obtenir expérimentalement, et en simulant l'émission d'antennes plus réalistes, nous avons réalisé que l'augmentation d'efficacité n'était pas significative. Les résultats expérimentaux confirment que l'augmentation de l'efficacité n'est pas significative, il faut donc utiliser des antennes avec des dimensions plus petites.

Dans le quatrième chapitre, nous utilisons donc une nouvelle stratégie pour réaliser les nanoantennes néces-

saires à nos sources de plasmons de surface, en utilisant des nanocubes fabriqués chimiquement. Ces nanocubes sont ensuite dispersés sur un film d'or couvert d'un nanofilm de molécules isolantes, qui forme la jonction tunnel. L'originalité de cette expérience est de polariser la jonction métal (nanocube) - isolant (molécule) - métal (film d'or) non pas en utilisant des connecteurs électriques lithographiés mais un AFM avec une pointe conductrice. Cette nouvelle méthode de polarisation d'une nanojonction tunnel pour l'excitation de plasmons de surface propagatifs permet une grande liberté dans le test des différentes jonctions puisqu'il suffit de scanner la surface avec l'AFM pour localiser la nanosource, puis d'établir un contact électrique entre la pointe et le cube pour exciter des plasmons de surface. Ces nanosources de plasmons propagatifs démontrent une intensité prometteuse, mais l'efficacité reste basse. Afin d'améliorer cette efficacité, un meilleur contrôle de l'épaisseur du film moléculaire et de la dimension des cubes serait nécessaire. Nous avons fait des simulations pour mieux comprendre les modes excités dans ces nanosources, et obtenu un bon accord qualitatif entre le spectre théorique et expérimental des plasmons de surface détectés, malgré le fait que toute la complexité des conditions expérimentales ne soit pas prise en compte dans le modèle (par exemple la rugosité du film d'or ou du film moléculaire, ou encore l'arrondi des bords des nanocubes).

Ces résultats montrent donc la possibilité d'exciter électriquement des plasmons de surface propagatifs en utilisant une nanojonction, ce qui serait nécessaire pour alimenter un nanocircuit plasmonique. En variant les matériaux du cube et du film sur lequel les plasmons se propagent (aluminium, argent, etc) ainsi que l'épaisseur du film isolant et la taille des nanocubes, il serait alors possible d'avoir une nanosources de plasmons de surface propagatifs avec une résonance à la longueur d'onde souhaitée sur une large gamme de longueur d'onde.

Acknowledgements

J'aimerais remercier en premier lieu ma directrice de thèse, Elizabeth Boer Duchemin pour la fantastique opportunité qu'elle m'a offert avec cette thèse, ainsi que pour son aide tout au long de ce projet. J'ai été extrêmement chanceuse de l'avoir eu pour me guider, car son enthousiasme, sa patience avec mes nombreuses questions, et nos longues discussions quand je me heurtais à des difficultés m'ont été d'une aide inestimable. Elle a été une excellente encadrante, à la fois sur le plan scientifique, mais également quelqu'un avec qui j'ai toujours pu parler face aux difficultés, et pour ça, je la remercie chaleureusement !

J'aimerais également remercier Éric le Moal pour m'avoir offert l'opportunité d'étudier les semiconducteurs 2D ainsi que pour m'avoir encadré sur cette partie de ma thèse. J'ai beaucoup apprécié nos discussions, ses réponses mesurées, et son aide sur l'expérience ainsi que pour m'aider à comprendre les phénomènes en jeu. Grâce à lui, j'ai également eu l'occasion de publier en 1ère auteure un article dans PRL, ce qui est une grande fierté. Merci beaucoup !

J'ai eu la grande chance de faire ma thèse au sein de l'équipe Nanophysique de l'ISMO, que je voudrais remercier, et en particulier Gérald Dujardin pour avoir relu ce manuscrit et pour son aide avec mes questions, ainsi que George Raseev pour nos nombreuses discussions.

Les travaux présentés dans cette thèse ont été faits en collaboration avec différents groupes sans qui ce projet n'aurait pas pu être possible. En ce qui concerne le travail sur les semiconducteurs 2D, il a été effectué en collaboration avec Stéphane Berciaud, Guillaume Schull et Luis Parra-Lopez de l'IPCMS, que je remercie grandement pour la fabrication des échantillons de TMDs en couche mince ainsi que pour leur aide à la compréhension des résultats. J'ai également pu bénéficier de l'aide de Julien Chaste du C2N pour l'analyse Raman des échantillons. Le travail sur les antennes plasmonique a été effectué dans le cadre du projet ANR INTELPLAN, et j'ai ainsi pu bénéficier du soutien de plusieurs équipes. Les premiers échantillons sur lesquels j'ai travaillé, avec des antennes en or sur film d'or ont ainsi été fabriqués par Anne-Lise Coutrot, qui m'a été d'une grande aide sur ce travail. Au LPS, j'ai appris à fabriquer des jonctions tunnel par évaporation grâce à Julien Gabelli et Marco Aprili, qui m'ont également offert l'opportunité d'explorer de nouveaux sujets en post-doc, ce pour quoi je leur suis très reconnaissante. Les derniers échantillons, constitués de nanocubes d'or sur film d'or fonctionnalisés, ont été réalisés à Hong Kong par Yunhe Lai, dans l'équipe de Jianfang Wang, que je remercie pour leur aide. Enfin, l'analyse des résultats a été facilitée par des travaux de simulations, qui ont été possible grâce à un programme développé par l'équipe de Jean-Jacques Greffet au laboratoire Charles Fabry. Je remercie donc grandement Christophe Sauvan pour son aide avec le programme et nos questions. J'aimerais également remercier en particulier Cheng Zhang pour son aide avec le programme ainsi que pour avoir pris le temps de me fabriquer deux échantillons d'antennes avec jonction tunnel intégrée durant sa thèse.

De plus, j'ai eu la chance d'être dans un laboratoire avec une très bonne ambiance, où j'ai rencontré des doctorants géniaux sans qui cette thèse aurait été beaucoup plus terne ! Merci beaucoup pour toutes ces soirées et ces fous rires, ils ont certainement sauvé ma santé mentale ! Merci en particulier à Olivia Chitarra, qui est une amie géniale à qui j'ai toujours pu me confier.

Au sein même de mon équipe, les doctorants formaient un groupe soudé, et je me souviendrais toujours avec nostalgie (et gourmandise) de nos soirées "fondue chinoise" avec Shuiyan Cao (qui m'a beaucoup aidé au début de ma thèse !), Moustafa Achlan, Wei Zhang, Rémi Bretel, Nianjheng Wu et Peng Pan. Merci à vous !

Et finalement, j'aimerais remercier ma famille pour leurs encouragements constants, leurs conseils et leur soutien qui m'a aidé à traverser les difficultés. C'est à travers eux que j'ai découvert le monde gigantesque et fascinant de la science, et en particulier grâce à ma mère, Sylvie Pommier, à qui je dédie cette thèse. Son enthousiasme sans borne pour mes travaux de recherche et sa fierté ont été une source inestimable de motivation pour moi !

Contents

1	Context and methods	4
1.1	Context	4
1.1.1	An introduction to surface plasmons	4
1.1.2	Electrical excitation of surface plasmons using inelastic tunneling current	5
1.1.3	SPPs: important parameters and the Kretschmann configuration	6
1.1.4	STM-excitation of surface plasmons on a thin gold film	8
1.1.5	An introduction to excitons in transition metals dichacolgenides	9
1.2	Tools and methods	12
1.2.1	Scanning tunneling microscopy	12
1.2.2	Atomic Force Microscopy	13
1.2.3	Resolution in ambient scanning probe microscopy	14
1.2.4	Optical excitation	15
1.2.5	Optical detection	15
1.3	Summary	19
2	STM excitation of excitons in transition metal dichacolgenides	21
2.1	Local exciton excitation using an STM	21
2.2	Excitation mechanism	26
2.3	Exciton diffusion and the measurement of the local exciton excitation efficiency	31
2.4	Summary	33
3	STM excitation of surface plasmons with a nanoantenna	35
3.1	Introduction	35
3.2	Theoretical understanding through simulation: the impact of a nanoantenna on the STM excitation of surface plasmons	37
3.2.1	Theoretical understanding of the impact of a nanoantenna: small spherical tip	37
3.2.2	Calculations meet reality: taking into account a more realistic tip shape and the experimental nanoantenna dimensions	43
3.3	Experimental excitation of surface plasmons using an STM	43

3.3.1	Sample fabrication and characterization	44
3.3.2	STM excitation of surface plasmon polaritons with the help of a nanoantenna	45
3.3.3	Analysis of the surface plasmon excitation efficiency	48
3.3.4	Spectra	51
3.4	Summary	56
4	Excitation of surface plasmons with a nanoantenna tunneling junction	57
4.1	Introduction	57
4.2	New method for locally contacting a “nanoparticle-on-a-mirror” tunneling junction	58
4.2.1	Establishing an electrical contact using CAFM	58
4.3	Bottom-up fabricated “nanocube-on-a-mirror” nanoantenna tunneling junction, contacted via CAFM	60
4.3.1	Sample fabrication, structural and electrical characterization	60
4.3.2	Integrated tunneling junction excitation of light and surface plasmons	64
4.3.3	Spectra	64
4.3.4	Simulation of the emission from a tunneling junction in a “nanoantenna-on-a-mirror” geometry	66
4.3.5	Simulation results for nanocubes on a gold film functionalized with insulating molecules	70
4.3.6	Comparison of experimental and simulation results for nanocube antennas on a gold film functionalized with insulating molecules	72
4.3.7	Efficiency	75
4.4	Summary	78
5	Summary	79
A	Maxwell equations for propagating surface plasmons	93
B	Magnification of the optical detection system	99
C	Description of the AFM laser	100
D	Fourier space imaging of MoSe ₂ electroluminescence	103
D.1	Bright excitons in monolayer MoSe ₂ : transition dipole moment orientation	103
D.2	Excitation of an in-plane dipole with a vertical dipole	104
E	STM-induced alteration of a TMD monolayer	105
F	Parameter study for the non-destructive STM excitation of a nanoantenna	107
G	CAFM tip comparison	111
G.1	AFM tips with a conducting layer	111

G.2	AFM tips made entirely of a conducting material	111
H	Gold nanoantennas on aluminum	115
H.1	Tunneling junction in an alumina layer, with a top-down fabricated gold nanoantenna, contacted via CAFM	115
H.2	Simulation results for a gold nanoantenna on aluminum	118
I	Correction factors for the comparison of the experimental efficiency values measured with different detectors	122

Chapter 1

Context and methods

1.1 Context

In this thesis, we study two types of optical nanosources driven by inelastic tunneling current. In Chapter 2, we will focus on the local, electrical excitation of the excitonic luminescence from a 2D semiconductor (called transition metal dichalcogenides, and presented later in Section 1.1.5). These lamellar materials have sparked great interest for their possible use in nanodevices as these monolayers combine the advantages of being extremely thin (a monolayer is composed of three atomic layers, and is typically less than a nanometer thick), of being flexible, of having a direct band-gap and of having novel excitonic properties. Thus, the study of the electroluminescence properties of these materials is important in order to pave the way for future nanodevices. In this thesis we will study molybdenum diselenide (MoSe_2). In particular, we present a new method to locally induce excitonic luminescence using inelastic tunneling current (thus with no background light), which has been published in Ref. [1].

In Chapters 3 and 4, we will consider nanosources of propagating surface plasmons excited by inelastic electron tunneling. Surface plasmon polaritons are an electromagnetic wave propagating on a metal/dielectric interface, coupled to a collective charge oscillation. Plasmonic devices, based on propagating surface plasmons, may benefit from improved bandwidth as compared to electronic components. Also, since plasmonic components may be successfully miniaturized, they are thus superior to optical components in this regard since photonic devices are limited in size by the diffraction limit. This thesis is part of the ANR project INTELPLAN, whose goal is to realize a local, electrical source of propagating surface plasmons that may be integrated into current technology. Thus, in this thesis, we will study nanosources of propagating surface plasmons excited electrically, a necessary requirement for future integration in an electronic circuit. In particular, we study how a nanoantenna affects the propagating surface plasmons excited using a biased tunneling junction .

1.1.1 An introduction to surface plasmons

A goal of this thesis is to study how a nanoantenna can modify the excitation efficiency and emission of electrically excited propagating surface plasmons. Surface plasmon polaritons (called surface plasmons in this thesis for simplification purposes) are collective oscillations of the surface charges on a metal/dielectric interface coupled to an electromagnetic wave.

We may distinguish between two categories of surface plasmons: surface plasmons may either propagate on the surface to which they are bound, in which case they are propagating surface plasmons (SPPs), or they may consist of a localized oscillation of the surface electrons, for example on a nanoparticle, and be referred to as localized surface plasmons (LSPs). Surface plasmons are only supported at an interface between two materials with permittivities of opposite sign, or in other words, between a dielectric and a metal. The permittivity of a dielectric may be considered real (negligible losses) and varies little as a function of frequency in general. A plasmonic metal, on the other hand, is highly dispersive, has a permittivity whose real part has a large absolute value and is negative. An additional condition for a good plasmonic material is a small imaginary part of the

permittivity, in order to minimize the losses when surface plasmons propagate.

Surface plasmons were first discovered experimentally by Powell and Swan in 1959 [2], when they were investigating the energy loss of electron beams scattered by thin aluminum films and found peaks in the loss spectra that fit well with a theoretical prediction of Ritchie published in 1957 [3]. Even though the discovery of surface plasmons was made using a high-energy electron beam, optical means of excitation have since become the norm, once Otto and Kretschmann published separately two different optical excitation methods in 1968, referred to as the “Otto configuration” [4] and the “Kretschmann configuration” [5] (see Section 1.1.3). Both configurations excite surface plasmons at an air/metal interface using photons in glass (see Section 1.1.3 for details). Another method of optical excitation was proposed the same year by Ritchie et al., using a grating to compensate for the momentum mismatch between propagating surface plasmons at an air/metal interface and photons in air [6].

Electrical excitation of surface plasmons with low-energy electrons was then demonstrated in 1976 by Lambe and McCarthy [7]: by applying a low bias voltage to a metal-insulator-metal planar junction (insulating layer thickness \sim a few nanometers), they detected light from the junction. The spectrum of this emitted light was broad, with a maximum energy corresponding to the applied voltage. The excitation of surface plasmons using tunneling current was then carried out in 1989 using the tunneling junction between the tip of a scanning tunneling microscope (STM) and a plasmonic metal in an article published by Gimzewski et al. in 1989 [8].

1.1.2 Electrical excitation of surface plasmons using inelastic tunneling current

In order to integrate plasmonics with current technology, we need to be able to electrically excite surface plasmons at the nanoscale. As described above, the first excitation of surface plasmons was carried out using high-energy electron beams. Such an electrical source of surface plasmons, however, is not suitable for future devices, as we also require a solution that can fit into a miniaturized integrated circuit. Thus we propose using inelastic tunneling current as a source instead.

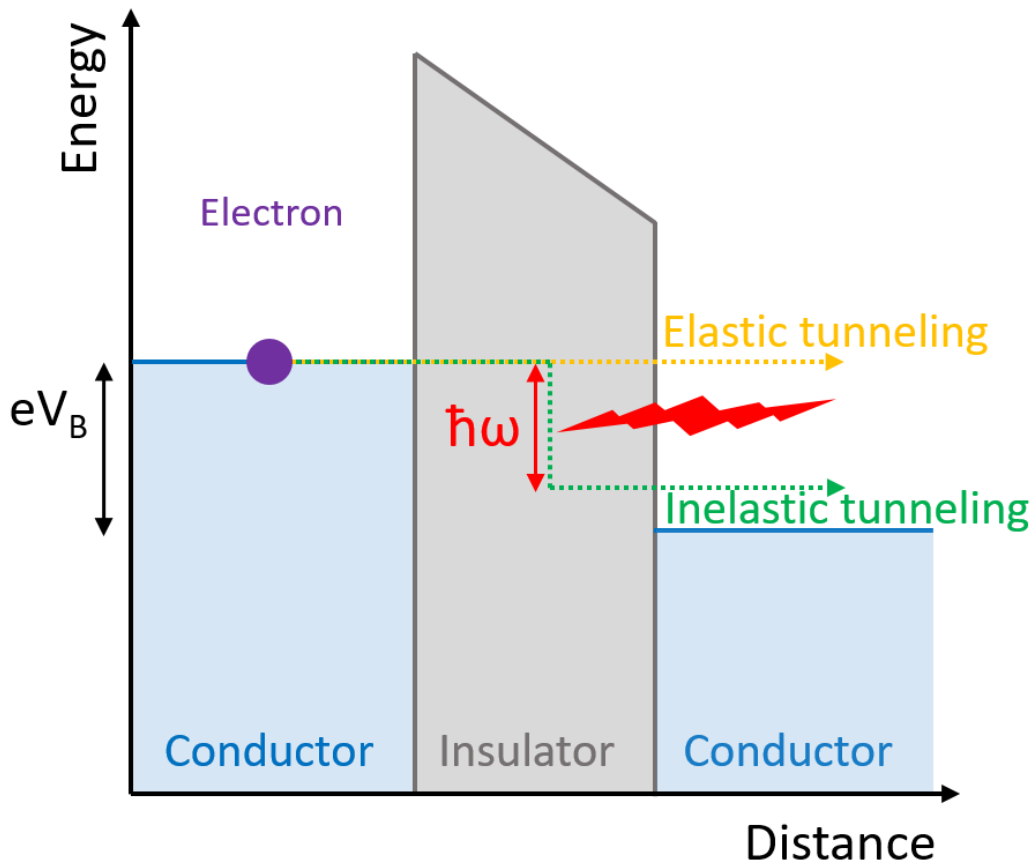


Figure 1.1: Schematic of the different tunneling processes in a tunneling junction: in yellow, the electron tunnels elastically and does not lose any energy in the junction. In green, the electron tunnels inelastically and loses all or part of its energy in the junction, exciting for example an optical mode (represented in red) with an equivalent energy $\hbar\omega$.

“Tunneling” describes a phenomenon occurring when two conductors are separated by a thin insulator (on

the nanometer scale): when a bias voltage is applied between the conductors, electrons may tunnel through the potential barrier. Most of the tunneling electrons do so elastically: there is no energy loss in the junction (see Fig. 1.1). However, a small percentage of the electrons passing through the potential barrier ($\simeq 1\%$ [9]) lose all or part of their excess energy in the junction. This energy may excite optical modes such as localized or propagating surface plasmons. Berndt et al. showed clear evidence in 1991 that the emission of light from a scanning tunneling microscope (STM) can occur via the inelastic tunneling current excitation of a tip-induced localized surface plasmon mode [10].

Note that the excitation of the available optical modes depends on the local density of electromagnetic states (EM-LDOS). The EM-LDOS may be defined as the number of electromagnetic modes at a particular energy existing at a particular point in space, where the contribution of each mode is determined by the intensity of the mode at that point. It is the sum of the radiative and non-radiative EM-LDOS, with contributions from the radiative and non-radiative electromagnetic modes respectively [11, 12].

While still under debate, several articles measure the tunneling time for an electron in a metal-insulator-metal junction to be of the order of magnitude of a few tens of attoseconds to femtoseconds [13–15]. Thus tunneling will not be the physical phenomenon which limits the bandwidth of future devices. Another advantage is that by using tunneling current to excite propagating surface plasmons, the source dimension is only limited by the electrode dimensions and the resulting localized surface plasmon mode.

1.1.3 SPPs: important parameters and the Kretschmann configuration

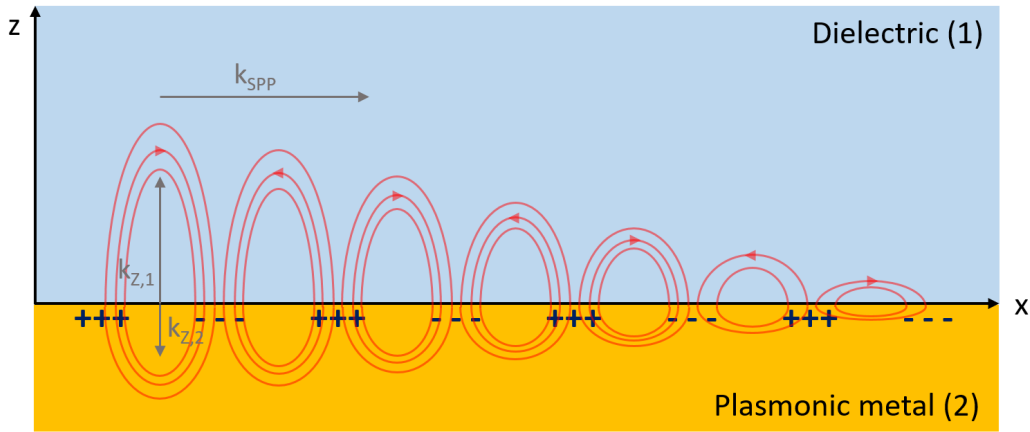


Figure 1.2: Schematic of the electric field for propagating surface plasmons.

Figure 1.2 shows a schematic of the electric field in the xz plane for propagating surface plasmons on a metal/dielectric interface (interface normal in the z direction). The electric field of propagating surface plasmons is evanescent in the direction perpendicular to the metal/dielectric interface (thus the wavevector components in the z direction are purely imaginary), but the surface plasmon field is propagating in the direction parallel to the interface. Thus the parallel wavevector k_x , which we call k_{SPP} in the following, is complex with a non-zero real part characterizing the propagation and an imaginary part characterizing the propagation losses:

$$k_{SPP} = \sqrt{\frac{\epsilon_1 \epsilon_2}{\epsilon_1 + \epsilon_2} \frac{\omega^2}{c^2}} \quad (1.1)$$

$$|k_{z,j}| = \sqrt{\frac{\epsilon_j^2}{\epsilon_1 + \epsilon_2} \frac{\omega^2}{c^2}}, \quad j = \text{dielectric (1) or metal (2)}$$

More details on these equations may be found in Appendix A.

Using the Drude model to describe the dependence of the permittivities on frequency, we may plot the surface plasmon energy as a function of the parallel wavevector k_{SPP} (dispersion curve): see Fig. 1.3. On the same graph, we plot the energy of photons in air and in glass as a function of the wavevector component parallel to the interface.

As a match in energy and parallel wavevector is necessary for propagating surface plasmons to decay into photons, surface plasmons propagating at the interface between a metal and air cannot decay directly into

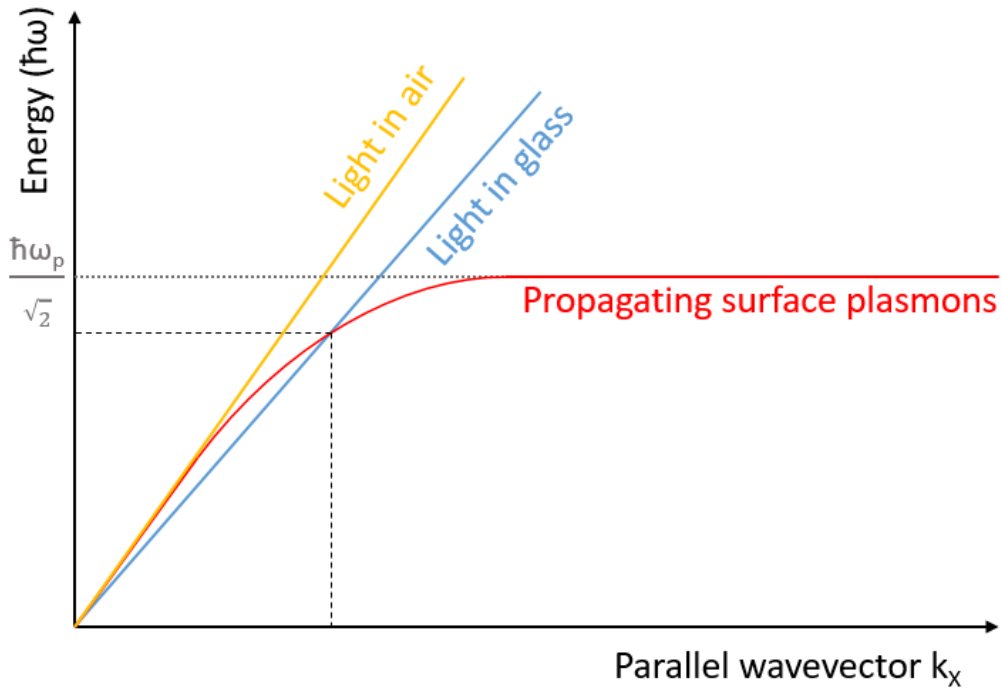


Figure 1.3: Dispersion curves for propagating surface plasmons on a air/metal interface (red curve), for light in air (yellow curve), and for light in glass (blue curve). For small values of k_{SPP} , the propagating surface plasmon dispersion curve is tangent to the curve for photons in air, but as k_{SPP} increases, the curve bends towards an asymptotic value ($\frac{\hbar\omega_p}{\sqrt{2}}$ with ω_p the plasma frequency).

photons in air. Propagating surface plasmons are thus confined to the interface between the plasmonic film and the dielectric, and we cannot directly detect them in the far field. However, they may decay into photons in a dielectric of higher refractive index (e.g., glass see Fig. 1.3). In the “Kretschmann configuration”[5], a thin metal film is deposited on a glass prism. Thanks to the evanescent SPP field in the direction perpendicular to the interface, surface plasmons propagating on the air/metal interface may decay into photons in the glass (see Fig. 1.4).

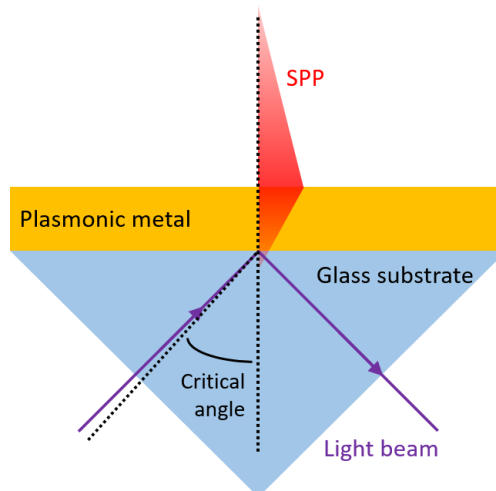


Figure 1.4: Kretschmann configuration for SPPs propagating on an air/metal interface. This configuration may be used either to detect light from propagating surface plasmons, or to excite them using a light beam, as is shown schematically in the figure. As the incident angle of the light beam is higher than the air/glass critical angle, an evanescent wave forms on the glass/metal interface.

In order for the propagating surface plasmons to decay into photons through the plasmonic film and into the higher refractive index medium below, the surface plasmon penetration depth in the metal must be longer or of the same order of magnitude as the plasmonic film thickness. The penetration depth (or skin depth) of

the evanescent wave into either medium depends on k_z (see Eq. 1.2):

$$d_{z,j} = \frac{1}{2|k_{z,j}|}, \quad j = \text{dielectric (1) or metal (2)} \quad (1.2)$$

Another important parameter for SPPs is the propagation length. Since metals are lossy, the propagating surface plasmon intensity decreases with propagation. The propagation length is derived from k_{SPP} and depends on the plasmonic material:

$$L_{SPP} = \frac{1}{2\text{Im}(k_{SPP})} \quad (1.3)$$

Using the permittivity values at a wavelength of 700 nm from Refs. [16] ($\epsilon_{Au} = -16.486 + i1.0643$ at 700 nm) and [17] ($\epsilon_{Al} = -61.874 + i26.797$ at 700 nm, from the Brendel-Bormann model), we may calculate the theoretical values of the penetration depth and the propagation length for propagating surface plasmons on different plasmonic metals.

We calculate $d_{z,2} \approx 7$ nm and $d_{z,1} \approx 434$ nm for surface plasmons propagating at an interface between an aluminum film (2) and air (1), and $d_{z,2} \approx 13$ nm and $d_{z,1} \approx 219$ nm for surface plasmons propagating at an interface between a gold film (2) and air (1), for SPPs with an energy corresponding to a photon wavelength of $\lambda_0 = 700$ nm. The theoretical propagation length for SPPs ($\lambda_0 = 700$ nm) is around $26 \mu\text{m}$ on a gold film, and around $16 \mu\text{m}$ on an aluminum film (both in air).

1.1.4 STM-excitation of surface plasmons on a thin gold film

The scanning tunneling microscope (STM), whose principle will be described in detail in Section 1.2.1, may be used to excite surface plasmons on a local scale (~ 10 nm). Figure 1.5 shows the result when the ‘‘STM-nanosource’’ is used to locally and electrically excite local and propagating surface plasmons on a thin (50-nm) gold film on glass. Using leakage radiation microscopy (see Section 1.2.5), similar to the Kretschmann configuration described above (Section 1.1.3), the light emitted from decaying SPPs may be detected. This experimental signal may be considered proportional to the surface plasmon intensity. In particular, the spatial distribution of the excited propagating surface plasmons may be modeled as an outgoing circular wave (with r the distance from the excitation point):

$$I_{SPP}(r) \propto \frac{e^{-r/L_{SPP}}}{r} \quad (1.4)$$

This expression, along with the data of Fig. 1.5, may be used to determine the SPP propagation length. Figure 1.5-a is a real plane image of surface plasmons excited using an STM and propagating on a gold film. We see that the signal is divided into three parts: at the source, the light is dominated by a pattern characteristic of the emission from a vertical oscillating dipole (ring of light with a dip in the intensity at the source point), due to localized surface plasmons. Indeed, the inelastic tunneling current may be modeled as vertical oscillating electric point dipole [18]. Thus, we cannot take into account this section to evaluate the propagation length of propagating surface plasmons. On the other hand, after a few micrometers, the signal is too low. By fitting the middle part of our signal in Fig. 1.5-a, we measure a value of $4.1 \mu\text{m}$ for the experimental propagation length for an air/gold interface.¹

The ‘‘STM-nanosource’’ may not only be used for the local, electrical excitation of surface plasmons, but may also excite light from semiconductors. In this thesis, we study a specific kind of semiconductor: transition metal dichalcogenide monolayers.

¹This experimental value is lower than the theoretical value possibly due to the roughness of the plasmonic film on which the surface plasmons propagate, which may act as a grating and cause them to decay into photons or to the fact that the signal is not very intense, and thus the noise may mask the tail of the exponential decay, thus artificially reducing the propagation length.

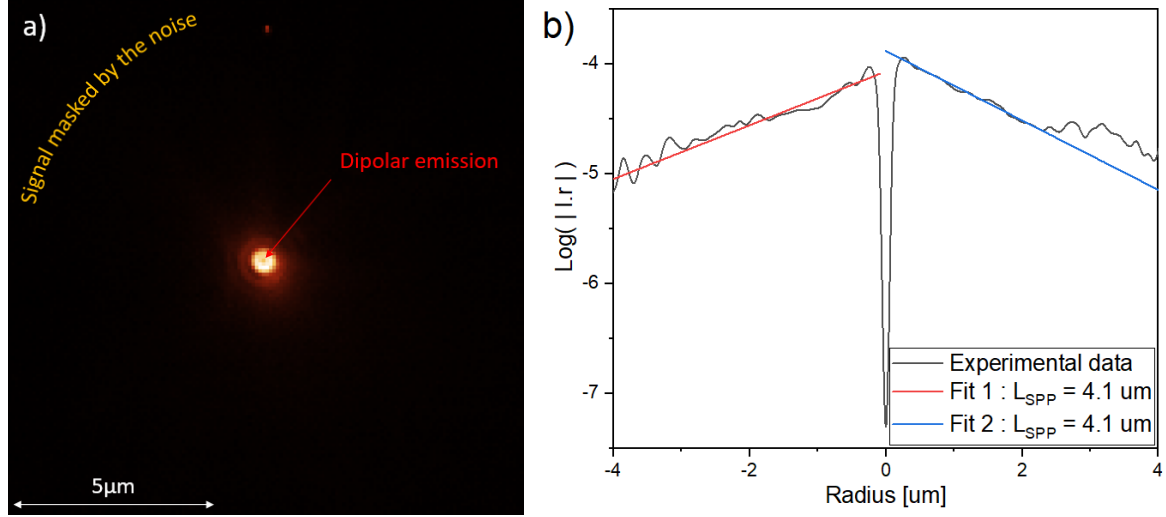


Figure 1.5: Light detected in transmission using leakage radiation microscopy a) for surface plasmons propagating on a gold film in air, with the fit represented in b). A linear fit is carried out on the curve $\log(Ir) \propto -r/L_{SPP}$ with r the distance from the excitation point.

1.1.5 An introduction to excitons in transition metals dichalcogenides

Transition metal dichalcogenides (TMDs) are MX_2 materials with M a metal atom (typically molybdenum Mo or tungsten W) and X a chalcogen atom (such as sulfur S, selenium Se or tellurium Te) organized in a X-M-X hexagonal mesh stacked in layers. We show in Fig. 1.6 the structure of a single TMD layer, which is composed of three covalently-bonded atomic planes in a compact hexagonal mesh. Subsequent layers are held together by van der Waals forces.

The electronic and luminescence properties of these materials are highly dependent on the number of layers in the sample: when in multilayers, the TMD photoluminescence is extremely low compared to the photoluminescence of a monolayer. This is due to a shifting of the gap, from a direct configuration for monolayers to an indirect gap for multilayers due to interlayer interactions [19]. As a goal of this thesis is to study the luminescence of such materials, we will only study monolayer TMDs.

Another particularity of this family of materials is their excitonic properties. The luminescence from most semiconductors is generally band-edge luminescence: an electron in the conduction band recombines with a hole in the valence band, emitting a photon with the electronic gap energy. However, in monolayer TMDs, due to reduced dielectric screening because of the 2D geometry, the luminescence is principally from exciton recombination. An exciton is a neutral quasiparticle composed of an electron bound to a hole, whose energy differs from the electronic gap energy by the binding energy (see Fig. 1.7). The exciton energy thus corresponds to the optical bandgap energy, which is defined as the lowest energy for the absorption of a photon.

In most semiconductors such as gallium arsenide, the exciton binding energy is on the order of a few tens of meV. For TMD monolayers however, the exciton binding energy is on the order of several hundreds of meV. It is for this reason that the luminescence from these materials is dominated by exciton recombination.

However, excitonic luminescence may not be reduced to a single peak in the luminescence spectrum: indeed, several types of excitons exist, and have different energies. In a monolayer TMD, due to spin-orbit coupling, the bands of spin-up and spin-down electrons are split, i.e., are of different energy. This energy splitting is on the order of 10 meV or a few hundred meV for the conduction and valence band electrons respectively [20, 21]. Thus, this means there are four different exciton configurations possible: two where the electron and the hole in the exciton have the same spin (i.e., both spin-up or both spin-down), in which case they form a “bright” exciton that, according to selection rules, is able to decay radiatively; and two configurations where they have a different spin (i.e., spin-up hole and spin-down electron or vice-versa), in which case they form a “dark” exciton that cannot radiatively decay. Thus, we have two bright excitons, which may recombine and emit a photon, and two dark excitons, which recombine non-radiatively, of different energies.

Moreover, the calculations for the “neutral” excitons in Ref. [20] and [21] consider that the TMD monolayer is a perfect crystal, which may not be the case experimentally. Indeed, the monolayer may be stretched locally if the substrate is not atomically flat, or cracked, and some atoms may be missing or replaced, forming defects. These defects are known to alter the band structure, thus the excitons may propagate in the monolayer until they encounter a defect in which they become trapped. We call excitons trapped in defects localized excitons,

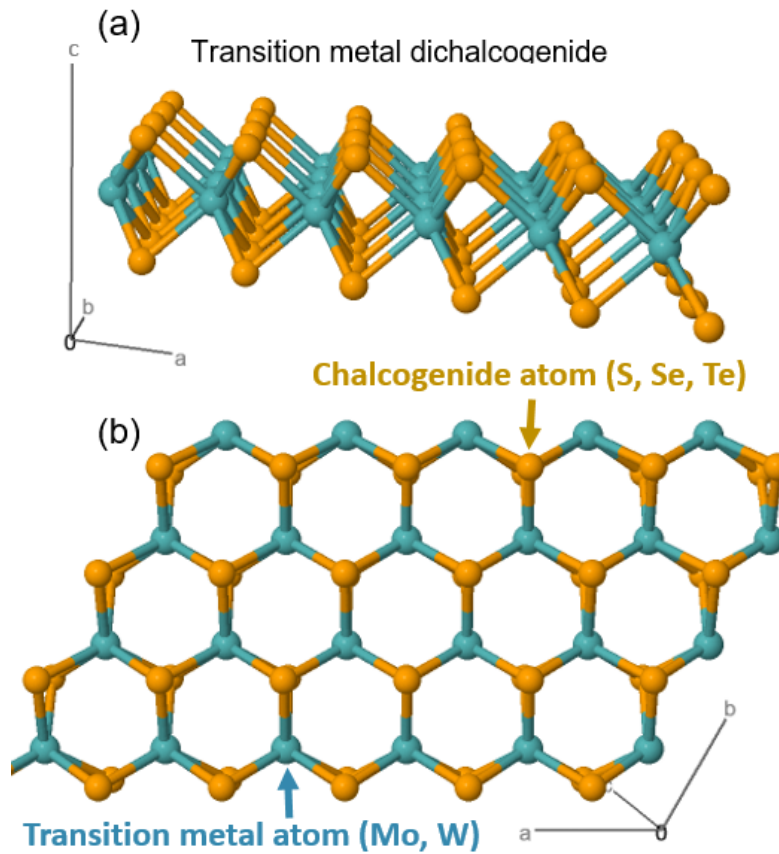


Figure 1.6: Stick-and-ball schematic of a TMD monolayer, with (a) a side and (b) a top view, with the transition metal atom (either molybdenum or tungsten) in blue and the chalcogen atom (either selenium, sulfur or tellurium) in orange.

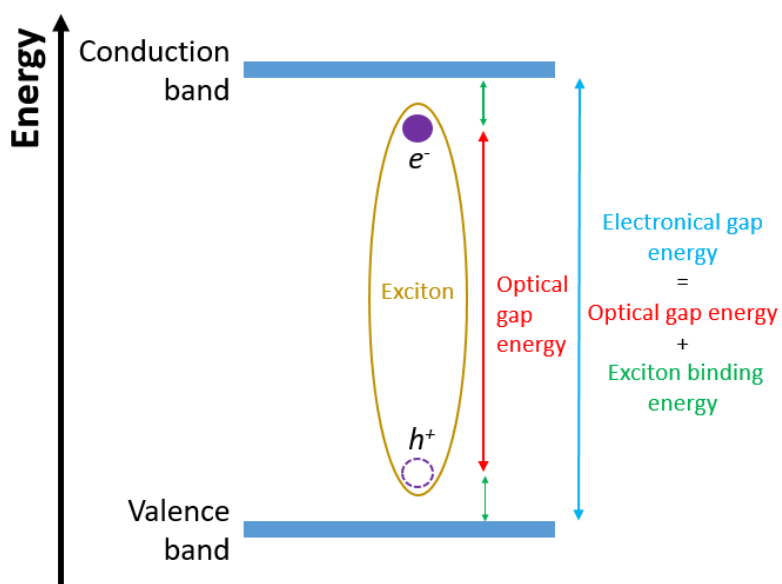


Figure 1.7: Schematic of the band structure of a TMD, with the excitonic states in the electronic bandgap and the different energies mentioned. The electronic bandgap differs from the optical bandgap by the exciton binding energy, which is higher than in most semiconductors.

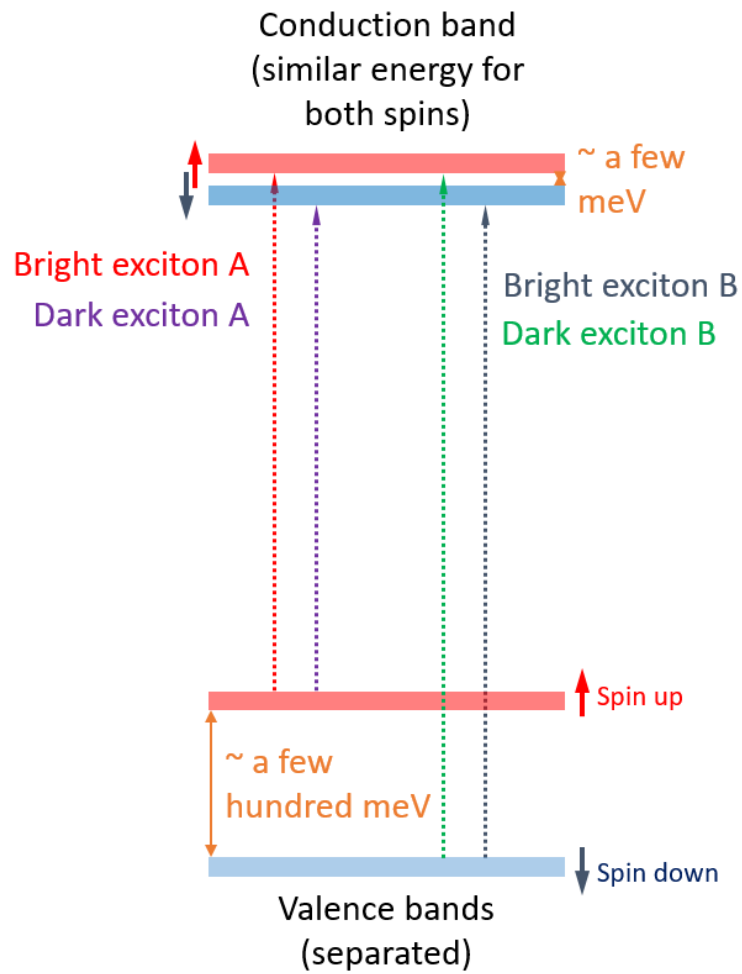


Figure 1.8: Schematic of the band structure for a TMD monolayer: due to spin-orbit coupling, the bands for spin-up and spin-down electrons are at different energies. The conduction bands are quasi-degenerated as the spin-up and the spin-down conduction bands are only different by a few meV in energy. However, the valence band splitting is much higher, with a splitting of around 150 meV for MoS₂ to around 460 meV for WSe₂ [20]; thus two bright excitons (A) and (B) of different energy contribute to the spectra.

which in general have a lower energy than neutral excitons [22–29].

Another contribution to excitonic luminescence may come from the recombination of charged excitons or trions, which are quasiparticles composed of two electrons and one hole (negatively charged exciton) or two holes and one electron (positively charged exciton). The binding energy of a charged exciton is higher than that for a neutral exciton, thus their contribution to the luminescence spectrum is of lower energy [21, 30, 31].

1.2 Tools and methods

In this thesis, we study two types of systems: on one hand, we study how a nanoantenna can modify the excitation and emission of electrically excited propagating surface plasmons (see Chapters 3 and 4), and on the other hand we study the electrical excitation of excitons in transition metal dichalcogenides (TMDs) (see Chapter 2). Both of these experiments are carried out using inelastic tunneling current as the excitation using the different setups presented here.

1.2.1 Scanning tunneling microscopy

One of the most important instruments used in this thesis is the scanning tunneling microscope (STM). This technique was invented in 1981 by Binnig and Rohrer [32], who were awarded the Nobel Prize in 1986 in recognition of the great impact this new technology would have on the field of nanoscience [33]. Indeed, an STM measures the topography of conducting samples on the nanoscale by monitoring the tunneling current between a sharp metallic tip and a conducting sample (see Fig. 1.9). As the tunneling current decays exponentially with the distance between the two conductors, a feedback loop precisely corrects the position of the tip using a piezoelectric crystal so that the tunneling current measured corresponds to a given setpoint (with a vertical precision on the order of magnitude of a few hundred pm in our setup). This gives us a very accurate measurement of the sample’s height variations.

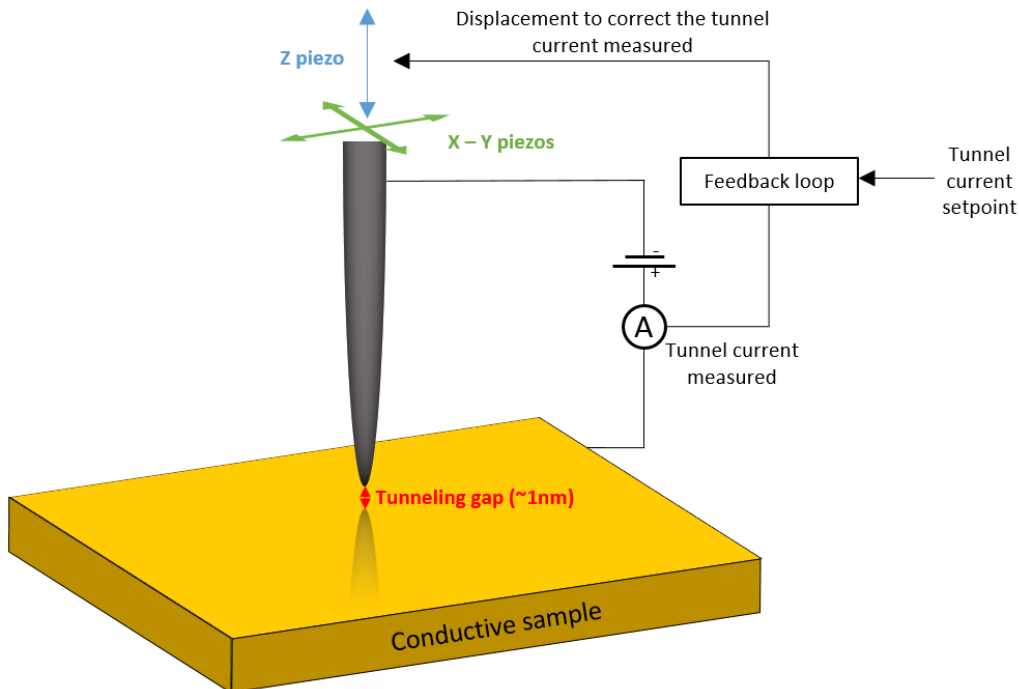


Figure 1.9: Operation of an STM.

One of the great advantages of the STM, as seen earlier, is that it may also act as an excitation tool: as the tunneling current used in the STM is composed of both elastic tunneling current and inelastic tunneling current (see Section 1.1.2), the inelastic tunneling current may excite surface plasmons on plasmonic nanostructures (see Chapter 3) or excitons in a monolayer TMD (see Chapter 2).

In our experiments, we use an STM module with the Nanowizard 3 head from JPK Instruments and chemically etched tungsten tips [34]. This STM works in air, and as we will see later, we couple this STM to an

optical microscope to detect the emission of light through the sample after STM excitation.

1.2.2 Atomic Force Microscopy

However, an STM is not the only option for using tunneling current as an excitation: we may use integrated tunneling junctions between two conductors separated by an insulating layer to excite surface plasmons for example, as will be presented in Chapter 4. In this case the excitation occurs in the integrated tunneling junction, provided that we may contact both conductors to apply a voltage. In order to do so, in this work we use an atomic force microscope (AFM).

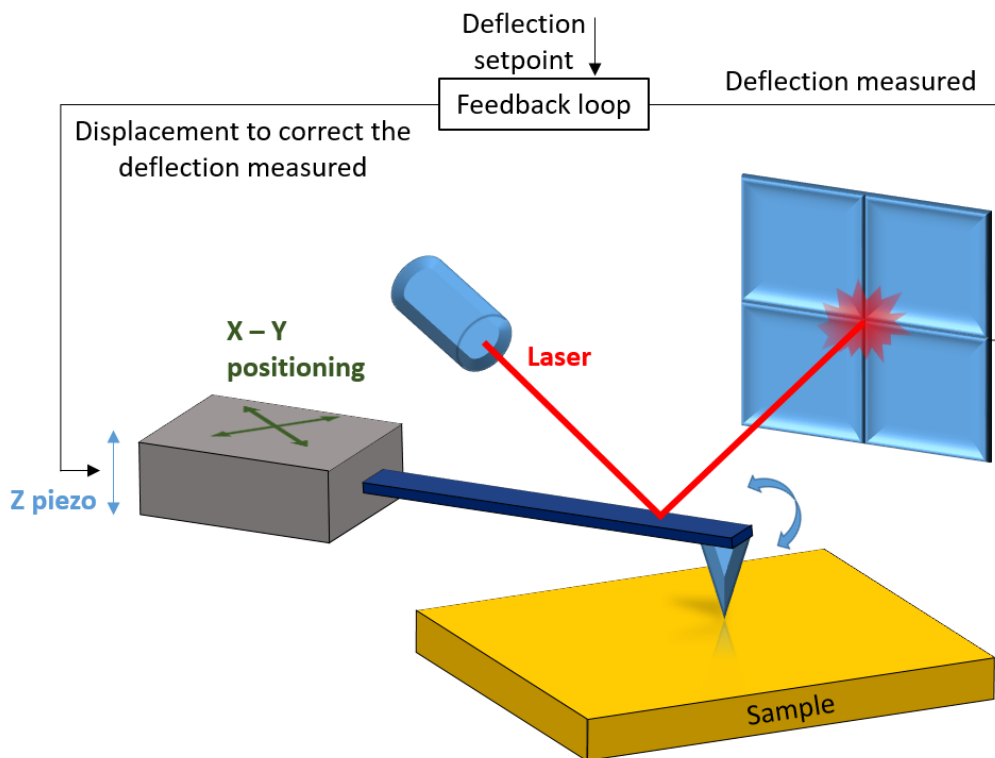


Figure 1.10: Operation of an AFM.

Invented by Binnig, Quate and Gerber in 1986 [35], the AFM may be used to measure the topography of a sample, be it conducting or insulating. An AFM has a cantilever with a sharp tip at the extremity that is displaced horizontally and vertically by applying different voltages to piezoelectric crystals (see Fig. 1.10). A laser illuminates the back of the cantilever, which is generally covered with a reflective layer so that the laser is reflected onto a four-quadrant detector. The movement of the laser spot on this detector is due to the bending of the cantilever, which is called the deflection. When the cantilever is far from the surface, there are no forces applied on the tip, so no deflection is measured. When we approach the surface, the tip will be subjected to both attractive van der Waals forces and repulsive forces (due to the Pauli exclusion principle), which will cause the cantilever to bend (see Fig. 1.11).

In our setup, we use two different conducting AFM modules with the Nanowizard 3 head from JPK Instruments, one which is optimized for low currents (~ 10 pA of noise, but with a maximum current measurement of 120 nA) and another for high currents (with a maximum current measurement of 120 μ A, but ~ 10 nA of noise).

The AFM may be used in different modes. In this thesis, we will use two different modes, which are called “contact mode” and “tapping mode” (see Fig. 1.11). When we are in “contact mode”, we fix a deflection setpoint for the cantilever and when we move the tip on the surface, the feedback loop adjusts the height of the tip by applying different voltages on the piezocrystals so that the cantilever deflection does not change from the chosen deflection setpoint.

“Tapping mode” refers to a mode for which the cantilever is made to oscillate with a fixed amplitude. When we approach the surface, the effective amplitude of the cantilever oscillation will be smaller: the forces applied on the tip will shift the resonance frequency and decrease the oscillation amplitude. This decrease in amplitude will prompt the feedback loop into sending a signal to the piezoelectric crystal which controls the height of the

tip, in order to lift the tip until the oscillation amplitude is again at the chosen amplitude setpoint.

Contact mode was the first mode used historically, and is necessary in some measurements using the AFM such as friction [36, 37], elasticity [38, 39] or surface force measurements [40, 41], but it may also damage softer samples or move unattached particles on the surface of the sample. To avoid such problems, we use tapping mode, as the interaction between the tip and sample is smaller in tapping mode. Concerning the probe, the main difference between the probes used for each mode is the rigidity of the cantilever: a contact mode probe will have a flexible cantilever (spring constant $k \sim 0.1$ N/m) whereas a tapping mode probe will be much more rigid (spring constant $k \sim 50$ N/m).

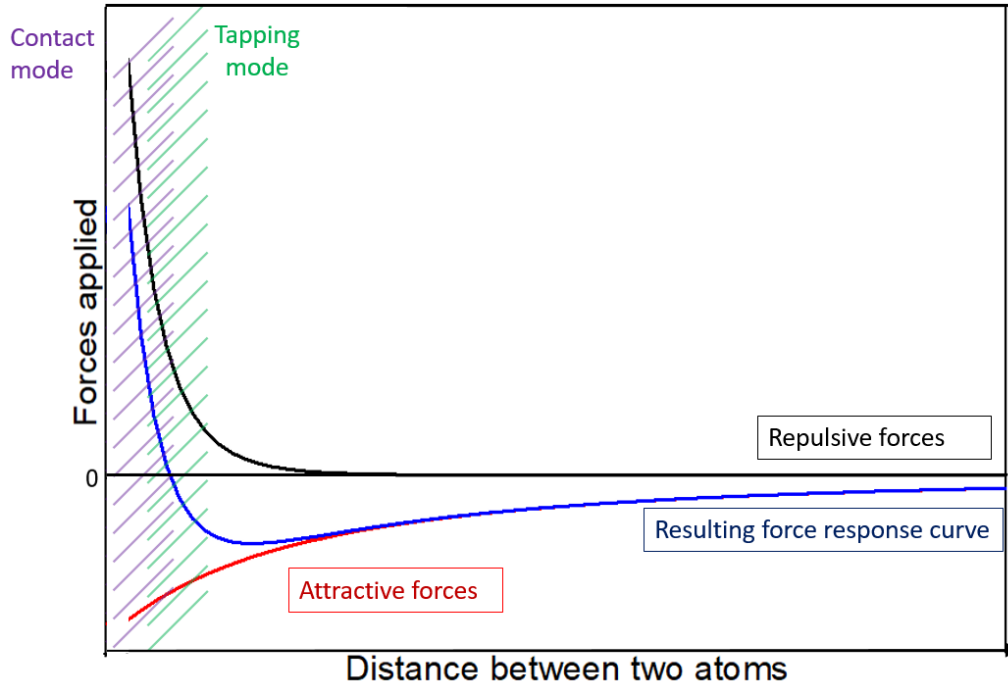


Figure 1.11: For simplification purposes, the forces between the AFM tip and the sample are approximated by the derivative of the Lennard-Jones potential, which describes the forces between two atoms. Here the force as a function of separation is plotted, along with the different regions for the different AFM modes: when in contact mode, the repulsive forces (due to Pauli’s exclusion principle, $F \propto 1/r^{13}$) are dominant. In tapping mode, the forces applied on the tip are attractive on average (van der Waals, $F \propto -1/r^7$).

1.2.3 Resolution in ambient scanning probe microscopy

It is important to note that while both the STM and the AFM are known for their atomic resolution when working at low-temperature and in ultrahigh vacuum [42–44], different factors degrade the resolution for both instruments when operating under ambient conditions. One of these factors is thermal drift [45–47]: under ambient conditions, temperature gradients are common, and lead to a dilatation or a shrinkage of the sample, the tip, the tip holder, etc. As the thermalization of the system is slow, we subtract a vertical offset from each line of the scan to compensate for a possible change in the tip-sample distance due to thermal drift. In this thesis, every STM and AFM image will be corrected for the vertical (but not in-plane) thermal drift. Another factor is the air currents and vibrations carried in the air (mostly due to the room air conditioning in our case), which we dampen by enclosing our system in a box equipped with dampening foam in the panels.

There are other factors which affect the quality of our AFM or STM images, which we cannot control or correct. The main one is that any surface in air has a thin film of water adsorbed on it (up to 10 nm thick for a humidity of 50% [48]). When we use an STM tip on a conducting surface, the two thin films of water merge and a water bridge appears between the tip and the sample. If we apply a voltage higher than the dissociation potential of water (1-1.5 V, see [49]), an ionic current contribution may appear and perturb our measurement, as was discovered previously in our group (see [50]). Moreover, as our sample is exposed to ambient conditions, unavoidable contaminants settle on the surface. The impact of these contaminants is well known, especially when measuring the barrier height under ambient conditions [51]. (This will be discussed more in detail in Sections 4.2.1 and 4.3.1). Finally, the uncorrected in-plane thermal drift may deform our topography images.

Another factor affects the lateral resolution: tip-sample convolution. When scanning the sample, be it with

an AFM or an STM, the resulting image will be the product of the topography convoluted with the tip shape [45, 52, 53]. This is due to the fact that in the case of the AFM, the tip has a sharp conic shape whose sides may also be in contact with high aspect ratio nanostructures: see Fig. 1.12-a. Similarly, in the case of the STM, the tunneling current, which is supposed to travel through the gap between the atom at the end of the tip and the surface, may also go through the side of the tip and a high aspect ratio nanostructure: see Fig. 1.12.b.

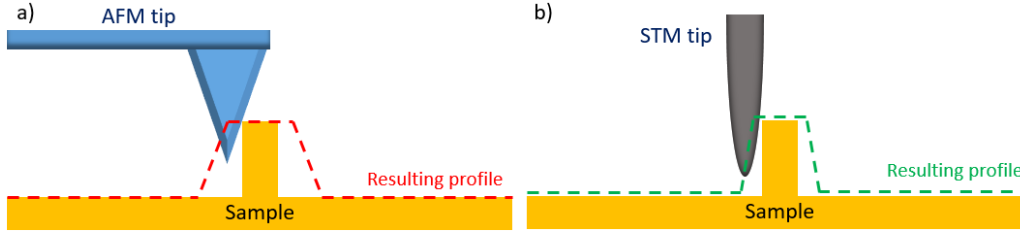


Figure 1.12: Convolution for a) an AFM image, b) an STM image.

1.2.4 Optical excitation

Lastly, we may use light as a means of exciting excitons when working with TMDs (see Chapter 2): we use either an argon ion laser ($\lambda_{Ar} = 465.8$ nm) or a diode laser ($\lambda_{diode} = 405$ nm), which is collimated and illuminate the sample to excite excitons emitting in the 600 – 900 nm range. The light coming from the sample is filtered for the reflected laser light so that the only photons collected from the sample are the ones resulting from exciton recombination.

1.2.5 Optical detection

Once the sample has been excited, either by a light source (see the light path in orange in Fig. 1.13) or by electrical means (AFM and STM head in purple in Fig. 1.13), we want to analyze the light emitted from the sample, be it due to surface plasmon relaxation or exciton recombination. In order to do so, we use an inverted optical microscope to collect the light (blue square in Fig. 1.13). In our setup, we use an oil immersion objective with a 1.49 numerical aperture from Nikon (model CFI apochromat TIRF 100x) to collect the emitted light. The light then goes through several stages in which we can introduce filters to block the laser light if needed, and mirrors to direct the light either to the optical microscope's eyepiece or toward the detectors (either the CCD camera or the spectrometer, light path in yellow in Fig. 1.13). The elements are chosen so as to be most efficient in the visible range, so our setup is best suited for light detection in the 400 – 900 nm spectral range (see Fig. 1.14).

Spectra

In this thesis, all the spectral measurements will be presented corrected by the detection efficiency of the instruments. The light may be directed to detector 1, a liquid-cooled (-70°C) Andor CCD camera (iKon-M) or to detector 2, a liquid-cooled (-80°C) Horiba spectrometer composed of an iHR320 grating turret with a choice of two gratings combined with a Synapse CCD detector. As our spectrometer has two gratings with different groove densities that may be used, we can either obtain a broad spectrum ($\Delta\lambda = 536$ nm) with a lower resolution ($\delta\lambda = 0.5$ nm) with a 150 grooves/mm grating, or a narrower spectrum ($\Delta\lambda = 135$ nm) with a higher resolution ($\delta\lambda = 0.13$ nm) with a 600 grooves/mm grating. Both gratings have a 500 nm blaze wavelength.

Real and Fourier plane imaging

In the yellow light path in Fig. 1.13, we can add polarizers or filters, and flipable lenses (marked in green in Fig. 1.13) so that we may choose whether to image the real plane (spatial distribution of the emitted light: Fig. 1.15-a) or the Fourier plane (angular distribution of the emitted light: Fig. 1.15-b). A flipable mirror (marked in red in Fig. 1.13) then redirects the light toward the detector 1 or 2. The real plane is an image where all the light coming from the same object point is focused on the same image point. Using such an image, we can determine where the light is coming from on the sample: for example we are able to see how far excitons

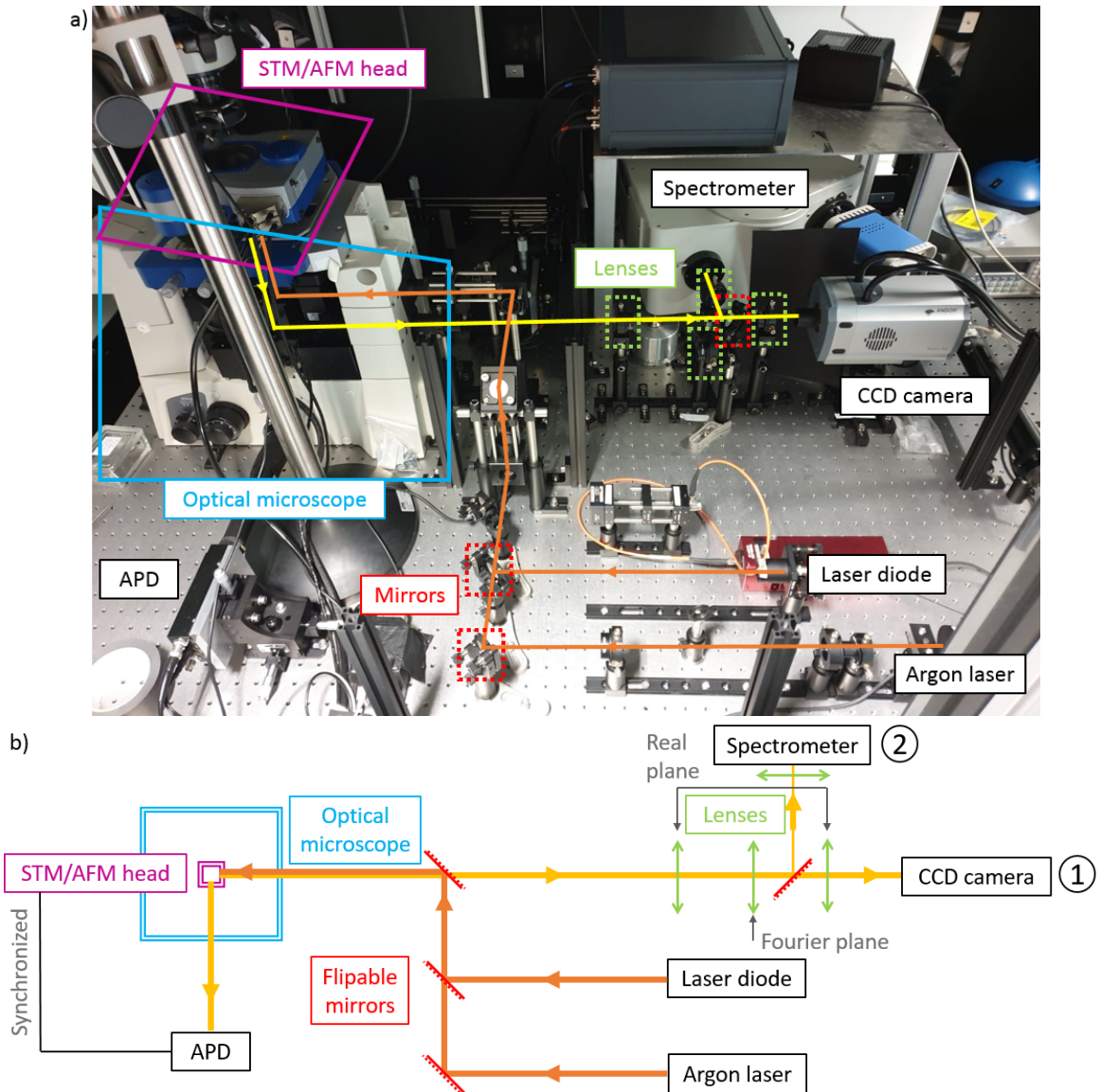


Figure 1.13: a) Experimental setup, b) Light path schematic. The CCD camera is labeled “detector 1” and the spectrometer “detector 2”.

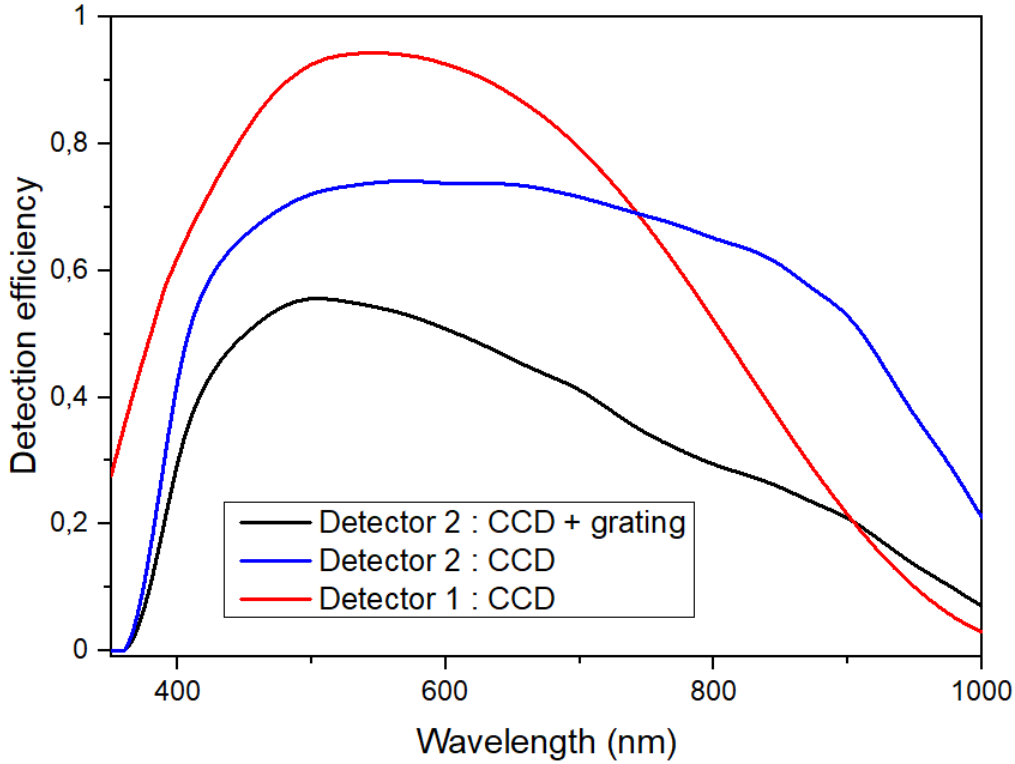


Figure 1.14: Detection efficiency of the Andor CCD (detector 1, red line), of the CCD of the Horiba spectrometer (detector 2, blue line), and of CCD and grating for spectral measurements with the Horiba spectrometer (black line). The different detection efficiencies were obtained from the manufacturers.

propagate in a TMD layer before recombining and emitting light (see Chapter 2). The Fourier plane on the other hand is an image in which all the light emitted at the same angle is focused on the same image point. Using such an image, we may determine at what angle the light is emitted. For example in our experiments, we can recognize the emission of light from propagating surface plasmons. This is because propagating surface plasmons on a thin film on a glass substrate may only decay through the film into photons in the substrate at a certain angle. Thus, the Fourier plane image of propagating surface plasmon relaxation will show only a narrow circle of light in the case of a point source excitation. The radius of this circle corresponds to the leakage radiation angle, i.e., the angle of photon emission from SPPs in the Kretschmann configuration (more details on the decay of propagating surface plasmons into photons using the Kretschmann configuration in Section 1.1.3). This type of measurement is known as leakage radiation microscopy [54].

Spatial resolution

In order to determine what limits the spatial resolution of our optical system, we have to compare the pixel size of our detectors to the diffraction limit in our setup. The magnification of our setup is $\times 150$ for detector 1 and $\times 75$ for detector 2 (see Appendix B for more details). Detector 1 has 1024×1024 pixels, each pixel being $13 \mu\text{m} \times 13 \mu\text{m}$ in size and detector 2 has 1024×256 pixels, each pixel being $26 \mu\text{m} \times 26 \mu\text{m}$ in size. Thus, the distance between two pixels on the images is 86 nm ($13 \mu\text{m}/150$) on detector 1 and 347 nm ($26 \mu\text{m}/75$) on the detector 2.

Due to the diffraction of light, the distance between two distinguishable points using the Rayleigh criterion is [55]:

$$d = \frac{\lambda_0}{2 n \sin\theta_{max}} \quad (1.5)$$

with a vacuum wavelength λ_0 of 700 nm and knowing that our objective numerical aperture $n \sin\theta_{max}$ is 1.49 (with θ_{max} the maximum acceptance angle of the objective and $n = 1.52$ the index of refraction), the diffraction limit is 235 nm , which is larger than the detector 1 pixel image size, for which we are thus only limited by the diffraction of light. It is however slightly smaller than the detector 2 pixel image size, for which our spatial resolution is limited by the pixel size. Note that in our experiments, the number of emitted photons

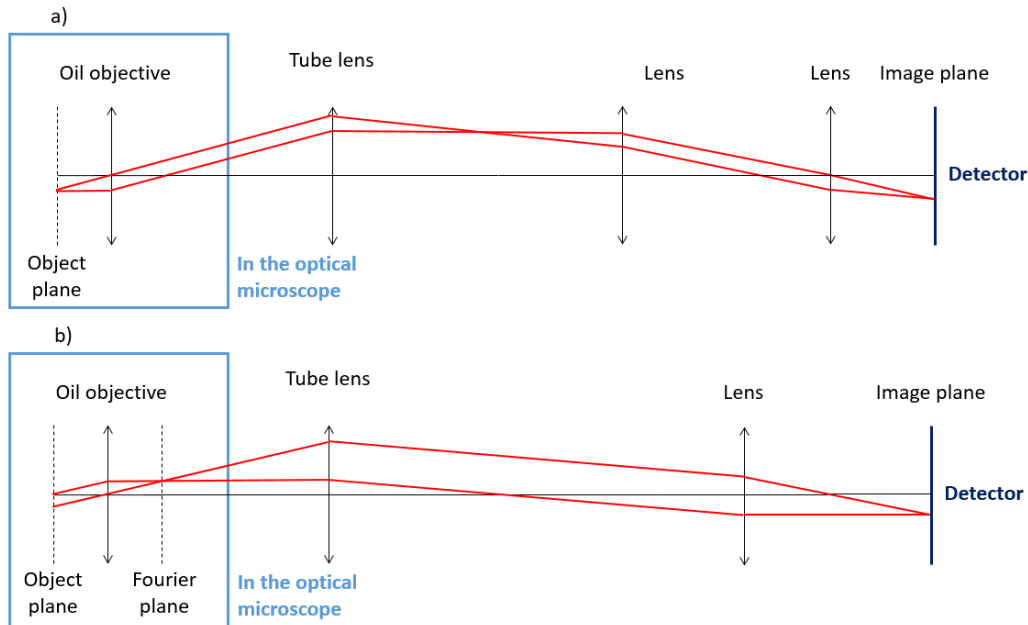


Figure 1.15: a) 4F setup for real plane imaging, b) setup for Fourier plane imaging.

is quite low, so when the photons are spread over the detector pixels to obtain the spatial, angular or spectral information we need to integrate the signal for a long time (50 to 200 seconds) to obtain a good signal-to-noise ratio.

Avalanche photodiode

Another detector available in the set-up is an Excelitas SPCM Avalanche Photodiode (APD): as its name indicates, the APD is a photodiode where the absorption of a photon triggers the creation of new charge carriers in an avalanche process. Therefore, this detector is very sensitive, with a 65% detection efficiency at 650 nm. It also has a recovery time of 35 ns after receiving a photon during which the recovery circuit restores the bias voltage after the avalanche, and thus the detector cannot detect the arrival of a new photon.² This detector cannot be used to collect spatial, angular or spectral information as all the light is collected on a single “pixel”, but it is very useful for collecting a low signal in a short time. On average, Excelitas guarantees a maximum dark count (number of counts recorded with no illumination) of 25 counts per second, but with our detector we measure an average dark count of 4 ± 2 counts per second, which is much better than what was expected. We collect the light emitted over a $250 \mu\text{m}^2$ area with this APD, which is a much larger than the area over which we would expect to have light emitted in our experiments.

Photon mapping

The short acquisition time of the APD gives us a new tool for our experiment: photon mapping. If we synchronize the acquisition of light with the APD with the STM scan, we use the STM both as an excitation source and as a topography imaging system simultaneously. We scan the surface of the sample very slowly, with a fixed tunneling current setpoint, and we collect the light emitted in the field of view with the APD for each point scanned by the STM on the surface. We may then associate each pixel of the STM image to the average measured tunneling current (which gives us the number of tunneling electrons passing between the tip and the sample while the STM tip is positioned at this specific pixel), and the total light collected while the STM tip is at this position. From these measurements, we calculate the experimental excitation efficiency (number of photons collected per electron) and correlate this information with the topography of the sample. This measurement can, for example, reveal nanometric defects in a TMD monolayer that impact the electroluminescence, as is presented in Chapter 2.

This setup is used in Chapters 3 and 4 to characterize the emission of photons from propagating surface plasmons and in Chapter 2 to characterize the emission from exciton recombination in TMDs.

²Note that an interesting article on the breakdown flash that appears in avalanche photodiodes and the vulnerability it induces in optical communications may be found here: <https://www.osapublishing.org/oe/fulltext.cfm?uri=oe-25-24-30388&id=377078>

1.3 Summary

In this chapter, we have presented the different excitation tools we use in our experiments, and the corresponding detectors. As we mainly use inelastic tunneling current to excite surface plasmons and excitons, the two most important tools are the STM (scanning tunneling microscope) which serves directly as an excitation source, and the AFM (atomic force microscope) which serves to electrically connect an integrated tunneling junction. These two techniques are also used to image the topography. We can also use light as a mean of excitation, with either a laser diode or an argon ion laser.

To detect and analyze the light emitted from the sample, we use a CCD camera to image either the real plane (which gives us spatial information) or the Fourier plane (which gives us angular information), or a spectrometer to collect the spectral information on the light emitted from the sample. Lastly, we use an avalanche photodiode synchronized with the STM to determine the experimental excitation efficiency by collecting the emitted light and the number of electrons passing through the junction for each pixel of the topography image.

The setup used for our experiments is presented in Fig. 1.13.

Chapter 2

STM excitation of excitons in transition metal dichalcogenides

In this chapter, we use our “STM-nanosource” (see Section 1.2) to excite the excitonic luminescence of transition metal dichalcogenides (TMDs). As discussed briefly in Section 1.1.5, monolayer TMDs are two-dimensional direct bandgap semiconductors whose excitons (bound electron-hole pairs) have relatively high binding energies (\sim several hundreds of meV) compared to most semiconductors and especially compared to thermal energy at room temperature ($\simeq 25$ meV at 300 K). The originality of the results reported here is that the emission of light is shown to be the result of locally-excited exciton recombination that does not involve the participation of surface plasmons, unlike what is the case in other work [24, 56–58].

The excitonic luminescence in the TMD MoSe₂ is locally activated using our ambient STM combined with an inverted optical microscope. This chapter is based on the work published in an article in Physical Review Letters [1]. In particular, thanks to local excitation and wide-field optical imaging, excitonic recombination at particular “hot spots” on the sample may be observed. As well, using a “mapping” technique (see Section 1.2) structural features, barely visible in STM topographs, may be identified in luminescence images.

2.1 Local exciton excitation using an STM

Electroluminescence investigations have recently been reported in TMD-based p-n junctions [59–62], tunnel junctions [63] and quantum-light emitting diodes [64]. In these studies, spatial control over exciton formation was typically limited to the micrometer scale due to the size of the devices. Investigating the optoelectronic response of 2D semiconductors at the nanometer scale may not only provide fundamental insights into their complex exciton dynamics but also improve the performances of future devices. Achieving such control on the nanoscale is a major challenge that has been tackled using tip-enhanced optical excitation recently [65, 66]. One particularly promising approach that suppresses the need for optical excitation is the use of a scanning tunneling microscope (STM), since the tunneling current is an extremely local, low-energy, electrical excitation [67–70].

In this chapter, we will use our STM-nanosource (see Section 1.2 and Fig. 2.1-a) to excite excitonic luminescence in a MoSe₂ monolayer without the participation of any surface plasmons. The sample in this experiment is an exfoliated MoSe₂ microflake that is deposited onto an indium tin oxide (ITO)-coated glass coverslip (ITO thickness of 85 nm) using a dry transfer method [71] (see Fig. 2.1). The sample was realized by Luis Parra Lopez from the Institut de Physique et Chimie des Matériaux de Strasbourg (IPCMS). The cracks and folds in the flake that are visible in the optical micrograph of Fig. 2.1-b result from the transfer process. Note that ITO is not plasmonic in the wavelength range of interest (i.e., the real part of the permittivity is positive) [72] (ITO refractive index in the supplementary materials).

Before proceeding with the STM-excitation experiment, wide-field photoluminescence is excited using an

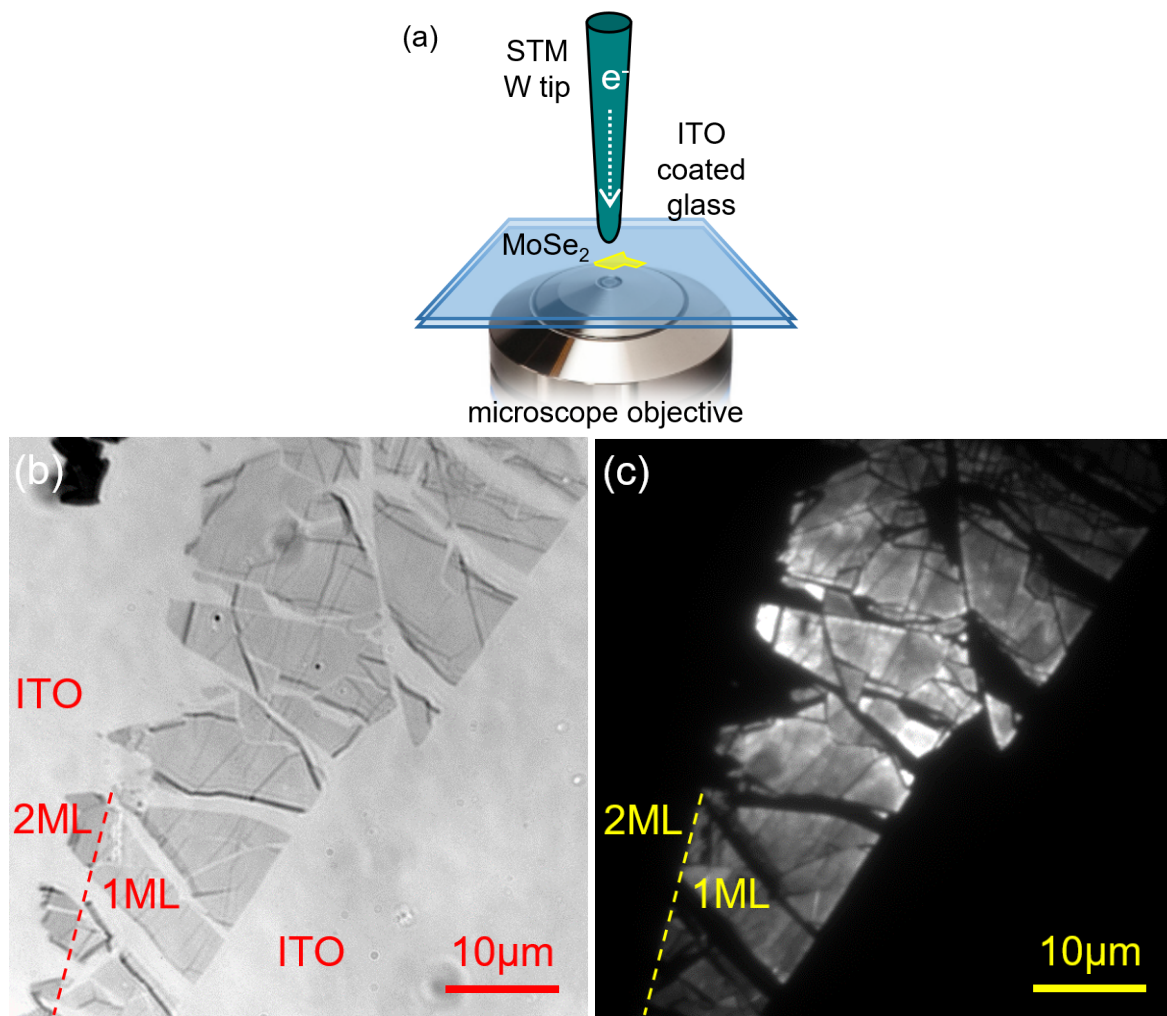


Figure 2.1: a) System used to electrically excite light in a MoSe₂ flake. b) Optical transmission image of the sample and c) photoluminescence image (excited using an argon ion laser). The MoSe₂ monolayers are unambiguously identified from their strong photoluminescence signal. The photoluminescence signal is not completely uniform in the image in part because the intensity of the excitation laser is not perfectly uniform over the field of view.

argon ion laser ($\lambda_{Ar} = 465.8$ nm, see Section 1.2.4). Comparing the photoluminescence and optical transmission images in Fig. 2.1-b and -c, we can easily discriminate between the mono and bi layers of the sample, as the luminescence abruptly decreases when passing from a monolayer to a bilayer due to the gap transition from a direct bandgap for a monolayer to an indirect bandgap for multilayer MoSe₂ [19]. In this way, an appropriate location on the flake for the local electrical excitation with the STM may be chosen as the monolayer is easily recognizable.

As described in Section 1.1.2 for surface plasmons, a bias of 1 to 4 V is applied between the non-plasmonic [73] electrochemically-etched tungsten STM tip and the ITO substrate in order to locally and electrically excite the MoSe₂ flake¹. The resulting emitted light is collected through the transparent substrate and focused on the entrance slit of a spectrometer (see Section 1.2.5). A typical electroluminescence spectrum is shown in red in Fig. 2.2.

In order to identify the source of the emitted light during STM-excitation of the MoSe₂ flake, we compare the laser-induced photoluminescence spectrum to an STM-induced electroluminescence spectrum in Fig. 2.2.

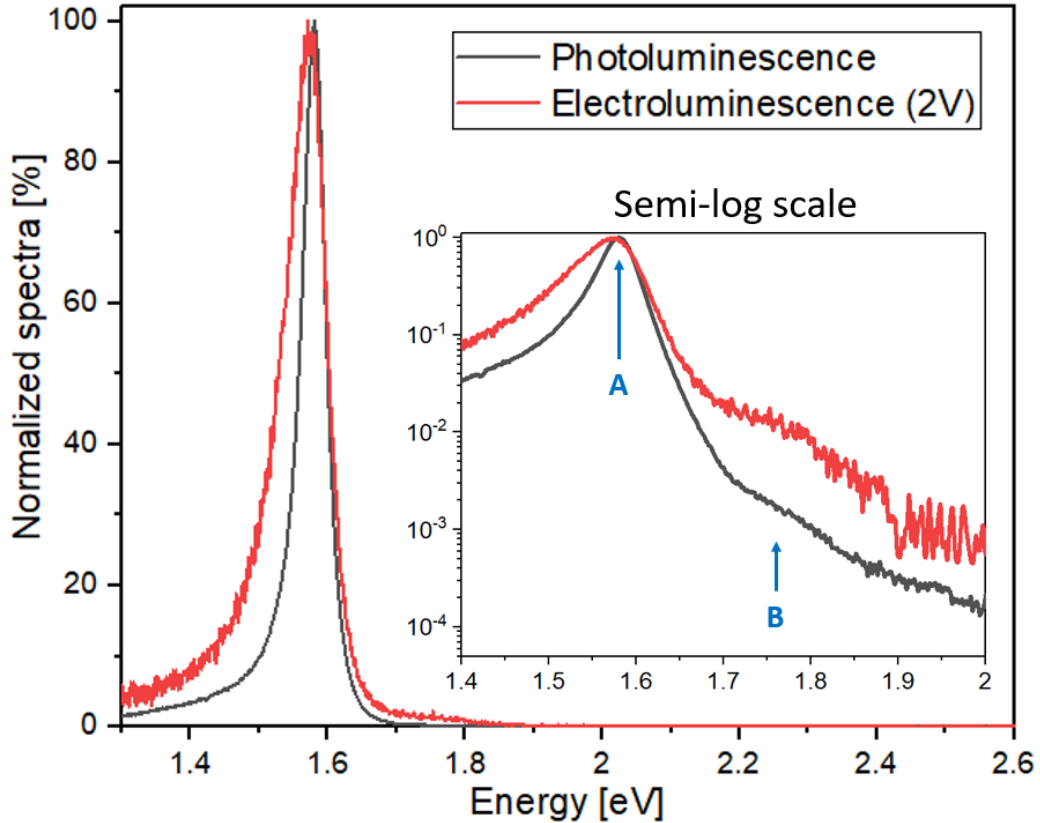


Figure 2.2: Photoluminescence (PL) and STM-induced electroluminescence (STM-EL) spectra, normalized by their maximum value. The inset shows the spectra on a semi-log scale, thus making a second peak (labeled B) more visible. The STM-EL spectrum is obtained for an excitation at $V_S = 2$ V, $I_{Setpoint} = 10$ nA and acquisition time = 150 s. Note that the spectra are obtained as a function of wavelength and we use the Jacobian transformation for nm-to-eV unit conversion [74]. The spectra are corrected for the setup transmission. These corrections will be applied to every spectra in this chapter unless stated otherwise.

From Fig. 2.2, we note that the STM-induced electroluminescence and laser-induced photoluminescence spectra from monolayer MoSe₂ are similar to each other. Both spectra exhibit an emission peak at 1.58 eV (labeled A in the inset) and another, visible in the semi-log plot in the inset, blue-shifted at 1.78 eV (labeled B).

In Fig. 1.8 of Section 1.1.5 the different types of excitons in TMDs are explained. The values of the peaks in Fig. 2.2 are typical of bright excitons in MoSe₂ at room temperature [75], with a 180 meV shift between the two, which matches the energy splitting of the valence band (the conduction band splitting is only a few meV [21]). Thus, we ascribe the peak at 1.58 eV to the bright exciton A and the blue-shifted peak at 1.78 eV to the bright exciton B. Due to this similarity between the photoluminescence and the electroluminescence spectra, we propose that the dominant emission process of STM-induced electroluminescence from monolayer MoSe₂ on ITO

¹The STM-excitation may alter the sample. See Appendix E for details. To eliminate this possible effect, each excitation is carried out on a fresh part of the flake, where no excitation has been carried out before, and we continuously scan a 50 nm x 50 nm zone during each electroluminescence measurement.

is the radiative recombination of A excitons in MoSe₂, with a smaller contribution from the B excitons. Other emission mechanisms such as blackbody radiation or radiative electronic transitions between tip and surface states may be ruled out because of the close match of the EL results to the photoluminescence spectrum.

Both the electroluminescence and photoluminescence peaks in Fig. 2.2 appear to be broadened on the low-energy side. This may be due to a luminescence contribution from charged excitons or trions [21, 30, 31]. Trions are quasiparticles consisting of two electrons and a hole or two holes and an electron. Other reasons for this broadening of the luminescence peaks toward the lower energies may be due to additional contributions from vibronic transitions [76, 77] or localized charged excitons in defects [22, 23], all of which cannot be resolved in our room-temperature experiment. The shape of the spectra will be discussed further in Section 2.2.

Another possible contribution to the luminescence spectra could be from the ITO substrate. In order to verify this, photoluminescence and electroluminescence measurements are performed on an ITO layer on glass (see Fig. 2.3). The relative intensity of the photoluminescence signal on ITO is three orders of magnitude lower than that from monolayer MoSe₂ and may be easily distinguished since its spectrum is comparatively broad (see the dark blue curve of Fig. 2.3). Two broad peaks at 1.80 eV ($\lambda = 690$ nm) and 2.30 eV ($\lambda = 540$ nm) each with a full-width-at-half-maximum of around 0.5 eV may be seen. The electroluminescence spectrum of ITO shown in Fig. 2.3 (light blue curve) is very different from both the electroluminescence of monolayer MoSe₂ and the photoluminescence of ITO. Note, however, that the ITO EL spectrum is reminiscent of the result obtained when light is scattered by a sharp W tip [78]. Plotting the PL and EL data from monolayer MoSe₂ on the same graph (red and orange curves in Fig. 2.3), it appears that no contribution from ITO is present in the MoSe₂ spectra.

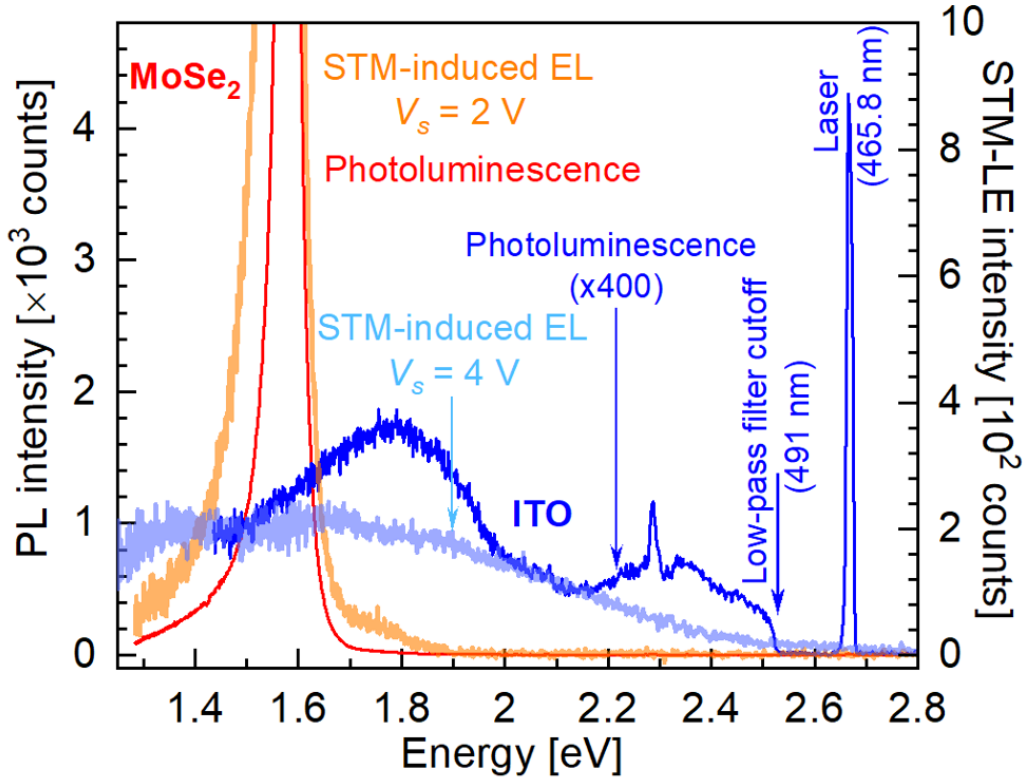


Figure 2.3: Laser-induced photoluminescence and STM-induced luminescence spectra of ITO, compared to what we obtain on monolayer MoSe₂. The laser excitation is at a wavelength of 465.8 nm and a long-pass filter starting at a wavelength of 491 nm is used at detection. The STM tunneling current setpoint is 0.1 nA and the sample bias is 4 V for the ITO electroluminescence, and the parameters are 10 nA and 2 V for the MoSe₂ electroluminescence. Acquisition time is 150 s. The small peak at 2.28 eV is believed to be the Raman signal from the oil of the oil immersion objective.

The emitted light may be analyzed further using Fourier-space imaging (see Section 1.2.5). Figure 2.4-a shows an experimental Fourier-space image of the angular distribution of the STM-induced electroluminescence from monolayer MoSe₂. We note that the experimental Fourier image consists of a disk of approximately constant intensity, surrounded by a brighter ring. The maximum intensity of this ring occurs at its inner diameter and decreases with increasing emission angle (see the black crosses in Fig. 2.4-d). The intensity of the central disk is equal to approximately 70 % of the intensity of the inner diameter of the ring. This result is then compared to the results of a simple analytical model. Because excitons in monolayer TMDs have a Bohr radius of only about 1 nm [79], they may be modeled as a dipole point source. Thus we calculate the far-field

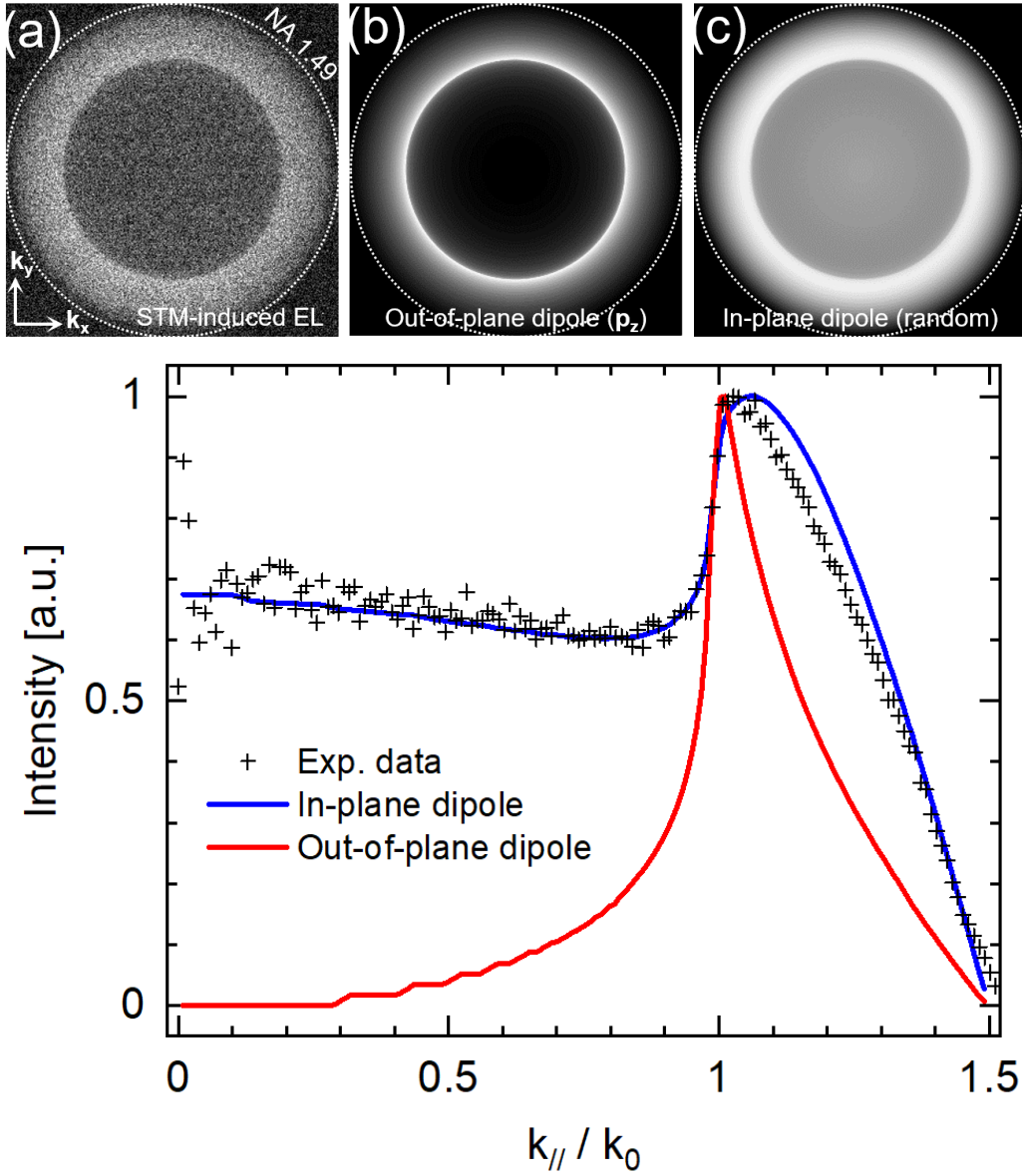


Figure 2.4: a) Fourier image of the emitted light ($V_S = 4$ V, $I_{Setpoint} = 5$ nA, acquisition time = 150 s), as compared to b) a simulation of the emission from an out-of-plane dipole and c) the emission from an averaged collection of in-plane dipoles of different orientation. A comparison of the three radial profiles is shown in d).

emission pattern from an oscillating electric point dipole on an air-glass interface (see Fig. 2.4-b and c).

Depending on the exciton, its transition dipole may be oriented in- or out-of-plane. Thus, in Fig. 2.4-b, we plot the intensity for a source dipole oriented out-of-plane, perpendicularly to the sample, and in Fig. 2.4-c, we consider an average over randomly oriented in-plane dipoles as there is no reason for the in-plane transition dipoles to have a particular orientation in our experiment (more details in Appendix D). For both figures, we have axial symmetry, but as shown in Fig. 2.4-d, the experimental radial profile clearly differs from that of an out-of-plane dipole. We find excellent agreement with the in-plane dipole model, in particular within the sub-critical angular range and for the angle of maximum emission, without the use of any fitting parameters.

These observations confirm that the detected light is not due to a nanocavity mode of the tip-surface junction, since inelastic tunneling exhibits an emission pattern similar to that of an out-of-plane dipole [80]. These results also confirm that we measure the luminescence from bright excitons in monolayer MoSe₂, which have an in-plane transition dipole, unlike dark excitons, which have a vertical transition dipole [81]. This result is not unexpected, since in molybdenum-based TMDs, bright excitons are of lower energy than their dark counterparts, and unlike in other work [66, 82], no interaction with a plasmonic tip or substrate exists which could render the dark excitons optically active. This result further confirms that STM-induced electroluminescence from monolayer MoSe₂ is due to bright excitons in our experiment. Thus, we conclusively demonstrate that the electrical excitation from the STM can induce luminescence from the same excitons as those responsible for the photoluminescence of MoSe₂.

2.2 Excitation mechanism

Now that we have determined that our signal arises from the recombination of MoSe₂ excitons, we will consider how tunneling electrons lead to the creation of these excitons. While several excitation mechanisms are possible, (multi-electron excitation, diode-like excitation, binding of injected electrons or holes with charges already present due to doping, resonant energy transfer, etc), here we will consider only two that may be involved in the creation of excitons in a direct-bandgap semiconductor.

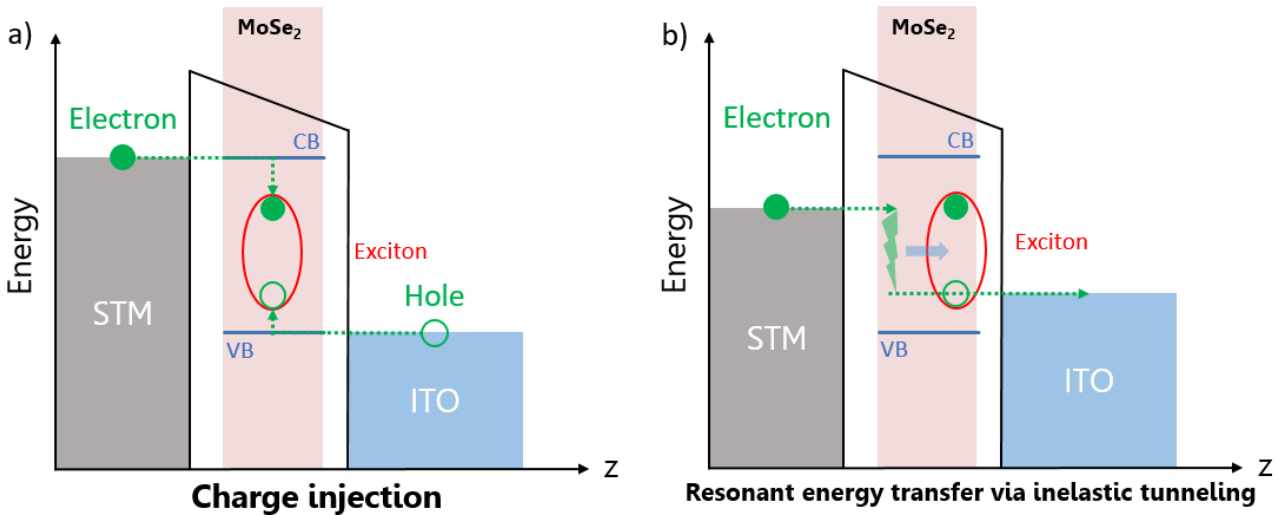


Figure 2.5: Schematic of the considered excitation mechanisms: in the case of charge injection (a), once the potential difference between the STM tip and the ITO is higher than the *electronic* bandgap of MoSe₂, an electron and a hole may transfer to the conduction and valence bands respectively and form an exciton. In the case of resonant energy transfer via inelastic tunneling (b), once the potential difference between the STM tip and the ITO is higher than the *optical* bandgap, an electron tunneling inelastically in the gap may transfer all of its excess energy to excite an exciton.

◇ The first mechanism relies on electrical charge carrier injection as in a light emitting diode (in which potential doping of the sample is ignored). In order to form an electron-hole pair, an electron is injected in the conduction band and, simultaneously, an electron vacancy is created in the valence band of the semiconductor. For this process to occur, electrons must be able to tunnel from the negatively biased electrode (STM tip) to the conduction band and from the valence band to the positively biased electrode (ITO). This requires an energy level arrangement that only occurs above a certain bias voltage, which is generally equal to or higher than (in corresponding electron energy) the electronic band gap energy of the semiconductor [70] (around $\simeq 2.15$ eV for monolayer MoSe₂ [21, 83]).

◇ A second possible mechanism is based on resonant energy transfer, or virtual photon coupling [84]. In a classical picture, the inelastic tunneling current generates an oscillating electric dipole in the tip-surface gap, which transfers energy to the semiconductor via near-field electromagnetic coupling. The only requirement for this process to occur is that the electron energy exceeds the optical gap energy, which differs from the “free-particle” electronic gap by the exciton binding energy.

Monolayer MoSe₂ has an optical gap of 1.58 eV and an exciton binding energy of 0.55 eV [21, 83, 85]. Therefore, the two mechanisms may be distinguished by investigating the bias dependence of the photon emission quantum efficiency and determining the lowest bias at which luminescence from MoSe₂ may be detected. Thus we examine the dependence of the STM-induced electroluminescence on the applied bias voltage in order to elucidate the excitation mechanism through which the excitons are electrically excited. Working towards this goal, a series of electroluminescence spectra from monolayer MoSe₂ are measured at current setpoints of 0.1 nA and 10 nA and sample biases V_S varying within the 1.3 – 4.0 V range. The photon emission quantum efficiency (i.e., the number of emitted photons per tunneling electron) is obtained by dividing the total number of photons from STM-induced electroluminescence spectra by the simultaneously measured tunneling current integrated over the acquisition time.

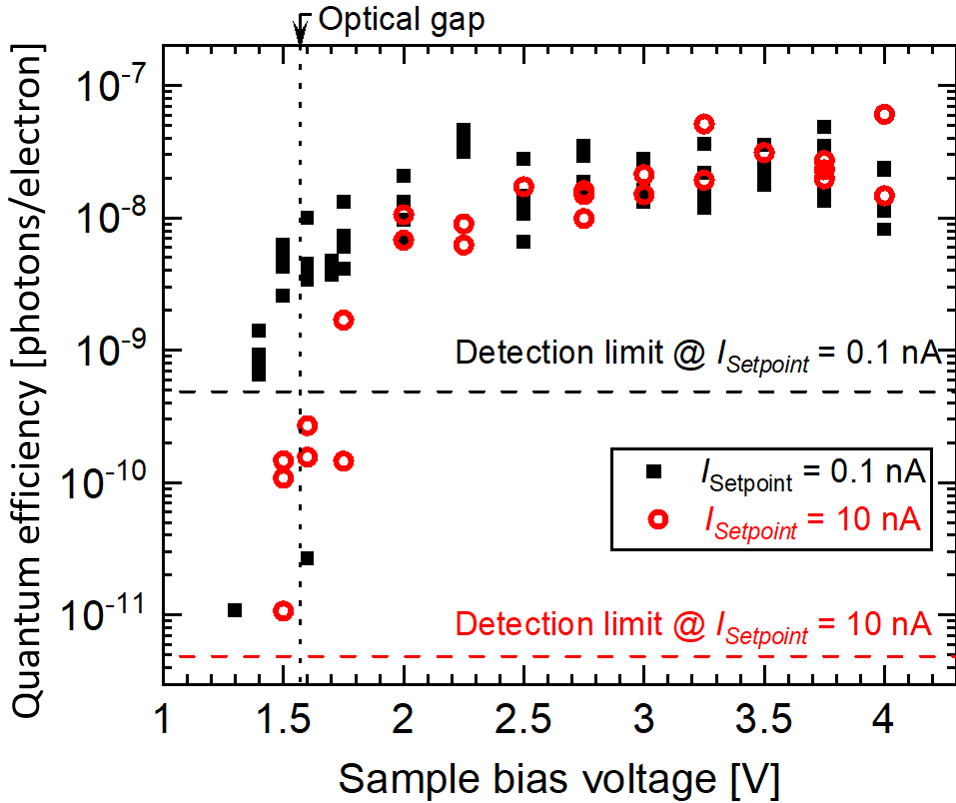


Figure 2.6: Photon emission quantum efficiency (in number of emitted photons per tunneling electron) versus the sample bias voltage, obtained from STM-induced luminescence spectra of monolayer MoSe₂ measured at current setpoints of 0.1 nA and 10 nA (see spectra in Fig. 2.7). The detection limit is defined from the standard deviation of the dark current of the CCD camera and the STM setpoint current. The vertical dotted line indicates the optical gap energy of monolayer MoSe₂.

Figure 2.6 shows the photon emission quantum efficiency versus bias voltage. At $V_S = 4$ V, about 3×10^{-8} photons per electron are detected, which corresponds to 10^{-7} photons per electron after correction for the detection efficiency (31% at $\lambda_0 = 783$ nm). At both current setpoints, 0.1 nA and 10 nA, the onset of luminescence occurs at electron energies close to 1.5 eV, matching the optical gap of monolayer MoSe₂ [21, 83, 85]. The latter observation is a strong indication that the luminescence is excited by resonant energy transfer from the tunneling current to the excitons, through virtual photon coupling.

We describe the excitation mechanism in terms of virtual photon coupling because the energy transfer from the tunneling current to the excitons occurs without the participation of an intermediary optical mode such as a localized surface plasmon polariton [86]. For STM electroluminescence of single molecules, a comparable excitation mechanism has recently been reported in terms of inelastic electron-molecule scattering [87]. Nevertheless, at sufficiently high electron energies above the electronic bandgap, the two processes (energy transfer and charge injection) may be present.

Finally, we observe a slight difference, of about 0.1 to 0.2 eV, between the luminescence onset with increasing

bias and the optical bandgap energy. This difference is consistent with the observation of overbias emission in the spectra, where light is emitted up to 0.2 eV above the quantum cut-off at $V_S = 1.4$ V. This overbias ($h\nu \geq eV_S$) emission is visible in Fig. 2.6 and 2.7 at low sample bias ($V_S \leq 1.6$ V), both at 0.1 nA and 10 nA. Light is emitted up to 200 meV below the quantum cutoff ($E_{cutoff} = eV_S$) at $V_S = 1.4$ V.

This result is similar to previous STM-induced electroluminescence studies [88]. Nonlinear electronic processes involving surface plasmons [89–91] cannot be invoked here, since the tip and the substrate are made of non-plasmonic materials. Instead, we propose that overbias emission may be due to phonon-assisted upconversion processes in the TMD [92, 93], exciton-exciton Auger scattering [94, 95], or local heating effects under the STM tip. In general, overbias emission in electroluminescence relies on excitation mechanisms involving several electrons. Nevertheless, the data shown in Fig. 2.6, which have been measured at setpoint currents of 0.1 nA and 10 nA, may not be used to confirm a nonlinear dependence of the overbias emission on the current as we only record the efficiency for two different tunneling current setpoints. Additional experiments on the current dependence of the overbias emission are necessary to address this specific issue.

Spectra analysis

In Fig. 2.7, we present a series of spectra measured from monolayer MoSe₂ at current setpoints of 0.1 nA and 10 nA, respectively, and sample biases V_S varying within the 1.3 - 4.0 V range. We note that the STM-induced electroluminescence peak position and line shape are nearly independent of V_S at a current setpoint of 0.1 nA.

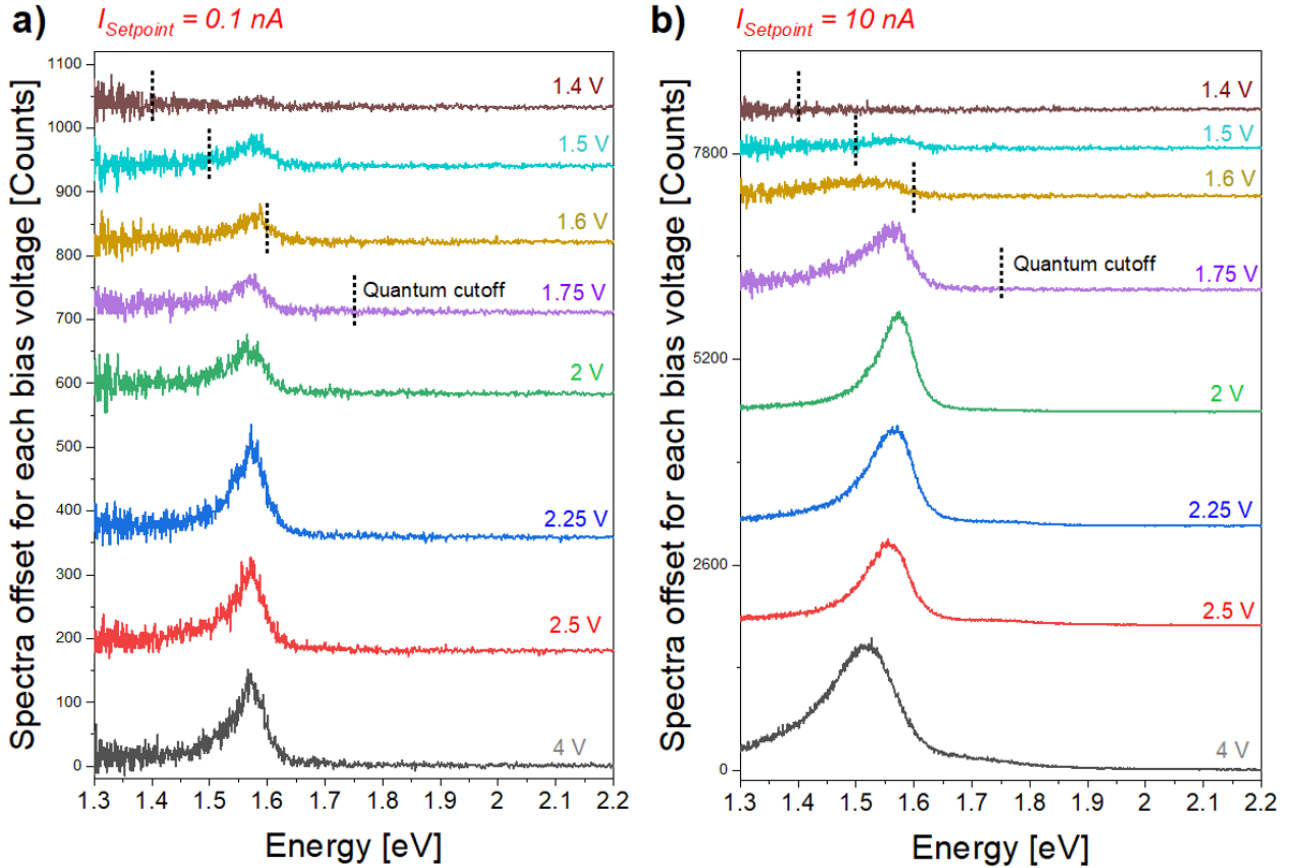


Figure 2.7: STM-induced electroluminescence spectra of monolayer MoSe₂ versus sample bias at current setpoints of (a) 0.1 nA and (b) 10 nA. The dashed lines indicate the expected quantum cutoff, which is below the maximum energy of the photons emitted in the case of excitations at 1.5 V. Acquisition time is 150 s. The spectra are vertically offset for clarity.

The emission peak remains at 1.572 ± 0.005 eV in energy and at about 55 meV in FWHM within the 1.5 – 3.0 V bias range. Stronger spectral dependence on V_S is found at a current setpoint of 10 nA as compared to 0.1 nA (see Fig. 2.7). The emission peaks increasingly broaden and red shift as the sample bias is raised from 2 to 4 V. A quantitative analysis of the red shift versus V_S is shown in Fig. 2.8.

A general tendency is observed in Fig. 2.8, where both the A and B exciton energies red shift by roughly 30 meV/V as the sample bias is increased within the 2 – 4 V range. Nevertheless, the data recorded at each bias voltage exhibits a statistical variation, with a standard deviation that increases at higher sample bias. This distribution of the efficiency is observed because each spectrum is measured on a “fresh” area of the sample, where no STM-induced luminescence experiments have been carried out before (see Appendix E for more details).

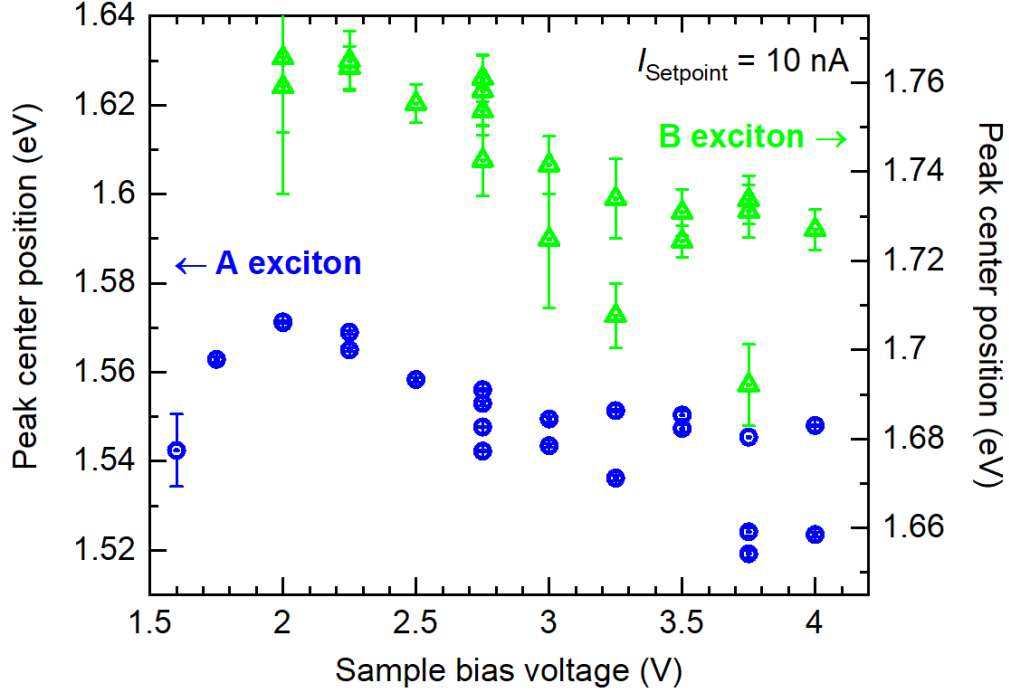


Figure 2.8: Analysis of STM-induced luminescence spectra of monolayer MoSe₂ on ITO. Sample-bias dependence of the A and B exciton energy at a current setpoint $I_{\text{Setpoint}} = 10$ nA. Exciton energy and uncertainties (error bars) are obtained from the fit of the emission peaks with Voigt profiles.

Moreover, the scanned areas on the sample may exhibit slight geometrical differences in roughness or in defect density. In addition, different areas on the sample may exhibit slightly different coupling to the underlying ITO layer, which exhibits some spatial heterogeneity in surface conductivity on the sub-micrometer scale, due to its granular geometry. Consequently, the effect of the strong electric field in the tip-substrate junction on the energy positions of the excitons may differ from one area to another. Such variations are inherent to the experimental method used, where the experiments are carried out in air on samples that are not controlled at the atomic scale. Nonetheless, it is expected that such variations would not occur if similar experiments were carried out under surface science conditions, i.e., in vacuum on an atomically flat surface.

The increasing spectral broadening and the red shift of the emission peaks when the sample bias is raised from 2 V to 4 V may be explained in several ways:

- Exciton-exciton annihilation and exciton interactions with charge carriers may yield such spectral modifications of the emission peaks [96]. Due to the low current (0.1 – 10 nA) and the low efficiency of the electrical excitation process (inelastic tunneling is only 1% of the total tunneling current [9]), exciton and charge carrier densities are expected to be much lower than in previous photoluminescence and electroluminescence studies. Nevertheless, since the excitation is comparatively much more localized in our case, exciton-exciton annihilation and exciton interactions with charge carriers cannot be excluded.
- Secondly, the observed spectral broadening and red shift of the emission peaks may also result from the Stark effect due to the strong electric field in the tip-substrate junction, which has been previously observed in other STM experiments [97]. However, the contribution of the Stark effect is difficult to model or to distinguish from other effects in the present case, because all STM experiments are carried out in constant current mode (not constant height) and the spatial distribution of the in-plane and out-of-plane components of the electric field in and around the tip-substrate junction may be highly heterogeneous.
- Thirdly, it is possible that the red shift of the emission peaks may reflect an increase of the trions recombinations contribution compared to the excitons recombinations contribution. Indeed, we cannot distinguish between the contribution of the trion recombination and the exciton recombination in our setup, as the difference in energy between the trion and the exciton is masked by the thermal broadening at room temperature.
- Finally, the observed spectral broadening and red shift of the emission peaks may also result from local heating effects under the STM tip, due to the electronic current.

STM excitations at a negative bias voltage

In the previous section, we only considered excitations carried out with a positive bias voltage applied to the substrate. Indeed, when we attempt excitations at a negative bias voltage, we observe a strong deformation of the MoSe₂ sample (see Fig. 2.9):

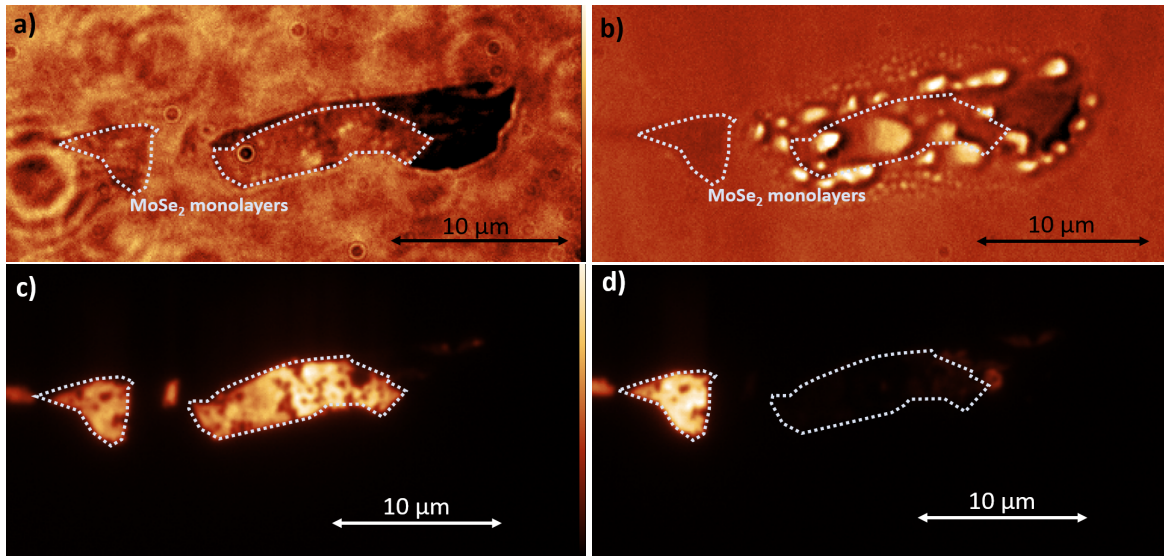


Figure 2.9: Optical transmission image of a MoSe₂ monolayer a) before and b) after an STM excitation with a negative bias voltage of -4 V ($I_{Setpoint} = 0.1$ nA, acquisition time = 150 s). Photoluminescence images c) before and d) after the excitation show that the photoluminescence is greatly reduced by the electrical excitation.

We note that a single STM excitation at a negative bias voltage drastically changes the MoSe₂ monolayer, and strongly affects the subsequent photoluminescence. The STM excitation is carried out on a small area (500 nm \times 500 nm) in the middle of the monolayer, yet the whole flake is affected. In Fig. 2.9, the separate monolayer on the left, 10 μm away from the STM excitation spot, appears unchanged. In order to estimate the influence of the substrate, we observe the damage induced by an STM excitation with a negative bias voltage on ITO:

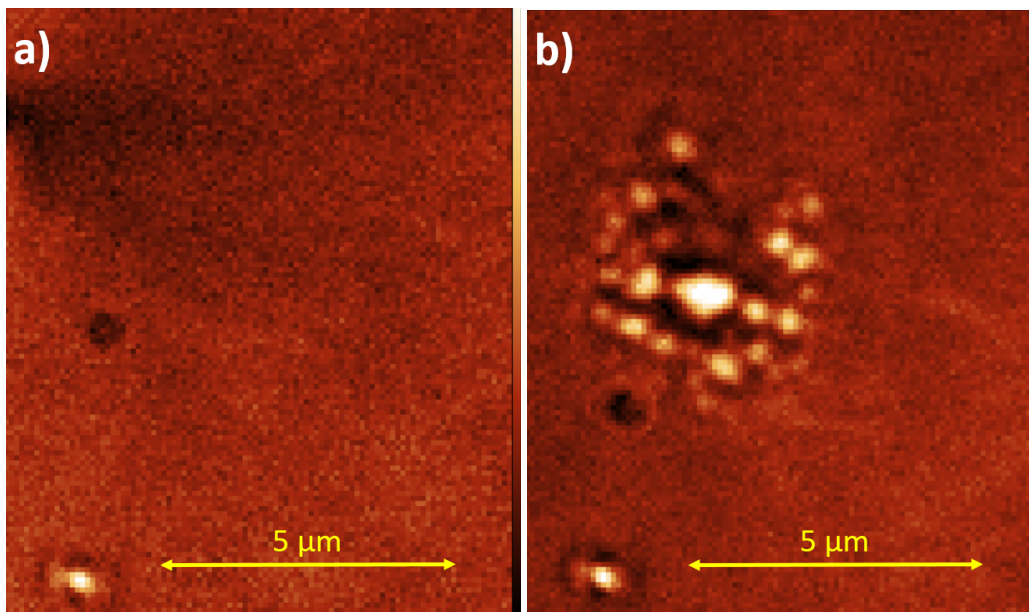


Figure 2.10: Optical transmission image of an ITO substrate a) before and b) after an STM excitation with a negative bias voltage of -4 V ($I_{Setpoint} = 0.1$ nA, acquisition time = 150 s).

In Fig. 2.10, we observe that the ITO substrate alone seems to be highly impacted by an STM excitation at a negative bias voltage, which indicates that the problem may come from the substrate and not the MoSe₂ itself. The deformation observed may be due to the oxidization of the substrate or other electrochemical reactions with contaminants within the water film that covers our sample as we are working in air [48]. In future work, we will study the impact of negatively-biased STM excitations on TMD-covered ITO in order to better understand the phenomena at play.

2.3 Exciton diffusion and the measurement of the local exciton excitation efficiency

Using our STM-nanosource setup, as described in Section 1.2, we can locally excite excitons in a MoSe₂ monolayer and obtain a wide-field optical real plane image which will show where on the sample the excitons recombine and emit light. As presented in Fig. 2.1, the sample is made by exfoliation, which induces cracks and folds in the monolayer, and thus defects. In Fig. 2.11-b, we use the STM tip to locally excite a monolayer MoSe₂ domain (same area as the one shown in the transmission image in Fig. 2.11-a). An intensity profile taken along a line crossing the location of the STM tip is shown in the inset: not only is light emitted from below the STM tip, but also from a microscale area around the tip, as defined by the flake boundaries. In addition, localized emission from several “hot spots”, one to two micrometers away from the tip, is detected.

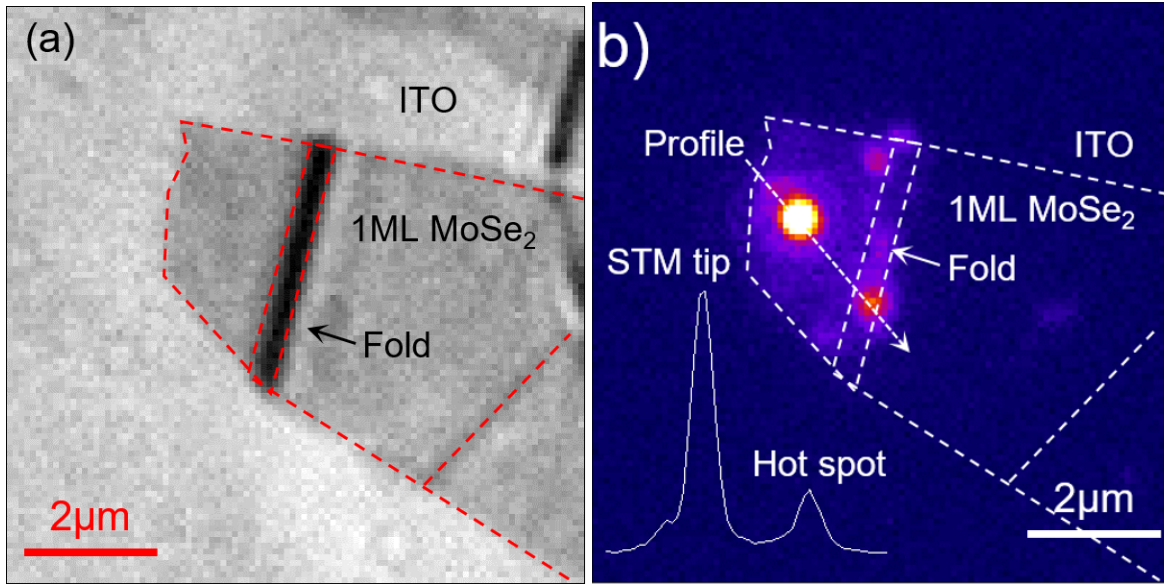


Figure 2.11: a) Transmission image of a MoSe₂ monolayer with the corresponding b) optical real plane image upon STM excitation ($V_S = 4$ V, $I_{Setpoint} = 5$ nA, acquisition time = 200 s) showing that exciton recombination occurs all over the flake. Some hot spots are present in the image, presumably due to defects in which the excitons are trapped until they recombine and emit light.

These observations confirm that excitons in monolayer TMDs at room temperature can diffuse micrometers away from the excitation source before radiatively decaying [98–100]. Hot spots at the flake edges and along folds and cracks in the flake may result from longer exciton residence times, or trapping. It is thus interesting to further probe the MoSe₂ locally to understand these phenomena.

As described in the Section 1.2.5, we can carry out a “photon mapping” experiment. In such a measurement, for every point in an image, we record the topography, tunneling current, and the number of photons emitted from the field of view of the APD (a 250 μm² area). Thus, we are able to compute a map of the photon emission quantum efficiency by dividing the optical signal by the measured current and expressing this ratio as a number of emitted photons per tunneling electron.

Figure 2.12-a and -b show respectively the STM topography and photon emission quantum efficiency maps of an area where both bilayer and monolayer MoSe₂ may be seen. Height and intensity profiles obtained along the white lines in Figs. 2.12-a and -b are shown in -c. The emission of light is spatially correlated with the presence of monolayer MoSe₂ in the tunneling junction and reveals geometrical features of the sample with deep subwavelength lateral resolution, which is not attainable in standard optical microscopy. In particular, the quantum efficiency map exhibits a sharp transition between the bilayer and monolayer areas. This transition occurs over a distance of less than 20 nm. The two areas differ by 0.9 ± 0.1 nm in STM height, which is close to the expected thickness of a MoSe₂ layer (i.e., 0.65 nm). The photon emission quantum efficiencies measured on the two areas differ from each other by two orders of magnitude. Thus, monolayer versus bilayer MoSe₂ may be identified without ambiguity.

Furthermore, the imaging of nanoscale defects is demonstrated, for example on folds that form in monolayer MoSe₂ flakes due to the deposition process and which may extend over micrometers. As shown in Fig. 2.12-a, such folds are 1.7 ± 0.1 nm in height (as compared to the rest of the monolayer) and $\simeq 10$ to 100 nm in lateral width. In standard optical microscopy, such structures appear as one-dimensional objects. In contrast, the map

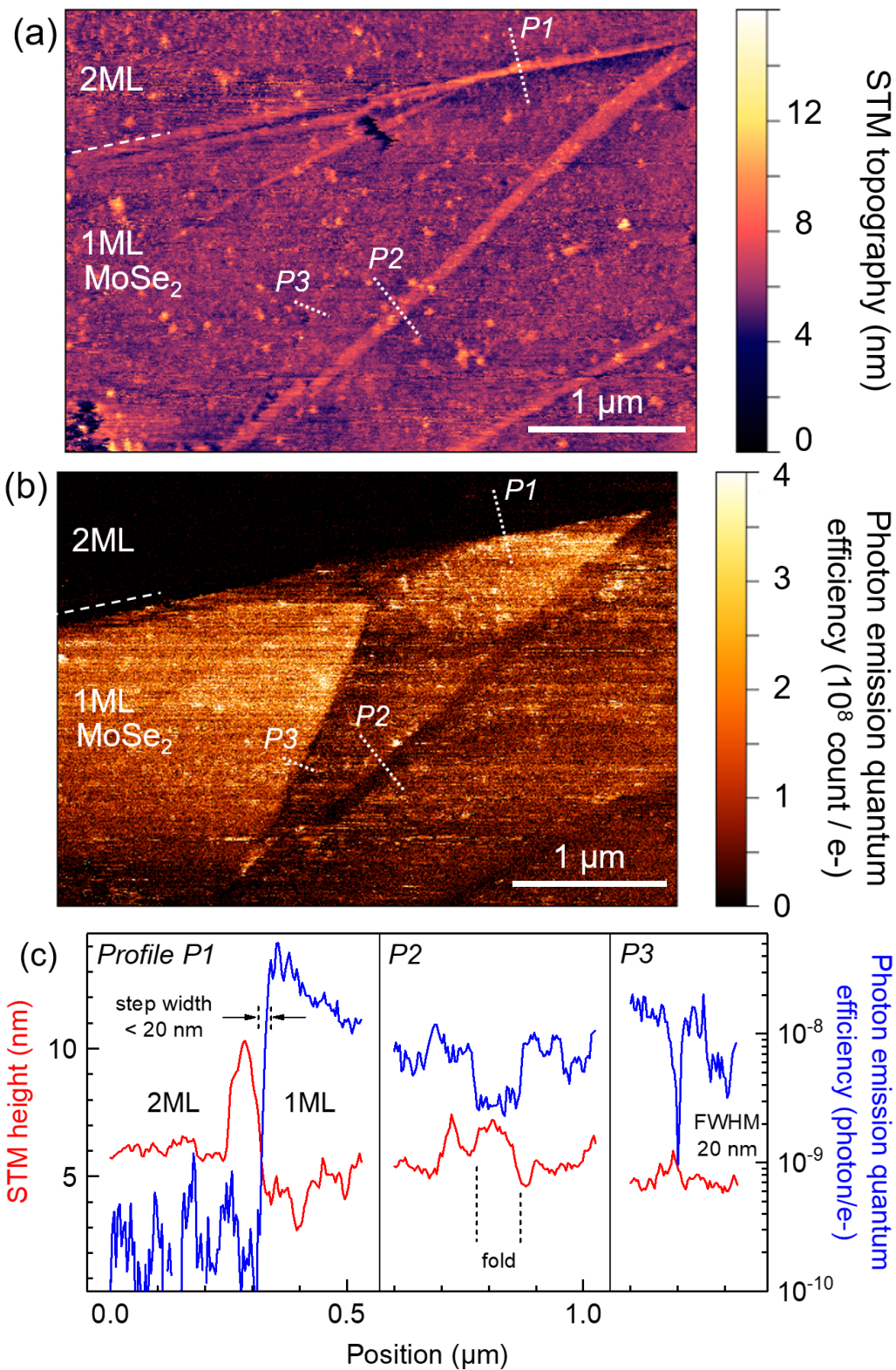


Figure 2.12: a) STM image ($V_S = 4$ V, $I_{Setpoint} = 10$ nA) of the sample and b) photon emission quantum efficiency. The bilayer of MoSe₂ is unambiguously identified both by the increase in height of 0.9 nm and its very low luminescence efficiency. Profiles are obtained along the white dotted lines and are shown in c).

shown in Fig. 2.12-b reveals lateral variations of STM-induced electroluminescence on a 10 to 20 nm scale, with a decrease in the photon emission quantum efficiency on the folds. Moreover, STM-induced electroluminescence makes it possible to uncover geometrical features such as domains with different photon emission efficiencies in Fig. 2.12-b, which are presumably separated by nanometer-wide cracks in the monolayer, almost undetectable in the STM topography image (see profile P3). This domain boundary has a strong effect on the photon emission quantum efficiency, which drops by a factor of about 5 over a distance of 10 to 20 nm. Further work would be to investigate the impact of defects (for example cracks, folds, missing or impurity atoms) on the exciton spectra.

2.4 Summary

In this chapter, we presented a new method to locally excite the electroluminescence of a TMD monolayer using an STM in ambient conditions. Through a comparison with photoluminescence measurements, and an analysis of Fourier-plane images, we show that the emitted light is due to the radiative recombination of bright excitons in MoSe₂. As the voltage threshold for electroluminescence is on the order of the optical bandgap of MoSe₂, the excitation mechanism we propose is resonant energy transfer from the tunneling current to the excitons in the MoSe₂ monolayer. Additional mechanisms such as multi-electron effects (at high tunneling current setpoints), or charge injection (at bias voltage higher than the electronic bandgap) may also play a role. We demonstrate efficiencies up to 10^{-7} photons/electron despite the absence of plasmons to enhance the luminescence. From real-space images, exciton diffusion and recombination at “hot spots” is observed. Finally, as we are using a local excitation, we can identify the location of nanoscale defects on the sample with a precision of 20 nm. Thus, the long sought-after goal of locally and spectroscopically probing excitons of two-dimensional semiconductors is attained using a scanning tunneling microscope, as a new technique for investigating the excitonic and optoelectronic properties of 2D semiconductors and their heterostructures at the nanometer scale [1].

Chapter 3

STM excitation of surface plasmons with a nanoantenna

3.1 Introduction

As described in Section 1.1.2, a tunneling junction may be used to electrically excite propagating surface plasmons and light. In the next two chapters we will explore both theoretically and experimentally how a plasmonic nanoantenna can influence this emission. In this first chapter, the excitation source is the tunneling current between the tip of a scanning tunneling microscope (STM) and a metallic nanoantenna (see Fig. 3.1).

The emission of light from an STM tunneling junction has been studied in numerous systems due to its great versatility: light emission with atomic resolution was achieved soon after the invention of the STM [101, 102], leading to new opportunities. Indeed, due to this high resolution, the STM is a great tool for the spectroscopy of molecular vibrations [67, 70, 103, 104], or for imaging dipole-dipole coupling and energy exchange between molecules [68, 69]. A review of the electroluminescence induced by STM is presented in [105], and the important role of the cavity plasmon modes in STM-excited molecular fluorescence is underlined. Along with the successful decoupling of the molecules from the metallic substrates, the plasmonic nano- or picocavity between the STM and substrate has led to impressive results in molecular fluorescence [68, 69, 106–108].

As discussed in Section 1.1.1, the idea of this chapter is to investigate how a nanoantenna can influence the energy and number of surface plasmons excited using this technique. While the use of antennas in the micro- and radiowave regimes is well-established, the use of antennas working in the optical wavelength range was initially hampered by the fact that antenna components must be a fraction of the size of the wavelength of light [109]. Optical antennas have several functions, similar to those for micro- and radiowaves: they may be used i) to convert freely propagating optical radiation into localized energy and vice versa [109], ii) to control the wavelength of the emission, iii) and/or to control the spatial characteristics of the emission (omni-directional or uni-directional [80]). In what follows, we use what we call a plasmonic antenna, that is, a structure of plasmonic material that will be used to help convert an inelastic tunneling current into propagating surface plasmons, and influence the emission spectrum. Note that a plasmonic nanoparticle may be considered as a sort of nanoantenna; in past work it has been shown that by changing the STM excitation position on a nanoparticle, different modes of the particle may be excited, leading to different spectra [110–112], and emission directions [113].

Optical nanoantenna engineering is an active field of research with a broad spectrum of applications. Nanoantennas are used in spectroscopy, in order to enhance the fluorescence of single molecules or quantum dots [114–116], or to increase weak non-linear phenomena [117, 118]. Other fields of research that integrate nanoantennas into opto-electronical devices for different applications include photovoltaics [119], miniaturized photodetectors [120, 121], or molecular sensors [122]. Nanoantennas have also been used for surface plasmon excitation [123–126].

In order to increase the excitation of propagating surface plasmons by the inelastic tunneling current in

a nanometric junction, the idea is to use a resonant plasmonic nanoantenna [126–128]. The low excitation efficiency in a tunneling junction may be explained as the result of quenching [127]: the excitation, trapped in a tiny 1 nm gap between two metals, most often de-excites into non-radiative modes, leading to Joule heating in the metals. The idea is thus to engineer a radiative antenna mode with a high local density of electromagnetic states (EM-LDOS), so high that this radiative mode might compete with quenching. Secondly, this radiative antenna mode must efficiently excite the propagating surface plasmon mode on the gold film. Thus this plasmonic nanoantenna “localizes” the excitation into the antenna mode and plays the role of a transducer between this localized plasmon mode, and the propagating surface plasmon mode.

In Section 3.2 of this chapter, we consider a cylindrically-shaped nanoantenna on a thin gold film, as proposed in Ref. [127], and investigate through simulations how the nanoantenna dimensions affect the resulting propagating surface plasmon excitation efficiency as well as the spectrum of the resulting light. In Section 3.3 we use our STM-nanosource to study experimentally plasmonic nanoantennas made by electron beam lithography. In particular, we look for a possible impact of the nanoantenna on the number of emitted photons per tunneling electron, and study the spectrum of the emitted light.

3.2 Theoretical understanding through simulation: the impact of a nanoantenna on the STM excitation of surface plasmons

As stated in the introduction of this chapter, we will investigate experimentally and through simulations the impact of a nanoantenna on the excitation of propagating surface plasmons polaritons using a scanning tunneling microscope (STM). A schematic representation of the experiment is shown in Fig. 3.1-a. The sample is a gold nanocylinder or disc on a thin gold film deposited on a glass substrate (see Section 3.3.1 for the sample fabrication and Section 3.3.2 for the experimental results). To excite the SPPs, the STM tip is placed above the nanoantenna; the small percentage of tunneling current which is inelastic excites the modes of the nanoantenna which then excite SPPs on the Au film. The excited SPPs are then detected via leakage radiation microscopy (see Section 1.2.5 for details). In order to understand the impact of the different parameters of the sample on the results we perform simulations with an electromagnetic solver based on an aperiodic Fourier modal method dedicated to body-of-revolution structures and developed by collaborators at the Charles Fabry Laboratory [127, 129].

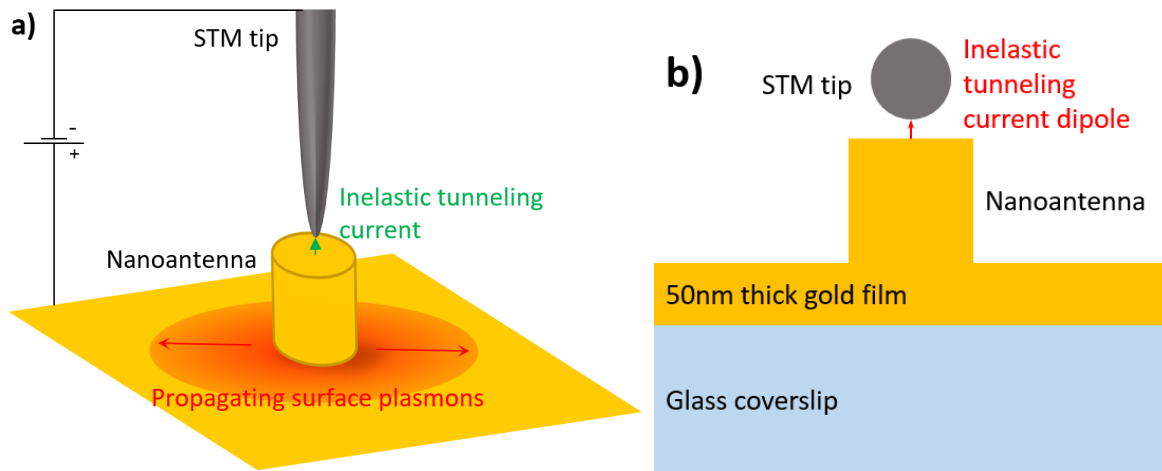


Figure 3.1: a) Schematic of the experiment: an STM is used to form a tunneling junction between its tip and a gold nanoantenna. The inelastic contribution to the tunneling current excites surface plasmons, with an efficiency and wavelength determined by the presence of the nanoantenna. b) Schematic of the simulation: the STM tip is approximated by a tungsten sphere (10 nm in diameter) and the nanoantenna by a gold cylinder. The inelastic tunneling current is modeled as a vertical oscillating dipole in the center of the gap between the spherical tip and cylindrical antenna. In the following simulations, we assume the gap thickness to be 1 nm.

3.2.1 Theoretical understanding of the impact of a nanoantenna: small spherical tip

As in the article from Bigourdan et al. [127], we approximate the sample as a cylindrical gold nanoantenna on a 50-nm-thick gold film on a glass substrate, considered as semi-infinite in the simulation. As the surface plasmons are excited by the inelastic tunneling current from an STM, we model the STM tip as a tungsten sphere on top of the nanoantenna, and the inelastic tunneling current as a vertical oscillating electric point dipole source in the center of the gap between the sphere and the antenna [18] (see Fig. 3.1-b).

The source dipole is initially considered to have a flat power spectrum, which is not representative of an experimental tunneling junction, in which the power spectrum of the inelastic tunneling current source depends on the applied voltage [130]. To correct this, every simulated spectrum is multiplied by the correction factor below. This factor is related to the probability of an inelastic transition at a certain energy for a given bias voltage. The typical applied bias voltage in our experiments is 2.5 V. This correction factor is from Ref. [130], equation 2:

$$\text{Correction} = 1 - \frac{\hbar\omega}{eV_S} \quad (3.1)$$

with V_S the bias voltage applied (on the sample, with the STM tip being grounded). The correction factor as a function of wavelength for different applied voltages is shown in Fig. 3.2:

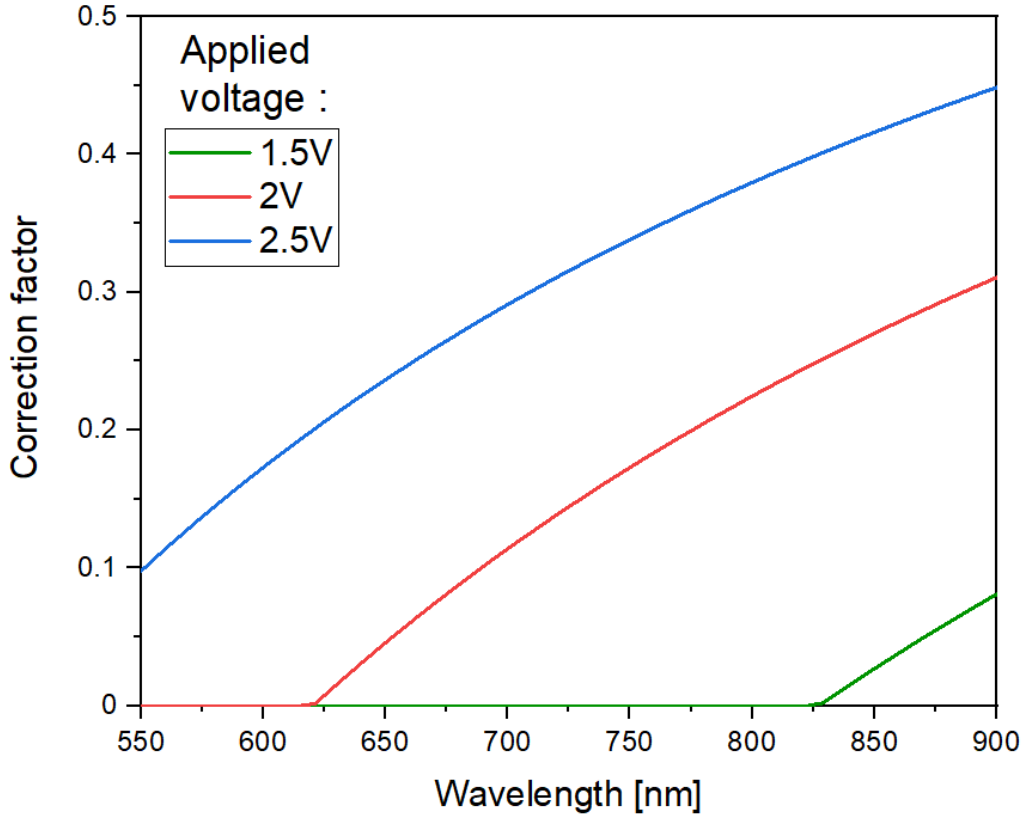


Figure 3.2: Correction factor as a function of wavelength for different bias voltages applied to the tunneling junction.

The program used computes the electromagnetic field excited by a point dipole source in structures with a symmetry of revolution (in this case, a sphere on top of a cylinder). In other words, we calculate one component of the Green's tensor for a fixed source position. The program uses an aperiodic Fourier modal method described in [127, 129] to calculate the total field emitted by the source and extract the following physical parameters:

Name	Definition
P_{Tot}	Total power emitted by the dipole
P_{rad}	Radiative power: power radiated in the far-field
P_{NR}	Non-radiative power: power dissipated in the structure
A_{SPP}	Amplitude of surface plasmon propagating away from the antenna
P_{SPP}	Power in propagating surface plasmons
k_{SPP}	Propagating surface plasmon propagation constant (absolute value of the surface plasmon wavevector)

Table 3.1: Summary of the computed physical parameters and their abbreviations.

Conservation of energy gives us $P_{Tot} = P_{rad} + P_{NR}$. The amplitude of the electric field of surface plasmons propagating on the metallic film surface A_{SPP} is extracted using a near-to-far field transformation described in [131]. As explained in [127], the Poynting vector associated with the fraction of the field corresponding to propagating SPPs is proportional to $\frac{4}{|k_{SPP}|} |A_{SPP}|^2 \exp(-2k''_{SPP}r)$ (with k''_{SPP} the imaginary part of the surface plasmon propagation constant). The exponential factor describes the propagating surface plasmon decay as it propagates on the surface (at a distance r from the excitation point on the film). Thus, we use the following definition of P_{SPP} to quantify the power in the propagating surface plasmon mode on the metal surface:

$$P_{SPP} = \frac{4}{|k_{SPP}|} |A_{SPP}|^2 \quad (3.2)$$

The term P_{SPP} contains both a radiative component corresponding to the surface plasmons which leak into photons propagating in the glass substrate and thus radiate into the far field, and a non-radiative part corresponding to the power absorbed along the metal interface.

In this first section, following Bigourdan et al., we consider the STM tip to be a tungsten sphere with a 10 nm diameter, and the nanoantenna to be of cylindrical shape, with diameters of 10 – 70 nm and heights of 30 – 70 nm. Unless stated otherwise, the dielectric constants used are from Johnson and Christy [16] for the gold and Palik [132] for the tungsten, and the distance between the tungsten sphere and the nanoantenna is fixed at 1 nm. The oscillating vertical dipole source is positioned in the center of this gap. In Section 3.2.2, a more realistic tip and experimentally-realized nanoantenna will be considered.

In order to better visualize the nanoantenna modes, we plot the imaginary part of the transverse magnetic field $\text{imag}(H_Y)$ (transverse to the cross-section plane, which we define as the xz plane, see Fig. 3.3). We choose to plot this part of the electromagnetic field for clarity: it would be more natural to plot the electric field as it is more directly linked to the charge distribution, but the electric field is strongly confined in the gap and thus saturates the image, whereas the magnetic field spreads much more out of the gap and is thus easier to see. For the same reason of improved visibility, we plot the imaginary part of the field as the singularity at the source position (singularity of the Green's tensor) completely saturates the real part.

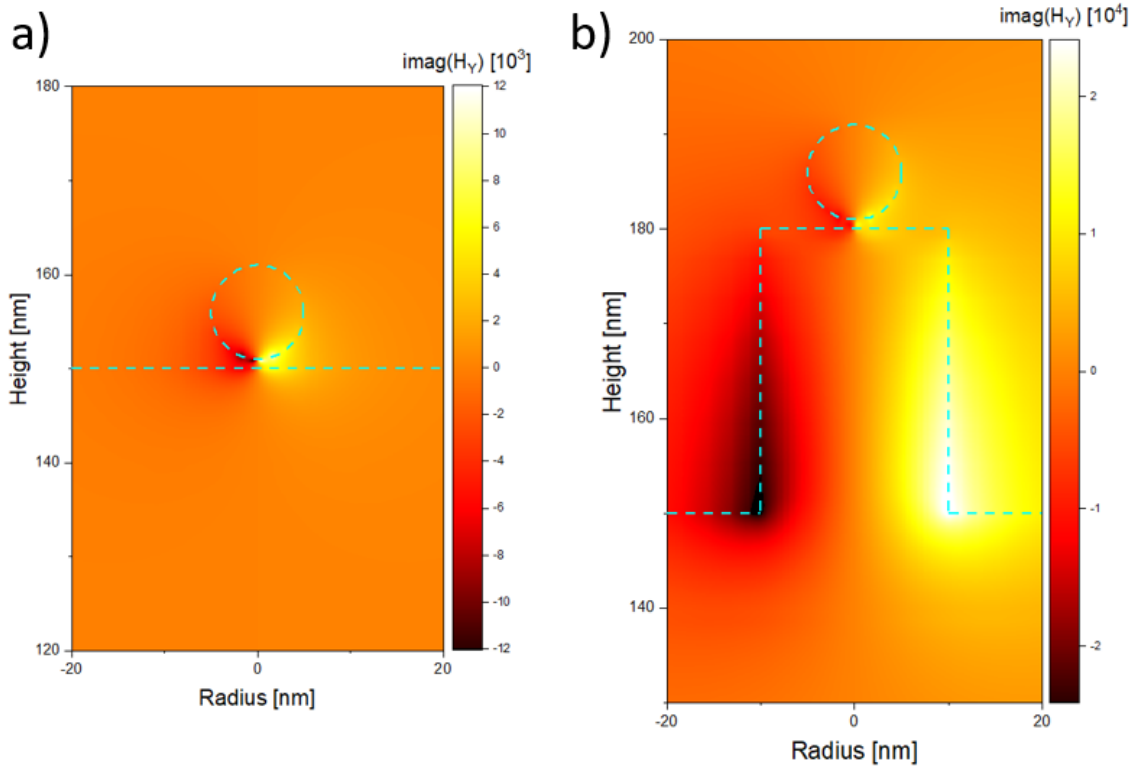


Figure 3.3: Transverse magnetic field distribution from a vertical point dipole source a) situated between tungsten sphere and a thin gold film, b) situated between a tungsten sphere and a gold nanoantenna on a gold film. Antenna dimensions: height = 30 nm, diameter= 20 nm. The diameter of the tungsten sphere is 10 nm.

In Fig. 3.3, we see that adding a nanoantenna to a simple gold film adds a strong dipole-like longitudinal nanoantenna mode to the electromagnetic fields. The hot spot between the tip and antenna is at the location of the dipole source. To evaluate the increase of the EM-LDOS due to the nanoantenna, we compute the EM-LDOS (\sim proportional to the total emitted power of the source, P_{Tot}) with and without this nanoantenna (Fig. 3.4-a) and plot the ratio between the two in Fig. 3.4-b.

From Fig. 3.4-b, due to the presence of the nanoantenna, the EM-LDOS spectrum shows a net increase of a factor of about 1.2 at the wavelength of the nanoantenna mode around 700 nm. Indeed, in Fig. 3.4-a, we see that while there is an increase in the EM-LDOS at 700 nm, the large EM-LDOS at shorter wavelengths due to quenching slightly decreases when the nanoantenna is present.

However, the nanoantenna is not only expected to increase the EM-LDOS at the wavelength of the antenna mode, but also to efficiently radiate power into the propagating surface plasmon mode. To confirm that the increase in the EM-LDOS does indeed increase the power emitted into propagating surface plasmons and not simply the power in the local non-radiative modes (absorption), we compare the propagating surface plasmon excitation efficiency $\frac{P_{SPP}}{P_{Tot}}$ with and without a nanoantenna (see Fig. 3.5). $\frac{P_{SPP}}{P_{Tot}}$ is the ratio between the power

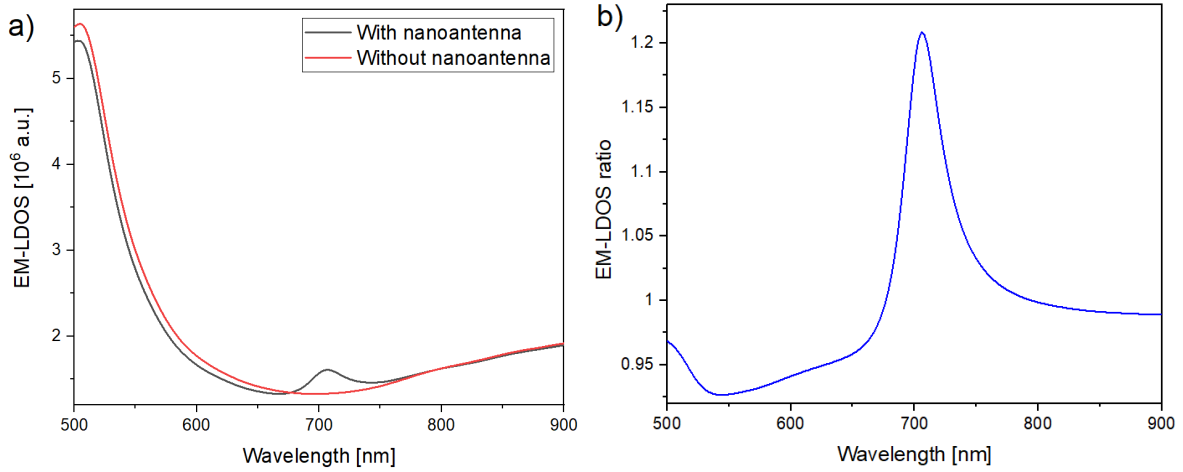


Figure 3.4: a) EM-LDOS and b) EM-LDOS ratio (EM-LDOS with a nanoantenna divided by the EM-LDOS without a nanoantenna) for a sample with a 30-nm high, 20-nm wide cylindrical nanoantenna where plasmons are excited using an STM, modeled as a tungsten sphere with a 10 nm diameter 1 nm above the nanoantenna. The dipole source is positioned between the sphere and the sample.

emitted into the propagating surface plasmon mode and the total power emitted by the source.

As expected, the nanoantenna indeed has a dual impact on the surface plasmon excitation efficiency. In Fig. 3.5, we note that the antenna increases the surface plasmon excitation efficiency by a factor of 38 (by comparing P_{SPP}/P_{Tot} with and without the nanoantenna, integrated over the wavelength range of interest, i.e., 500 – 900 nm). The mean theoretical surface plasmon excitation efficiency (P_{SPP}/P_{Tot}) is 0.38% with the nanoantenna, when averaged over our wavelength range of interest, with a maximum of 2.8% at 726 nm. This result is three hundred times higher than the surface plasmon excitation efficiency on a thin gold film at this wavelength ($9.3 \times 10^{-3}\%$ at 726 nm). This is a much higher increase factor than for the EM-LDOS thanks to the antenna’s ability to radiate surface plasmons. Secondly, the resulting spectrum is tailored by the nanoantenna resonance and exhibits the same peak that we observed in the EM-LDOS (see Fig. 3.4). By varying the dimensions and aspect ratio of the nanoantenna (we define the aspect ratio as $AR = \frac{Height}{Diameter}$), we may tune the intensity and position of the antenna resonance peak [133]:

In Fig. 3.6-a we plot the power emitted into the SPP mode as a function of wavelength (P_{SPP}) for different nanoantenna heights, and a fixed antenna diameter of 40 nm. We note that the small change of 10 nm in the nanoantenna height shifts the resonance peak of the longitudinal mode from 660 nm to 710 nm: this demonstrates the significant tunability potential of this surface plasmon nanosource. In Fig. 3.6-b for small nanoantennas (height ≤ 40 nm), we note that changing the nanoantenna dimensions for a fixed aspect ratio does not greatly affect the resonance wavelength. Indeed, we measure only a 35-nm shift in the resonance when we double the antenna dimensions (height increase of 20 nm) for a fixed aspect ratio of 1.5 in Fig. 3.6-b. The fact that a small nanoantenna’s resonant wavelength depends on the aspect ratio rather than the length has been studied as early as 1912 [134] and observed since then in several experimental articles on nanowires [135–137] and explained theoretically [138–143]. An intuitive explanation is presented in Ref. [133].

Finally, in Fig. 3.7 the plasmon excitation efficiency (P_{SPP}/P_{Tot}) as a function of nanoantenna height and diameter for a wavelength of $\lambda = 700$ nm, the center of our 500 nm - 900 nm detection range, is plotted. We note that the surface plasmon excitation efficiency at 700 nm is highest for small nanoantennas following a line with a 1.5 aspect ratio, (see also Fig. 3.6-b). As the dimensions increase however, retardation effects come into play and red shift the resonance compared to small nanoantennas with the same aspect ratio. Thus the surface plasmon excitation efficiency at this wavelength drastically falls with increasing nanoantenna size. The important point to note is that for the theoretical case where the STM tip is approximated as a small tungsten sphere (diameter 10 nm), the most efficient antennas are of cylindrical form (that is, their height is larger than their diameter) and their absolute dimensions are small ($\lesssim 50$ nm).

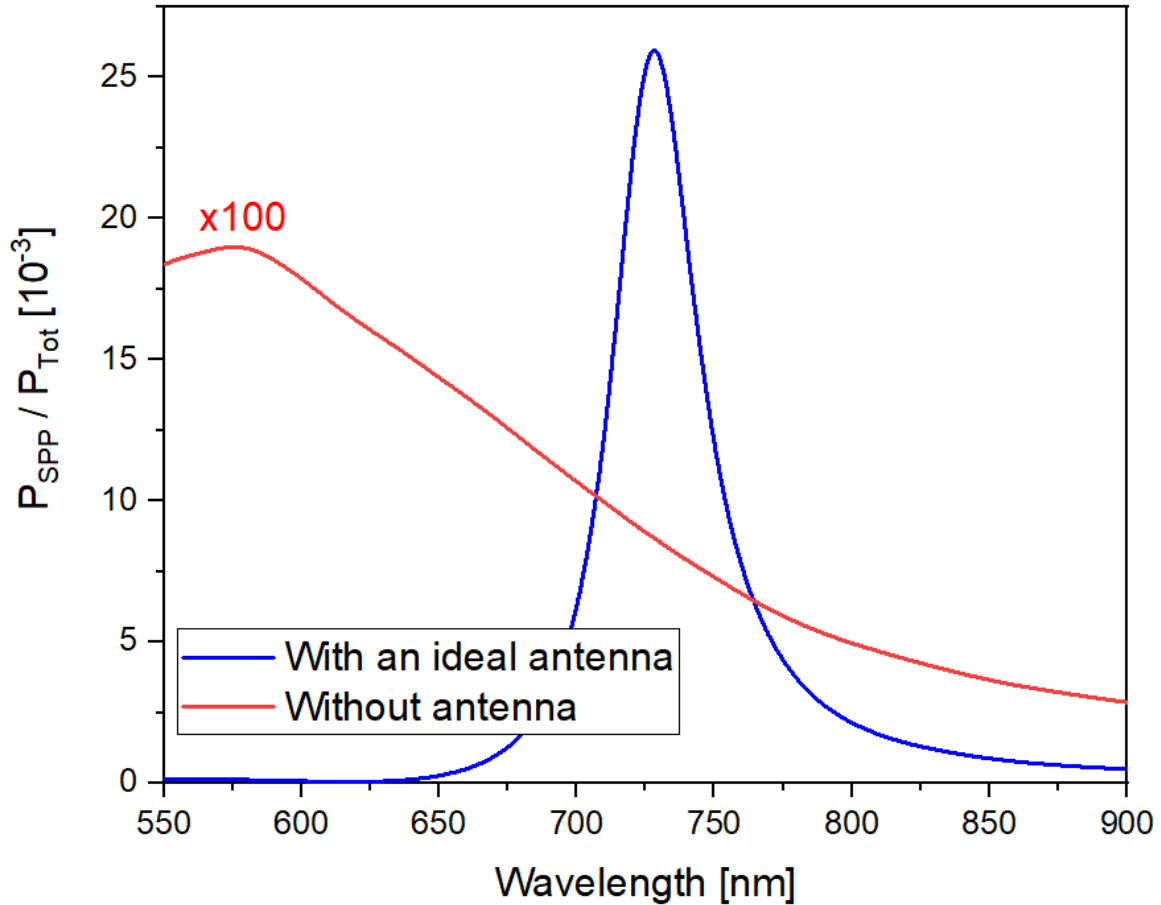


Figure 3.5: Propagating SPP excitation efficiency $\frac{P_{SPP}}{P_{Tot}}$ for a gold film with a 30-nm high and 20-nm diameter cylindrical nanoantenna (in blue) and for a simple gold film (in red, multiplied by a factor of 100 for clarity). The tip is a tungsten sphere with a diameter of 10 nm.

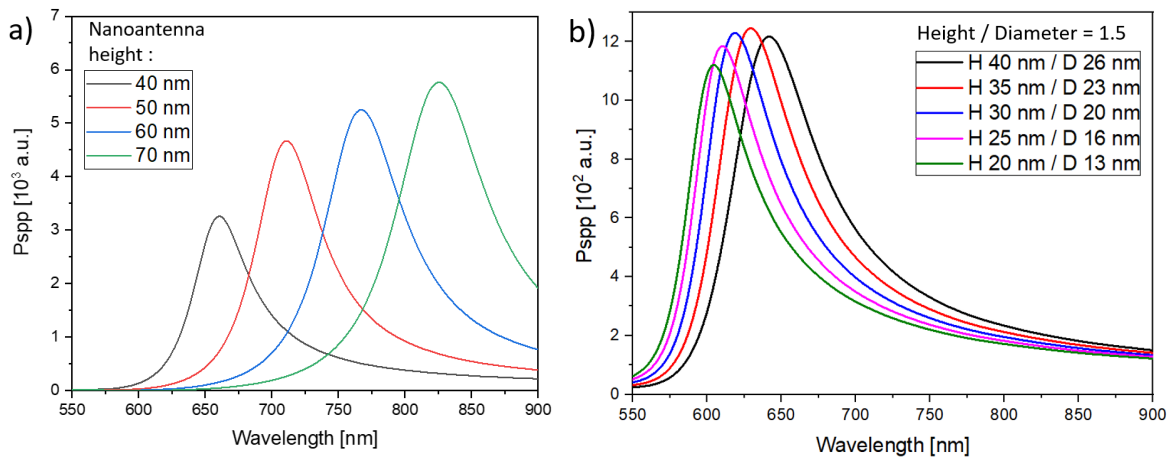


Figure 3.6: a) Power emitted into the SPP mode as a function of wavelength (P_{SPP}), for different nanoantenna heights, and a nanoantenna diameter of 40 nm (fixed diameter, changing aspect ratio, tip diameter 10 nm). b) Power emitted into the SPP mode as a function of wavelength (P_{SPP}) for varying nanoantenna dimensions with an aspect ratio of 1.5 and an STM tip with a 10 nm diameter.

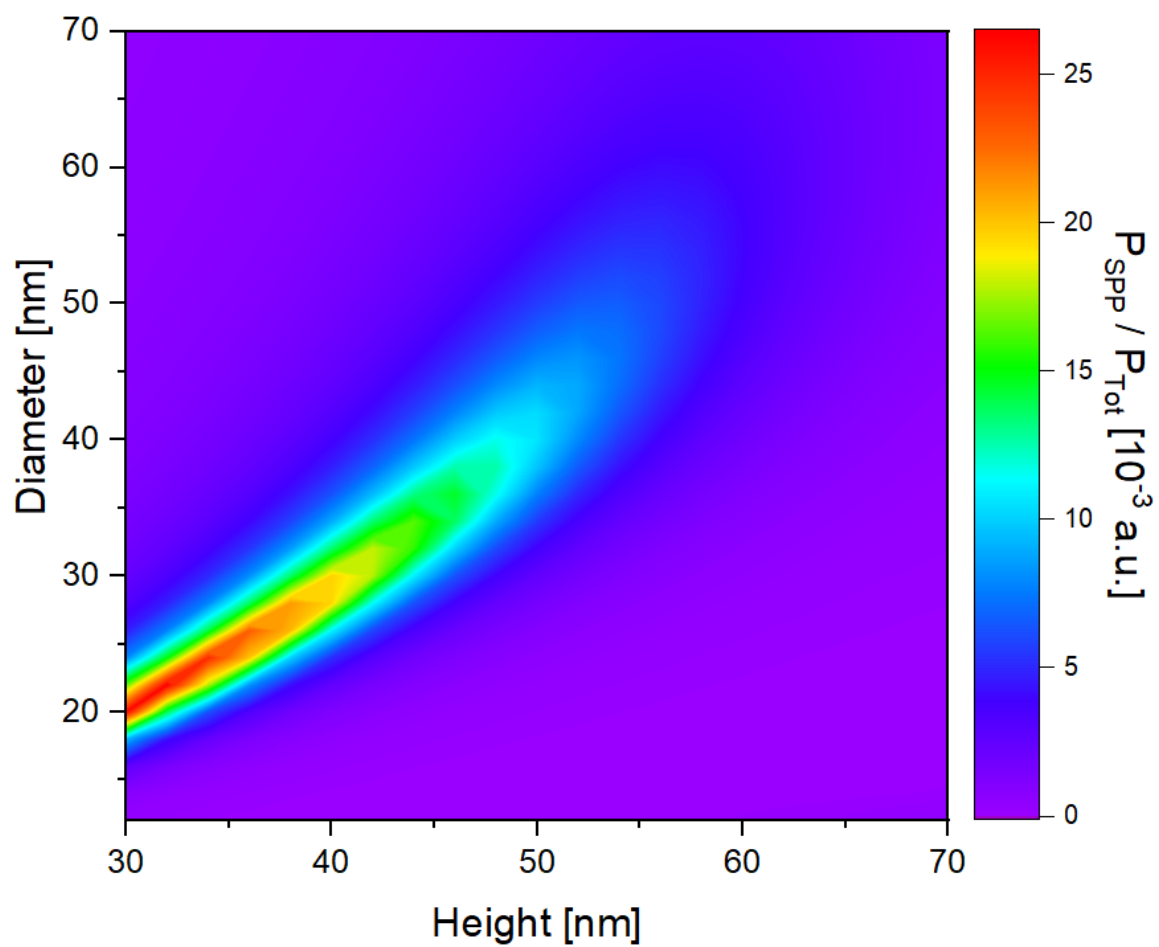


Figure 3.7: Surface plasmon excitation efficiency (P_{SPP}/P_{Tot}) at $\lambda = 700$ nm as a function of nanoantenna height and diameter, with an STM tip modeled as a tungsten sphere with a 10 nm diameter.

3.2.2 Calculations meet reality: taking into account a more realistic tip shape and the experimental nanoantenna dimensions

Evidently, while the end of an STM tip may be approximated as a small sphere, the entire tip is much larger. Figure 3.8-a shows the geometry that is used in the calculations of this section. The tip is now approximated as a tungsten cylinder of diameter 30 – 100 nm, and a height of 200 nm (this value is a compromise between the reality of a few millimeters and a reasonable calculation time). Also, as will be detailed in Section 3.3.1 below, the mean diameter of the experimentally-realized antennas varies from ~ 80 to 120 nm and the measured nanoantenna heights are on the order of 70 to 120 nm.

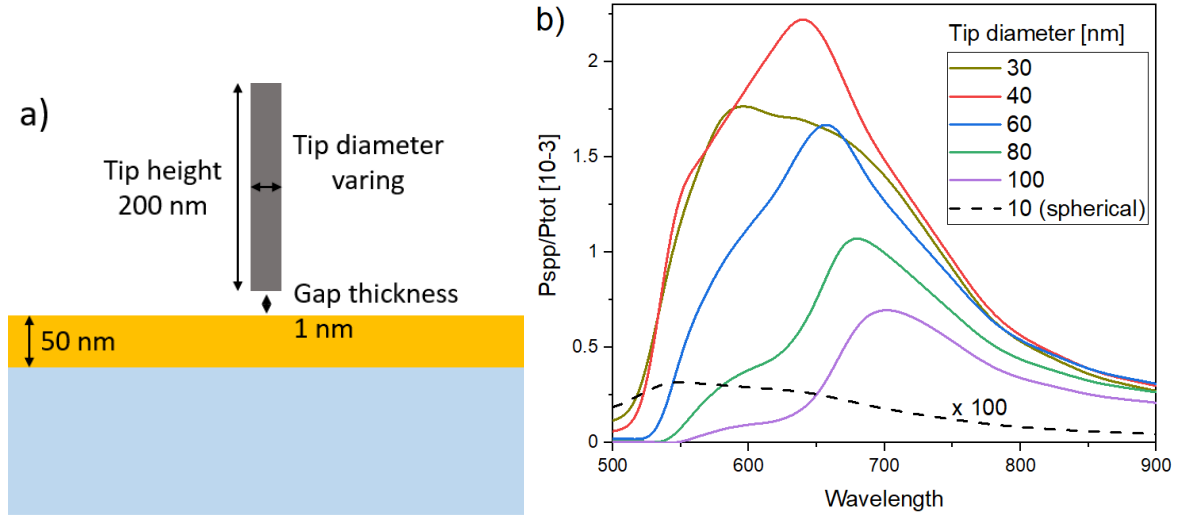


Figure 3.8: Simulations with a more realistic tip shape for the STM-excitation of surface plasmons on a thin Au film. a) Geometry of the tip and sample: the tip is now approximated as a tungsten cylinder 200-nm high, with diameters ranging from 30 to 100 nm. b) SPP excitation efficiency (P_{SPP}/P_{Tot}) on a thin Au film using the cylindrical tip of part -a (solid lines), as well as the result using a tungsten sphere with a radius of 10 nm (dashed black line).

Figure 3.8-b compares the SPP excitation efficiency (P_{SPP}/P_{Tot}) for a small spherical tungsten tip (diameter 10 nm) to that of a more realistic tip (diameters 30 to 100 nm) for a vertical dipole excitation on a thin gold film (no nanoantenna present). Unlike the small tungsten sphere which shows a relatively flat dependence on wavelength, the more realistic tips give rise to a resonance which red shifts with increasing tip diameter, presumably due to a photonic gap mode resonance. Indeed, we use a tungsten STM tip to excite surface plasmons on a thin gold film: tungsten has a permittivity of $\epsilon_W = 7.3 + 22i$ at 700 nm, which means it cannot support plasmonic modes at this wavelength and the absorption is high (especially compared to gold, which has a permittivity of $\epsilon_{Au} = -16 + 1.1i$ at 700 nm). Thus, there is no plasmonic resonance of the STM tip itself at this wavelength, but increasing the diameter of the tip changes the EM-LDOS at the source location as the surface plasmons under the tip act as gap plasmons, with the gap changing with the tip diameter. Thus it appears that the exact tip diameter, which is unknown in our experiments, will have an influence on the results.

Figure 3.9 is analogous to Fig. 3.5, but for a more realistic tip, tip-sample distance and an experimentally-realized nanoantenna. In this case, however, the result for the STM-excitation of the thin gold film is plotted on the same scale as the result on the disc-shaped antenna (diameter 120 nm, height 70 nm). For the more realistic situation (larger tip, disc-shaped antenna), averaging P_{SPP}/P_{Tot} over the wavelength range of interest gives a value of 2.09×10^{-2} % on the antenna, as compared to 2.14×10^{-2} % on the thin gold film. At the respective maxima the surface plasmon excitation efficiency is 4.42×10^{-2} % (at 710 nm) on the antenna, and 5.1×10^{-2} % (at 650 nm) on the thin gold film. Clearly, when the system is composed of a more realistic tip (200 nm high and 30 nm in diameter) and nanoantenna (with $AR < 1$, i.e., disc-shaped instead of in the form of a cylinder), the benefit of adding a nanoantenna greatly decreases as compared to an ideal system.

3.3 Experimental excitation of surface plasmons using an STM

In this section we will investigate experimentally the impact of the nanoantenna on the excitation of propagating surface plasmons polaritons using a scanning tunneling microscope (STM). A schematic of the experiment may

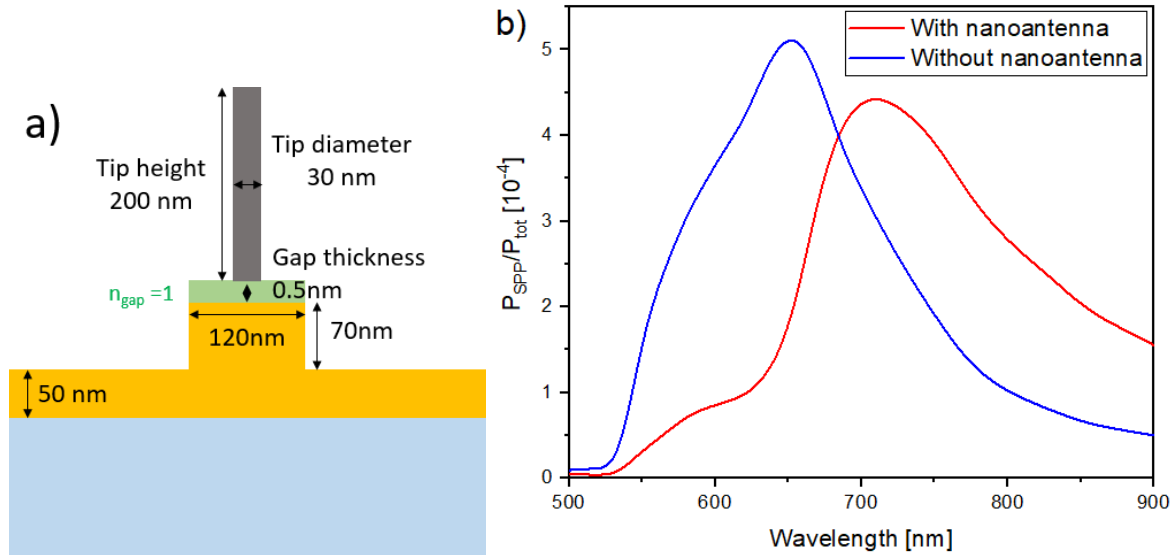


Figure 3.9: Surface plasmon excitation efficiency (P_{SPP}/P_{Tot}) using a more realistic tip and tip-sample distance. a) Schematic of the sample and tip: the tungsten tip is considered a cylinder of length 200 nm and diameter 30 nm, separated from the sample by a 0.5-nm gap. The disc-shaped gold antenna has a diameter of 120 nm and a height of 70 nm. b) P_{SPP}/P_{Tot} for an excitation on the antenna (red curve) and directly on the gold film (blue curve). Note that in this case the results with and without the nanoantenna are of the same order.

be found in Fig. 3.1-a.

3.3.1 Sample fabrication and characterization

Sample fabrication

The sample substrate is a cleaned glass coverslip whose thickness (170 μm) is appropriate for the aberration correction of our oil immersion microscope objective (see Chapter 1.2.5). A 50-nm thick gold film is first deposited by electron-beam evaporation in the clean room of the former Institut d'Electronique Fondamentale (see Fig. 3.10-a). The rest of the fabrication is carried out by Anne-Lise Coutrot from the Charles Fabry Laboratory (IOGS, Palaiseau). The nanoantennas are realized using electron beam lithography as described in Fig. 3.10. This method uses a positive resist (PMMA A4) which is deposited onto the surface via spin-coating (Fig. 3.10-b): when exposed to an electron beam (Fig. 3.10-c), a chemical reaction increases the solubility of the exposed resist in a specific solvent (here methylisobutylketone). The designs written in the resist with the electron beam of a scanning electron microscope (SEM) are developed using the solvent (Fig. 3.10-d). Gold is then deposited on the sample, filling the holes left behind and covering the remaining resist (Fig. 3.10-e). Lastly, another solvent (acetone) is used to strip the remaining resist, leaving behind only the desired structures (Fig. 3.10-f).

The sample design includes antennas with five different diameters (see Fig. 3.11). All nanoantennas should have a similar height as they are all deposited at the same time. For each diameter, four lines of six antennas, with different periods between 750 nm and 900 nm are repeated on the sample sixteen times. This arrangement of the antennas, along with the use of markers, makes it possible to find antennas of a particular diameter with the optical microscope. The fact that there are many groups of antennas repeated several times on the sample means that we may repeat the experiment multiple times on the same type of antenna and thus evaluate the repeatability of the results.

From the simulation results (see Fig. 3.7), it was seen that the best nanoantennas are small (< 50 nm) and of cylindrical (rather than disc-like) shape. However, such small nanoantennas are difficult to fabricate: the fabrication of high aspect ratio ($AR > 1$) nanostructures with diameters of less than 100 nm is challenging, even using e-beam lithography. Most high aspect ratio records achieved by e-beam lithography involve larger structures [144] or use additional steps such as double etching [145], gold electroplating instead of gold evaporation [146, 147], or reactive ion etching [148, 149] for example. Nanostructures with dimensions under 30 nm may be fabricated using e-beam lithography [150]. However, the aspect ratio for these structures is lower ($AR < 1$). It is thus quite difficult to realize such small nanostructures with an aspect ratio ≥ 1 using our direct writing e-beam

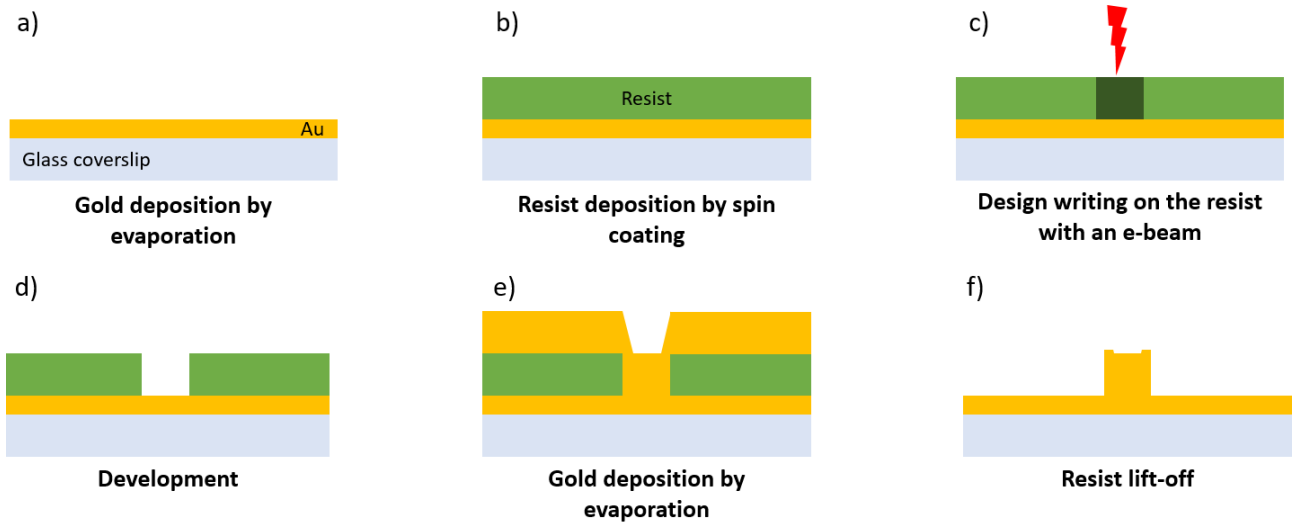


Figure 3.10: Sample fabrication process: a) gold is evaporated onto the glass substrate, b) resist is spin-coated onto the gold and c) the sample design is written in the resist using the electron beam of an SEM and d) developed. e) Gold is deposited by evaporation in the holes left behind before f) the remaining resist is stripped.

lithography method. Since the ideal dimensions are too small for our lithography method, we are constrained to using larger nanoantennas.

Sample characterization

To determine the nanoantenna diameters, we use a scanning electron microscope (SEM), either at the Institut d’Optique Graduate School (courtesy of Anne-Lise Coutrot) or at Ecole Polytechnique (courtesy of Mélanie Poggi): unlike STM or AFM imaging, where the lateral dimensions of the objects are convoluted with the tip shape (which may be a few tens of nanometers large), an SEM image obtained with a high enough energy electron beam gives us a more precise measurement of the nano-object diameter as the e-beam diffraction is negligible (a few nanometers, for structures with a diameter of $\simeq 100$ nm). Figure 3.11 shows a graph of the measured diameters from SEM images as a function of the target diameter (that is, the diameter we intended to fabricate). It is clear that the measured diameter is always higher than the target diameter. Our fabricated nanoantennas have average diameters between ~ 80 and 120 nm, and their average height from AFM measurements (not shown) is 95 ± 24 nm.

This result is not unexpected as top-down fabrication methods do not allow for the precise fabrication of extremely small ($<1 \mu\text{m}$) structures with a high aspect ratio ($\text{AR} > 1$). E-beam lithography may be used to fabricate smaller structures than those that are possible using UV-lithography (as the beam diameter is much smaller than the diffraction limit in the UV), but the effective beam broadening in the resist still limits the size of the nanostructures [151, 152] (see Fig. 3.12-a). Moreover, in the case of high aspect ratio nanostructures, the gap in the resist after the design development may act as a bottleneck, which the deposited gold atoms might plug before reaching the substrate, creating a nanostructure with a conic cross-section (see Fig. 3.12-b). If the base is smaller than the top of the nanoantenna, it may break during liftoff, or in extreme cases not adhere at all to the substrate.

3.3.2 STM excitation of surface plasmon polaritons with the help of a nanoantenna

As explained in Section 1.1.2, we use the inelastic tunneling current of an STM to excite propagating surface plasmons polaritons on a gold film. In what follows, we will use the same “STM-nanosource” but on a nanoantenna (see Fig. 3.1).

In order to understand the impact of the presence of the nanoantenna on the surface plasmon excitation, we use the following experimental protocol, which gives us two reference measurements for each STM excitation on a nanoantenna:

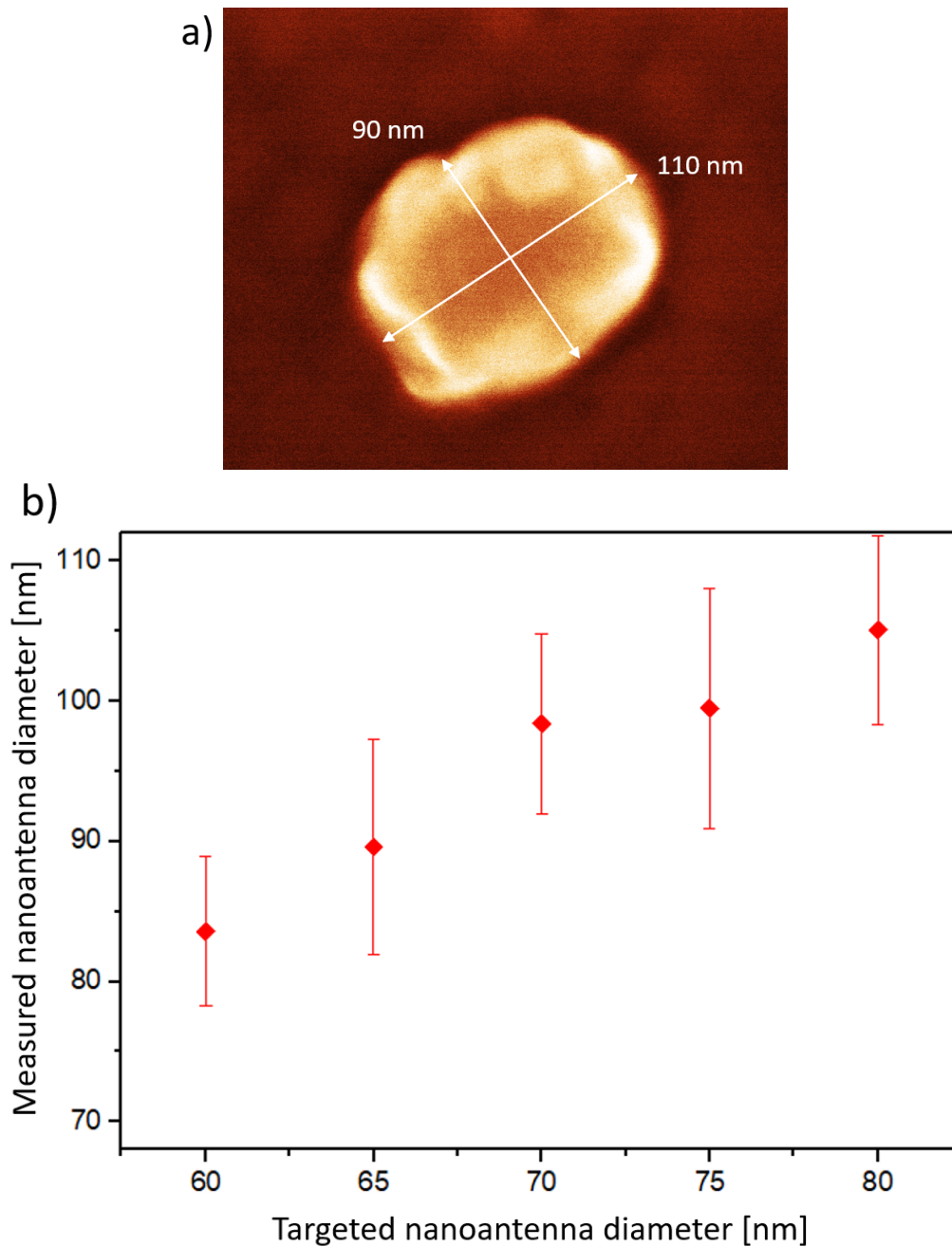


Figure 3.11: a) SEM image of a nanoantenna with the measured diameter (rounded to the nanometer), b) mean nanoantenna diameters, as measured by SEM and averaged over both directions, as a function of target diameter (with the error bars marking the standard deviation).

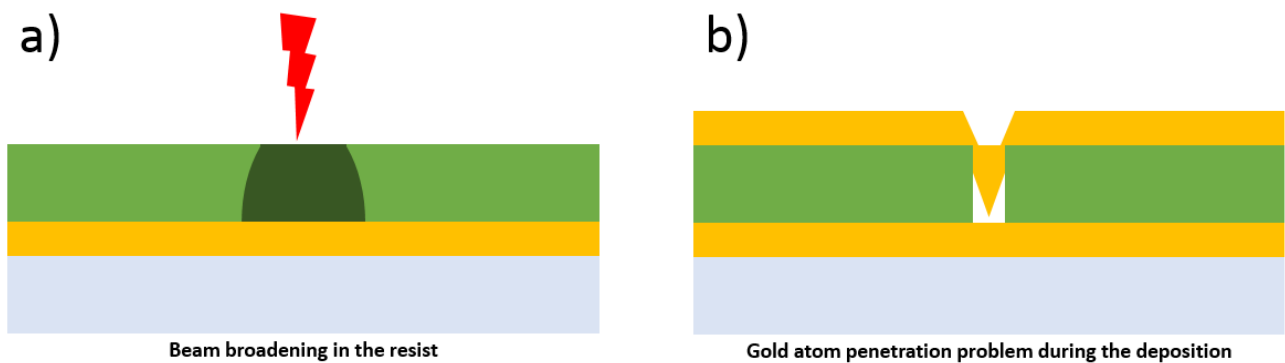


Figure 3.12: a) Beam broadening in the resist, and b) illustration of the gold atom penetration problem for high aspect ratio nanostructures.

1. Localization and first STM image of an antenna: a combination of optical and scanning tunneling microscopy is used to find an appropriate nanoantenna. Using a piezo stage, the antenna is placed in the center of the objective field of view.
2. STM image of a region on the gold film to the side of the nanoantenna, which will be used to collect a reference spectrum.
3. Acquisition of reference data on the gold film. We use the STM tunneling current to excite surface plasmons on the gold sample. The STM tip is stationary during the measurement (that is, not scanning) and the feedback loop tunneling current setpoint is 1 nA. The applied voltage is 2.5 V so that surface plasmons with energies up to 2.5 eV ($\lambda \simeq 500$ nm) may be excited. Thanks to an oil immersion objective of high numerical aperture (see Section 1.2.5), we collect the light emitted from surface plasmons which decay into photons through the thin gold film into the glass substrate. As the experimental efficiency is low (on the order of 10^{-7} photons per electron in general for our experiment), we excite surface plasmons and collect the resulting photons over a time of 100 seconds in order to obtain a good signal-to-noise ratio. The light is detected with the real plane CCD camera or with the CCD camera of the spectrometer (see Section 1.2.5).
4. Second STM image of the antenna: the purpose of this step is to verify if the STM tip has changed shape during the previous excitation on the gold film. This can be determined from changes in the STM image (differences between the true sample topography and the STM image are due to the convolution of the topography with the tip shape, as explained in Section 1.2). We also compensate for any thermal drift that might have shifted the relative position of the antenna with respect to the STM tip position during the previous step.
5. Data acquisition on the nanoantenna: for the acquisition of this data set, we keep the STM tip above the nanoantenna without scanning, with a bias voltage of 2.5 V and a tunneling current setpoint of 1 nA for 100 seconds. As above, we again collect the light that results from surface plasmons decaying into photons through the thin gold film into the glass substrate. Figure 3.13 shows a real plane image / spectrum from such a measurement.

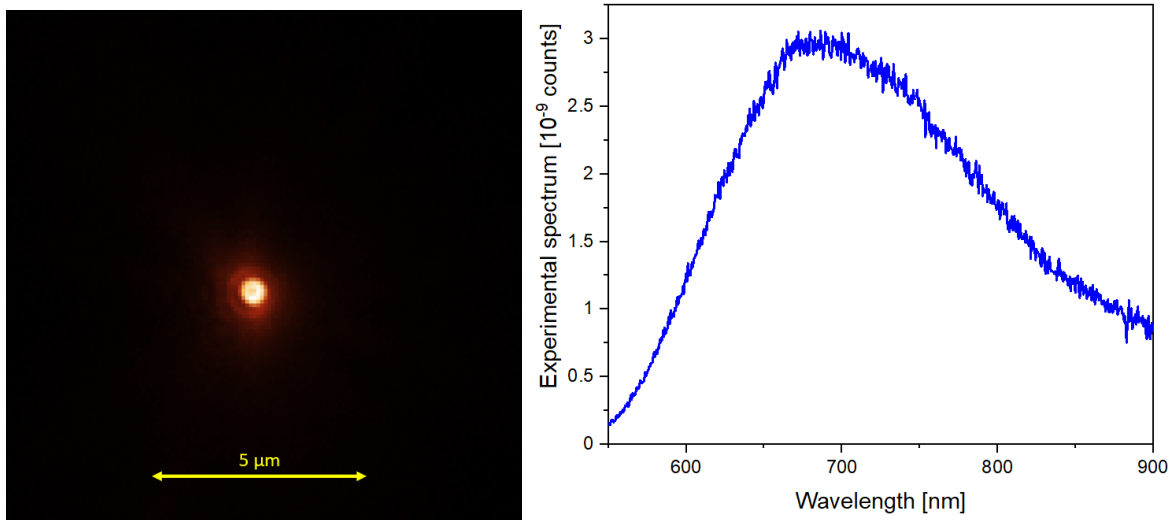


Figure 3.13: Antenna data. STM excitation of surface plasmons on a nanoantenna. a) Real plane CCD image of the surface plasmons propagating on the thin gold film and decaying into photons through the transparent substrate and b) spectrum of the light collected during the surface plasmon excitation ($V_S = 2.5$ V, $I_{Setpoint} = 1$ nA, acquisition time = 100 s).

6. Third STM image of the nanoantenna: the purpose of this image is to detect possible changes in the tip or in the shape of the nanoantenna.
7. Identification of a new region on the thin gold film to the side of the nanoantenna, which will be used to collect a new reference spectrum.
8. Acquisition of new reference data on the thin gold film.

For each excitation set, we have 3 images, or spectra, of the collected light: 2 reference measurements on the gold film (points 3 and 8), and one on the antenna (point 5). We also have 3 STM images of the antenna, before the first reference excitation on the gold film (1), before the excitation on the nanoantenna (4) and after the excitation on the nanoantenna (6). Thanks to this set of data, we can (i) determine from the STM images

if the nanoantenna or the tip has changed during the excitation, and (ii) determine if this change affects the surface plasmon emission (by comparing the reference data from the gold film obtained before and after the experiment on the nanoantenna).

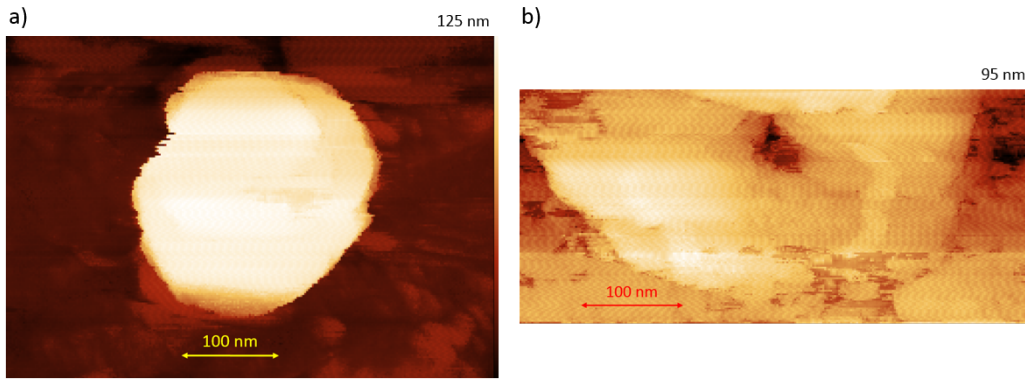


Figure 3.14: STM image of the nanoantenna, a) before the STM excitation and b) after the excitation.

Figure 3.14 shows the STM images obtained before and after the STM excitation of surface plasmons on the nanoantenna with a higher tunneling current setpoint and a longer integration time (bias voltage 2.5 V, 5 nA tunneling current setpoint, 200 seconds acquisition time). We clearly see that the excitation has damaged the nanoantenna. This problem and its solution is studied in detail in Appendix F. The solution involves choosing appropriate feedback gain parameters (so that the current is as constant as possible), and using lower current setpoint values such as 1 nA and shorter integration times such as 100 s (possibly to reduce heating—see Appendix F). In the rest of this chapter, we use the optimized excitation parameters and only consider excitations that did not damage the nanoantenna.

3.3.3 Analysis of the surface plasmon excitation efficiency

Experimental efficiency: definition and significance

The experimental efficiency is defined as the number of collected photons per electron. It is determined by measuring the intensity of the light collected below the sample during an “STM-nanosource” excitation on one hand and the tunneling current passing through the junction between the STM tip and the sample on the other hand, and by dividing one by the other:

$$\text{Experimental efficiency} = \frac{\text{Number of detected photons}}{\text{Number of electrons passing through tunnel junction}} \quad (3.3)$$

This quantity may not be directly considered equivalent to an experimental measurement of the propagating surface plasmon efficiency (that is, the number of excited SPPs per electron) for several reasons.

- Source of the emitted photons: the light collected by our setup is not only from propagating surface plasmons decaying into photons through the substrate, we also collect signal due to photons from localized surface plasmons or LSPs (surface plasmons confined between the STM tip and the surface), which are also excited by the inelastic tunneling current. It is difficult to separate the two. These two contributions cannot be separated in a spectral measurement, but we may measure a signal originating exclusively from propagating surface plasmons by collecting only the signal a certain distance away from the STM tip. Indeed, the localized plasmons are located under the tip in a nanoscale area, which is smaller than the diffraction limit, while the propagating surface plasmons may propagate on the surface before decaying into photons (see Section 1.1 for more details on the difference between the two types of surface plasmons). On the other hand, the propagating surface plasmons are also the most intense under the tip as they decay exponentially with distance (see Section 1.1). Thus, as we would lose much of the light from the SPPs as well if we excluded the signal from LSPs, we choose to take into account the light from both propagating and localized surface plasmons (that is, all the detectable light).
- “Undetected” SPPs: we do not detect all the excited SPPs with our leakage radiation microscope for two reasons; first of all, we do not detect any photons from surface plasmons that are emitted outside

of the collection angle of the microscope objective (e.g., emitted above the surface due to roughness or defects or emitted below the surface, but at an angle above our maximum collection angle of 72°). This lost contribution is expected to be small. The second source of “undetected” SPPs, however, is expected to be more significant, as it includes surface plasmons which decay non-radiatively into heat instead of radiatively into far-field photons (see Section 1.1).

In order to investigate the validity of the experimental efficiency as a measure of the propagating surface plasmon efficiency, we consider different parameters obtained from the modeling of Section 3.2.2, using a more realistic tip and nanoantenna. In Fig. 3.15-a we compare P_{SPP} (power in the SPP mode) and P_{rad} (power radiated into photons in the far field in the collection angle of our set-up) for the excitation of a disc-shaped antenna (diameter 120 nm, height 70 nm) using a tungsten cylindrical tip (length 200 nm, diameter 30 nm, see the schematic in Fig.3.9-a). The real shape of the STM tip would be better modelled by a cylinder with a conic, rounded end, however for simplification purposes in the model, we use a cylindrical STM tip in this simulation. From these results we see that while P_{rad} and P_{SPP} depend similarly on wavelength, by measuring the emitted photons instead of the SPPs directly, we will slightly underestimate the efficiency (by a factor of 0.44, found by dividing P_{rad} by P_{SPP} in Fig. 3.15 after integrating over the wavelength range of interest). Note, however, that experimentally we do not directly measure the radiated power, but the number of photons per wavelength. This experimentally relevant calculation is found dividing by the energy of the photons ($P_{rad}(\lambda)/\frac{hc}{\lambda}$) and is shown in Fig. 3.15-b).

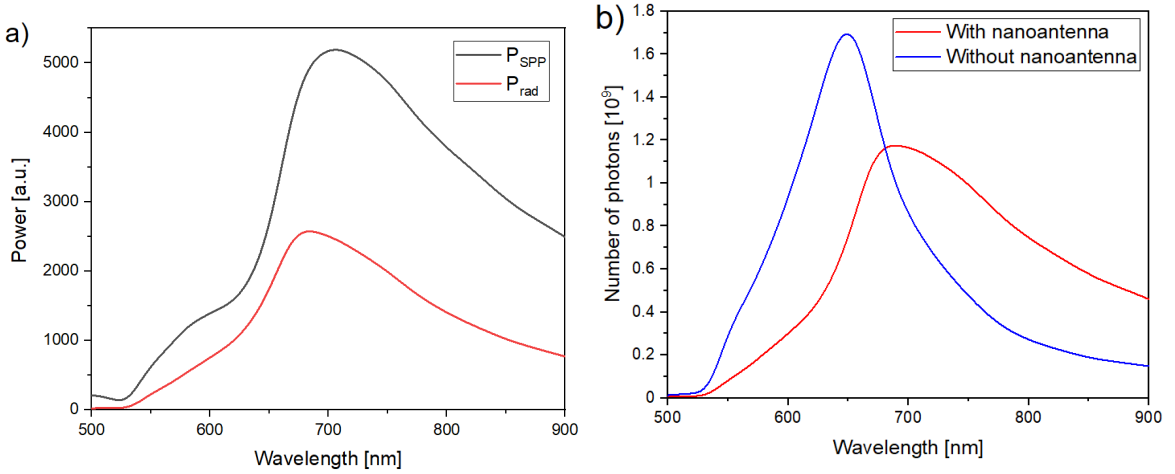


Figure 3.15: Comparison of the calculated parameters P_{SPP} (power in the propagating surface plasmon mode), P_{rad} (power radiated into photons in the far field), and the power radiated in the far field expressed in terms of number of photons per wavelength. a) Comparison between P_{SPP} and P_{rad} for the STM tip and sample shown in Fig. 3.9-a. b) Comparison between the spectrum (in number of photons per wavelength) for an STM excitation on a thin gold film (see Fig. 3.8-a) and on the nanoantenna (again from Fig. 3.9-a). The STM tip is represented by a 200-nm long cylinder with a 30-nm diameter, and is separated by a 0.5 nm gap from the disc-like antenna, which is 120 nm in diameter and 70 nm high.

From Fig. 3.15-b we can determine the expected ratio of the experimental efficiency with and without the nanoantenna. By integrating the number of photons in the wavelength range of interest for both the case with and the case without a nanoantenna, and determining the ratio of the two, we obtain a value just slightly higher than one (~ 1.03). This is far from the value of 38 seen for the ratio of the averaged propagating surface plasmon excitation efficiency with and without the nanoantenna found in Fig. 3.5, for the case of a small spherical tip and an ideal nanoantenna. Thus, given the “real” shape of the STM tip and the disc-like (instead of cylinder-like) form of the fabricated nanoantennas, a significant increase in the experimental efficiency is unlikely to be measured.

Measurements on the 50-nm-thick gold film

As described above, the experimental efficiency may be determined by dividing the number of collected photons by the total number of electrons participating in the tunneling current. Before investigating the nanoantennas, first we use points 2 and 3 in the protocol explained in Section 3.3.2 to determine the experimental efficiency for the STM excitation of surface plasmons on a thin (50 nm-thick) gold film. We use five different STM tips. For each STM tip, we repeat the measurement with the same parameters ten times. We determine the number of photons by integrating the counts on real plane images such as the one in Fig. 3.13 (from which we subtract the background noise signal). The number of electrons is determined by integrating the current measured with

the STM module (with the total number of electrons passing through the junction during the excitation time $= \frac{\Sigma I \times dt}{q}$ with I the measured tunnel current, dt the time interval between two current measurements and q the electron charge). Figure 3.16 shows the average experimental efficiency as a function of STM tip. The inset to the figure shows what we define as the relative variation, that is:

$$\text{Relative variation} = \frac{100 \% * \text{Std dev. of the experimental efficiency for a given STM tip}}{\text{Mean value of the experimental efficiency for a given STM tip}} \quad (3.4)$$

Two important points may be noted from the results of Fig. 3.16. First of all, we see that there may be a great variability between tips, with, in particular, one tip whose average experimental efficiency is several orders of magnitude higher than the others.¹ Thus the protocol of Section 3.3.2 is important in order to investigate the effect of the nanoantenna. Secondly, we see that for the same tip, the relative variation may be over 100 %. In other words, only if the nanoantenna leads to an increase in the experimental efficiency of more than a factor of 2 may such an increase be detected. Note, however, as was seen just above, that the STM excitation of the fabricated nanoantennas (e.g., with a height of around 70 nm and diameter on the order of 120 nm) is expected to lead to an increase of only ~ 1.03 .

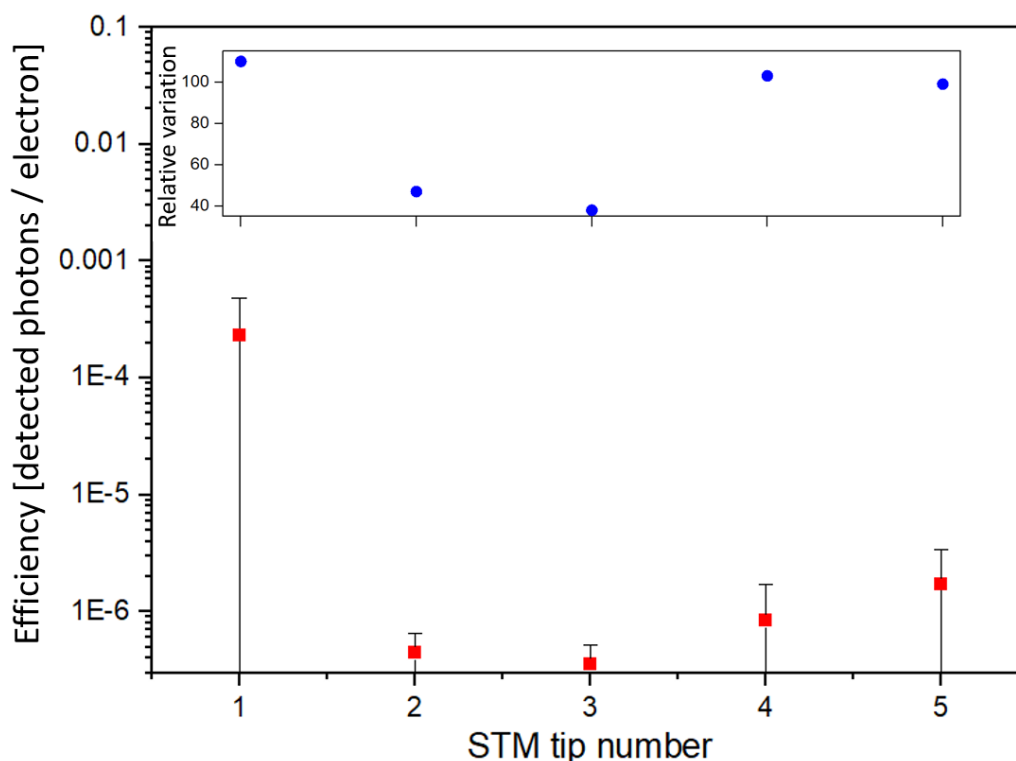


Figure 3.16: Average experimental efficiency as a function of STM tip, with the relative variation for each tip shown in the inset (standard deviation of the data set for each tip, divided by the average value, in %). For better visibility purposes, the experimental efficiency is plotted on a log scale.

Measurements on the nanoantennas

The experimental efficiency of the fabricated nanoantennas is measured using the protocol of Section 3.3.2. By imaging the nanoantenna before and after the excitation, destructive excitations may be identified and excluded from our results. As previously, the number of photons is determined by integrating the number of counts from real plane images such Fig. 3.13, and the number of electrons by integrating the current measured with the STM module as explained in the section above. The antenna data are shown in Fig. 3.17, along with the reference measurements.

¹A possible reason for why the experimental efficiency depends on the tip could be that the STM tip may not always have the same radius. Our tips are fabricated using the chemical etching of a tungsten wire as described in [34]: this STM tip fabrication method was developed at the Centre de Nanosciences et de Nanotechnologies (former LPN), and applied in our laboratory by Benoit Rogez, a former PhD student in our group. STM tips with a diameter as small as 20 nm may be fabricated using this method. However, the tip diameter may range from 20 to 100 nm and is on average around 60 nm. Moreover, the radius of the STM tip may change from one excitation to the next, as the tip might touch the surface and acquire atoms during the imaging or the excitation, and change shape, which would impact the emission [153]. As our sample is made of gold, the STM tip may end up covered is gold, thus leading to an exaltation of the surface plasmon emission.

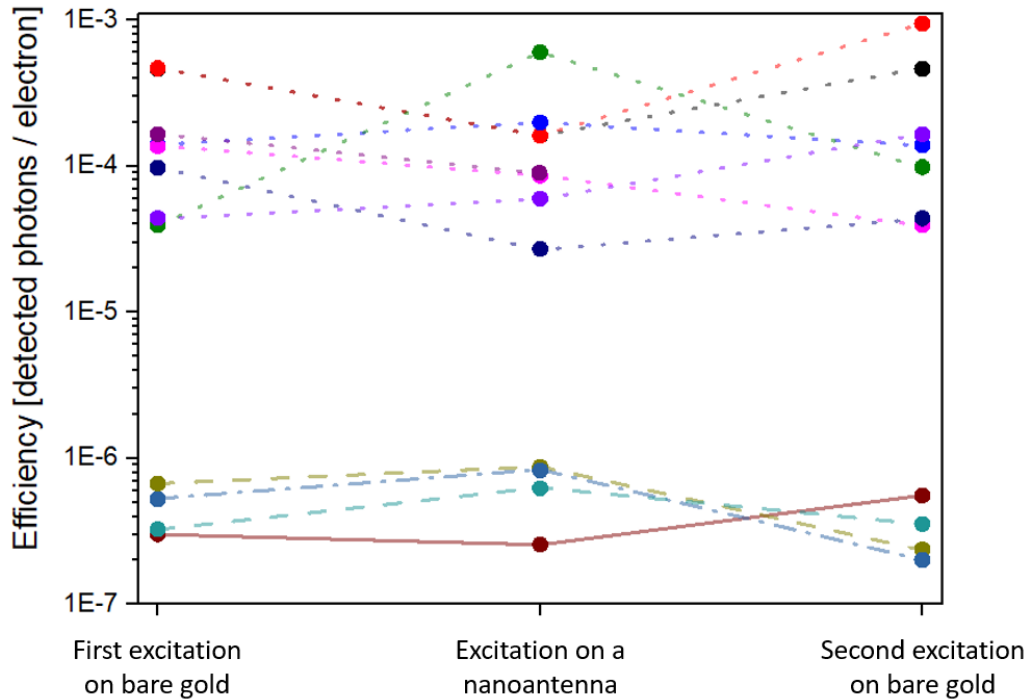


Figure 3.17: Experimental efficiency for excitations on the thin gold film and on a nanoantenna, color-coded for each set of data obtained as described in the protocol and plotted on a log scale. Four different tips are used. The data from each tip may be identified from the connecting line (dot, dash, dash + dot or solid line).

We note that, as expected after the measurements on the thin gold film above, the experimental efficiency on the different nanoantennas fluctuates significantly! We observe that the efficiency values are also split in two different groups, one with efficiencies around 10^{-4} and the other around 10^{-7} : this difference is probably due to the fact that the excitations were carried out using different STM tips.² The second point of interest is that the excitation on the nanoantenna results in a higher experimental efficiency than on the thin gold film only in about 40 % of the data sets. When the experimental efficiency for the excitations on the nanoantenna is indeed higher than the experimental efficiency for both the “before” and “after” excitations on the thin gold film, we see an increase in the experimental efficiency of a factor of 3 on average, with a maximum increase of experimental efficiency of a factor of 9 (green data set in Fig. 3.17). The fact that no net increase in the experimental efficiency is found with a nanoantenna is completely consistent with the simulations taking into account a more realistic tip shape and nanoantenna size (see Figs. 3.9 and 3.15-b) and the variability in the measurement found in Fig. 3.16. Note also that variations in the nanoantenna dimensions (see Figs. 3.6 and 3.11) contribute to the large spread in the measurements.

3.3.4 Spectra

Figure 3.18-d shows the experimentally measured spectrum of the light emitted when the “STM-nanosource” is used to excite a nanoantenna. Figure 3.18-c shows the profile of the nanoantenna measured by STM. As detailed in Section 1.2.5, the STM image shows the convolution of the STM tip with the actual shape of the nanoantenna.

Using the more realistic tip (200-nm long cylinder with a 30-nm diameter) and an antenna with the dimensions shown in Fig. 3.18-b, the corresponding emission spectra is simulated. This spectrum is determined from the simulated power radiated into the far-field in our collection angle (see Fig. 3.15). The simulated spectra of the radiated power per wavelength is divided by the energy for each wavelength in order to obtain the number of radiated photons per wavelength as in Fig. 3.15.

The simulated spectrum is quite similar to the experimental spectrum, but shows a net red shift. This

²The group with efficiencies around 10^{-4} is composed exclusively of data sets obtained with the same STM tip on the same day, whereas the other measurements were carried out on different days and with different STM tips. This exceptional STM tip was fabricated with the same method as the others, thus we have no clear explanation for this difference. We have several hypotheses: the STM tip may be covered in gold, thus acting as a plasmonic antenna. It is also possible that the tungsten wire used to fabricate the STM tip is not completely homogeneous, and that this STM tip has a specific shape (due to the etching not being homogeneous), and thus that the plasmonic cavity between this tip and the sample is different from the other tips, and enhances the plasmon excitation efficiency.

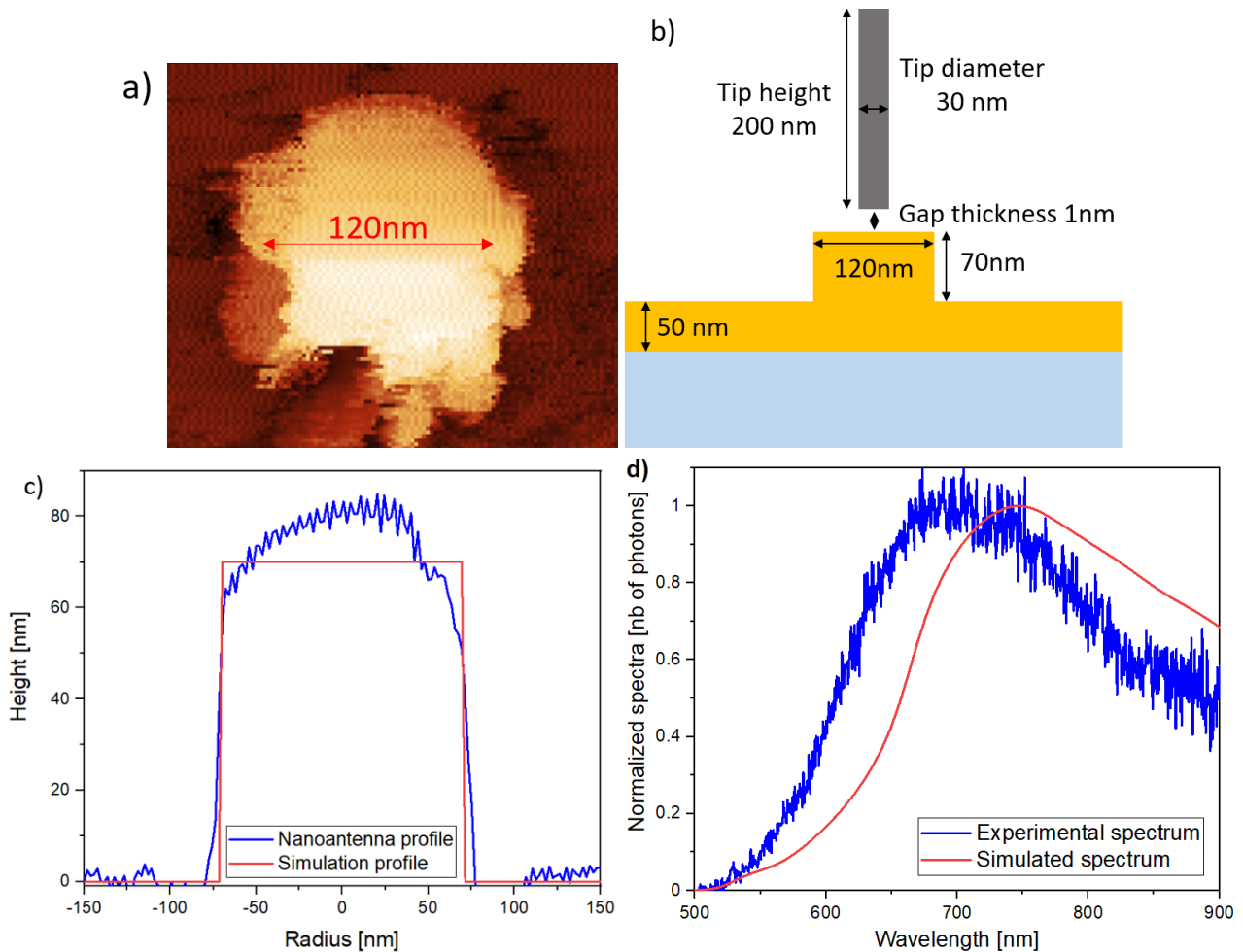


Figure 3.18: a) STM image of the nanoantenna with which we excite surface plasmons. b) Model of the antenna for the simulations with a cylindrical STM tip. c) Topography cross-section measured by STM (blue curve) compared to the cross section of the convolution of the 120 nm large, 70 nm high antenna with a 30-nm diameter STM tip (red line) used for the simulations. d) Emission spectrum for an excitation of 100 s at 2.5 V, 5 nA (blue line) compared to the simulation result for a realistic system (30-nm diameter, 200-nm long cylindrical STM tip, 70-nm high, 120-nm diameter nanoantenna, red line) in number of photons ($P_{rad}(\lambda)/\frac{hc}{\lambda}$). Both curves are normalized.

difference between the simulated and experimental spectrum may be due to different factors, which will be detailed here:

- First, while a distance on the order of 1 nm is expected between the STM tip and the sample, the exact value is unknown. The impact of the gap thickness is shown in Fig. 3.19. Note that the vertical point dipole source is always located in the center of the gap, thus as the gap increases, so does the distance between the source and the antenna. In Fig. 3.19 it is seen that a thicker gap leads to a decrease in the emitted light. This decrease in the number of emitted photons may be due to the fact that as the source is further away from the antenna, it couples less efficiently to the antenna mode. By comparing the shape of the experimental spectrum of the emitted light in our system to the simulated spectra, we note that the best fit corresponds to a gap thickness of 0.5 nm. Thus, in the following simulations, we fix the gap thickness in our system at 0.5 nm.

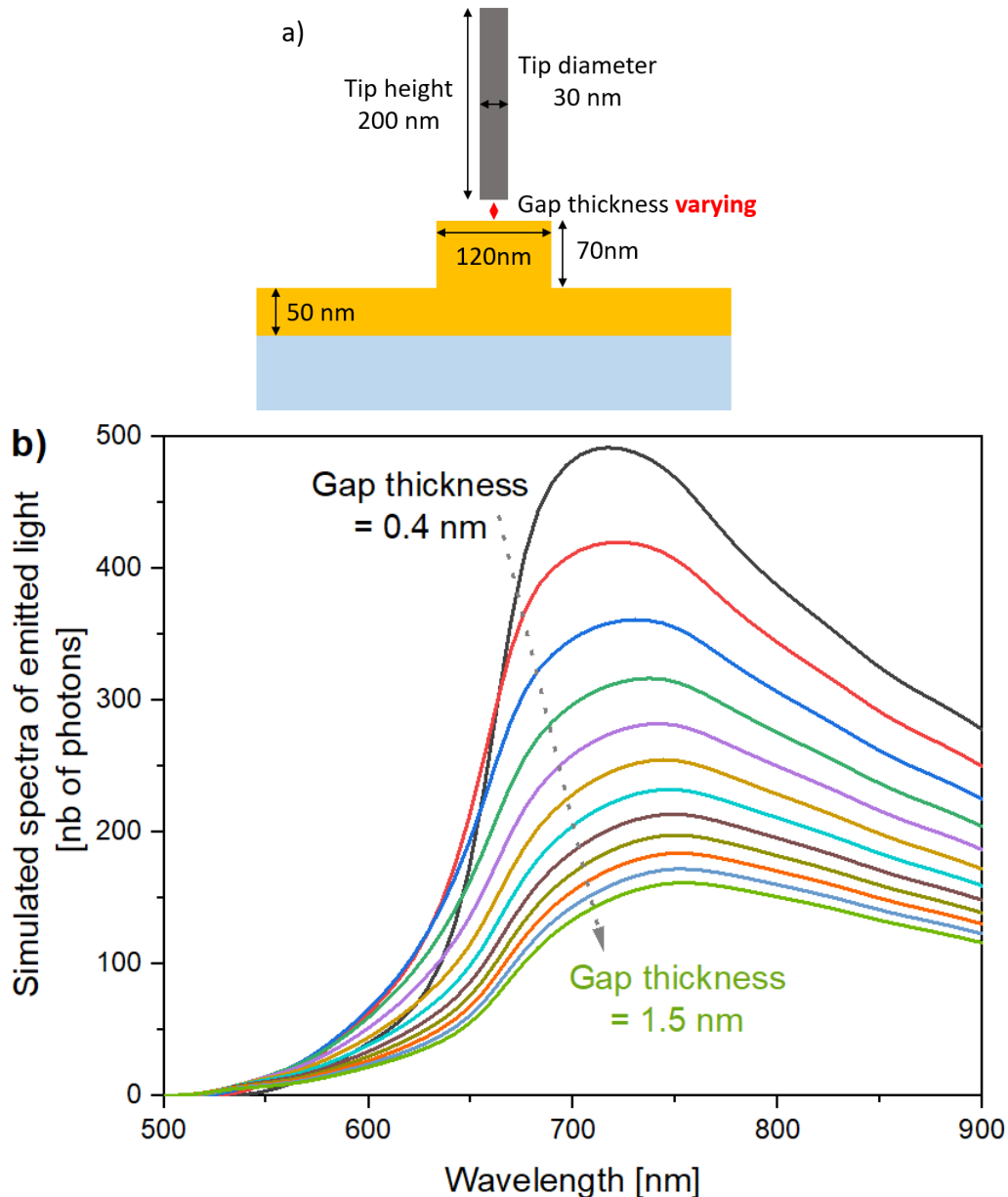


Figure 3.19: a) Simulation conditions to calculate b) the spectra of the emitted light for a varying gap thickness between 0.4 nm and 1.5 nm (with a 0.1 nm step).

- Secondly, we consider that our sample is in air (index of refraction of 1) in our simulations. However, under ambient conditions, as described in Appendix F, a water film covers the surface. This phenomenon might change the refractive index inside the gap. The exact refractive index may not be exactly 1.33 either (which is the refractive index of water at 590 nm for a temperature of 20° C and a pressure of 1 bar, see [154]) as pollutants may have settled on the surface. We may thus consider the impact of the gap index of refraction: see Fig. 3.20. Due to the limitations of the simulation program, we model the

water and pollutant layer only between the STM tip and the antenna, even though we probably have a water layer on our surface with a thickness of up to $\simeq 10$ nm [48]. However, as this thickness is negligible compared to the penetration depth of the propagating surface plasmon evanescent field in air (which is $\simeq 200$ nm, see Section 1.1.3), we consider that we may neglect this layer on the thin gold film. We still take into account this possible layer of different index of refraction between the nanoantenna and the tip as the localized modes under the STM tip are much more confined and thus will be more impacted by a change in the refractive index. We note that increasing the refractive index between the STM tip and the nanoantenna greatly reduces the emission of light, especially at smaller wavelengths (550-650 nm). This may be due to increased confinement and thus increased interaction with the metals, leading to higher losses. By comparing the shape of the experimental spectrum of the emitted light in our system to the simulated spectra, we note that the best fit corresponds to a refractive index of 1. Thus, in the following simulations, we fix the refractive index of the gap equal to 1.

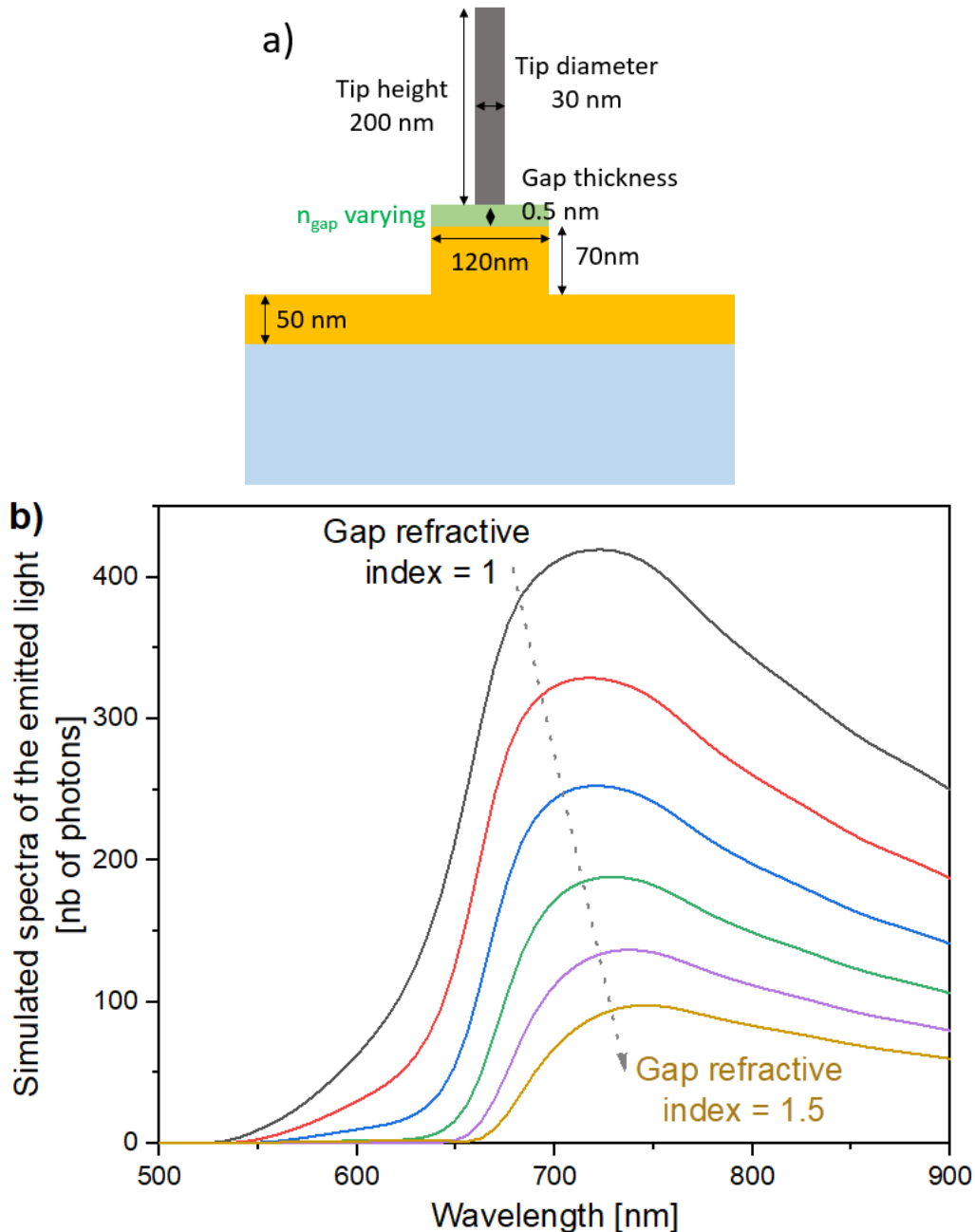


Figure 3.20: a) Simulation conditions to calculate b) the spectra of the emitted light for varying gap refractive indices.

- Thirdly, the refractive indices chosen for the simulations (Au from Ref. [16], W from Ref. [132]) may not be the exact indices of the sample. We test the dependence of the spectrum on the gold and tungsten indices by changing the literature reference used for the refractive index. In order to more easily visualize the losses, we plot the permittivity for each reference ($\epsilon = n^2$) rather than the refractive index itself: see Fig. 3.21. This result gives us two pieces of information: the permittivities of gold and tungsten show

only small variations in the literature, but these variations are enough to significantly shift the spectrum of the emitted light in our simulations (with a resonance wavelength difference of 68 nm between the dark green/Au2-W1 and light pink/Au3-W3 curves in Fig. 3.21). The refractive indices of the material used in the experiment were not measured, but it is likely that there is a difference between the index used in the simulation and the real indices, which may explain part of the differences between the calculated and the experimental spectra.

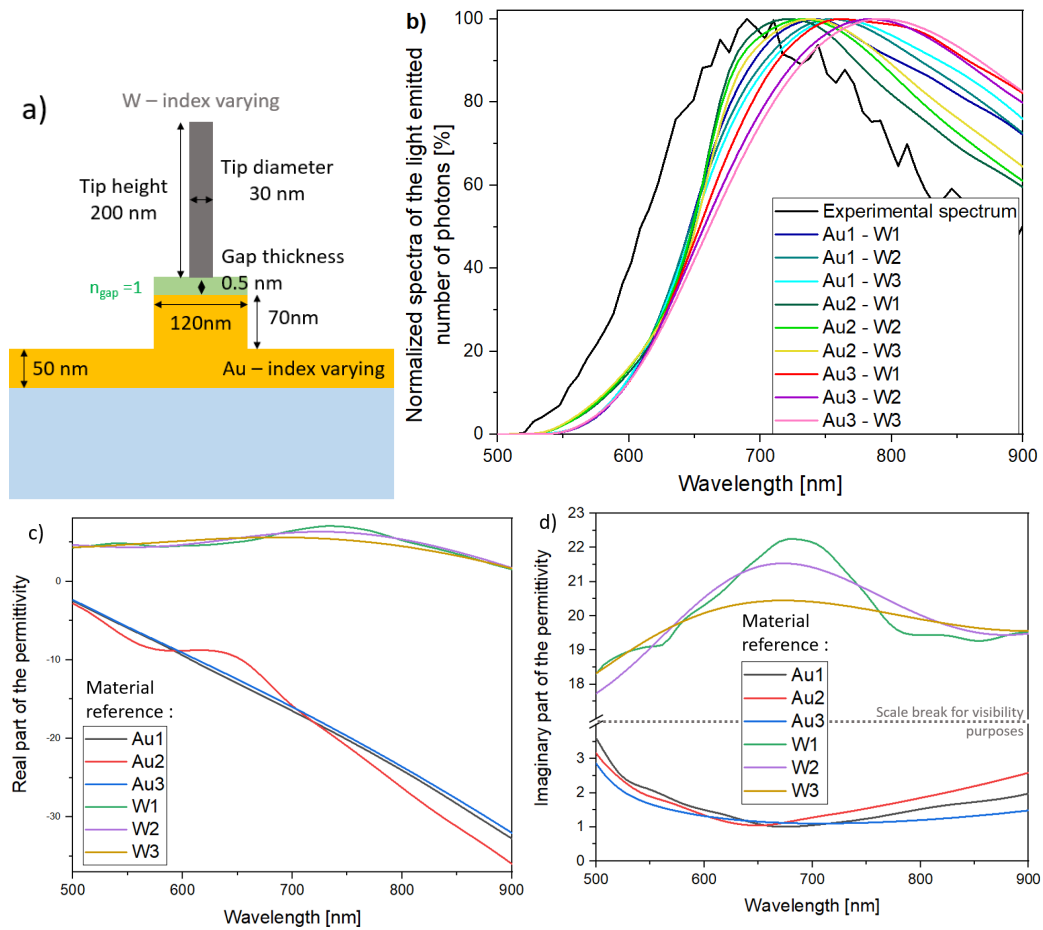


Figure 3.21: a) Simulation conditions to calculate b) the spectra of the emitted light using material permittivities from various references in the literature: Au1 the permittivity of gold and W1 the permittivity of tungsten from Ref. [16], Au2 the permittivity of gold from Ref. [132], Au3 the permittivity of gold from Ref. [155], W2 and W3 the permittivities of tungsten from Ref. [17], with W2 following the Lorentz-Drude model and W3 the Brendel-Bormann model. The real and imaginary parts of the permittivities over the wavelength range of interest for each reference are shown respectively in c) and d).

3.4 Summary

In summary, in this chapter, we evaluate the impact of the presence of a nanoantenna on the STM excitation of propagating surface plasmons. Theoretically, we consider the STM tip as a small tungsten sphere (10 nm in diameter), and study how the radiated power and the power emitted into the propagating surface plasmon mode varies as a function of the nanoantenna dimensions. We see the impact of the presence of the nanoantenna in the spectrum (see Fig. 3.5) in the form of a resonance peak whose position depends on the size of the nanoantenna. Indeed, we observe that the resonance wavelength depends on the aspect ratio for small nanoantennas (height ≤ 40 nm), while for larger antennas, due to retardation effects, the resonance wavelength changes for two antennas with a similar aspect ratio but with a different height. In this case when the STM tip is approximated by a small sphere, according to our simulations, the best nanoantennas for the enhancement of the surface plasmon excitation efficiency are small in size and of cylindrical shape (for example, 30-nm high and 20-nm in diameter). With such a tip and nanoantenna, the surface plasmon excitation efficiency may be increased by a factor 38 when averaged over our wavelength range of interest (with an increase of two orders of magnitude at the nanoantenna resonance) compared to the STM excitation of surface plasmons directly on a thin gold film (see Fig. 3.5). However, a more realistic tip shape and the true shape of the fabricated nanoantennas must be taken into account for comparison with the experimental results. When the nanoantennas have the aspect ratio of a disc and the tip is approximated as a tungsten cylinder, the impact of the nanoantenna is disappointing as the number of photons radiated into the collection angle for an excitation with a nanoantenna is similar for an excitation without a nanoantenna (ratio of ~ 1).

The effect of a nanoantenna on the STM excitation of surface plasmons is also studied experimentally. Nanoantennas are fabricated by electron-beam lithography, which limits the minimum radius and aspect ratio available. After characterization, it is shown that our nanoantennas have diameters of 80 to 120 nm, and heights of 70 to 120 nm. The experimental efficiency (number of detected photons per tunneling electron) is measured and is found to depend greatly on the STM tip used, and to vary significantly between measurements. The spectrum of the emitted light is also studied and the possible effects of the distance between the STM tip and nanoantenna during the excitation, and variations in the index of refraction in this gap are also discussed.

In conclusion, comparing the experimental results with the simulations using a more realistic model, we realize that due to our technical fabrication limits, both for the STM tip diameter and the antenna dimensions, the system dimensions are too large. Simulations carried out with a more realistic system show that the fabricated nanoantenna does not increase the number of photons radiated into the far field significantly, which explains why we measure no significant experimental efficiency increase in our experiments: the size of the nanoantenna and the STM tip are too large to properly enhance the surface plasmon excitation efficiency in our wavelength range of interest.

The fact that the STM tip affects the results is clearly a drawback. In order to minimize this problem, in the next chapter, the biased tunneling junction which excites propagating surface plasmons will no longer be between an STM tip and a nanoantenna, but between the nanoantenna and the gold film. Please see the next chapter for details.

Chapter 4

Excitation of surface plasmons with a nanoantenna tunneling junction

4.1 Introduction

In the previous chapter, we studied the impact of the presence of a nanoantenna on the excitation of surface plasmons. To do this, we used the tunneling junction between an STM tip and the sample. This was a first step toward the long term goal of an efficient and nanoscale tunneling junction for the excitation of propagating surface plasmons in an integrated plasmonic device. The next step is to study a nanoscale metal-insulator-metal tunneling junction incorporating a nanoantenna, with the idea of shaping the surface plasmon spectrum, and the excitation efficiency.

Lambe & McCarthy were the first to report on the excitation of light using tunneling current in a macroscopic metal-insulator-metal (MIM) tunneling junction in 1976 [7]. They used the oxidization of aluminum to grow an alumina tunneling junction between two electrodes, and attributed the resulting emission of light to surface plasmons. This result sparked interest in the community, and in the following decades, several articles studied the integrated tunneling junction principle as a light source. In particular, the question of how to efficiently extract the light was addressed, primarily by using surface roughness or a grating to overcome the momentum mismatch between the propagating surface plasmons and photons [156–158], but also by using a prism so that the propagating surface plasmons could decay into photons in the prism through the aluminum electrode [159] (Kretschmann configuration, see Section 1.1.3).

In the last decade, thanks to progress in nanofabrication methods, great advances have been made in nano-optics in general and in MIM junctions combined with nanostructures in particular. For example, tunneling junctions have been made using electromigration and a gold nanowire [123, 124], and tunneling junctions involving metamaterials have been fabricated via the electrodeposition of gold in porous alumina templates [125]. A 1D nanoantenna (gold stripe) deposited on an oxidized aluminum sample (with thus the aluminum oxide serving as the tunneling barrier) has been shown experimentally and theoretically to improve the SPP excitation efficiency [126, 128]. Another example of a 1D nanoantenna used to enhance the electrical surface plasmon excitation may be found in Ref. [160], where a silver nanowire is separated from a gold stripe by an insulating molecular layer.

Lateral tunneling junctions (i.e., where the tunneling occurs in the horizontal direction on the sample) have been used to produce directional and/or efficient nanosources of light. In the group of B. Hecht, a gold nanoparticle is positioned in the feed gap of an optical nanoantenna in order to produce a lateral tunneling junction [161] which may be combined with a Yagi Uda antenna with the aim of producing a directional electrically excited light source [162]. This was also the aim of Ref. [163]. A similar system (i.e., a lateral tunneling junction) was also used in Ref. [164], and a particularly high electron-to-photon external efficiency of $\sim 2\%$ was measured: in this work Qian et al. used two silver nanocrystals edge-to-edge to form the tunneling junction, thus increasing the local electromagnetic density of states (very high along the edges of nanocubes as

compared to a flat MIM junction).

Other examples of the combination of nanostructures and tunneling junctions may be found in the work of L. Novotny and coworkers. They published an article using slot antennas in 2015 [165]. Another experiment from this group uses the tunneling junction formed in a gold, hexagonal boron nitride, graphene layer stack, which is capped by a silver nanocube [166]. They have published a review of the recent work in electrically excited nanoantennas as tunneling-current driven nanoscale light sources in [167] and [168].

In an exceptional case, presented in Ref. [169] and patented in 2019 (patent US 10,254,479 B2), the authors claim an effective electron-plasmon coupling efficiency of 14 %. Their system is made of two tunneling junctions coupled together by a gold strip, one serving as a nanosource to excite surface plasmons and the second acting as a detector. The authors suggest that their high efficiency is due to the direct detection method using a tunneling junction, without the losses involved when surface plasmons decay into photons. Their results have been challenged by the theoretical calculations of others [170] and the authors have responded in kind with calculations including the possible role of roughness in near-field outcoupling [171].

Most of the electrically driven nanosources presented above are designed to emit light and not plasmons, and involve large planar electrodes. In what follows, we present an electrically excited source of propagating surface plasmons, with a nanoscale footprint, and thus without large planar electrodes. This system incorporates a nanoscale antenna with a tunneling junction integrated between the nanoantenna and a plasmonic substrate. In order to contact the nanoantennas electrically, we develop a new method using the conducting tip of an atomic force microscope, so no carefully lithographed contact electrodes are necessary.

4.2 New method for locally contacting a “nanoparticle-on-a-mirror” tunneling junction

In the previous chapter, we studied the impact of a nanoantenna on the emission from a biased tunneling junction. The nanoantenna, made by electron-beam lithography, was a gold disc or cylinder on a gold film, and the exciting tunneling junction was between an STM tip and the nanoantenna. We now want to include a tunneling junction in our system so that the nanosource of surface plasmons does not require an STM. In what follows, we will study the emission from a “nanoantenna-on-a-mirror” sample, where the nanoantenna is separated from a metallic film by a thin insulating layer. It is this thin layer that now plays the role of the exciting tunneling junction. The system is a gold nanocube on a gold film functionalized with a film of insulating molecules (see Fig. 4.1). This system is studied in detail in this chapter.

In order to excite propagating surface plasmons on an Au film with the “nanocube-on-a-mirror” tunneling junction, a bias voltage must be applied between the nanocube antenna and the gold film. Here we introduce a new method to locally apply a bias voltage to nanoscale optoelectronic structures using the conducting tip of an atomic force microscope (AFM). This tool opens up new possibilities for applying a local electrical contact for the study of electroluminescence on the nanoscale. In particular, this technique may be used to test several different structures sequentially on a sample, without the need of lithographed contact wires for each structure. The challenge of the technique, however, is to successfully avoid the light from the laser which is used to measure the AFM feedback parameter (see Appendix C for details).

4.2.1 Establishing an electrical contact using CAFM

Background light from the AFM laser

As mentioned above and described in Appendix C, the AFM laser diode is a considerable source of background light which masks the signal to be measured. A solution would be to change the AFM head to one with a laser whose wavelength is out of our detection range. This, however, would be expensive. A second possibility would be to filter out the laser diode light, which is again difficult since the wavelength is in the range of the expected signal. Otherwise, we could use a “tuning fork” AFM cantilever, which does not require a laser [172]. However, our commercial AFM does not have a tuning fork module with which we can also apply a voltage and detect a current. Note also that conducting tuning fork tips are not commercially available, and considerable development would be necessary to gain the required expertise to fabricate such tips.

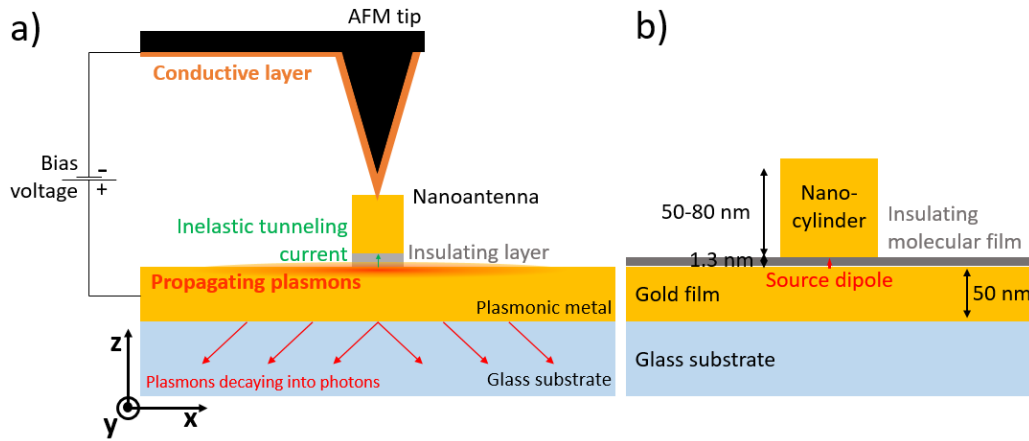


Figure 4.1: a) Schematic of the experiment and b) the corresponding simulation conditions: the conducting tip of an atomic force microscope is used to apply a bias voltage to the tunneling junction. The tunneling junction is formed between a nanocube nanoantenna separated from a thin (50 nm) gold film by an insulating molecular layer (~ 1 nm thick). The surface plasmon polaritons excited using this nanosource then propagate on the plasmonic gold film and decay into photons through the film into the glass substrate, thus radiating into the far field where they are detected.

As the above possibilities require a complete change of our experimental setup and bring their own complications, we developed the following solution. After allowing the system to thermally stabilize, we approach the conducting AFM tip to the sample until a stable electrical contact is established, and then shut down the laser while maintaining the voltage applied to the piezoelectric element commanding the z-position of the tip, thus maintaining its extension. Note, however, that since the laser is off, there is no feedback maintaining the tip-sample interaction constant (see Section 1.2.2). The thermalization step is essential: even if the AFM tip is not scanning, it is not immobile, as thermal drift will affect its position relative to the surface. As a result, if the system is not thermally stabilized beforehand, the electrical contact is often lost after a few tens of seconds. We observed that this phenomenon may be minimized by letting the system thermally stabilize for half an hour prior to the experiment.

Details of the method

Several other considerations must be taken into account when forming an electrical contact between a conducting AFM tip and a nano-object:

- First, it is well-known that nano-objects on surfaces are often moved in AFM contact mode imaging [173, 174]. Thus, in order to locate the nanocube antenna on the sample, we need to image the nanocube antenna in tapping mode, in which case there is less interaction between the tip and sample than in contact mode (see Section 1.2.2). However, in order to have a continuous and good quality electrical contact during the tunneling junction excitation, we need to use the AFM in contact mode. In other words, we must compromise: we need an AFM cantilever that is stiff enough to be used in tapping mode, yet soft enough that the smallest detectable deflection does not correspond to an applied pressure that will damage the nanoantenna. Note also that our nanostructures are made of gold, which is a relatively soft material, so indeed such possible damage must be considered (see Appendix F).
- Secondly, in order to excite propagating surface plasmons in the visible, we need to apply a bias voltage on the order of 2.5 V to the junction. However, an electrical contact obtained with a conducting AFM tip is not completely lossless, and we have to take into account the AFM tip resistance and the contact resistance (which may vary as a function of the deflection setpoint). As the voltage applied to the tunneling junction must be sufficient to excite light in the visible, we need to choose a conducting AFM tip with a low total electrical resistance (resistance of the conducting AFM tip itself plus the contact resistance between the tip and sample). This total resistance must be negligible compared to the tunneling junction electrical resistance so that the vast majority of the voltage drop occurs across the tunneling junction and not in the AFM tip.
- Thirdly, in order to carry out the experiments efficiently and not have to change the conducting AFM tip after each image and electrical contact, we need to use a mechanically resistant conducting tip that can withstand abrasion. Indeed, as we need to image in tapping mode before contacting electrically the

nanoantenna, the conducting tip may be damaged by the intermittent contact during the scans. And more importantly, as we require a low electrical contact resistance between the tip and the sample, we use a high deflection setpoint for the electrical contact. Added to the fact that once the laser is shut down, there is no feedback loop to correct the small displacements between the AFM tip and the surface, this means that when electrically exciting the tunneling junction, the contact force between the tip and antenna is expected to be large. In turn, this contact force may increase due to thermal drift, thus eroding the conducting layer and making the tip unusable.

We compare several conducting AFM tips by testing them with the same method on a thin gold film. The results are in Appendix G.1 and Appendix G.2. The best coated tips are silicide probes coated with a platinum silicide (PtSi) layer (cantilever stiffness 2.8 N/m), but a better alternative is an AFM tip made entirely of a conducting material (Rocky Mountain Nanotechnology, see <https://rmnano.com/>). The optimum metallic AFM tip for our experiment is a tip made entirely of platinum with a 8 N/m spring constant.

Test measurement

In order to test the protocol described page 59, a macroscopic tunneling junction is considered (no plasmonic nanoantenna resonance in our wavelength range of interest). We fabricated this sample at the Laboratoire de Physique des Solides (LPS) ¹. The sample consists of gold discs of radius $\sim 1 \mu\text{m}$ and a thickness of 50 nm deposited on a thin ($\sim 1 \text{ nm}$) alumina layer on aluminum (25 nm thick). Please see a schematic of the experiment and sample in Fig. 4.2-a and an optical transmission image of the sample in Fig. 4.2-c.

Before attempting to excite light and plasmons using this macroscopic tunneling junction, we use the conducting AFM tip to complete the circuit and measure the electrical characteristics of the junction (AFM laser and feedback still on). All the excitations in this section were carried out using an AFM tip which has a conducting PtSi coating.

Figure 4.2-b shows the measured tunneling current as a function of the applied bias voltage (in contact mode) using a PtSi tip with a 2.8 N/m spring constant. Good agreement with the theoretical tunneling current characteristic is obtained using Simmons' model [175] for a tunneling junction with a 1.7 nm thick alumina layer, a gold disc with a 930 nm diameter and a work function of 1.6 eV, and an aluminum film with a work function of 1.8 eV. ²

Finally, the developed protocol may be used to excite light and surface plasmons from this macroscopic junction. Once the necessary force for a good electrical contact has been determined, a tapping mode image is used to find the desired contact area and the conducting AFM tip is placed above it. Changing to contact mode, the tip is then lowered toward the sample. A 2.5 V bias is applied to the sample using a 50% duty cycle (100 ms) and the AFM feedback laser is turned off. Any emitted photons are collected through the transparent substrate during typical integration times of 50 s. Using the setup described in (see Section 1.2.5, Fig. 1.13), real space images such as the one shown in Fig. 4.2-d are obtained.

4.3 Bottom-up fabricated “nanocube-on-a-mirror” nanoantenna tunneling junction, contacted via CAFM

4.3.1 Sample fabrication, structural and electrical characterization

The “nanocube-on-a-mirror” nanoantenna tunneling junction sample to be studied is shown schematically in Fig. 4.3. The sample consists of gold nanocubes (50-80 nm in size) deposited on a 50 nm thick gold film (on a glass substrate). Before nanocube deposition, the Au film is functionalized with 1,8-octanedithiol (HSC_8SH)

¹To make this sample, we deposit 25 nm of aluminum on a glass coverslip. The Al layer is oxidized for 3 minutes using an oxygen plasma. We then deposit 50 nm of gold using a transmission electron microscope grid as a mask. The holes in the grid are small enough to deposit discs with a diameter of about $1 \mu\text{m}$.

²The work functions which lead to the best fit are lower than the work function for crystalline gold (5.3 eV) [176] and aluminum (4.2 eV) [177]. This may be due to the fact that we have amorphous or polycrystalline material in thin film form, which may have a lower work function than bulk single crystals [177, 178]. Note also that contamination in the tunneling barrier may also play a role. In similar work, values of the work function lower than what is found in the literature have also been measured [15, 126].

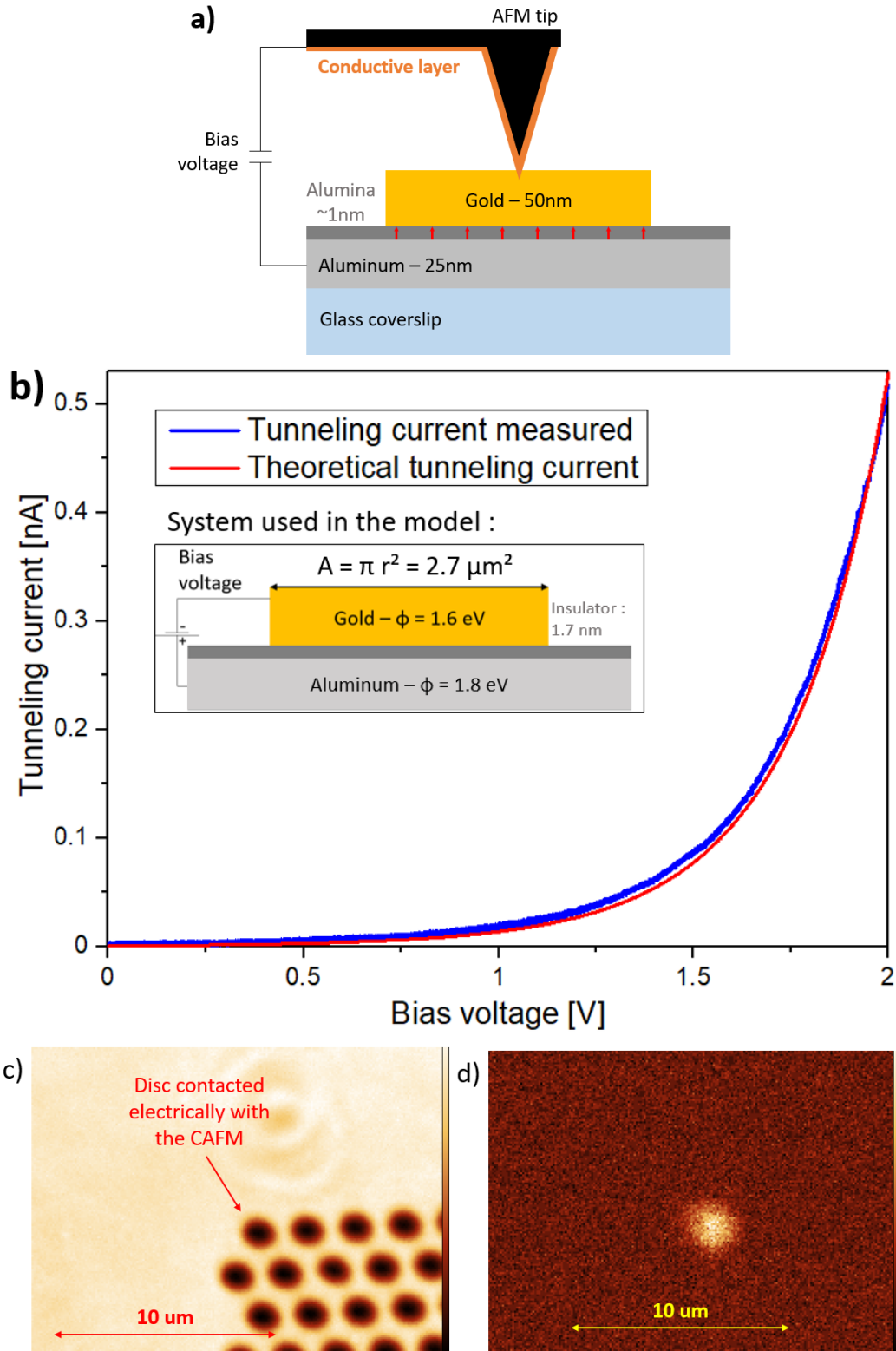


Figure 4.2: Locally contacting a macroscopic tunneling junction. a) We use a conducting AFM tip to electrically contact the sample and apply a bias voltage. b) $I(V)$ curve measured when applying a voltage to the gold disc (blue line) compared to the theoretical $I(V)$ curve for a 1.7 nm thick tunneling junction between a gold disc with an area of $2.7 \mu\text{m}^2$ and a work function of 1.6 eV and an aluminum film with a work function of 1.8 eV (the system used for the model is detailed in the inset). c) Optical microscope transmission image of the sample and the gold disc which we contact using the AFM to apply a bias voltage between the gold disc and the aluminum substrate. d) Optical real plane image obtained when the tunneling junction is biased with the AFM tip and the AFM laser is turned off: the detected light is from the biased tunneling junction.

molecules, which are insulating. These samples were synthesized by Dr. Yunhe Lai, a student of Prof. Jianfang Wang from the Chinese University of Hong Kong, using the method described in Fig. 4.3.

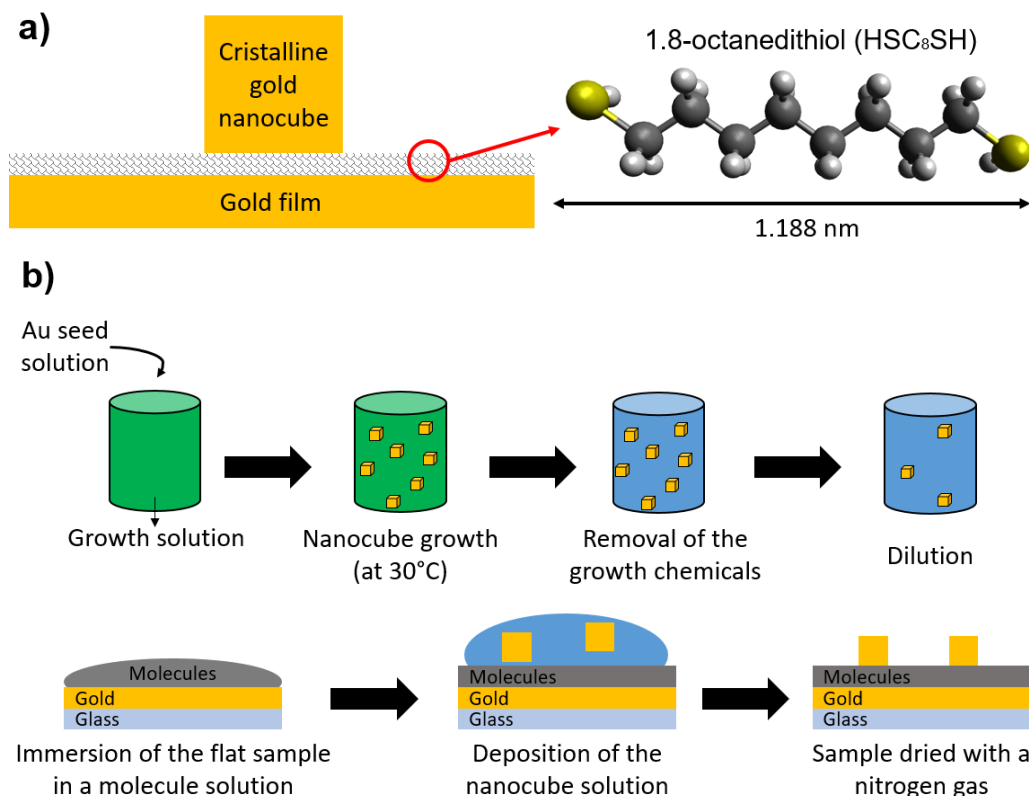


Figure 4.3: a) Schematic of the gold nanocube sample: we use a gold nanocube deposited on a thin gold film functionalized with insulating molecules made of an 8-carbon atom chain with thiols at each end. b) Fabrication method: the nanocubes were grown following the synthesis process in Ref. [179]. First, a seed solution is added to a growth solution, which is maintained at 30°C until the nanocubes reach the target dimension. The growth chemicals and surfactant are then removed by centrifugation, and the nanocube solution is diluted to obtain the target nanocube density. The glass substrate with a 50 nm gold film is immersed in an ethanol solution containing the octanedithiol molecules. Drops of the diluted nanocube solution are then deposited on the sample and dried using a high pressure nitrogen gas flow. These samples were fabricated by Dr. Yunhe Lai.

This new sample has two advantages over the ones of Sections 3 and H.1: first, the gold cube is crystalline, so it is expected to evacuate the heat more easily than polycrystalline gold. This should reduce the risk of nanoantenna damage due to tunneling current heating. Secondly, this method may be used to fabricate nanocubes with well-controlled and smaller dimensions as compared to e-beam lithography (side lengths as small as 20 nm are possible; here we will use 50-80 nm side lengths). However, a drawback of this method is that the aspect ratio of the structures is fixed at 1 as it grows chemically as a cube (thus the aspect ratio = 1). Hence we have lost a degree of freedom that could have been used to optimize the nanoantenna response.

Figure 4.4 shows a scanning electron microscope (SEM) image of the nanocubes made in Hong Kong. We see here in the SEM image that the nanocubes' dimensions are quite uniform, with the average side length of a nanocube being $45 \text{ nm} \pm 5 \text{ nm}$. We may note, however, that not all nanoparticles are cubic, with around 30 % of the nanoparticles being triangles, rods or spheres. When choosing a particle to excite surface plasmons, we use AFM imaging to choose particles approaching the correct shape.

Figure 4.5 shows a tapping mode AFM image of a nanocube deposited on a functionalized gold film. We note that the shape is not perfectly cubic. Even if the particle is a perfect cube, the AFM image corresponds to the convolution of the cubic shape with the AFM tip shape, thus giving the particle a rounded aspect in the image (more details in Fig. 1.12). Note also that given the compromise that must be made for the choice of AFM tip (see Section 4.2.1), the chosen tip is not ideal for imaging. In this section, all excitations were carried out using an AFM tip made entirely of platinum (see 4.2.1).

In Fig. 4.6, we present an $I(V)$ curve obtained when the conducting AFM tip used to complete the circuit for the "nanocube-on-a-mirror" nanoantenna tunneling junction sample (AFM laser and feedback still on). The result is compared to a simulation of the tunneling current found using Simmons' model for a tunneling barrier between similar electrodes [180]. The experimental $I(V)$ measurement fits well with a model using a gold nanocube with a 70 nm side length and a work function for gold of 1.2 eV, with a tunneling junction

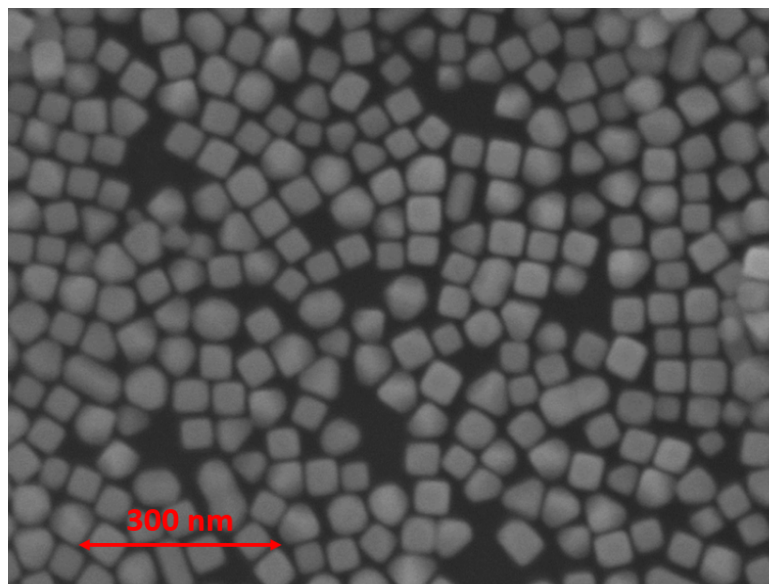


Figure 4.4: SEM image of the nanocubes: a drop of the undiluted nanocube solution is deposited onto a substrate suitable for SEM imaging. Image courtesy of Prof. Jianfang Wang's group, Hong Kong.

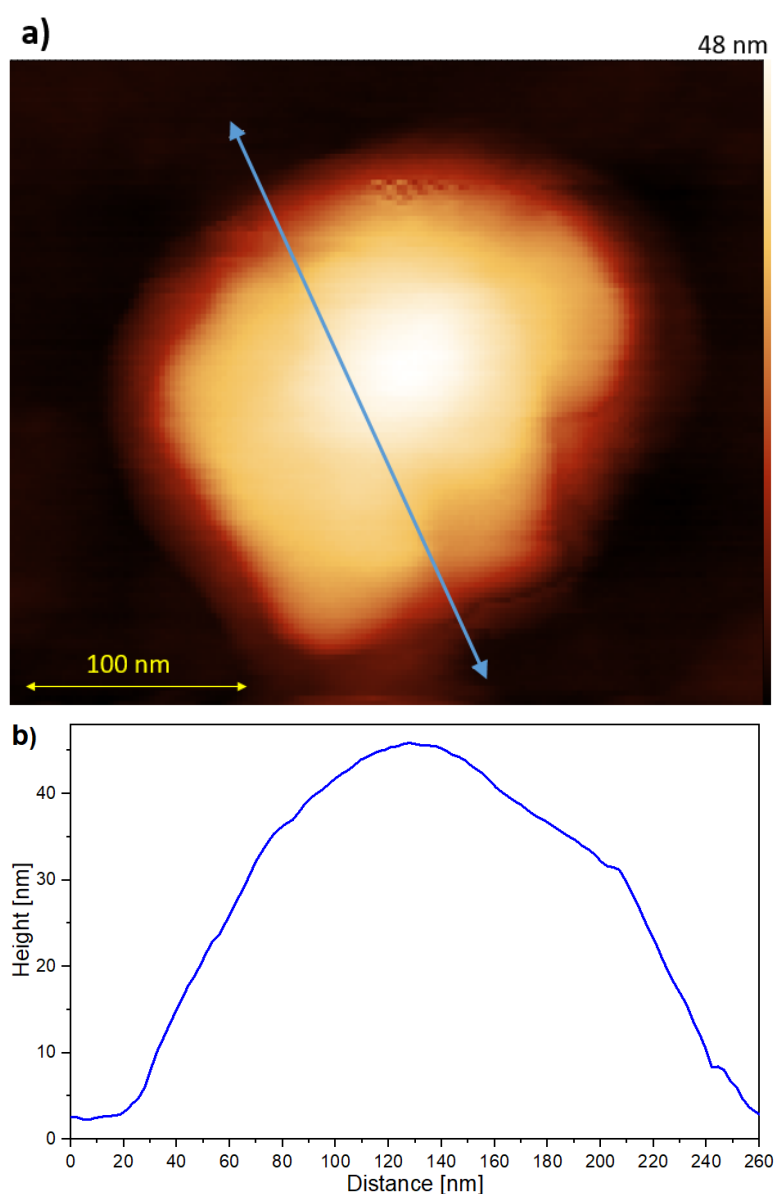


Figure 4.5: a) Tapping mode AFM image of a nanocube on a gold film functionalized with insulating molecules, and b) the height profile along the blue line in a). (AFM parameters: oscillation amplitude setpoint at 0.7 V for a free oscillation amplitude of 1 V and a scan speed of 300 nm/s).

tion 1.336 nm thick. The expected length of the molecules, as calculated using the Avogadro software (see <https://avogadro.cc/>), is 1.188 nm, which is slightly smaller but of the same order of magnitude. As for the previous samples, the work function used for the gold nanocube and film is lower than the gold work function in the literature for crystalline bulk samples (1.2 eV instead of 5.3 eV [176]). This discrepancy may be due to the possible presence of contaminants in the barrier, which are known to lower the work function [51, 181].

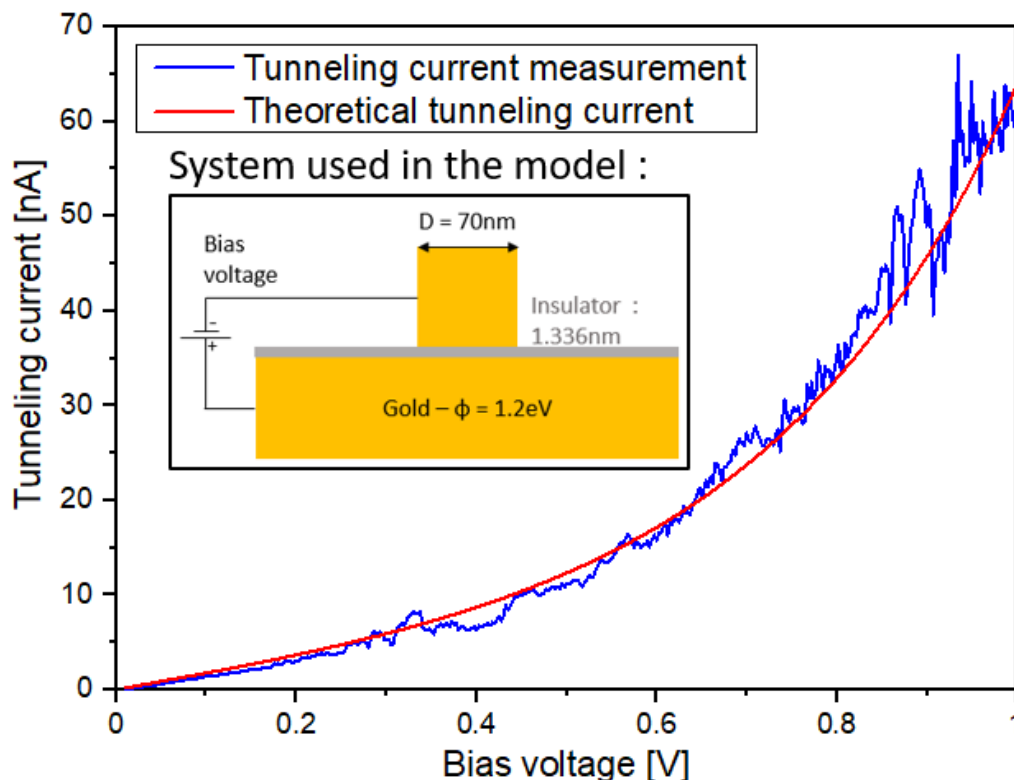


Figure 4.6: (blue line) $I(V)$ curve measured on a “nanocube-on-a-mirror” nanoantenna tunneling junction (with a cube height of 70 nm measured by AFM), biased using the conducting tip of an AFM, (red line) fit to the data obtained with a simulation using Simmon’s model, with a gold ($\phi = 1.2$ eV) nanocube with a side length of 70 nm, and a 1.336 ± 0.002 nm thick tunneling junction.

4.3.2 Integrated tunneling junction excitation of light and surface plasmons

Using the protocol described in Section 4.2.1 above, we use the conducting AFM to apply a bias voltage between the nanocube antenna and the gold film (AFM laser turned off). In Fig. 4.7, we see two examples of real plane images (see Section 1.2.5, Fig. 1.15) obtained when the nanocube-insulating molecules-Au film tunneling junction is biased and the resulting emitted photons are collected through the transparent substrate. In the first example (Fig. 4.7-a), the saturated image shows a bright spot under the cube and the continued emission of light over a large ($> 20 \mu\text{m}^2$) area; this suggests that the inelastic tunneling current of the nanocube-Au film junction has indeed excited an outgoing circular wave of propagating surface plasmons on the Au film, which progressively decays into photons in the transparent substrate. Note in particular the contaminants on the sample which act as scattering centers for the propagating surface plasmons: the contrast in the image between the areas where the surface plasmons continue to propagate and where they are “blocked” by the scattering centers highlights how far the surface plasmons propagate. In the second example (Fig. 4.7-b and -c), we see that the signal follows the spatial distribution of a dipole-like source, with a dip in the intensity at the center. This is typical for the tunneling junction excitation of a thin gold film [182].

4.3.3 Spectra

As discussed in the last chapter (Section 3), a nanoantenna may be used to increase the efficiency and determine shape the spectrum of the source. In Fig. 4.8 we show a remarkable, yet untypical result where the signal

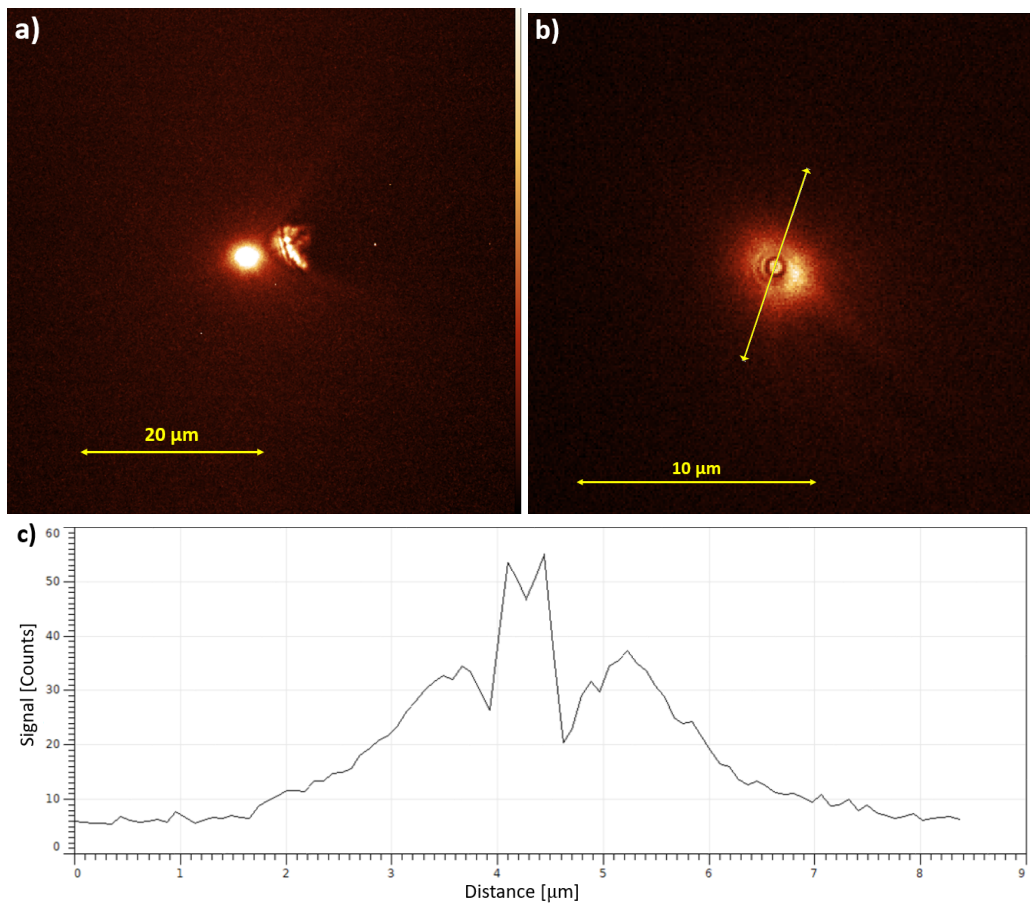


Figure 4.7: Real plane images of the light emitted from a AFM-biased “nanocube-on-a-mirror” tunneling junction with a 2.5 V bias voltage. a) Saturated image showing the effect of contaminants acting as scattering centers: areas “behind” the contaminants are darker in the image (the red dotted lines act as a visual guide), suggesting that indeed propagating surface plasmons have been excited by the inelastic tunneling current of the junction (nanocube height measured by AFM: 63 nm). b) Saturated image (nanocube height measured by AFM: 52 nm) with c) the cross-section obtained along the yellow line in b), showing a visible dip in intensity at the source location, which is characteristic for the tunneling junction excitation of a thin gold film (see Appendix A for more details).

saturates the spectrometer detector ³. While this is not a typical result, it is encouraging since it suggests that ideal parameters exist which lead to a high-power electrical nanosource of surface plasmons and light.

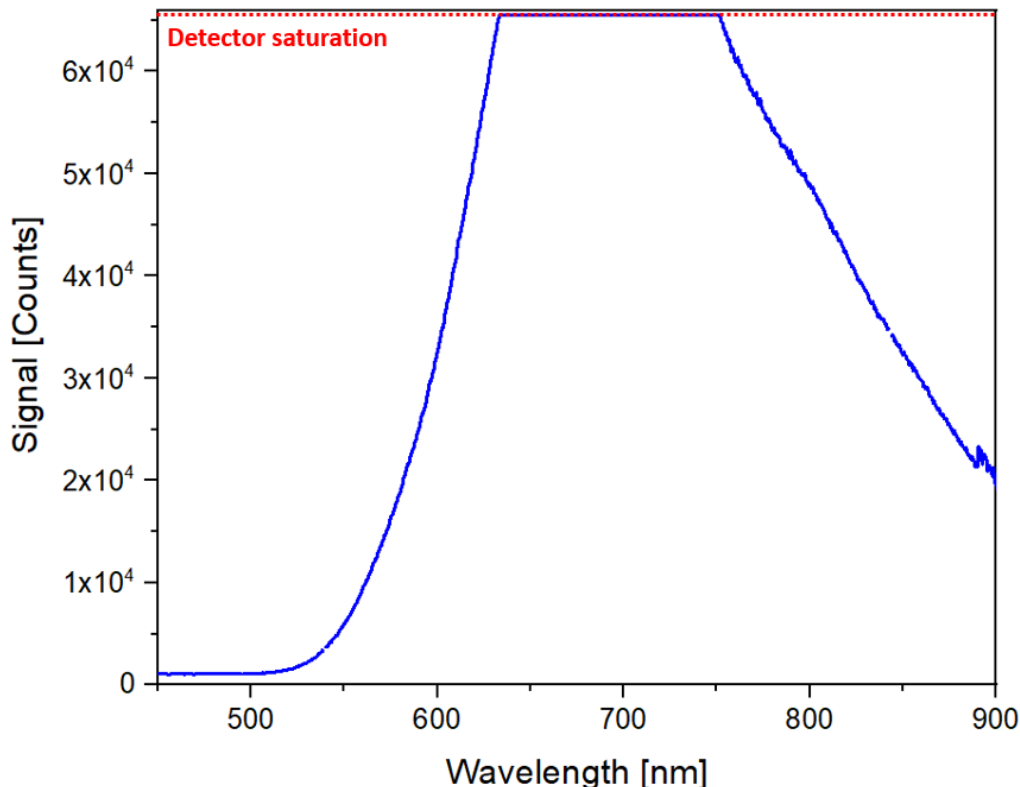


Figure 4.8: Uncorrected spectrum of the emitted light for an excitation at 2.5 V, with a 200 second excitation, but where we detected a tunneling current (above 6 nA) only during the first 40 seconds, which may be due to the loss of electrical contact. Cube height measured by AFM: 57 nm.

Typical spectra recorded when the biased AFM tip contacts a nanocube antenna on a functionalized Au film and the light through the transparent substrate is collected are shown in Fig. 4.9. Most often, two distinct peaks are seen. In order to understand this spectral shape, modeling is carried out.

4.3.4 Simulation of the emission from a tunneling junction in a “nanoantenna-on-a-mirror” geometry

Introduction to the simulation

In order to simulate the “nanoantenna-on-a-mirror” system, we again use the full-wave electromagnetic solver from collaborators at the Charles Fabry Laboratory [128, 129]. The nanocube is approximated as a cylinder and the molecular film is considered a dielectric with an index of refraction of 1.5. The inelastic tunneling current is again modeled as a vertical oscillating point dipole in the center of the junction [183] (see Fig. 4.10).

A nanoscale plasmonic system possesses eigenmodes of different specific frequencies and field/charge distributions. The type of system studied here with integrated tunneling junctions (often called nanoparticle-on-a-mirror, or metal-insulator-metal nanoresonators) will have different modes as compared to the system studied in Chapter 3. In particular, in the current situation, we have longitudinal plasmonic nanoantenna modes involving oscillating charges in the cube and image charges in the substrate, and transverse plasmonic gap modes supported in the insulating layer gap and reflecting on the edges of the cylinder [184, 185] (see Fig. 4.12). In this chapter, the transverse gap modes will be denoted as S_{mn} and the longitudinal nanoantenna modes as L_{mn} (following the notation used in refs [128, 184]), with n being the mode order and m the azimuthal number. Here the mode order n corresponds to the number of nodes in the vertical electric field below the antenna. Thanks to the symmetry of revolution of our system, we decompose the electromagnetic field in a sum of azimuthal eigenmodes where for each mode the electromagnetic field varies as $e^{im\theta}$ with θ the angle in the plane of the film

³As a measure of comparison, note that acquisitions with similar excitation parameters generally yield an emission maximum of a few thousand counts, and rarely exceeding 5000 counts.

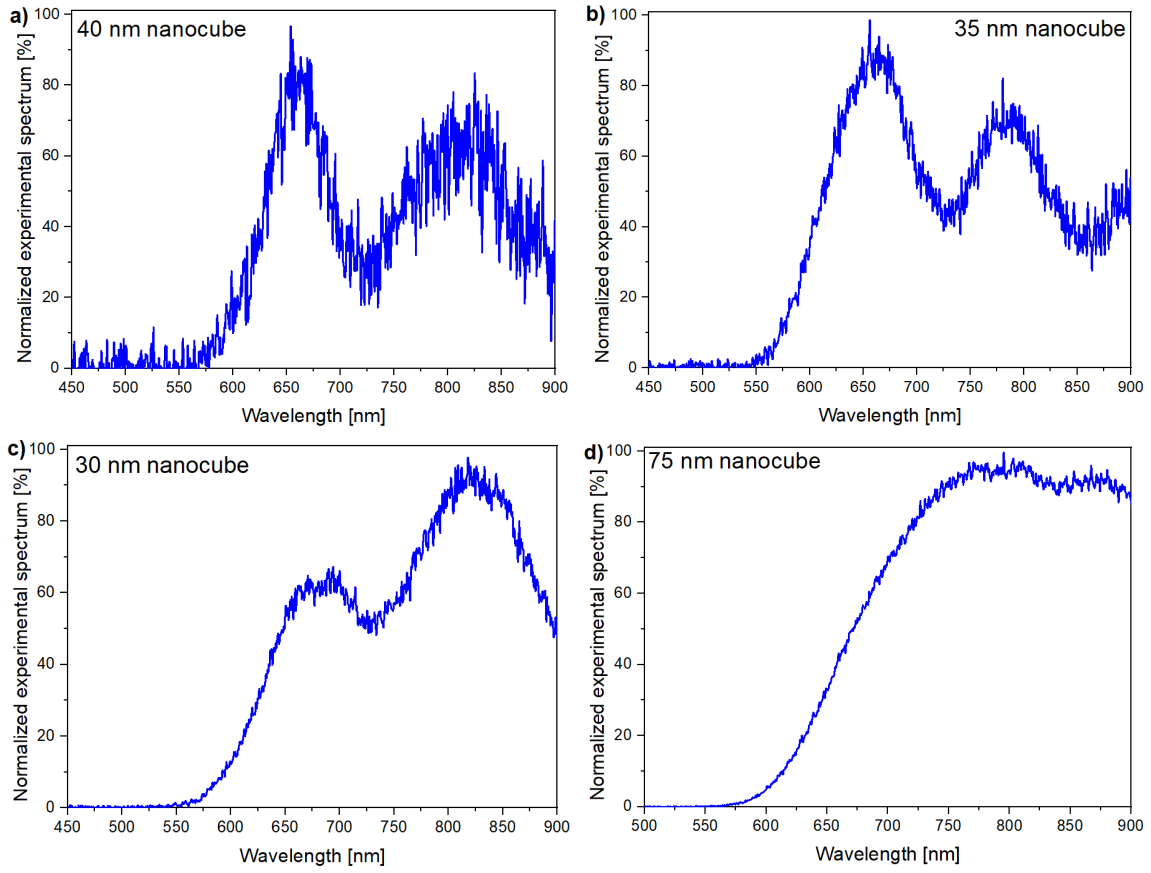


Figure 4.9: Spectra from different nanocube antenna. The applied voltage is 2.5 V, the integration time is 100 s.

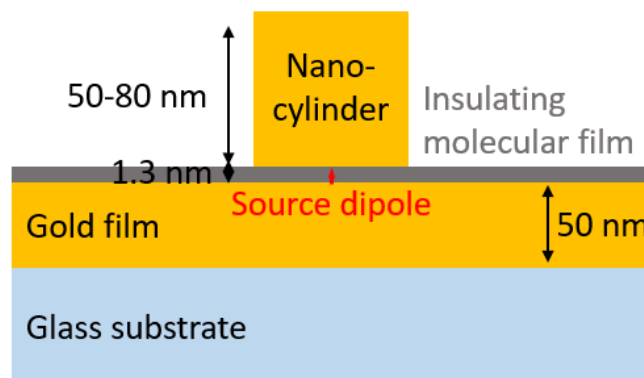


Figure 4.10: System for the simulation: gold nanocylinder on a gold film functionalized by insulating molecules.

(as usually defined in cylindrical coordinates) and m the azimuthal number. Note that hybridization between two modes is only possible if they have the same azimuthal number [128, 186]. Moreover, only modes with the azimuthal number $m = 0$ may be excited by a vertical point dipole source on the antenna axis. More details on the modal formalism used for this simulation may be found in [128].

In Fig. 4.11 we plot the power emitted into propagating surface plasmons as a function of wavelength and as a function of the nanoantenna height, for a fixed antenna diameter. Since the diameter is fixed, the transverse gap mode resonance will be unaffected; on the other hand, the longitudinal antenna mode resonance will shift significantly as a function of the varied parameter. Using this reasoning, we identify the gap and antenna modes in Fig. 4.11. Note that when the resonances of both modes overlap, we see an enhancement in the surface plasmon emission, which is due to mode coupling [129].

The nature of the antenna and gap modes and their hybridization is further investigated in Fig. 4.12. The magnetic field distributions of the antenna and gap modes are shown in Fig. 4.12-a and -b respectively, for a nanoantenna with a 60 nm diameter and a 100 nm height. Part -a is calculated at a wavelength of $\lambda = 880$ nm, and part -b for $\lambda = 760$ nm (see the crosses on Fig. 4.11). The very different nature of the two types of modes is evident from the magnetic field distributions. This transverse magnetic field calculation is also very useful for visualizing the charge distributions, in particular for gap modes. As shown schematically in Fig. 4.12-c, an “alternating” charge distribution on both side of the gap will create current loops, which induce perpendicular magnetic fields. Thus, the bright and dark spots in $\text{imag}(H_Y)$ (Fig. 4.12-b) are indicative of the charge distribution expected for the S_{04} gap mode. In this way we can accurately identify and label the gap modes in Fig. 4.11. The hybridization of the antenna and gap modes in terms of charge is schematically explained in Fig. 4.12-d.

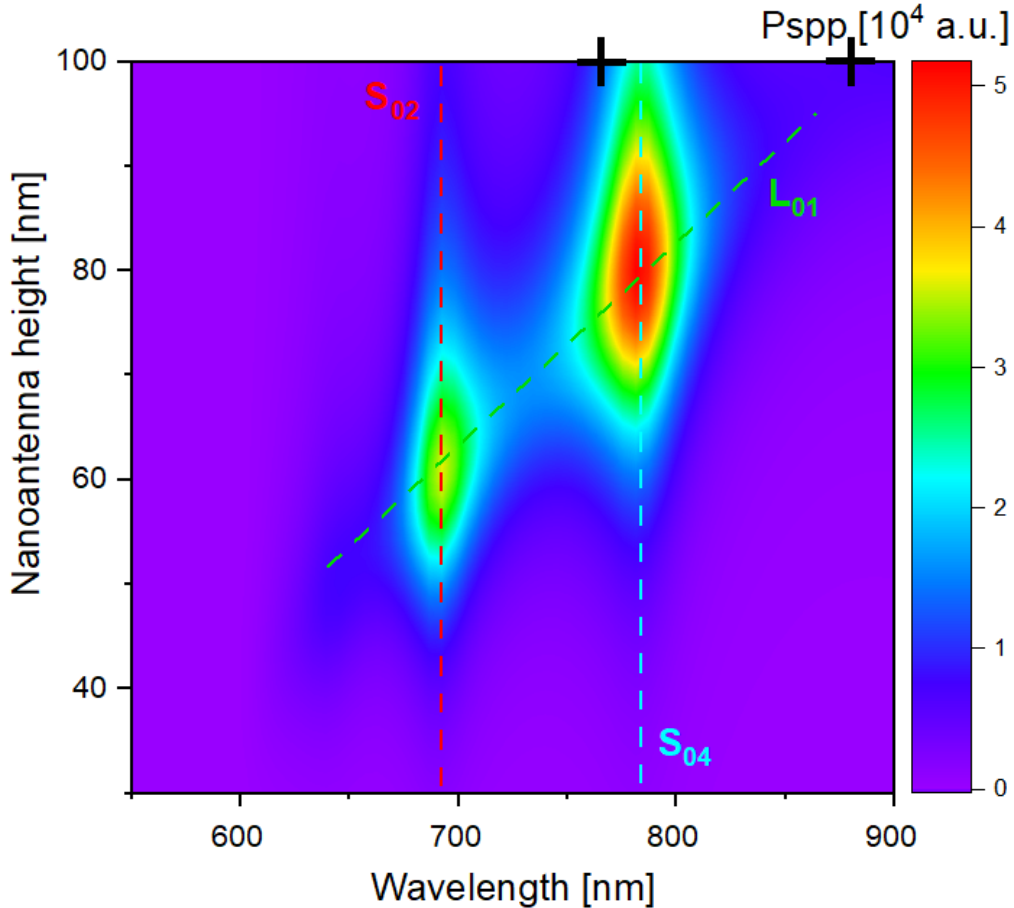


Figure 4.11: Surface plasmon mode power spectrum (P_{SPP}) as a function of height for a gold nanoantenna with a diameter of 60 nm and a gap thickness of 1 nm between the nanoantenna and a gold film. Dashed lines are added as a visual guide to see the different modes: the gap modes (red and blue lines) do not vary with the nanoantenna height whereas the antenna mode (green line) does. Black crosses mark the dimension and wavelength for the field distribution calculation in Fig. 4.12. The insulating layer refractive index is 1.5; gold dielectric constant from [16].

As discussed previously in Chapter 3, we expect that the longitudinal nanoantenna modes will radiate very efficiently, whereas the gap modes should greatly increase the EM-LDOS as they confine the electromagnetic field in the gap. As shown in Fig. 4.11, coupling between these two modes leads to an increase in the propagating

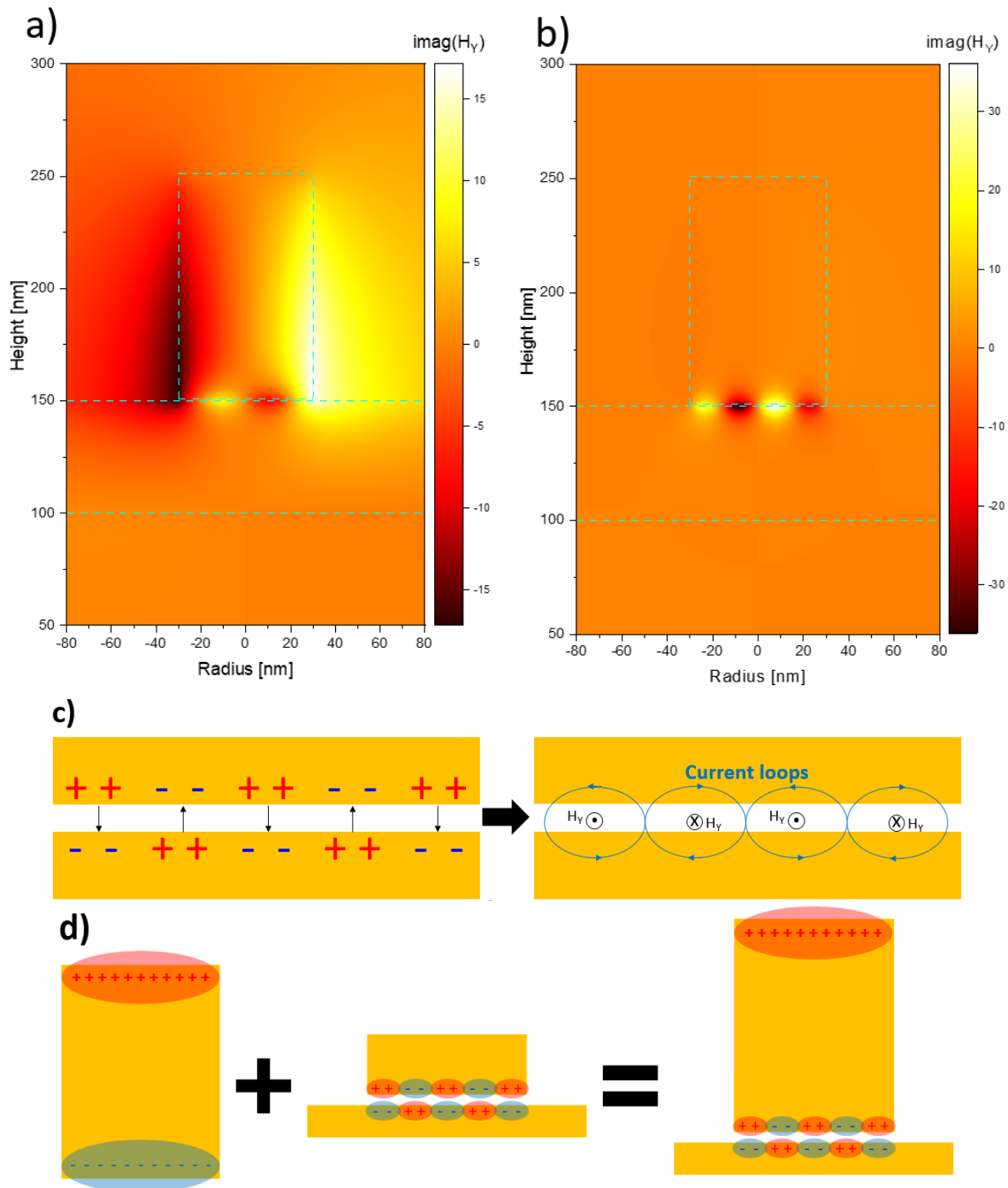


Figure 4.12: Field distribution for a) the L_{01} antenna mode (at $\lambda = 880$ nm, with a small contribution from the S_{02} gap mode) and b) the S_{04} gap mode (at $\lambda = 760$ nm) in a system with an integrated tunneling junction between a gold nanoantenna and a gold film. The antenna height is 100 nm, the diameter is 60 nm and the junction thickness is 1 nm. The insulating layer refractive index is 1.5; gold dielectric constant from [16]. c) Schematic of the correspondence between H_Y and the charge distribution: the charge distribution may be considered as a current loop in the gap, which induces a perpendicular magnetic field. d) Schematic representation of the mode hybridization in terms of charge, adapted from [128].

surface plasmon emission [128].

4.3.5 Simulation results for nanocubes on a gold film functionalized with insulating molecules

After the above introduction to the model, we now apply it to the experimental situation at hand. Due to the fabrication method, recall that we are limited to a cubic shape: the nanoantennas are nanocubes grown chemically, so their height and diameter will be the same. For simplification purposes, we still model them as cylinders with an aspect ratio of 1. Analogously to Fig. 4.11, we compute the spectrum of the power emitted into the far-field (P_{rad}) as a function of cube side length or dimension in Fig. 4.14.

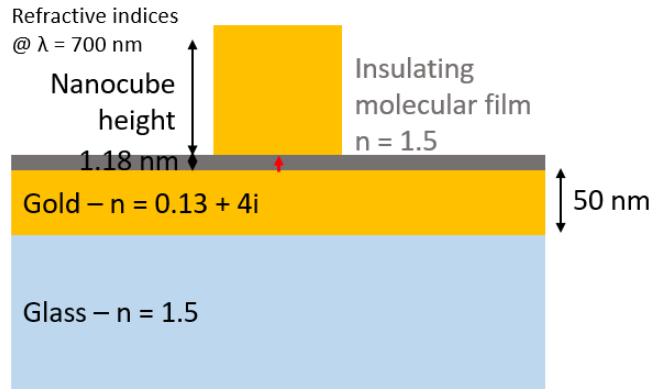


Figure 4.13: Simulation conditions for Fig. 4.14 below.

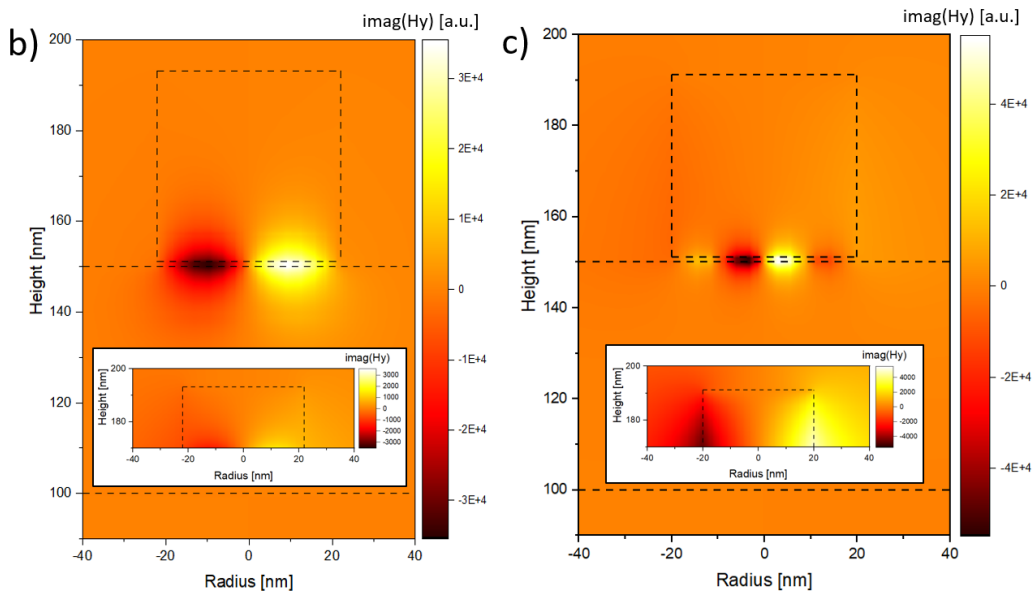
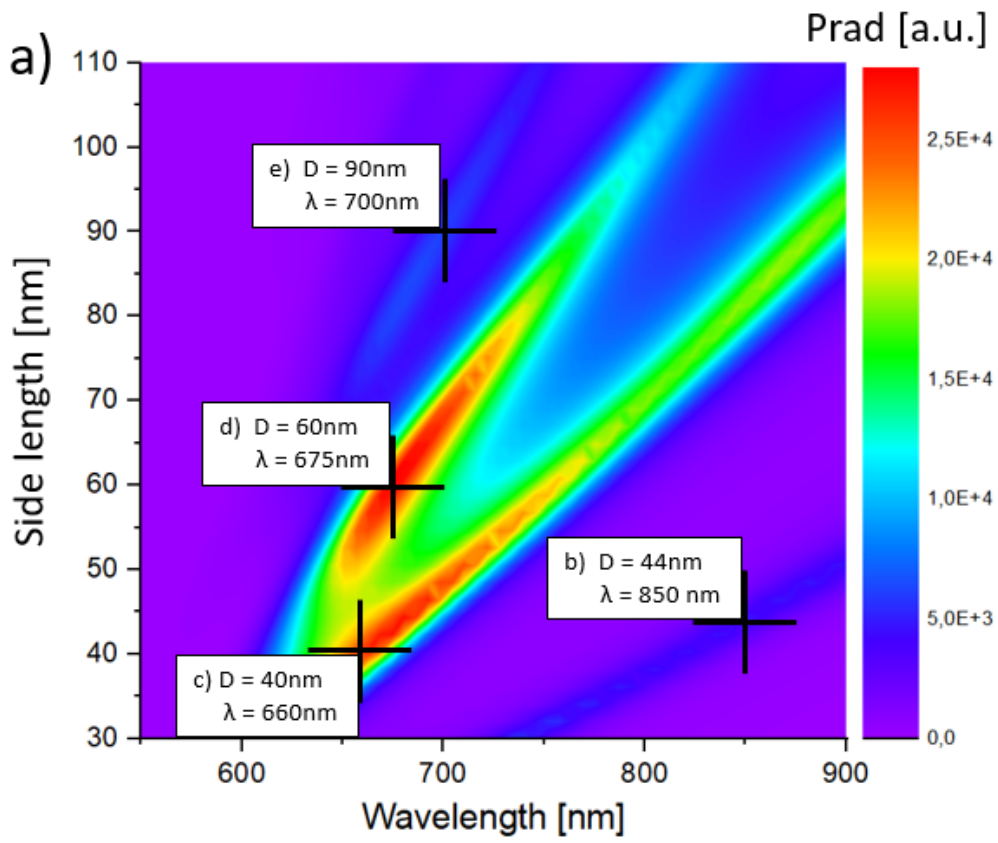
In Fig. 4.14-a we see four “lines” at an angle, two of which are intense. In this case, as the aspect ratio of the antenna is always equal to 1, the diameter increases at the same rate as the height. As a result, it is more difficult to identify the nature of the modes than in Fig. 4.11, where the antenna diameter was fixed and thus the gap mode was expected to remain constant with increasing antenna height, while the antenna mode was expected to red-shift. Instead, we attempt to identify what modes are at play for each bright line by plotting the EM field for specific nanocube side- and wavelengths: see Fig. 4.14-b to -e.

Starting with calculations on the less intense lines, Fig. 4.14-e shows the calculation of the imaginary part of the transverse magnetic field for a nanocylinder with a height and radius of 90 nm and a vertical dipole excitation of wavelength 700 nm centered in the 1 nm gap ($n = 1.5$). The field intensity is highest in the gap and the number of nodes in the magnetic field pattern suggest that we excite the gap mode S_{010} for this type of antenna at this wavelength. The inset to Fig. 4.14-e shows the transverse magnetic field in the upper part of the antenna, with the colour scale reduced by a factor of 10. The lack of contrast in this image suggests that the gap mode S_{010} is by far the dominant mode excited using a dipole excitation in the gap of such an antenna at a wavelength of 700 nm.

Figure 4.14-b shows a similar calculation, but for a nanocylinder with a height and radius of 44 nm and a vertical dipole excitation at a wavelength of 850 nm. For this longer-wavelength calculation in a smaller cube, we see the typical two-lobe pattern expected for the S_{02} mode. We again plot the field in the upper part of the antenna using a reduced colour scale: the observed contrast is reminiscent of the S_{02} mode, suggesting again that the gap mode is the by far the dominant excited mode.

Calculations of the transverse magnetic field for wavelengths and nanoantenna dimensions corresponding to points on the intense lines of Fig. 4.14-a are found in parts -c and -d. Here again we see a lobe pattern typical of a gap mode, here assigned to the S_{04} and S_{06} modes in parts -c and -d respectively. This time, when we change the colour scale by a factor of 10 and replot the transverse magnetic field, the result is distinct from the gap mode: the result is much more reminiscent of the antenna mode, as seen in Fig. 4.12-a. Thus we propose that the enhancement of the emission seen for certain wavelengths in Fig. 4.14-a may be attributed to the coupling between the gap modes and the antenna mode L_{01} . When the gap and antenna modes couple, we could expect to see an anti-crossing of the modes due to strong coupling. However, this splitting is masked by large mode widths combined with small coupling strengths (and thus small differences in energy between the hybridized modes)[128].

Emission “maps” such as the one shown in Fig. 4.14-a may be used to determine the expected spectrum for a dipole excitation in the gap of a “nanocylinder-on-a-mirror” system. Figure 4.15 shows two examples for



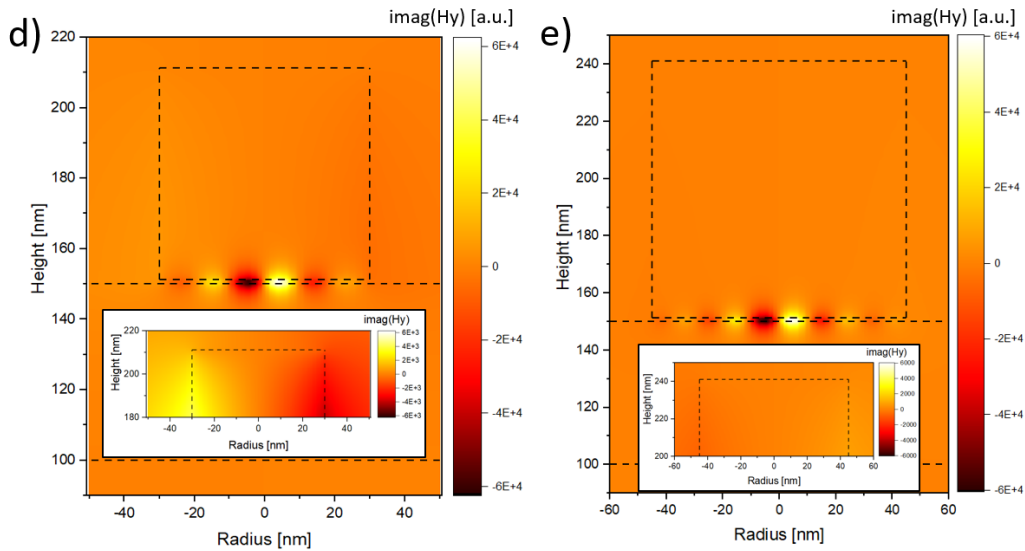


Figure 4.14: a) Calculated spectrum of the power radiated into the far field (P_{rad}) by a vertical oscillating dipole located in the 1.336 nm gap ($n = 1.5$) between a gold nanocylinder and a 50 nm thick gold film, as a function of nanoantenna side length. b)-e) The imaginary component of the transverse magnetic field is plotted for the side- and wavelengths indicated by the crosses in part -a. The insets to the figures plot the imaginary component of the transverse magnetic field of the upper part of the antenna, with the extent of the colour scale reduced by a factor of 10. Gold dielectric constant from [16].

antennas of side length 45 and 65 nm, which are obtained from horizontal cross-sections of Fig. 4.14-a. Note how the position of the peaks may be quite different for a 20 nm change in antenna size. In the next section, we will compare such calculated spectra to our experimental results.

4.3.6 Comparison of experimental and simulation results for nanocube antennas on a gold film functionalized with insulating molecules

Figure 4.16 shows the experimental results of Fig. 4.9 combined with simulated spectra obtained as described above in Section 4.3.5. These simulated spectra use the AFM-measured side length of the nanocubes, and a gap thickness of 1.336 nm as measured using Simmons' model in Fig. 4.6: in other words, no fitting has been carried out. Though not perfect, the agreement is quite good, with most often two peaks appearing in both the experimental and simulated spectra. From the analysis above, we can identify the excited modes corresponding to each peak. When comparing the collected spectra to the simulations, we see that while some spectra have very similar resonances as those predicted from the simulations (e.g., see Fig. 4.9-a), others may show a net red shift compared to the simulations (see Fig. 4.9-b or -c). In most cases, peak broadening is observed (see in particular Fig. 4.9-d).

Several factors may explain the differences observed between the simulated and the experimental spectra. A noticeable feature of the experimental results compared to the simulated spectra is that the width of the peaks are much broader, leading to the peaks overlapping. This may be due to increased losses in the real materials as compared to the simulations. Another possible source of loss is the conducting AFM tip we use to apply a bias voltage between the antenna and the gold film. Note that this tip is made of platinum, and may be considered plasmonic at 700 nm [187]. One possibility might be that the tip may increase the effective height of the nanoantenna, thus adding a red shift to the spectra. Future work will take into account the AFM tip in the spectral calculations.

Moreover, our simulations were carried out with the source dipole located in the middle of the gap, on the axis of the nanoantenna (see Fig. 4.13). However, in reality the tunneling current passes through the entire tunneling junction area, not just in the center (see Fig. 4.17). This distinction is important since when the source dipole is in the center of the gap, it only excites gap modes with an azimuthal number of 0. If we add sources away from the center, we excite different modes, which will lead to more resonances in the spectrum of the emitted light [113, 128].

Additionally, the program we use to compute the emitted light uses a symmetry of revolution, which means our system in the simulations is a cylinder with an aspect ratio of 1 on top of a gold film and not a nanocube.

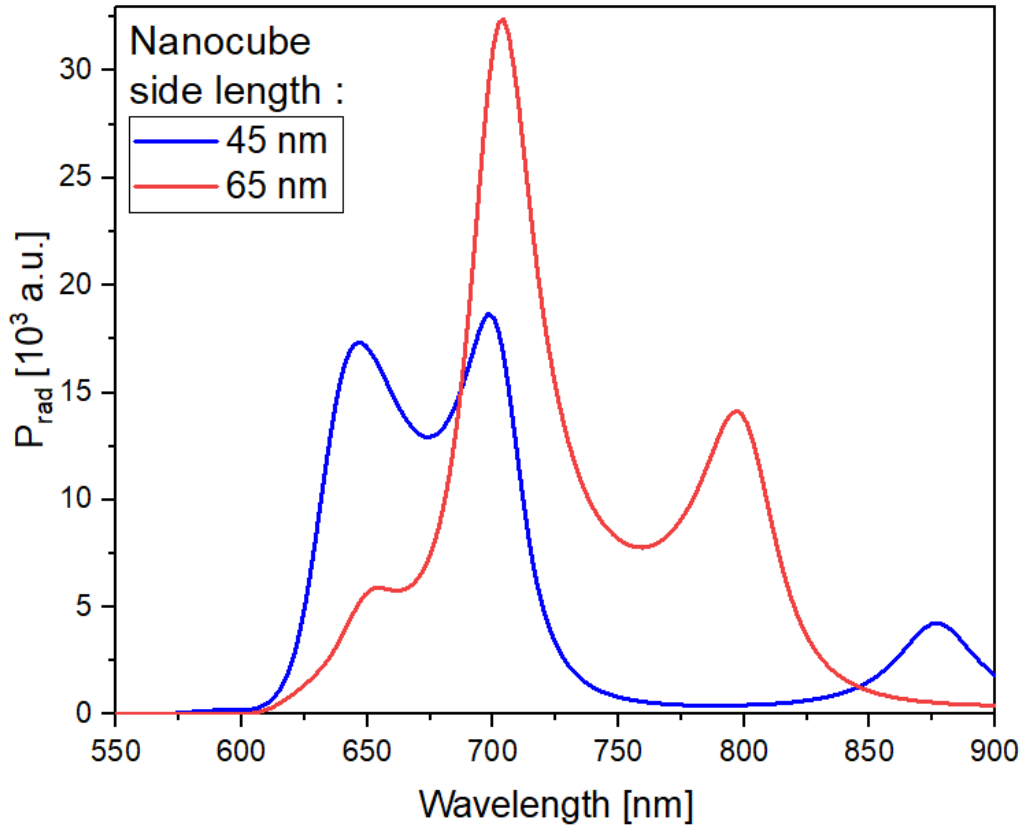


Figure 4.15: Simulated spectra of the power radiated into the far field (P_{rad}) for two specific nanoantenna dimensions (gap thickness of 1.336 nm), as determined from Fig. 4.14-a.

This distinction is important, especially when taking into account the current tunneling over the whole tunneling junction (not just in the center). As understood from symmetry considerations, the spectrum for an off-center excitation for a cube will be different than that for a cylinder. The cubic shape of the nanoantenna will be taken into account in future work.

It is worth noting that the spectrum also depends on the shape of the edges, which are not perfect sharp angles but rounded in our samples [188, 189]. This is visible in Fig. 4.4, where some strange shapes are also present, such as triangles, spheres or nanorods. By using the AFM to image the nanocube before exciting surface plasmon, we avoided nanoparticles with a shape that was obviously not a cube (nanorods with a high aspect ratio, or large triangles for example), but as the AFM image is the result of the convolution of the topography and the tip shape, it is difficult to differentiate between a nanocube and nanorod with an aspect ratio close to 1, especially as our tips were optimized for achieving electrical contact and not for imaging, thus the AFM images are not of high quality. This is important as the gap mode resonances depend on the particle shape [190, 191].

Finally, we will consider in more detail the possible effect of the gap thickness on the spectra. In Fig. 4.6, we estimate the gap thickness from an $I(V)$ curve on a nanocube with the conducting AFM in contact mode at the lowest contact setpoint for which we still have an electrical contact. From this measurement, we approximate the thickness of the molecular layer to be 1.336 ± 0.002 nm. Note, however, that the expected length of the molecules as calculated using the Avogadro software is 1.188 nm. Clearly, there is some uncertainty in the exact thickness of the tunneling barrier. There are several possible reasons for a variation in the gap thickness (see Fig. 4.17)

- The AFM tip may impact the gap thickness by pressing on the cube, or by pulling it off the surface, especially when the feedback is turned off (see Section 4.2).
- It is possible that the molecular layer is not uniform on the nanocube surface in contact with the sample, thus impacting the local gap thickness.
- Local surface roughness may lead to an irregular tunneling junction thickness.

In order to estimate the impact of the gap thickness, we plot the spectrum of the emitted light as a function of the gap thickness for a 50 nm nanocube: see Fig. 4.18. Using the same strategy as in Section 4.3.5, we can

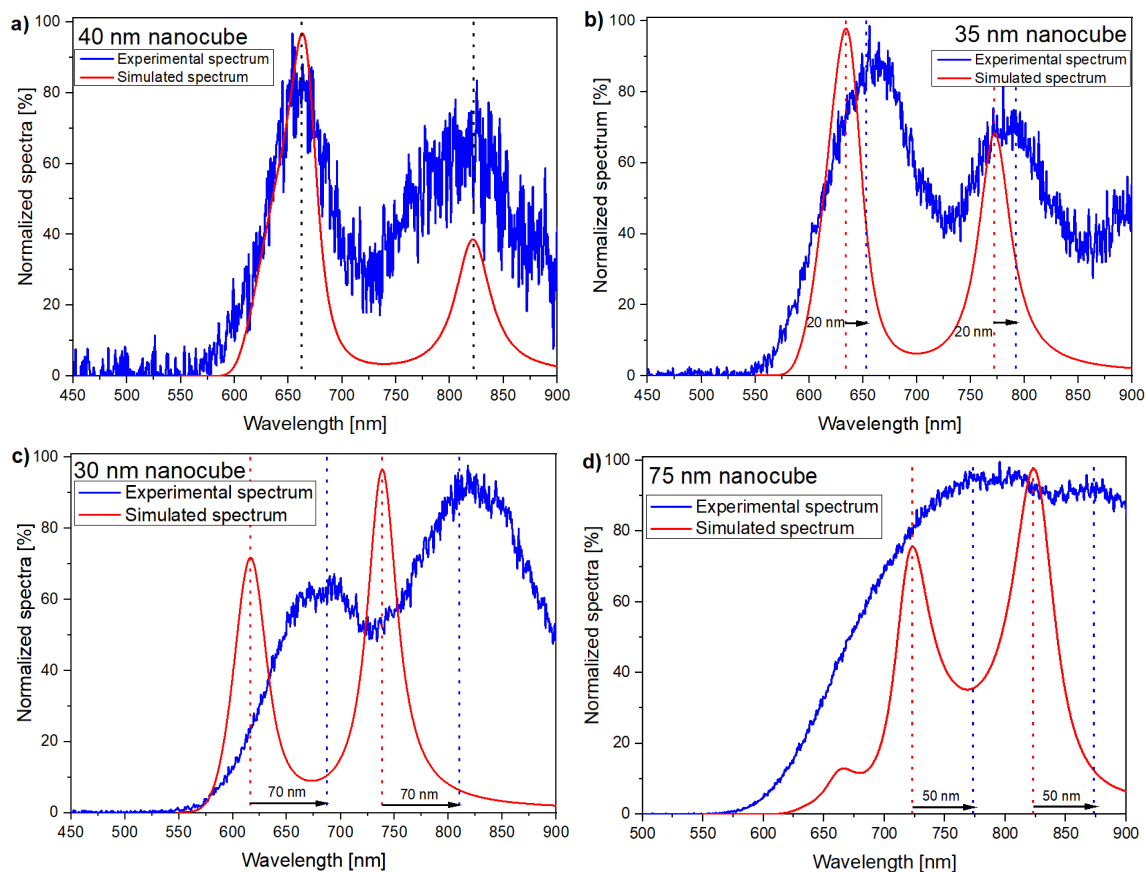


Figure 4.16: Experimental spectra from different nanocubes, compared to the simulations for a system with the same cube side length as what was measured by AFM, with a gap thickness of 1.336 nm (as was determined using Simmon's model see Fig.4.6). In a), the experimental spectrum fits well with the simulation, (the resonances are the same). In b) and c), the experimental spectrum is similar to the simulations, but with a noticeable red shift in the resonant wavelength. In d), the experimental spectrum is much broader than the simulated spectrum, with a noticeable red shift in the resonances.

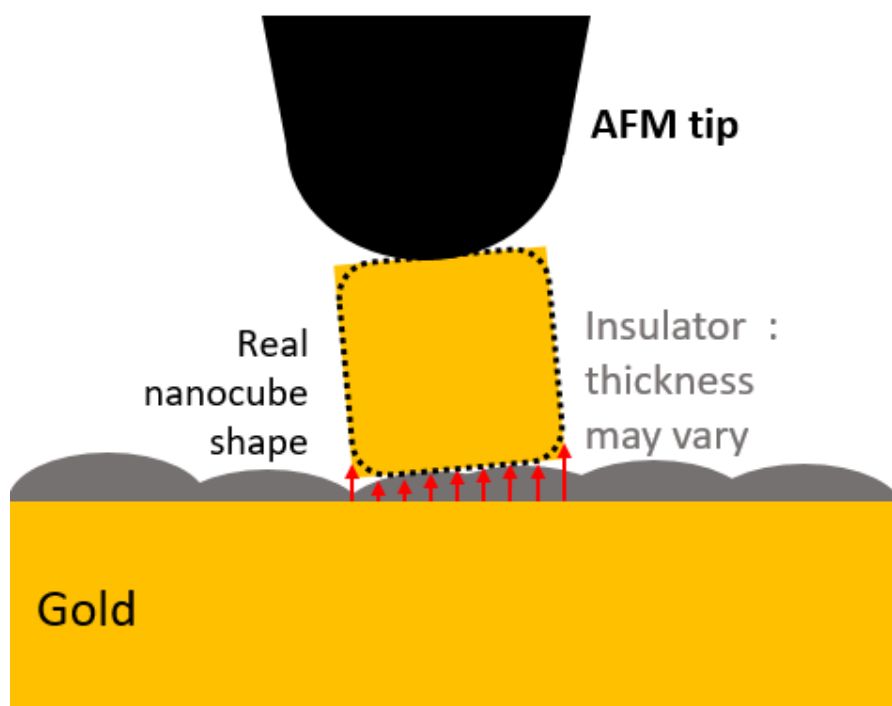


Figure 4.17: Schematic of a more realistic system, with a nanocube with rounded edges (black dashed line), uneven gap thickness and AFM tip.

plot the transverse magnetic field and identify the modes at play. The resonances of the gap modes are seen to blue shift with increasing gap thickness: when the gap thickness increases, the effective index of the gap plasmon decreases, which blue shifts the gap mode [192]. As in Fig. 4.14, we propose that the increase in the power radiated into the far field (P_{rad}) at the wavelength of 675 nm marks the coupling between an antenna mode and the gap modes, and that this antenna mode is not impacted by the gap-thickness variation. Thus, we see that a small variation of the gap thickness can shift the resonances in the simulated spectrum. The red shift of the resonances in the experimental spectra as compared to the simulated spectra may then be due in part to variations in the gap thickness.

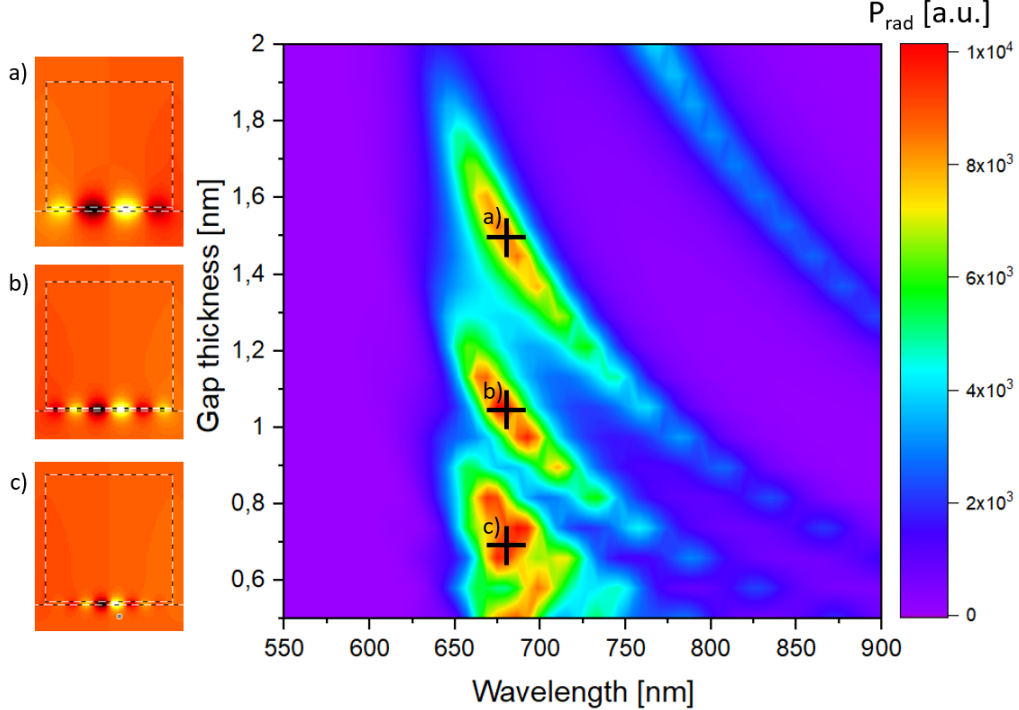


Figure 4.18: Simulated spectra of the light radiated into the far field as a function of the gap thickness, with a 50 nm nanocube, and a gap refractive index of 1.5. On the left are field distributions for three different gap thickness, thus for three different gap modes S_{04} (a), S_{06} (b), and S_{08} (c).

The differences cited above between our simulations and the experiment may explain the more complex spectra, such as the one in Fig. 4.16-d which are probably the result of multiple resonances with broad peaks. It is worth noting, however, that around 74 % of the over 30 collected spectra fit well with the simulations for the same measured dimensions (cube height measured using an AFM and gap thickness measured using Simmons' model, see Fig. 4.6) without fitting any of the simulation parameters, although this is taking into account red shifts and broadening.

Further work involves the study of the impact of the AFM tip on the surface plasmon emission, and the effect of the gap size by using carbon chains with different lengths. A more complex analysis of the modes at play may be performed by simulating the emitted light spectrum with several sources distributed horizontally in the gap and for different nanoantenna shapes.

4.3.7 Efficiency

As discussed in Section 3.2, one of the goals of using a nanoantenna is to see if the SPP excitation efficiency may be increased, or if, in other words, more propagating surface plasmons per tunneling electron may be excited. Recall that in Chapter 3 we measured an average excitation efficiency of $5.5 \times 10^{-7} \pm 3.9 \times 10^{-7}$ photons/electron for surface plasmon excitation on a 50 nm Au film using the tunneling current from a standard biased chemically-etched tungsten tip (see Fig. 3.16). In order to estimate theoretically the impact of the “nanoantenna-on-a-mirror” geometry on the excitation efficiency, we use the models of Sections 3.2 and 4.3.5 to calculate the spectra of the power radiated into the far field. We do this for the case of a gold nanocylinder above a gold film, and for a cylindrical tungsten tip above a gold film (see Fig. 4.19). As was seen in Figs 4.16, the “nanoantenna-on-a-mirror” geometry produces a double peak spectrum while the STM-excitation on the Au film spectrum is relatively flat. While at specific wavelengths the enhancement due to the nanoantenna is clear, when integrating the power radiated into the far field over the whole wavelength range of interest, we note an increase thanks to

the “nanoantenna-on-a-mirror” geometry of only a factor $\simeq 5$.

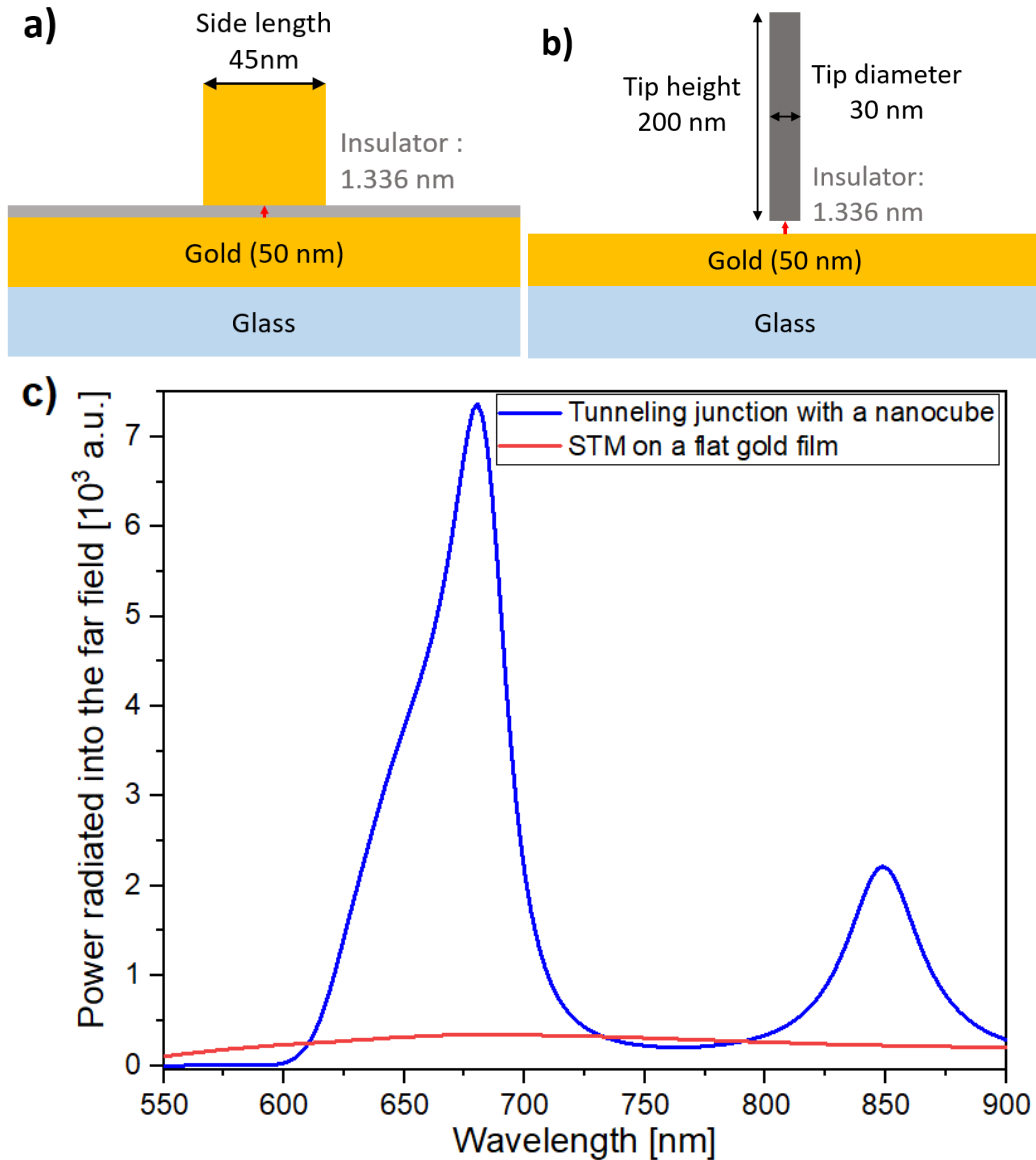


Figure 4.19: Simulation conditions for a) an excitation with a nanocube (45 nm side length) on a thin gold film with a 1.336 nm thick tunneling junction and b) for an STM (STM tip modelled as a 30 nm large, 200 nm high cylinder) excitation on a thin gold film, with a 1.336 nm gap between the two. For each system, we compute in c) the power radiated into the far field for an excitation using an STM on a thin gold film (red curve) and an integrated tunneling junction (blue curve), both corrected of the tunneling current density for an excitation at 2.5 V.

Figure 4.20 shows the over 40 estimates of the excitation efficiency determined in the following manner: the number of photons from each pixel in the image or spectra is summed, then multiplied by the correction factor (which takes into account the different detector efficiencies, see Appendix I for more details), and divided by the number of tunneling electrons (determined by integrating the current measured with the conducting AFM module).⁴ From this figure we find an average experimental efficiency for the “nanoantenna-on-a-mirror” tunneling junction of 6×10^{-7} photons per electron. This is in agreement, within experimental error, with the estimate from Fig. 4.19. Indeed, while the values obtained on the same nanocubes are relatively constant (see the violet dotted circles in Fig. 4.20 and the footnote below), the spread in results is large between different cubes. This may in part be understood from Figs. 4.14-a and 4.18 which show how the emitted power spectrum varies with cube side and gap thickness (average cube size length measured by AFM: 51.3 ± 12.5 nm). While the hoped-for large increase in efficiency has not been obtained here, results such as the saturated spectrum in Fig. 4.8 suggest that with sample optimization, a significant increase in efficiency is possible.

⁴In some cases, the tunneling junction shorted during the experiment and the measured tunneling current reached the saturation value. For this case, in the figure we use downward triangles to mark the maximum value of the experimental efficiency (calculated by counting the number of electrons passing through the junction until the *beginning* of the tunneling current surge toward the saturation value), and upward triangles to mark its minimum value (calculated by counting the number of electrons passing through the junction until the *end* of the tunneling current surge toward the saturation value). These two markers are linked with a dashed line. The current measurements are carried out with a 1 ms step between each point

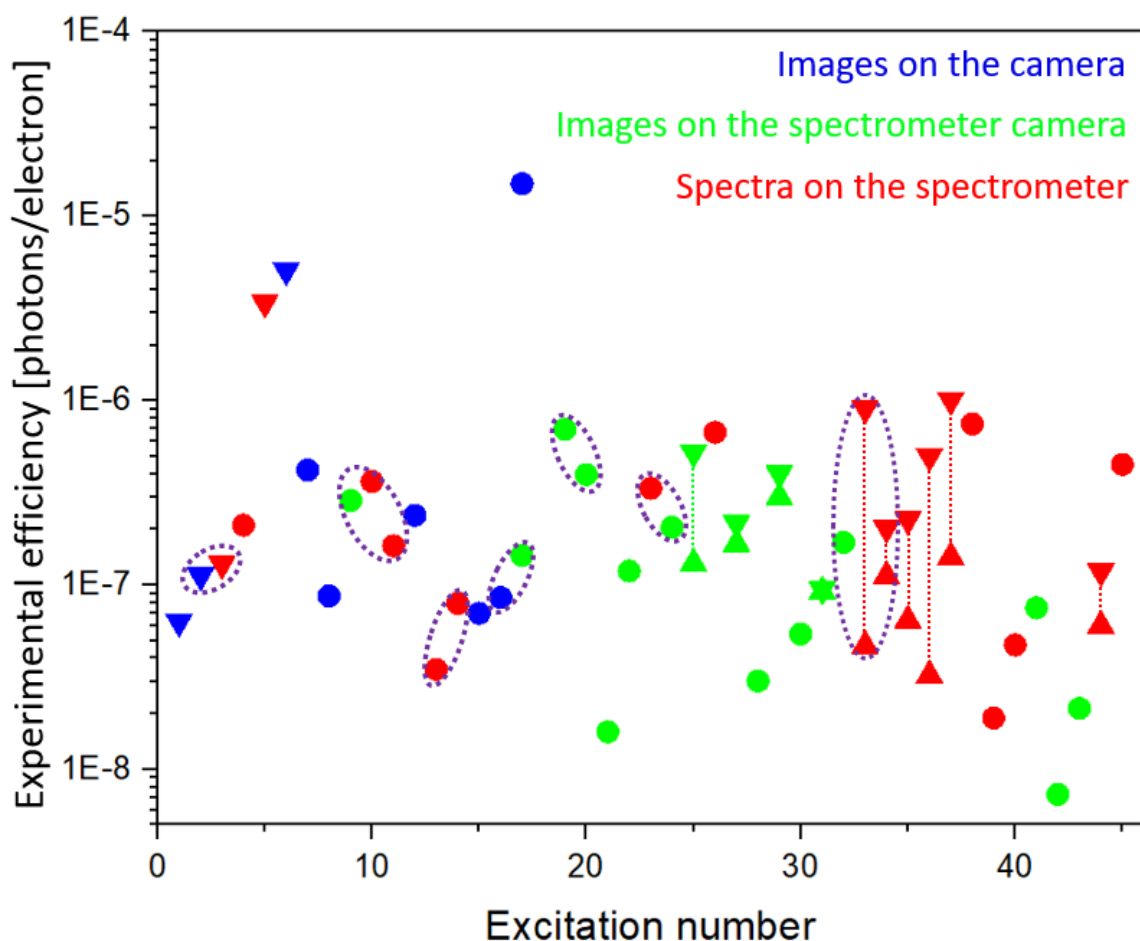


Figure 4.20: Experimental excitation efficiency in photons per electron for excitations with a 2.5 V applied bias voltage and a 100 s acquisition time. Each acquisition is corrected by the system detection efficiency (blue for the real plane measurements with the CCD camera, green for the real plane measurements with the spectrometer CCD camera and red for the spectra measurements with the spectrometer CCD camera and grating. See Section 1.2.5 for details on the detectors). Acquisitions on the same nanocubes are enclosed in a violet circle. The points joined by the dotted lines are explained in the footnote.

Besides the excitation efficiency, another important parameter to consider is the size of the nanosource for future applications. Thus we define the following figure of merit F :

$$F = \frac{\text{Number of photons emitted per second}}{\text{Nanoantenna area}} \quad (4.1)$$

Using the same images and spectra that led to Fig. 4.20 and the heights of the nanocubes measured by AFM, we calculate an average value for this figure of merit F . The average F is 77.6 photons/s/nm² and has a large variability. The standard deviation of F is calculated to be 212.2 photon/s/nm², if a normal distribution is assumed (although a more correct definition of the error would take into account that our data is not distributed with a Gaussian shape). Note that in the case of a 1D nanoantenna in the literature [126], the corresponding figure of merit $F = 9 \times 10^{-2}$ photons/s/nm². While a direct comparison must be done with care since the material systems are not the same, we may still note an increase in F of two orders of magnitude in our system.

4.4 Summary

In this chapter, we study a new system for the electrical excitation of propagating surface plasmons. The sample is made of a gold nanocube on a thin gold film functionalized with insulating molecules (thiols separated by an 8-carbon chain). The molecules act as a tunneling barrier and the nanocube as a nanoantenna. When this tunneling junction is biased, the inelastic tunneling current leads to the excitation of propagating surface plasmons on the thin gold film. We then collect the emitted light from these SPPs using leakage radiation microscopy.

In order to apply a bias voltage between the gold film and the nanocube, a new method for making an electrical contact, suitable for optical measurements, was developed. This method uses a conducting atomic force microscope tip. The development of this excitation method proved to be challenging, as the AFM cantilever movements are detected with a laser, which masks the signal to be detected and saturates our detectors. We contacted the nanoantenna electrically by using the AFM in contact mode and turning off the laser once the tip is in contact. Another key point of the solution was thermal stabilization of the system before the experiment.

Using this new method and the “nanoantenna-on-a-mirror” samples, the excitation of propagating surface plasmons was demonstrated. Most often, the resulting spectra showed the presence of two peaks. Through simulation it was demonstrated that these peaks correspond to different gap modes in the system, and that the dominant peak is likely to be from a coupled gap and antenna mode.

While the presence of the nanoantenna successfully influenced the shape of the spectra, its influence on the electron-to-photon efficiency was weak. An isolated yet spectacular result which saturated the detectors suggests that this efficiency may be greatly improved in an optimized device.

When considering the goal of an electrically excited source of propagating surface plasmons with a nanoscale footprint, we introduce the figure of merit F (photon flux per nanosource area). In our system, $F = 77.6$ photons/s/nm². This figure cannot be directly compared to the literature as the only propagating surface plasmons nanosources available are fabricated with different materials, and thus have a different plasmon-to-photon conversion efficiency. It is however worth noting that the system we studied has a figure of merit F two orders of magnitude higher than a 1D nanoantenna using a different material system [126], thus making our “nanoantenna-on-a-mirror” a promising nanosource for devices.

Chapter 5

Summary

In this thesis we studied how inelastic tunneling current may be used as a local excitation of both propagating surface plasmons on a metal/dielectric interface, and excitons in transition metal dichalcogenide monolayers.

We developed a new method to locally excite the electroluminescence of monolayer molybdenum diselenide (MoSe_2) using a scanning tunneling microscope (STM) in air. By comparing the photoluminescence and the electroluminescence signals, and by analysing the Fourier plane images of the electroluminescence, we have shown that the emitted light is due to the radiative recombination of bright excitons in MoSe_2 . An analysis of the voltage threshold for the electroluminescence showed that the dominant excitation mechanism appears to be resonant energy transfer from the inelastic tunneling electrons to the excitons (although additional mechanisms, such as multi-electrons processes or charge injection may also play a role). Efficiencies up to 10^{-7} photons/electron were measured despite the lack of surface plasmons to enhance the luminescence. Exciton diffusion away from the STM excitation position was observed, with preferential recombination at “hot spots”, which we assume are defects in the monolayer. As our method uses a local excitation, we were able to identify the location of nanometer-scale defects on the sample (with a 20 nm precision), which are barely visible in STM topographical images. These results show that it is possible to locally probe the excitonic properties of 2D semiconductors and their heterostructures at the nanometer scale. An article on this work was published in Physical Review Letters [1].

Several plasmonic systems were considered in this thesis with the aim of designing an electrically-driven nanosource of propagating surface plasmons based on a tunneling junction. In particular, the effect of a nanoantenna on the emission spectrum and excitation efficiency was considered. The first system considered was a cylindrical nanoantenna on a gold film and the exciting tunneling junction was between the tip of a scanning tunneling microscope and the nanoantenna. Simulations showed that with a small antenna (30-nm high and 20-nm in diameter) and a tungsten STM tip modelled as a 10 nm diameter sphere, we should observe an increase in the propagating surface plasmon excitation efficiency of a factor 38 (when averaged over the wavelength range of interest) as compared to the STM excitation of SPPs directly on a thin gold film (no antenna present). Calculations were also realized using a more realistic shape and size for the tip (tungsten cylinder, 200 nm high and 30 nm in diameter) and the fabricated nanoantenna dimensions (discs with diameters of 80 to 120 nm, and heights of 70 to 120 nm). Using more realistic parameters, the impact of such a nanoantenna was disappointing as we noted no increase in the propagating surface plasmon excitation efficiency when compared to an excitation on a simple gold film. This result was confirmed experimentally. In particular, the results were found to be highly dependent on the STM tip, and the ideal nanoantenna dimensions were difficult to realize using e-beam lithography.

The second system considered in detail involved using chemically-grown gold nanocubes as nanoantennas. In this case, the exciting tunneling junction was situated between the gold nanocube and the gold film on which the surface plasmons propagate. The gap material was composed of insulating molecules (thiols separated by an 8-carbon chain). In order to apply a bias voltage to this tunneling junction, a new method was developed so that an electrical contact could be made with the nanocube using an atomic force microscope (AFM) with a conducting tip. The development of this excitation method proved to be challenging as the AFM cantilever movements are detected with a laser; since we are detecting a comparably weak optical signal, this laser masks the signal to be detected and saturates the detectors. To solve this problem, we contact the nanoantenna electrically using the AFM in contact mode and turn off the laser once the tip is in contact. Another key point of the solution was thermal stabilization of the system before the experiment. Using this new method on this

sample with an integrated tunneling junction between the cube and the gold film, we obtained measurements on over 40 nanoantennas. These results were compared to simulations. The simulated spectra fit well with the experimental measurements, and showed that the observed peaks correspond to different gap modes coupled to an antenna mode. When analysing the efficiency measurements, we saw that while the nanoantenna clearly influenced the shape of the spectrum, the increase in the efficiency was negligible. A promising result was the output power compared to the size of this system: we introduced the figure of merit F (photon flux per nanosource area). In our system, $F = 77.6$ photons/s/nm². While this figure cannot be directly compared to the literature as the only propagating surface plasmon nanosources available are fabricated with different materials, and thus have a different plasmon-to-photon conversion efficiency. It is however worth noting that the system we studied has a figure of merit F two orders of magnitude higher than a 1D nanoantenna using a different material system [126], thus making our “nanoantenna-on-a-mirror” a promising nanosource for devices.

Bibliography

- [1] Delphine Pommier, Rémi Bretel, Luis E. Parra Lopez, Florentin Fabre, Andrew Mayne, Elizabeth Boer-Duchemin, Gérald Dujardin, Guillaume Schull, Stéphane Berciaud, and Eric Le Moal. Scanning tunneling microscope-induced excitonic luminescence of a two-dimensional semiconductor. *Phys. Rev. Lett.*, 123(2):027402, 2019.
- [2] C. J. Powell and J. B. Swan. Origin of the characteristic electron energy losses in aluminum. *Phys. Rev.*, 115(4):869–875, 1959.
- [3] R. H. Ritchie. Plasma losses by fast electrons in thin films. *Phys. Rev.*, 106(5):874–881, 1957.
- [4] Andreas Otto. Excitation of nonradiative surface plasma waves in silver by the method of frustrated total reflection. *Z. Physik*, 216(4):398–410, 1968.
- [5] KRETSCHMANN. Radiative decay of non radiative surface plasmons excited by light. *Zeitschrift für Naturforschung A*, 23(23):2135–2136, 1968.
- [6] R. H. Ritchie, E. T. Arakawa, J. J. Cowan, and R. N. Hamm. Surface-plasmon resonance effect in grating diffraction. *Phys. Rev. Lett.*, 21(22):1530–1533, 1968.
- [7] John Lambe and S. L. McCarthy. Light emission from inelastic electron tunneling. *Phys. Rev. Lett.*, 37(14):923–925, 1976.
- [8] J. K. Gimzewski, J. K. Sass, R. R. Schlitter, and J. Schott. Enhanced photon emission in scanning tunnelling microscopy. *EPL*, 8(5):435–440, 1989.
- [9] Peter Johansson. Light emission from a scanning tunneling microscope: Fully retarded calculation. *Physical Review B*, 58(16):10823–10834, 1998.
- [10] Richard Berndt, James K. Gimzewski, and Peter Johansson. Inelastic tunneling excitation of tip-induced plasmon modes on noble-metal surfaces. *Phys. Rev. Lett.*, 67(27):3796–3799, 1991.
- [11] Karl Joulain, Rémi Carminati, Jean-Philippe Mulet, and Jean-Jacques Greffet. Definition and measurement of the local density of electromagnetic states close to an interface. *Physical Review B*, 68(24):245405, 2003.
- [12] R. Carminati, A. Cazé, D. Cao, F. Peragut, V. Krachmalnicoff, R. Pierrat, and Y. De Wilde. Electromagnetic density of states in complex plasmonic systems. *Surface Science Reports*, 70(1):1–41, 2015.
- [13] Adrian N. Pfeiffer, Claudio Cirelli, Mathias Smolarski, Darko Dimitrovski, Mahmoud Abu-samha, Lars Bojer Madsen, and Ursula Keller. Attoclock reveals natural coordinates of the laser-induced tunnelling current flow in atoms. *Nature Physics*, 8(1):76–80, 2012.
- [14] Nicolas Camus, Enderalp Yakaboylu, Lutz Fechner, Michael Klaiber, Martin Laux, Yonghao Mi, Karen Z. Hatsagortsyan, Thomas Pfeifer, Christoph H. Keitel, and Robert Moshhammer. Experimental evidence for quantum tunneling time. *Phys. Rev. Lett.*, 119(2):023201, 2017.
- [15] Pierre Février and Julien Gabelli. Tunneling time probed by quantum shot noise. *Nature Communications*, 9(1):1–8, 2018.
- [16] P. B. Johnson and R. W. Christy. Optical constants of the noble metals. *Phys. Rev. B*, 6(12):4370–4379, 1972.
- [17] Jovan M. Elazar Aleksandar D. Rakić, Aleksandra B. Djurišić and Marian L. Majewski. Optical properties of metallic films for vertical-cavity optoelectronic devices. *Appl. Opt.*, AO, 37(22):5271–5283, 1998.

- [18] Peter Johansson, R. Monreal, and Peter Apell. Theory for light emission from a scanning tunneling microscope. *Phys. Rev. B*, 42(14):9210–9213, 1990.
- [19] Joongoo Kang, Lijun Zhang, and Su-Huai Wei. A unified understanding of the thickness-dependent bandgap transition in hexagonal two-dimensional semiconductors. *J. Phys. Chem. Lett.*, 7(4):597–602, 2016.
- [20] J. W. González K. Kośmider and J. Fernández-Rossier. Large spin splitting in the conduction band of transition metal dichalcogenide monolayers. *Physical Review B*, 88(24):245436, 2013.
- [21] Gang Wang, Alexey Chernikov, Mikhail M. Glazov, Tony F. Heinz, Xavier Marie, Thierry Amand, and Bernhard Urbaszek. Colloquium: Excitons in atomically thin transition metal dichalcogenides. *Rev. Mod. Phys.*, 90(2):021001, 2018.
- [22] T. Godde, D. Schmidt, J. Schmutzler, M. Akmann, J. Debus, F. Withers, E. M. Alexeev, O. Del Pozo-Zamudio, O. V. Skrypka, K. S. Novoselov, M. Bayer, and A. I. Tartakovskii. Exciton and trion dynamics in atomically thin MoSe₂ and WSe₂: Effect of localization. *Phys. Rev. B*, 94(16):165301, 2016.
- [23] Chitrleema Chakraborty, Kenneth M. Goodfellow, and A. Nick Vamivakas. Localized emission from defects in MoSe₂ layers. *Opt. Mater. Express*, OME, 6(6):2081–2087, 2016.
- [24] Bruno Schuler, Katherine A. Cochrane, Christoph Kastl, Edward S. Barnard, Edward Wong, Nicholas J. Borys, Adam M. Schwartzberg, D. Frank Ogletree, F. Javier Garcia de Abajo, and Alexander Weber-Bargioni. Electrically driven photon emission from individual atomic defects in monolayer WS₂. *Science Advances*, 6(38):eabb5988, 2020.
- [25] Zhengyu He, Xiaochen Wang, Wenshuo Xu, Yingqiu Zhou, Yuewen Sheng, Youmin Rong, Jason M. Smith, and Jamie H. Warner. Revealing defect-state photoluminescence in monolayer WS₂ by cryogenic laser processing. *ACS Nano*, 10(6):5847–5855, 2016.
- [26] Xin He, Hai Li, Zhiyong Zhu, Zhenyu Dai, Yang Yang, Peng Yang, Qiang Zhang, Peng Li, Udo Schwingschlogl, and Xixiang Zhang. Strain engineering in monolayer WS₂, MoS₂, and the WS₂/MoS₂ heterostructure. *Applied Physics Letters*, 109(17):173105, 2016.
- [27] E. Blundo, M. Felici, T. Yildirim, G. Pettinari, D. Tedeschi, A. Miriametro, B. Liu, W. Ma, Y. Lu, and A. Polimeni. Evidence of the direct-to-indirect band gap transition in strained two-dimensional WS₂, MoS₂, and WSe₂. *Physical Review Research*, 2(1):012024, 2020.
- [28] Yanlong Wang, Chunxiao Cong, Weihuang Yang, Jingzhi Shang, Namphung Peimyo, Yu Chen, Junyong Kang, Jianpu Wang, Wei Huang, and Ting Yu. Strain-induced direct-indirect bandgap transition and phonon modulation in monolayer WS₂. *Nano Research*, 8(8):2562–2572, 2015.
- [29] Jimmy C. Kotsakidis, Quianhui Zhang, Amadeo L. Vazquez de Parga, Marc Currie, Kristian Helmersson, D. Kurt Gaskill, and Michael S. Fuhrer. Oxidation of monolayer WS₂ in ambient is a photoinduced process. *Nano Letters*, 19(8):5205–5215, 2019.
- [30] Kai Hao, Lixiang Xu, Philipp Nagler, Akshay Singh, Kha Tran, Chandriker Kavir Dass, Christian Schüller, Tobias Korn, Xiaoqin Li, and Galan Moody. Coherent and incoherent coupling dynamics between neutral and charged excitons in monolayer MoSe₂. *Nano Lett*, 16(8):5109–5113, 2016.
- [31] P Kapuściński Y S Huang A Wójs J Jadczyk, J Kutrowska-Girzycka and L Bryja. Probing of free and localized excitons and trions in atomically thin WSe₂, WS₂, MoSe₂ and MoS₂ in photoluminescence and reflectivity experiments. *Nanotechnology*, 28(39):395702, 2017.
- [32] G. Binnig, H. Rohrer, Ch. Gerber, and E. Weibel. Surface studies by scanning tunneling microscopy. *Phys. Rev. Lett.*, 49(1):57–61, 1982.
- [33] The Nobel prize in physics 1986.
- [34] B. Rogez. Local electrical excitation of plasmonic nanostructures with a scanning tunnelling microscope. 2014.
- [35] G. Binnig, C. F. Quate, and Ch. Gerber. Atomic force microscope. *Phys. Rev. Lett.*, 56(9):930–933, 1986.
- [36] C. Mathew Mate, Gary M. McClelland, Ragnar Erlandsson, and Shirley Chiang. Atomic-scale friction of a tungsten tip on a graphite surface. In H. Neddermeyer, editor, *Scanning Tunneling Microscopy, Perspectives in Condensed Matter Physics*, pages 226–229. Springer Netherlands, 1993.
- [37] R. Erlandsson, G. Hadziioannou, C. M. Mate, G. M. McClelland, and S. Chiang. Atomic scale friction between the muscovite mica cleavage plane and a tungsten tip. *J. Chem. Phys.*, 89(8):5190–5193, 1988.

- [38] T. Namazu, Y. Isono, and T. Tanaka. Evaluation of size effect on mechanical properties of single crystal silicon by nanoscale bending test using AFM. *Journal of Microelectromechanical Systems*, 9(4):450–459, 2000.
- [39] Sriram Sundararajan and Bharat Bhushan. Development of AFM-based techniques to measure mechanical properties of nanoscale structures. *Sensors and Actuators A: Physical*, 101(3):338–351, 2002.
- [40] Nancy A. Burnham and Richard J. Colton. Measuring the nanomechanical properties and surface forces of materials using an atomic force microscope. *Journal of Vacuum Science & Technology A*, 7(4):2906–2913, 1989.
- [41] Nancy A. Burnham, Dawn D. Dominguez, Robert L. Mowery, and Richard J. Colton. Probing the surface forces of monolayer films with an atomic-force microscope. *Phys. Rev. Lett.*, 64(16):1931–1934, 1990.
- [42] O. K. Binnig, H. Rohrer, Ch. Gerber, and E. Stoll. Real-space observation of the reconstruction of Au(100). *Surface Science*, 144(2):321–335, 1984.
- [43] F. Ohnesorge and G. Binnig. True atomic resolution by atomic force microscopy through repulsive and attractive forces. *Science*, 260(5113):1451–1456, 1993.
- [44] Franz J. Giessibl, S. Hembacher, H. Bielefeldt, and J. Mannhart. Subatomic features on the silicon (111)-(7 \times 7) surface observed by atomic force microscopy. *Science*, 289(5478):422–425, 2000.
- [45] E. Tranvouez, E. Boer-Duchemin, G. Comtet, and G. Dujardin. Active drift compensation applied to nanorod manipulation with an atomic force microscope. *Review of Scientific Instruments*, 78(11):115103, 2007.
- [46] Yuliang Wang, Huimin Wang, and Shusheng Bi. Real time drift measurement for colloidal probe atomic force microscope: a visual sensing approach. *AIP Advances*, 4(5):057130, 2014.
- [47] G. Li, Y. Wang, and L. Liu. Drift compensation in AFM-based nanomanipulation by strategic local scan. *IEEE Transactions on Automation Science and Engineering*, 9(4):755–762, 2012.
- [48] J. Freund, J. Halbritter, and J. K. H. Hörber. How dry are dried samples? water adsorption measured by STM. *Microscopy Research and Technique*, 44(5):327–338, 1999.
- [49] F. E. Senftle, J. R. Grant, and F. P. Senftle. Low-voltage DC/AC electrolysis of water using porous graphite electrodes. *Electrochimica Acta*, 55(18):5148–5153, 2010.
- [50] B Rogez, S Cao, G Dujardin, G Comtet, E Le Moal, A Mayne, and E Boer-Duchemin. The mechanism of light emission from a scanning tunnelling microscope operating in air. *Nanotechnology*, 27(46):465201, 2016.
- [51] S. C. Meepagala and F. Real. Detailed experimental investigation of the barrier-height lowering and the tip-sample force gradient during STM operation in air. *Phys. Rev. B*, 49(15):10761–10763, 1994.
- [52] Jian Shen, Dan Zhang, Fei-Hu Zhang, and Yang Gan. AFM tip-sample convolution effects for cylinder protrusions. *Applied Surface Science*, 422:482–491, 2017.
- [53] U. D. Schwarz, H. Haefke, P. Reimann, and H.-J. Güntherodt. Tip artefacts in scanning force microscopy. *Journal of Microscopy*, 173(3):183–197, 1994.
- [54] A. Drezet, A. Hohenau, D. Koller, A. Stepanov, H. Ditlbacher, B. Steinberger, F.R. Aussenegg, A. Leitner, and J.R. Krenn. Leakage radiation microscopy of surface plasmon polaritons. *Materials Science and Engineering: B*, 149(3):220–229, 2008. E-MRS 2007 Spring Conference Symposium A: Sub-wavelength photonics throughout the spectrum: Materials and Techniques.
- [55] DANIEL J. Schroeder. Chapter 10 - diffraction theory and aberrations. In DANIEL J. Schroeder, editor, *Astronomical Optics (Second Edition)*, pages 240–276. Academic Press, 2000.
- [56] Julia M. Läger Gaël Reecht Nils Krane, Christian Lotze and Katharina J. Franke. Electronic structure and luminescence of quasi-freestanding MoS₂ nanopatches on Au(111). *Nano Lett.*, 16(8):5163–5168, 2016.
- [57] Ricardo Javier Peña Román, Yves Auad, Lucas Grasso, Fernando Alvarez, Ingrid David Barcelos, and Luiz Fernando Zagonel. Tunneling-current-induced local excitonic luminescence in p-doped WSe₂ monolayers. *Nanoscale*, 12(25):13460–13470, 2020.
- [58] Renaud Péchou, Shuai Jia, Joel Rigor, Olivier Guillermet, Grégory Seine, Jun Lou, Nicolas Large, Adnen Mlayah, and Roland Coratger. Plasmonic-induced luminescence of MoSe₂ monolayers in a scanning tunneling microscope. *ACS Photonics*, 7(11):3061–3070, 2020.

- [59] Marco M. Furchi, Andreas Pospischil, Florian Libisch, Joachim Burgdörfer, and Thomas Mueller. Photovoltaic effect in an electrically tunable van der waals heterojunction. *Nano Lett.*, 14(8):4785–4791, 2014.
- [60] Jason S. Ross, Philip Klement, Aaron M. Jones, Nirmal J. Ghimire, Jiaqiang Yan, D. G. Mandrus, Takashi Taniguchi, Kenji Watanabe, Kenji Kitamura, Wang Yao, David H. Cobden, and Xiaodong Xu. Electrically tunable excitonic light-emitting diodes based on monolayer WSe₂ p-n junctions. *Nature Nanotechnology*, 9(4):268–272, 2014.
- [61] Y. J. Zhang, T. Oka, R. Suzuki, J. T. Ye, and Y. Iwasa. Electrically switchable chiral light-emitting transistor. *Science*, 344(6185):725–728, 2014.
- [62] Britton W. H. Baugher, Hugh O. H. Churchill, Yafang Yang, and Pablo Jarillo-Herrero. Optoelectronic devices based on electrically tunable p-n diodes in a monolayer dichalcogenide. *Nature Nanotechnology*, 9(4):262–267, 2014.
- [63] Johannes Binder, Freddie Withers, Maciej R. Molas, Clement Faugeras, Karol Nogajewski, Kenji Watanabe, Takashi Taniguchi, Aleksey Kozikov, Andre K. Geim, Kostya S. Novoselov, and Marek Potemski. Sub-bandgap voltage electroluminescence and magneto-oscillations in a WSe₂ light-emitting van der waals heterostructure. *Nano Lett.*, 17(3):1425–1430, 2017.
- [64] Carmen Palacios-Berraquero. Atomically-thin quantum light emitting diodes. In Carmen Palacios-Berraquero, editor, *Quantum Confined Excitons in 2-Dimensional Materials*, Springer Theses, pages 71–89. Springer International Publishing, 2018.
- [65] Kyoung-Duck Park, Omar Khatib, Vasily Kravtsov, Genevieve Clark, Xiaodong Xu, and Markus B. Raschke. Hybrid tip-enhanced nanospectroscopy and nanoimaging of monolayer WSe₂ with local strain control. *Nano Lett.*, 16(4):2621–2627, 2016.
- [66] Kyoung-Duck Park, Tao Jiang, Genevieve Clark, Xiaodong Xu, and Markus B. Raschke. Radiative control of dark excitons at room temperature by nano-optical antenna-tip purcell effect. *Nature Nanotechnology*, 13(1):59–64, 2018.
- [67] X. H. Qiu, G. V. Nazin, and W. Ho. Vibrationally resolved fluorescence excited with submolecular precision. *Science*, 299(5606):542–546, 2003.
- [68] Yang Zhang, Yang Luo, Yao Zhang, Yun-Jie Yu, Yan-Min Kuang, Li Zhang, Qiu-Shi Meng, Yi Luo, Jin-Long Yang, Zhen-Chao Dong, and J. G. Hou. Visualizing coherent intermolecular dipole-dipole coupling in real space. *Nature*, 531(7596):623–627, 2016.
- [69] Hiroshi Imada, Kuniyuki Miwa, Miyabi Imai-Imada, Shota Kawahara, Kensuke Kimura, and Yousoo Kim. Real-space investigation of energy transfer in heterogeneous molecular dimers. *Nature*, 538(7625):364–367, 2016.
- [70] Benjamin Doppagne, Michael C. Chong, Etienne Lorchat, Stéphane Berciaud, Michelangelo Romeo, Hervé Bulou, Alex Boeglin, Fabrice Scheurer, and Guillaume Schull. Vibronic spectroscopy with submolecular resolution from STM-induced electroluminescence. *Phys. Rev. Lett.*, 118(12):127401, 2017.
- [71] Andres Castellanos-Gomez, Michele Buscema, Rianda Molenaar, Vibhor Singh, Laurens Janssen, Herre S. J. van der Zant, and Gary A. Steele. Deterministic transfer of two-dimensional materials by all-dry viscoelastic stamping. *2D Mater.*, 1(1):011002, 2014-04.
- [72] Robert J. Moerland and Jacob P. Hoogenboom. Subnanometer-accuracy optical distance ruler based on fluorescence quenching by transparent conductors. *Optica*, 3(2):112–117, 2016.
- [73] Mark A. Ordal, Robert J. Bell, Ralph W. Alexander, Lawrence A. Newquist, and Marvin R. Querry. Optical properties of Al, Fe, Ti, Ta, W, and Mo at submillimeter wavelengths. *Appl. Opt.*, AO, 27(6):1203–1209, 1988.
- [74] Jonathan Mooney and Patanjali Kambhampati. Get the basics right: Jacobian conversion of wavelength and energy scales for quantitative analysis of emission spectra. *J. Phys. Chem. Lett.*, 4(19):3316–3318, 2013.
- [75] Guillaume Froehlicher, Etienne Lorchat, and Stéphane Berciaud. Charge versus energy transfer in atomically thin graphene-transition metal dichalcogenide van der waals heterostructures. *Phys. Rev. X*, 8(1):011007, 2018.
- [76] Gunnar Berghäuser Robert Schmidt Iris Niehues Robert Schneider Ashish Arora Steffen Michaelis de Vasconcellos Rudolf Bratschitsch Ermin Malic Dominik Christiansen, Malte Selig and Andreas Knorr. Phonon sidebands in monolayer transition metal dichalcogenides. *Phys. Rev. Lett.*, 119(18):187402, 2017.

- [77] Matthias Drüppel Philipp Marauhn Dominik Christiansen Malte Selig Gunnar Berghäuser Daniel Wigger Robert Schneider Lisa Braasch Rouven Koch Andres Castellanos-Gomez Tilmann Kuhn Andreas Knorr Ermin Malic Michael Rohlfing Steffen Michaelis de Vasconcellos Iris Niehues, Robert Schmidt and Rudolf Bratschitsch. Strain control of exciton–phonon coupling in atomically thin semiconductors. *Nano Lett.*, 18(3):1751–1757, 2018.
- [78] C. C. Neacsu, G. A. Steudle, and M. B. Raschke. Plasmonic light scattering from nanoscopic metal tips. *Appl. Phys. B*, 80(3):295–300, 2005.
- [79] Pavel V. Ratnikov. Excitons in planar quantum wells based on transition metal dichalcogenides. *Phys. Rev. B*, 102(8):085303, 2020.
- [80] Eric Le Moal, Sylvie Marguet, Damien Canneson, Benoit Rogez, Elizabeth Boer-Duchemin, Gérald Dujardin, Tatiana V. Teperik, Dana-Codruta Marinica, and Andrey G. Borisov. Engineering the emission of light from a scanning tunneling microscope using the plasmonic modes of a nanoparticle. *Phys. Rev. B*, 93(3):035418, 2016.
- [81] Jon A. Schuller, Sinan Karaveli, Theanne Schiros, Keliang He, Shyuan Yang, Ioannis Kymissis, Jie Shan, and Rashid Zia. Orientation of luminescent excitons in layered nanomaterials. *Nature Nanotechnology*, 8(4):271–276, 2013.
- [82] You Zhou, Giovanni Scuri, Dominik S. Wild, Alexander A. High, Alan Dibos, Luis A. Jauregui, Chi Shu, Kristiaan De Greve, Kateryna Pistunova, Andrew Y. Joe, Takashi Taniguchi, Kenji Watanabe, Philip Kim, Mikhail D. Lukin, and Hongkun Park. Probing dark excitons in atomically thin semiconductors via near-field coupling to surface plasmon polaritons. *Nature Nanotechnology*, 12(9):856–860, 2017.
- [83] Miguel M. Ugeda, Aaron J. Bradley, Su-Fei Shi, Felipe H. da Jornada, Yi Zhang, Diana Y. Qiu, Wei Ruan, Sung-Kwan Mo, Zahid Hussain, Zhi-Xun Shen, Feng Wang, Steven G. Louie, and Michael F. Crommie. Giant bandgap renormalization and excitonic effects in a monolayer transition metal dichalcogenide semiconductor. *Nature Materials*, 13(12):1091–1095, 2014.
- [84] David L. Andrews and David S. Bradshaw. The role of virtual photons in nanoscale photonics. *Annalen der Physik*, 526(3):173–186, 2014.
- [85] Maciej Koperski, Maciej R. Molas, Ashish Arora, Karol Nogajewski, Artur O. Slobodeniuk, Clement Faugeras, and Marek Potemski. Optical properties of atomically thin transition metal dichalcogenides: observations and puzzles. *Nanophotonics*, 6(6):1289–1308, 2017.
- [86] Jörg Kröger, Benjamin Doppagne, Fabrice Scheurer, and Guillaume Schull. Fano description of single-hydrocarbon fluorescence excited by a scanning tunneling microscope. *Nano Lett.*, 18(6):3407–3413, 2018.
- [87] Gong Chen, Yang Luo, Hongying Gao, Jun Jiang, Yunjie Yu, Li Zhang, Yang Zhang, Xiaoguang Li, Zhenyu Zhang, and Zhenchao Dong. Spin-triplet-mediated up-conversion and crossover behavior in single-molecule electroluminescence. *Phys. Rev. Lett.*, 122(17):177401, 2019.
- [88] R. Pechou, R. Coratger, F. Ajustron, and J. Beauvillain. Cutoff anomalies in light emitted from the tunneling junction of a scanning tunneling microscope in air. *Appl. Phys. Lett.*, 72(6):671–673, 1998.
- [89] Guillaume Schull, Nicolas Néel, Peter Johansson, and Richard Berndt. Electron-plasmon and electron-electron interactions at a single atom contact. *Phys. Rev. Lett.*, 102(5):057401, 2009.
- [90] Natalia L. Schneider, Peter Johansson, and Richard Berndt. Hot electron cascades in the scanning tunneling microscope. *Phys. Rev. B*, 87(4):045409, 2013.
- [91] F. Xu, C. Holmqvist, and W. Belzig. Overbias light emission due to higher-order quantum noise in a tunnel junction. *Phys. Rev. Lett.*, 113(6):066801, 2014.
- [92] Aaron M. Jones, Hongyi Yu, John R. Schaibley, Jiaqiang Yan, David G. Mandrus, Takashi Taniguchi, Kenji Watanabe, Hanan Dery, Wang Yao, and Xiaodong Xu. Excitonic luminescence upconversion in a two-dimensional semiconductor. *Nature Physics*, 12(4):323–327, 2016.
- [93] J. Jadcak, L. Bryja, J. Kutrowska-Girzycka, P. Kapuściński, M. Bieniek, Y.-S. Huang, and P. Hawrylak. Room temperature multi-phonon upconversion photoluminescence in monolayer semiconductor WS₂. *Nature Communications*, 10(1):1–10.
- [94] M. Manca, M. M. Glazov, C. Robert, F. Cadiz, T. Taniguchi, K. Watanabe, E. Courtade, T. Amand, P. Renucci, X. Marie, G. Wang, and B. Urbaszek. Enabling valley selective exciton scattering in monolayer WSe₂ through upconversion. *Nature Communications*, 8(1):1–7, 2017.

- [95] B. Han, C. Robert, E. Courtade, M. Manca, S. Shree, T. Amand, P. Renucci, T. Taniguchi, K. Watanabe, X. Marie, L. Golub, M. Glazov, and B. Urbaszek. Exciton states in monolayer MoSe₂ and MoTe₂ probed by upconversion spectroscopy. *Phys. Rev. X*, 8(3):031073, 2018.
- [96] Nardeep Kumar, Qiannan Cui, Frank Ceballos, Dawei He, Yongsheng Wang, and Hui Zhao. Exciton-exciton annihilation in MoSe₂ monolayers. *Physical Review B*, 89(12):125427, 2014.
- [97] L. Limot, T. Maroutian, P. Johansson, and R. Berndt. Surface-state stark shift in a scanning tunneling microscope. *Physical Review Letters*, 91(19):196801, 2003.
- [98] Shinichiro Mouri, Yuhei Miyauchi, Minglin Toh, Weijie Zhao, Goki Eda, and Kazunari Matsuda. Non-linear photoluminescence in atomically thin layered WSe₂ arising from diffusion-assisted exciton-exciton annihilation. *Phys. Rev. B*, 90(15):155449, 2014.
- [99] Toshiaki Kato and Toshiro Kaneko. Transport dynamics of neutral excitons and trions in monolayer WS₂. *ACS Nano*, 10(10):9687–9694, 2016.
- [100] Marvin Kulig, Jonas Zipfel, Philipp Nagler, Sofia Blanter, Christian Schüller, Tobias Korn, Nicola Paradiso, Mikhail M. Glazov, and Alexey Chernikov. Exciton diffusion and halo effects in monolayer semiconductors. *Physical Review Letters*, 120(20):207401, 2018.
- [101] J. H. Coombs, J. K. Gimzewski, B. Reihl, J. K. Sass, and R. R. Schlittler. Photon emission experiments with the scanning tunnelling microscope. *Journal of Microscopy*, 152(2):325–336, 1988.
- [102] R. Berndt, R. Gaisch, W. D. Schneider, J. K. Gimzewski, B. Reihl, R. R. Schlittler, and M. Tschudy. Atomic resolution in photon emission induced by a scanning tunneling microscope. *Phys. Rev. Lett.*, 74(1):102–105, 1995.
- [103] Z.-C. Dong, X.-L. Guo, A. S. Trifonov, P. S. Dorozhkin, K. Miki, K. Kimura, S. Yokoyama, and S. Mashiko. Vibrationally resolved fluorescence from organic molecules near metal surfaces in a scanning tunneling microscope. *Phys. Rev. Lett.*, 92(8):086801, 2004.
- [104] Chi Chen, Ping Chu, C. A. Bobisch, D. L. Mills, and W. Ho. Viewing the interior of a single molecule: Vibronically resolved photon imaging at submolecular resolution. *Phys. Rev. Lett.*, 105(21):217402, 2010.
- [105] Klaus Kuhnke, Christoph Große, Pablo Merino, and Klaus Kern. Atomic-scale imaging and spectroscopy of electroluminescence at molecular interfaces. 2017.
- [106] Benjamin Doppagne, Tomáš Neuman, Ruben Soria-Martinez, Luis E. Parra Lopez, Hervé Bulou, Michelangelo Romeo, Stéphane Berciaud, Fabrice Scheurer, Javier Aizpurua, and Guillaume Schull. Single-molecule tautomerization tracking through space- and time-resolved fluorescence spectroscopy. *Nature Nanotechnology*, 15(3):207–211, 2020.
- [107] Z. C. Dong, X. L. Zhang, H. Y. Gao, Y. Luo, C. Zhang, L. G. Chen, R. Zhang, X. Tao, Y. Zhang, J. L. Yang, and J. G. Hou. Generation of molecular hot electroluminescence by resonant nanocavity plasmons. *Nature Photonics*, 4(1):50–54, 2010.
- [108] Yang Luo, Gong Chen, Yang Zhang, Li Zhang, Yunjie Yu, Fanfang Kong, Xiaojun Tian, Yao Zhang, Chongxin Shan, Yi Luo, Jinlong Yang, Vahid Sandoghdar, Zhenchao Dong, and J. Hou. Electrically driven single-photon superradiance from molecular chains in a plasmonic nanocavity. *Phys. Rev. Lett.*, 122(23):233901, 2019.
- [109] Lukas Novotny and Niek van Hulst. Antennas for light. *Nature Photonics*, 5(2):83–90, 2011.
- [110] Philipp Myrach, Niklas Nilius, and Hans-Joachim Freund. Photon mapping of individual Ag particles on MgO/Mo(001). *Phys. Rev. B*, 83(3):035416, 2011.
- [111] Shuiyan Cao, Mario Zapata-Herrera, Alfredo Campos, Eric Le Moal, Sylvie Marguet, Gérald Dujardin, Mathieu Kociak, Javier Aizpurua, Andrei G. Borisov, and Elizabeth Boer-Duchemin. Probing the radiative electromagnetic local density of states in nanostructures with a scanning tunneling microscope. *ACS Photonics*, 7(5):1280–1289, 2020.
- [112] Denis V. Lebedev, Vitaliy A. Shkoldin, Alexey M. Mozharov, Dmitry V. Permyakov, Lilia N. Dvoretckiaia, Andrey A. Bogdanov, Anton K. Samusev, Alexander O. Golubok, and Ivan S. Mukhin. Scanning tunneling microscopy-induced light emission and I(V) study of optical near-field properties of single plasmonic nanoantennas. *J. Phys. Chem. Lett.*, 12(1):501–507, 2021.
- [113] Eric Le Moal, Sylvie Marguet, Benoit Rogez, Samik Mukherjee, Philippe Dos Santos, Elizabeth Boer-Duchemin, Geneviève Comtet, and Gérald Dujardin. An electrically excited nanoscale light source with active angular control of the emitted light. *Nano Lett.*, 13(9):4198–4205, 2013.

- [114] Anika Kinkhabwala, Zongfu Yu, Shanhui Fan, Yuri Avlasevich, Klaus Müllen, and W. E. Moerner. Large single-molecule fluorescence enhancements produced by a bowtie nanoantenna. *Nature Photonics*, 3(11):654–657, 2009.
- [115] Anastasiya Puchkova, Carolin Vietz, Enrico Pibiri, Bettina Wünsch, María Sanz Paz, Guillermo P. Acuna, and Philip Tinnefeld. DNA origami nanoantennas with over 5000-fold fluorescence enhancement and single-molecule detection at 25 μm . *Nano Letters*, 15(12):8354–8359, 2015.
- [116] C. Belacel, B. Habert, F. Bigourdan, F. Marquier, J.-P. Hugonin, S. Michaelis de Vasconcellos, X. Lafosse, L. Coolen, C. Schwob, C. Javaux, B. Dubertret, J.-J. Greffet, P. Senellart, and A. Maitre. Controlling Spontaneous Emission with Plasmonic Optical Patch Antennas. *Nano Letters*, 13(4):1516–1521, April 2013. Publisher: American Chemical Society.
- [117] Stefano Palomba, Matthias Danckwerts, and Lukas Novotny. Nonlinear plasmonics with gold nanoparticle antennas. *J. Opt. A: Pure Appl. Opt.*, 11(11):114030, 2009.
- [118] Martti Kauranen and Anatoly V. Zayats. Nonlinear plasmonics. *Nature Photonics*, 6(11):737–748, 2012.
- [119] Harry A. Atwater and Albert Polman. Plasmonics for improved photovoltaic devices. In *Materials for Sustainable Energy*, pages 1–11. Co-Published with Macmillan Publishers Ltd, UK, 2010.
- [120] Liang Tang, Sukru Ekin Kocabas, Salman Latif, Ali K. Okyay, Dany-Sebastien Ly-Gagnon, Krishna C. Saraswat, and David A. B. Miller. Nanometre-scale germanium photodetector enhanced by a near-infrared dipole antenna. *Nature Photonics*, 2(4):226–229, 2008.
- [121] Mark W. Knight, Heidar Sobhani, Peter Nordlander, and Naomi J. Halas. Photodetection with active optical antennas. *Science*, 332(6030):702–704, 2011.
- [122] Hyungsoon Im, Huilin Shao, Yong Il Park, Vanessa M. Peterson, Cesar M. Castro, Ralph Weissleder, and Hakho Lee. Label-free detection and molecular profiling of exosomes with a nano-plasmonic sensor. *Nat Biotechnol*, 32(5):490–495, 2014.
- [123] Mickael Buret, Alexander V. Uskov, Jean Dellinger, Nicolas Cazier, Marie-Maxime Mennemanteuil, Johann Berthelot, Igor V. Smetanin, Igor E. Protsenko, Gérard Colas-des Francs, and Alexandre Bouhelier. Spontaneous hot-electron light emission from electron-fed optical antennas. *Nano Lett.*, 15(9):5811–5818, 2015.
- [124] Jin Qin, Yingjian Liu, Huiwen Luo, Zhongjun Jiang, Wenshan Cai, and Liang Wang. Tunable light emission by electrically excited plasmonic antenna. *ACS Photonics*, 6(10):2392–2396, 2019.
- [125] Alexey V. Krasavin, Pan Wang, Mazhar E. Nasir, Yunlu Jiang, and Anatoly V. Zayats. Tunneling-induced broadband and tunable optical emission from plasmonic nanorod metamaterials. *Nanophotonics*, 9(2):427–434, 2020.
- [126] Cheng Zhang, Jean-Paul Hugonin, Anne-Lise Coutrot, Christophe Sauvan, François Marquier, and Jean-Jacques Greffet. Antenna surface plasmon emission by inelastic tunneling. *Nature Communications*, 10(1):1–7, 2019.
- [127] Florian Bigourdan, Jean-Paul Hugonin, Francois Marquier, Christophe Sauvan, and Jean-Jacques Greffet. Nanoantenna for electrical generation of surface plasmon polaritons. *Phys. Rev. Lett.*, 116(10):106803, 2016.
- [128] Cheng Zhang, Jean-Paul Hugonin, Jean-Jacques Greffet, and Christophe Sauvan. Surface plasmon polaritons emission with nanopatch antennas: Enhancement by means of mode hybridization. *ACS Photonics*, 6(11):2788–2796, 2019.
- [129] Florian Bigourdan, Jean-Paul Hugonin, and Philippe Lalanne. Aperiodic-fourier modal method for analysis of body-of-revolution photonic structures. *J. Opt. Soc. Am. A, JOSAA*, 31(6):1303–1311, 2014.
- [130] B. N. J. Persson and A. Baratoff. Theory of photon emission in electron tunneling to metallic particles. *Phys. Rev. Lett.*, 68(21):3224–3227, 1992.
- [131] Jianji Yang, Jean-Paul Hugonin, and Philippe Lalanne. Near-to-far field transformations for radiative and guided waves. *ACS Photonics*, 3(3):395–402, 2016.
- [132] Edward D. Palik and Gorachand Ghosh. *The Electronic handbook of optical constants of solids*. Academic Press, 1999. Google-Books-ID: t_idMwEACAAJ.
- [133] Paolo Biagioni, Jer-Shing Huang, and Bert Hecht. Nanoantennas for visible and infrared radiation. *Reports on Progress in Physics*, 75(2):024402, 2012.

- [134] R. Gans. Über die form ultramikroskopischer goldteilchen. *Annalen der Physik*, 342(5):881–900, 1912.
- [135] T. A. El-Brollosy, T. Abdallah, M. B. Mohamed, S. Abdallah, K. Easawi, S. Negm, and H. Talaat. Shape and size dependence of the surface plasmon resonance of gold nanoparticles studied by photoacoustic technique. *Eur. Phys. J. Spec. Top.*, 153(1):361–364, 2008.
- [136] Jan Becker, Andreas Trügler, Arpad Jakab, Ulrich Hohenester, and Carsten Sönnichsen. The optimal aspect ratio of gold nanorods for plasmonic bio-sensing. *Plasmonics*, 5(2):161–167, 2010.
- [137] Baptiste Auguie and William L. Barnes. Collective resonances in gold nanoparticle arrays. *Phys. Rev. Lett.*, 101(14):143902, 2008.
- [138] Link. Simulation of the optical absorption spectra of gold nanorods as a function of their aspect ratio and the effect of the medium dielectric constant. 1999.
- [139] G. C. Papavassiliou. Optical properties of small inorganic and organic metal particles. *Progress in Solid State Chemistry*, 12(3):185–271, 1979.
- [140] Xochitl Lopez-Lozano, Hector Barron, Christine Mottet, and Hans-Christian Weissker. Aspect-ratio- and size-dependent emergence of the surface-plasmon resonance in gold nanorods : an ab initio TDDFT study. *Phys. Chem. Chem. Phys.*, 16(5):1820–1823, 2014.
- [141] Jana Olson, Sergio Dominguez-Medina, Anneli Hoggard, Lin-Yung Wang, Wei-Shun Chang, and Stephan Link. Optical characterization of single plasmonic nanoparticles. *Chem. Soc. Rev.*, 44(1):40–57, 2014.
- [142] R. Gans. Über die form ultramikroskopischer silberteilchen. *Annalen der Physik*, 352(10):270–284, 1915.
- [143] Bala Krishna Juluri, Yue Bing Zheng, Daniel Ahmed, Lasse Jensen, and Tony Jun Huang. Effects of geometry and composition on charge-induced plasmonic shifts in gold nanoparticles. *J. Phys. Chem. C*, 112(19):7309–7317, 2008.
- [144] Sergey Gorelick, Vitaliy A. Guzenko, Joan Vila-Comamala, and Christian David. Direct e-beam writing of dense and high aspect ratio nanostructures in thick layers of PMMA for electroplating. *Nanotechnology*, 21(29):295303, 2010.
- [145] Falco C. M. J. M. van Delft, Jos P. Weterings, Anja K. van Langen-Suurling, and Hans Romijn. Hydrogen silsesquioxane/novolak bilayer resist for high aspect ratio nanoscale electron-beam lithography. *Journal of Vacuum Science & Technology B: Microelectronics and Nanometer Structures Processing, Measurement, and Phenomena*, 18(6):3419–3423, 2000.
- [146] Jingyuan Zhu, Yifang Chen, Shanshan Xie, Lijuan Zhang, Chunpeng Wang, and Renzhong Tai. Nanofabrication of 30 nm Au zone plates by e-beam lithography and pulse voltage electroplating for soft x-ray imaging. *Microelectronic Engineering*, 225:111254, 2020.
- [147] Aaron D. Mueller, Landobasa Y. M. Tobing, and Dao Hua Zhang. Reliable fabrication of high aspect ratio plasmonic nanostructures based on seedless pulsed electrodeposition. *Advanced Materials Technologies*, 4(1):1800364, 2019.
- [148] H. Neubauer, S. Hoffmann, M. Kanbach, J. Haber, S. Kalbfleisch, S. P. Krüger, and T. Salditt. High aspect ratio x-ray waveguide channels fabricated by e-beam lithography and wafer bonding. *Journal of Applied Physics*, 115(21):214305, 2014.
- [149] Bo Feng, Jianan Deng, Bingrui Lu, Chen Xu, Yiwen Wang, Jing Wan, and Yifang Chen. Nanofabrication of silicon nanowires with high aspect ratio for photo-electron sensing. *Microelectronic Engineering*, 195:139–144, 2018.
- [150] Manfrinato. Aberration-corrected electron beam lithography at the one nanometer length scale. 2017.
- [151] Eunsung Seo, Bo Kyung Choi, and Ohyun Kim. Determination of proximity effect parameters and the shape bias parameter in electron beam lithography. *Microelectronic Engineering*, 53(1):305–308, 2000.
- [152] Wu Cen Shawn. High-energy electron beam lithography for nanoscale fabrication. 2010.
- [153] C. Maurel, R. Coratger, F. Ajustron, G. Seine, R. Péchou, and J. Beauvillain. Effect of multiple tips on light emission induced by STM from gold nanostructures. *Surface Science*, 529(3):359–364, April 2003.
- [154] I. Thormählen, J. Straub, and U. Grigull. Refractive index of water and its dependence on wavelength, temperature, and density. *Journal of Physical and Chemical Reference Data*, 14(4):933–945, 1985.
- [155] Robert L. Olmon, Brian Slovick, Timothy W. Johnson, David Shelton, Sang-Hyun Oh, Glenn D. Boreman, and Markus B. Raschke. Optical dielectric function of gold. *Phys. Rev. B*, 86(23):235147, 2012.

- [156] J. R. Kirtley, T. N. Theis, and J. C. Tsang. Diffraction-grating-enhanced light emission from tunnel junctions. *Appl. Phys. Lett.*, 37(5):435–437, 1980.
- [157] S. L. McCarthy and John Lambe. Enhancement of light emission from metal-insulator-metal tunnel junctions. *Appl. Phys. Lett.*, 30(8):427–429, 1977.
- [158] P. K. Hansma and H. P. Broida. Light emission from gold particles excited by electron tunneling. *Appl. Phys. Lett.*, 32(9):545–547, 1978.
- [159] S. Ushioda, J. E. Rutledge, and R. M. Pierce. Prism-coupled light emission from tunnel junctions. *Phys. Rev. Lett.*, 54(3):224–226, 1985.
- [160] Xiaobo He, Jibo Tang, Huatian Hu, Junjun Shi, Zhiqiang Guan, Shunping Zhang, and Hongxing Xu. Electrically driven highly tunable cavity plasmons. *ACS Photonics*, 6(4):823–829, 2019.
- [161] Johannes Kern, René Kulklock, Jord Prangmsma, Monika Emmerling, Martin Kamp, and Bert Hecht. Electrically driven optical antennas. *Nature Photonics*, 9(9):582–586, 2015.
- [162] René Kulklock, Maximilian Ochs, Philipp Grimm, Monika Emmerling, and Bert Hecht. Electrically-driven Yagi-Uda antennas for light. *Nature Communications*, 11(1):1–7, 2020.
- [163] Surya Prakash Gurunaryanan, Niels Verellen, Vyacheslav S. Zharinov, Finub James Shirley, Victor V. Moshchalkov, Marc Heyns, Joris Van de Vondel, Iuliana P. Radu, and Pol Van Dorpe. Electrically driven unidirectional optical nanoantennas. *Nano Lett.*, 17(12):7433–7439, 2017.
- [164] Haoliang Qian, Su-Wen Hsu, Kargal Gurunatha, Conor T. Riley, Jie Zhao, Dylan Lu, Andrea R. Tao, and Zhaowei Liu. Efficient light generation from enhanced inelastic electron tunnelling. *Nature Photonics*, 12(8):485–488, 2018.
- [165] M. Parzefall, P. Bharadwaj, A. Jain, T. Taniguchi, K. Watanabe, and L. Novotny. Antenna-coupled photon emission from hexagonal boron nitride tunnel junctions. *Nature Nanotechnology*, 10(12):1058–1063, 2015.
- [166] Áron Szabó Takashi Taniguchi Kenji Watanabe Mathieu Luisier Lukas Novotny Parzefall, Markus. Light from van der waals quantum tunneling devices. *Nature Communications*, 10(1):1–9, 2019.
- [167] Markus Parzefall and Lukas Novotny. Optical antennas driven by quantum tunneling: a key issues review. *Rep. Prog. Phys.*, 82(11):112401, 2019.
- [168] Markus Parzefall, Palash Bharadwaj, and Lukas Novotny. Antenna-coupled tunnel junctions. In Sergey I. Bozhevolnyi, Luis Martin-Moreno, and Francisco Garcia-Vidal, editors, *Quantum Plasmonics*, Springer Series in Solid-State Sciences, pages 211–236. Springer International Publishing, 2017.
- [169] Wei Du, Tao Wang, Hong-Son Chu, and Christian A. Nijhuis. Highly efficient on-chip direct electronic-plasmonic transducers. *Nature Photonics*, 11(10):623–627, 2017.
- [170] Markus Parzefall and Lukas Novotny. Light at the end of the tunnel. *ACS Photonics*, 2018.
- [171] Thorin J. Duffin, Vijith Kalathingal, Andreea Radulescu, Changjian Li, Stephen J. Pennycook, and Christian A. Nijhuis. Cavity plasmonics in tunnel junctions: Outcoupling and the role of surface roughness. *Physical Review Applied*, 14(4):044021, 2020.
- [172] Luis Botaya, Jorge Otero, Laura González, Xavier Coromina, Gabriel Gomila, and Manel Puig-Vidal. Quartz tuning fork-based conductive atomic force microscope with glue-free solid metallic tips. *Sensors and Actuators A: Physical*, 232:259–266, 2015.
- [173] Sébastien Decossas, Frédéric Mazen, Thierry Baron, Georges Brémond, and Abdelkader Souifi. Atomic force microscopy nanomanipulation of silicon nanocrystals for nanodevice fabrication. *Nanotechnology*, 14(12):1272–1278, 2003.
- [174] A. H. Korayem, M. H. Korayem, and M. Taheri. Robust controlled manipulation of nanoparticles using the AFM nanorobot probe. *Arabian Journal for Science and Engineering*, 40(9):2685–2699, 2015.
- [175] John G. Simmons. Electric tunnel effect between dissimilar electrodes separated by a thin insulating film. *Journal of Applied Physics*, 34(9):2581–2590, 1963.
- [176] W. M. H. Sachtler, G. J. H. Dorgelo, and A. A. Holscher. The work function of gold. *Surface Science*, 5(2):221–229, 1966.
- [177] R. M. Eastment and C. H. B. Mee. Work function measurements on (100), (110) and (111) surfaces of aluminium. *Journal of Physics F: Metal Physics*, 3(9):1738–1745, 1973.

- [178] A. W. Dweydari and C. H. B. Mee. Work function measurements on (100) and (110) surfaces of silver. *physica status solidi (a)*, 27(1):223–230, 1975.
- [179] Hsin-Lun Wu, Chun-Hong Kuo, and Michael H. Huang. Seed-mediated synthesis of gold nanocrystals with systematic shape evolution from cubic to trisectahedral and rhombic dodecahedral structures. *Langmuir*, 26(14):12307–12313, 2010.
- [180] John G. Simmons. Generalized formula for the electric tunnel effect between similar electrodes separated by a thin insulating film. *Journal of Applied Physics*, 34(6):1793–1803, 1963.
- [181] A. Mangin, A. Anthore, M. L. Della Rocca, E. Boulat, and P. Lafarge. Reduced work functions in gold electromigrated nanogaps. *Phys. Rev. B*, 80(23):235432, 2009.
- [182] Palash Bharadwaj, Alexandre Bouhelier, and Lukas Novotny. Electrical excitation of surface plasmons. *Phys. Rev. Lett.*, 106(22):226802, 2011.
- [183] Daniel Hone, B. Mühlischlegel, and D. J. Scalapino. Theory of light emission from small particle tunnel junctions. *Applied Physics Letters*, 33(2):203–204, 1978.
- [184] C. Tserkezis, R. Esteban, D. O. Sigle, J. Mertens, L. O. Herrmann, J. J. Baumberg, and J. Aizpurua. Hybridization of plasmonic antenna and cavity modes: Extreme optics of nanoparticle-on-mirror nanogaps. *Phys. Rev. A*, 92(5):053811, 2015.
- [185] Hyuck Choo, Myung-Ki Kim, Matteo Staffaroni, Tae Joon Seok, Jeffrey Bokor, Stefano Cabrini, P. James Schuck, Ming C. Wu, and Eli Yablonovitch. Nanofocusing in a metal-insulator-metal gap plasmon waveguide with a three-dimensional linear taper. *Nature Photonics*, 6(12):838–844, 2012.
- [186] Cheng Zhang. Electrical excitation of surface plasmon polaritons by inelastic tunneling electrons with resonant nanoantennas, 2019.
- [187] Wolfgang S. M. Werner, Kathrin Glantschnig, and Claudia Ambrosch-Draxl. Optical constants and inelastic electron-scattering data for 17 elemental metals. *Journal of Physical and Chemical Reference Data*, 38(4):1013–1092, 2009.
- [188] Rohit Chikkaraddy, Xuezi Zheng, Felix Benz, Laura J. Brooks, Bart de Nijs, Cloudy Carnegie, Marie-Elena Kleemann, Jan Mertens, Richard W. Bowman, Guy A. E. Vandenbosch, Victor V. Moshchalkov, and Jeremy J. Baumberg. How ultranarrow gap symmetries control plasmonic nanocavity modes: From cubes to spheres in the nanoparticle-on-mirror. *ACS Photonics*, 4(3):469–475, 2017.
- [189] Rémi Faggiani, Jianji Yang, and Philippe Lalanne. Quenching, plasmonic, and radiative decays in nanogap emitting devices. *ACS Photonics*, 2(12):1739–1744, 2015.
- [190] Felix Benz, Rohit Chikkaraddy, Andrew Salmon, Hamid Ohadi, Bart de Nijs, Jan Mertens, Cloudy Carnegie, Richard W. Bowman, and Jeremy J. Baumberg. SERS of individual nanoparticles on a mirror: Size does matter, but so does shape. *J. Phys. Chem. Lett.*, 7(12):2264–2269, 2016.
- [191] Sugimoto. Hybridized plasmonic gap mode of gold nanorod on mirror nanoantenna for spectrally tailored fluorescence enhancement. 2018.
- [192] Isabel Romero, Javier Aizpurua, Garnett W. Bryant, and F. Javier Garcia de Abajo. Plasmons in nearly touching metallic nanoparticles: singular response in the limit of touching dimers. *Opt. Express*, OE, 14(21):9988–9999, 2006.
- [193] Lukas Novotny and Bert Hecht. *Principles of Nano-Optics*. Cambridge University Press, 2012. Google-Books-ID: RHC_AwAAQBAJ.
- [194] Stefan Alexander Maier. *Plasmonics: Fundamentals and Applications*. Springer Science & Business Media, 2007. Google-Books-ID: yT2ux7TmDc8C.
- [195] M. Andreas Lieb, James M. Zavislan, and Lukas Novotny. Single-molecule orientations determined by direct emission pattern imaging. *J. Opt. Soc. Am. B*, JOSAB, 21(6):1210–1215, 2004.
- [196] Aurora Muñoz-Losa, Carles Curutchet, Brent P. Krueger, Lydia R. Hartsell, and Benedetta Mennucci. Fretting about FRET: Failure of the ideal dipole approximation. *Biophysical Journal*, 96(12):4779–4788, 2009.
- [197] Philippe K. Chow, Eklavya Singh, Bartolomeu Cruz Viana, Jian Gao, Jian Luo, Jing Li, Zhong Lin, Ana L. Elias, Yunfeng Shi, Zuankai Wang, Mauricio Terrones, and Nikhil Koratkar. Wetting of mono and few-layered WS₂ and MoS₂ films supported on Si/SiO₂ substrates. *ACS Nano*, 9(3):3023–3031, 2015.

- [198] Andrew Kozbial, Xiao Gong, Haitao Liu, and Lei Li. Understanding the intrinsic water wettability of molybdenum disulfide (MoS_2). *Langmuir*, 31(30):8429–8435, 2015.
- [199] Michael G. Boyle, J. Mitra, and Paul Dawson. The tip-sample water bridge and light emission from scanning tunnelling microscopy. *Nanotechnology*, 20(33):335202, 2009.
- [200] G. V. Samsonov. Mechanical properties of the elements. In G. V. Samsonov, editor, *Handbook of the Physicochemical Properties of the Elements*, pages 387–446. Springer US, 1968.
- [201] Gleb M. Akselrod, Christos Argyropoulos, Thang B. Hoang, Cristian Ciraci, Chao Fang, Jiani Huang, David R. Smith, and Maiken H. Mikkelsen. Probing the mechanisms of large purcell enhancement in plasmonic nanoantennas. *Nature Photonics*, 8(11):835–840, 2014.

Appendix A

Maxwell equations for propagating surface plasmons

Definition

Propagating surface plasmons (SPPs) are defined as collective surface electron oscillations coupled to electromagnetic waves at an interface between a metal and a dielectric. They are a solution to Maxwell equations for an interface between a material with a real positive permittivity (dielectric, ϵ_1) and a material with a complex dielectric function (metal, $\epsilon_2(\omega)$) [193, 194]. Figure A.1 shows the geometry of the situation. We call z the vertical axis, perpendicular to the interface, and we consider surface plasmons propagating along the x -axis

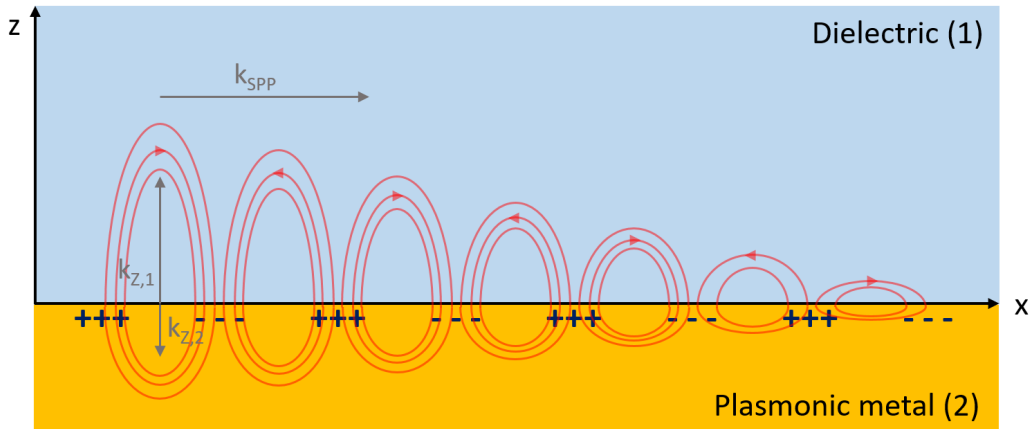


Figure A.1: Schematic of the SPP electric field at the interface

We define the electric and magnetic fields as :

$$\vec{E} = \begin{pmatrix} E_X \\ E_Y \\ E_Z \end{pmatrix}, \quad \vec{B} = \begin{pmatrix} B_X \\ B_Y \\ B_Z \end{pmatrix} \quad (\text{A.1})$$

Maxwell equations and wave propagation

Considering plane waves with harmonic time dependence with no free charges or currents, from Maxwell equations, we have:

$$\begin{aligned}\nabla \times \vec{E} &= i\omega \vec{B} \\ \nabla \times \vec{B} &= \frac{-i\omega \epsilon_j}{c^2} \vec{E}, \quad j = \text{dielectric (1) or metal (2)}\end{aligned}\tag{A.2}$$

From these equations, we may derive the Helmholtz equations :

$$\begin{aligned}\nabla^2 \vec{E} &= -\frac{\omega^2}{c^2} \epsilon_j \vec{E} \\ \nabla^2 \vec{B} &= -\frac{\omega^2}{c^2} \epsilon_j \vec{B}, \quad \text{with } j = 1,2\end{aligned}\tag{A.3}$$

We now consider the propagating mode of the surface plasmon on the interface. First, if we assume the surface plasmon to be a transverse-electric (TE) mode, we have:

$$\vec{E} = \begin{pmatrix} 0 \\ E_Y \\ 0 \end{pmatrix}, \quad \vec{B} = \begin{pmatrix} B_X \\ 0 \\ B_Z \end{pmatrix}\tag{A.4}$$

At the interface, the components of \vec{E} and \vec{B} parallel to the surface (E_Y and B_X) are continuous. Using Eq. A.2-a, we have:

$$B_X = \frac{\nabla \times \vec{E}}{i\omega} \cdot \vec{e}_x = \frac{-1}{i\omega} \frac{\partial E_Y}{\partial z}\tag{A.5}$$

which gives us the following continuity requirements:

$$\begin{aligned}E_{Y,1} &= E_{Y,2} \\ \frac{\partial E_{Y,1}}{\partial z} &= \frac{\partial E_{Y,2}}{\partial z}\end{aligned}\tag{A.6}$$

As the system is translation invariant in the y direction, the fields do not depend on y . Since the wave propagates on the surface and is evanescent in the directions perpendicular to the surface, we can define E_Y as:

$$\begin{aligned}E_{Y,1} &= A_1 e^{i k_x \cdot x} e^{-k_{z,1} \cdot z}, \quad \text{for } z > 0 \text{ and } \Re k_{z,1} \geq 0, \Im k_{z,1} = 0 \\ E_{Y,2} &= A_2 e^{i k_x \cdot x} e^{k_{z,2} \cdot z}, \quad \text{with } z \leq 0 \text{ and } \Re k_{z,2} \geq 0, \Im k_{z,2} = 0\end{aligned}\tag{A.7}$$

Thus, to fulfill the continuity requirements, we need:

$$k_{z,1} = -k_{z,2}\tag{A.8}$$

This is not possible as $k_{z,1}$ and $k_{z,2}$ both have to be positive for the wave to be evanescent in both directions perpendicular to the interface. Thus, propagating surface plasmons are not a TE mode. Looking now at the

fields for a transverse-magnetic (TM) mode instead, we have:

$$\vec{E} = \begin{pmatrix} E_X \\ 0 \\ E_Z \end{pmatrix}, \quad \vec{B} = \begin{pmatrix} 0 \\ B_Y \\ 0 \end{pmatrix} \quad (\text{A.9})$$

At the interface, the components of \vec{E} and \vec{B} parallel to the surface (E_X and B_Y) are continuous. Using Eq. A.2-a, we have:

$$\begin{aligned} E_X &= \frac{-c^2}{i\omega \epsilon_j} \nabla \times \vec{B} \cdot \vec{e}_x \\ &= \frac{c^2}{i\omega \epsilon_j} \frac{\partial B_Y}{\partial z} \end{aligned} \quad (\text{A.10})$$

This gives us the following continuity requirements:

$$\begin{aligned} B_{Y,1} &= B_{Y,2} \\ \frac{1}{\epsilon_1} \frac{\partial B_{Y,1}}{\partial z} &= \frac{1}{\epsilon_2} \frac{\partial B_{Y,2}}{\partial z} \end{aligned} \quad (\text{A.11})$$

As the system is translation invariant in the y direction, the fields do not depend on y . Since the wave propagates on the surface and is evanescent in the directions perpendicular to the surface, we can define B_Y as:

$$\begin{aligned} B_{Y,1} &= A_1 e^{i k_x \cdot x} e^{-k_{z,1} \cdot z}, \quad \text{for } z > 0 \text{ and } \Re k_{z,1} \geq 0, \Im k_{z,1} = 0 \\ B_{Y,2} &= A_2 e^{i k_x \cdot x} e^{k_{z,2} \cdot z}, \quad \text{for } z \leq 0 \text{ and } \Re k_{z,2} \geq 0, \Im k_{z,2} = 0 \end{aligned} \quad (\text{A.12})$$

Thus, to fulfill the continuity requirements, we need:

$$\begin{aligned} A_1 &= A_2 \\ \frac{k_{z,1}}{\epsilon_1} &= \frac{-k_{z,2}}{\epsilon_2} \end{aligned} \quad (\text{A.13})$$

Thus a TM mode is possible if the two materials at the interface have permittivities whose real parts are of opposite sign, such as between a metal and a dielectric.

k_z and k_x

We now want to calculate the propagation constant k_x and the z component of the wavevector $k_{z,j}$ of this TM mode at the interface between a dielectric ($j = 1$) and a metal ($j = 2$). From Eq. A.13-b and A.3, we get:

$$\begin{aligned} \frac{k_{z,1}}{\epsilon_1} &= \frac{-k_{z,2}}{\epsilon_2} \\ \frac{\omega^2}{c^2} \epsilon_j &= k_x^2 - k_{z,j}^2, \quad j = \text{dielectric (1) or metal (2)} \end{aligned} \quad (\text{A.14})$$

Thus:

$$\begin{aligned}
k_{z,1}^2 &= k_x^2 - \frac{\omega^2}{c^2} \epsilon_1 \\
&= k_{z,2}^2 + \frac{\omega^2}{c^2} \epsilon_2 - \frac{\omega^2}{c^2} \epsilon_1 \\
&= k_{z,1}^2 \frac{\epsilon_2^2}{\epsilon_1^2} + (\epsilon_2 - \epsilon_1) \frac{\omega^2}{c^2} \\
&= \epsilon_1^2 \frac{\omega^2}{c^2} \frac{\epsilon_2 - \epsilon_1}{\epsilon_1^2 - \epsilon_2^2} \\
&= -\frac{\omega^2}{c^2} \frac{\epsilon_1^2}{\epsilon_1 + \epsilon_2}
\end{aligned} \tag{A.15}$$

Thus, we have:

$$\begin{aligned}
k_{z,1} &= \sqrt{-\frac{\omega^2}{c^2} \frac{\epsilon_1^2}{\epsilon_1 + \epsilon_2}} \\
k_{z,2} &= \sqrt{-\frac{\omega^2}{c^2} \frac{\epsilon_2^2}{\epsilon_1 + \epsilon_2}}
\end{aligned} \tag{A.16}$$

We need $k_{z,j}$ to be real so that the propagating surface plasmon field is evanescent in the direction perpendicular to the surface. Thus, $k_{z,j}^2 > 0$, which means $\epsilon_1 + \epsilon_2 < 0$: in order for the system to support surface plasmons, we need to be at an interface between a metal and a dielectric, and the real part of the dielectric function of the metal must be sufficiently negative.

From Eq. A.14, we can find k_x :

$$k_x = \frac{\omega}{c} \sqrt{\frac{\epsilon_1 \cdot \epsilon_2}{\epsilon_1 + \epsilon_2}} \tag{A.17}$$

Propagation length and penetration depth

From the previous section, we note that while k_z is necessarily real, k_x may be complex ($k_x = k'_x + ik''_x$), with the imaginary part describing the damping of the electric field as the surface plasmons propagate on the surface. In the following, we assume that the imaginary part of the metal permittivity (ϵ''_2) is negligible compared to the real part (ϵ'_2):

$$\begin{aligned}
k'_x &= \sqrt{\frac{\epsilon'_2 \cdot \epsilon_1}{\epsilon'_2 + \epsilon_1}} \cdot \frac{\omega}{c} \\
k''_x &= \sqrt{\frac{\epsilon'_2 \cdot \epsilon_1}{\epsilon'_2 + \epsilon_1}} \cdot \frac{\epsilon''_2 \cdot \epsilon_1}{2 \cdot \epsilon'_2 \cdot (\epsilon'_2 + \epsilon_1)} \cdot \frac{\omega}{c} \\
k_{z,2} &= \frac{\omega}{c} \cdot \sqrt{\frac{\epsilon_2'^2}{\epsilon_2' + \epsilon_1}} (1 + i \frac{\epsilon_2''}{2\epsilon_2'}) \\
k_{z,1} &= \frac{\omega}{c} \cdot \sqrt{\frac{\epsilon_1^2}{\epsilon_2' + \epsilon_1}} (1 - i \frac{\epsilon_2''}{2(\epsilon_2' + \epsilon_1)})
\end{aligned} \tag{A.18}$$

This gives us an exponential decay of the electromagnetic fields when the surface plasmons propagate on the interface. We thus determine the propagation length $L_{SPP} = \frac{1}{|k''_x|}$ for the fields, and $L_{SPP} = \frac{1}{2|k''_x|}$ for the intensity.

Similarly, the exponential decay along the z axis gives us the penetration depth of the propagating surface

plasmon in each medium, with $d_j = \frac{1}{|k_{z,j}|}$ for the fields, and $d_j = \frac{1}{2|k_{z,j}|}$ for the intensity, with $j = 1$ for the dielectric and $j = 2$ for the metal.

Appendix B

Magnification of the optical detection system

Our optical detection system (combined with the JPK Nanowizard 3 STM) is composed of a microscope objective, a tube lens at the exit of the microscope, and two lenses which focus the light emitted from the sample onto the detectors: see Fig. B.1 below.

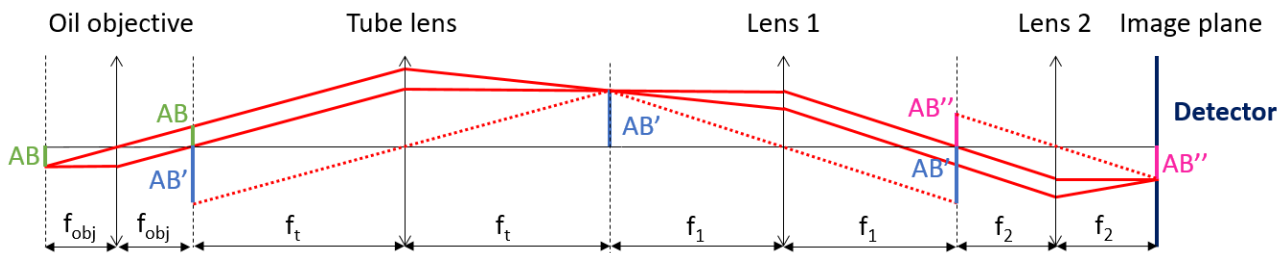


Figure B.1: Optical ray tracing through our system

By simply using Thales' theorem, we can determine the magnification $\frac{AB''}{AB}$ with:

$$\begin{aligned} \frac{AB'}{AB} &= \frac{f_t}{f_{obj}} \\ \frac{AB''}{AB'} &= \frac{f_2}{f_1} \\ \frac{AB''}{AB} &= \frac{AB''}{AB'} \cdot \frac{AB'}{AB} \\ &= \frac{f_2}{f_1} \cdot \frac{f_t}{f_{obj}} \end{aligned}$$

The objective focal length is 2 mm, the tube lens focal length is 300 mm, and the lens 1 focal length is 100 mm. The focal length of lens 2 depends on whether detector 1 or detector 2 is used (see Section 1.2.5): for detector 1, the focal length is 100 mm, and for detector 2, the focal length is 50 mm. Thus, the magnification is $\times 150$ for images acquired with detector 1 (CCD camera) and $\times 75$ for data acquired with detector 2 (imaging spectrometer).

Appendix C

Description of the AFM laser

In the experiments described in Section 4.3, we use a conducting AFM tip to electrically contact a nanoantenna. A bias voltage is then applied between the antenna and the plasmonic film, allowing tunneling to occur, leading to the excitation of surface plasmons. We wish to detect the light emitted from these surface plasmons through the transparent substrate. However, as described in Section 1.2.2, an AFM uses a laser to detect the deflection of the cantilever. This laser light will mask the signal that we wish to detect. The spectrum of the AFM laser may be found in Fig. C.1.

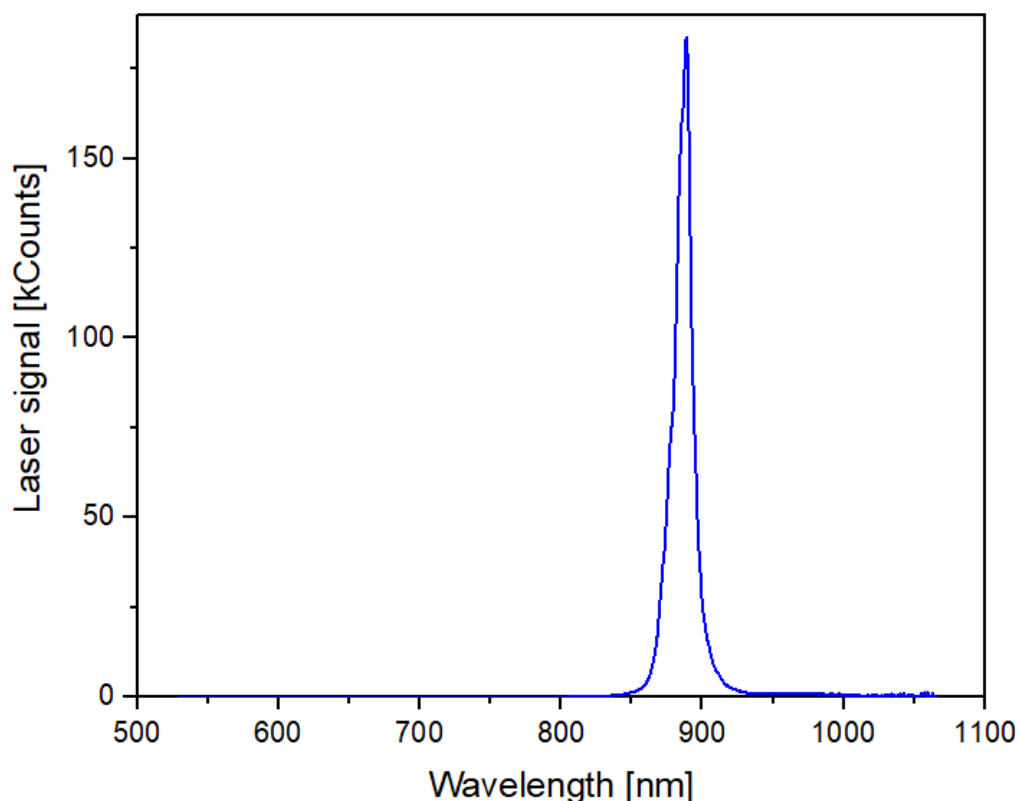


Figure C.1: Spectrum of the AFM detection laser, corrected for the transmission of the optical system. The acquisition time is 10 seconds and the spectrometer entrance slit width is 0.1 mm. Note that the spectrometer entrance slit is normally kept open as wide as possible (2 mm). However for this experiment, the signal was too intense and saturated our detector, thus we closed the slit in order to reduce the number of received photons.

As our wavelength range of interest is between 500 nm and 900 nm, even while blocking the laser signal with a short pass filter (a FES0800 filter from Thorlabs with a transmission factor of 5.9×10^{-6} at $\lambda = 880$ nm), the laser completely drowns out our signal and saturates our detectors when using the exposition time necessary to detect light coming from our junction. Thus, we choose to turn off the laser once the electrical contact is obtained in order to detect the plasmonic signal.

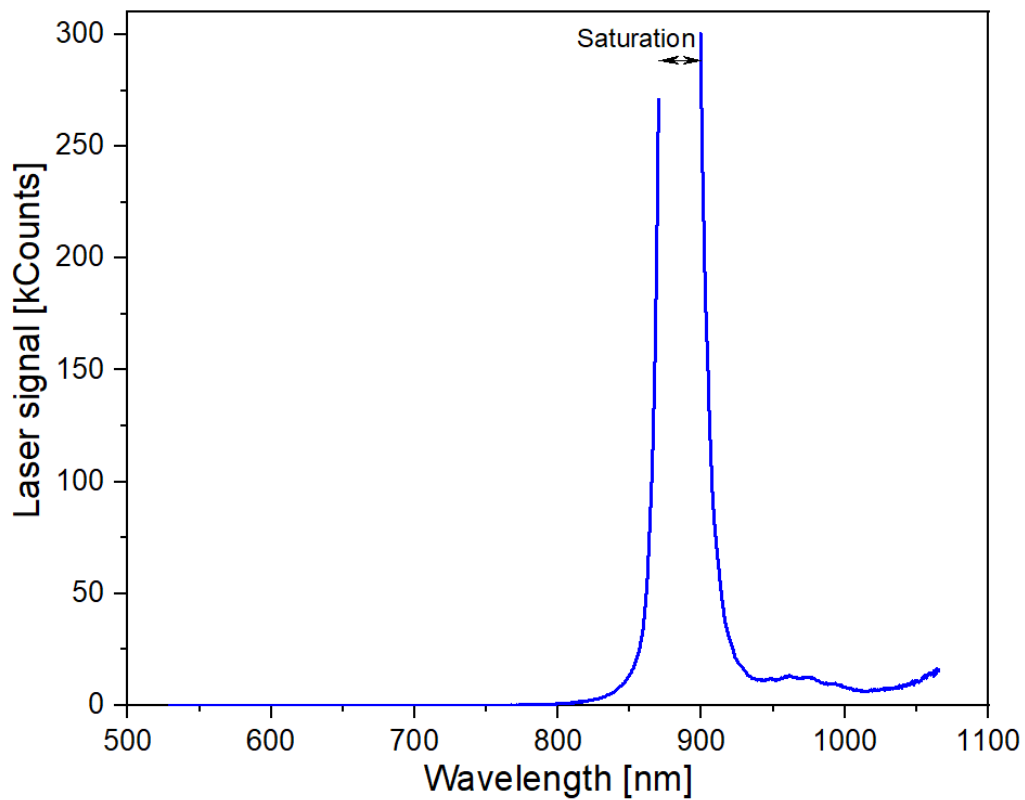


Figure C.2: Spectrum of the AFM detection laser with a $\lambda = 800$ nm short pass filter in the optical path, corrected for the transmission of the optical system. The acquisition time is 100 seconds and the spectrometer entrance slit width is 0.1 mm.

Appendix D

Fourier space imaging of MoSe₂ electroluminescence

D.1 Bright excitons in monolayer MoSe₂: transition dipole moment orientation

Figure 2.4 from Section 2.1 shows the angular distribution of the STM-induced electroluminescence from monolayer MoSe₂ compared to the theoretical emission patterns of an oscillating point-like electric dipole on an air-glass interface. In the calculation shown in Fig. 2.4, this dipole is either oriented out-of-plane, or randomly in the xy plane (i.e., the plane orthogonal to the tip axis and to the optical axis of the microscope objective). From the data of Fig. 2.4, the luminescent sample exhibits no optical anisotropy in the plane. Comparing in Fig. D.1 the theoretical emission patterns of an oscillating point-like electric dipole on an air-glass interface, oriented (a) along the x -axis, (b) along the y -axis, and (c) randomly oriented in the xy plane, we clearly see that the result for the randomly-oriented in-plane dipoles is the best match to the experimental data. Thus we assume that there is no preferential in-plane orientation for the transition dipole moment of the bright excitons in monolayer MoSe₂. In addition, the excitation source (i.e., the tunneling current between the tip and the sample) has cylindrical symmetry with respect to the tunneling junction axis; therefore, the excitation is isotropic in the plane. As a result, the measured luminescence images are averaged over all possible in-plane orientations of the transition dipole moment of the bright excitons, and the measured Fourier space images exhibit circular symmetry with respect to the center of Fourier space.

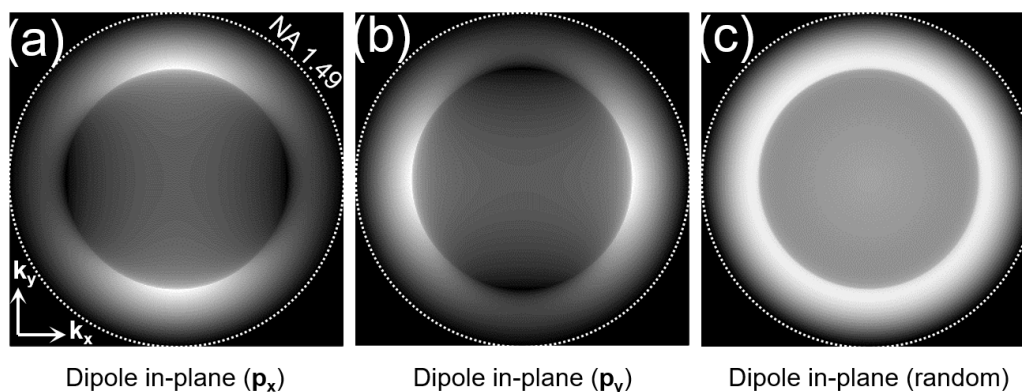


Figure D.1: Theoretical emission patterns in Fourier-space, calculated for an oscillating point-like electric dipole on an air-glass interface, oriented (a) along the x -axis, (b) along the y -axis, and (c) randomly in the xy plane.

Therefore, unlike in previous work where single molecules with fixed in-plane orientation were considered [195], the symmetry argument cannot be used in our case to distinguish between in-plane and out-of-plane emit-

ting dipoles. In our case, emission patterns averaged over all possible in-plane orientations must be considered. Nevertheless, other arguments may be used to distinguish between in-plane and out-of-plane emitting dipoles. In particular, the subcritical angular distribution is clearly different and the angle of maximum intensity is also not the same. In Fig. 2.4, the juxtaposition of the experimental results with the emission pattern for the different dipole orientation shows that the light comes from bright excitons with a random in-plane dipole orientation.

D.2 Excitation of an in-plane dipole with a vertical dipole

Here, we clarify the apparent contradiction that STM-induced luminescence from monolayer MoSe₂ on ITO is primarily due to excitons that have in-plane oriented transition dipole moments, even though the tunneling current is oriented along the direction orthogonal to the sample plane.

Most often, the emission of light from below the tip of an STM is ascribed to inelastic electron tunneling through the tip-sample junction [7, 8, 10]. Such a process is equivalent to an oscillating electric dipole, the orientation of which is orthogonal to the surface of the sample [9]. It is generally admitted that the origin of this effect is the time-dependent fluctuations of the electronic current (i.e., the shot noise) at optical frequencies [90, 91]. In the case of a metal surface, taking into account image charges is crucial and primarily out-of-plane optical modes are excited, due to strong enhancement of the optical fields along the tip-sample axis. However, in our case, the luminescent sample is not on a metal surface: the substrate is transparent and not metallic. Moreover, the tip is not plasmonic within the investigated frequency range. As a result, the contribution of image charges is comparatively weak. Nevertheless, due to the symmetry of the tip-surface junction, inelastic electron tunneling is expected to be equivalent to an electric dipole oscillating along the tip direction, i.e., orthogonal to the surface.

However, this does not necessarily prevent the tunneling current from exciting excitons having their transition dipole moment parallel to the surface. In the resonance energy transfer theory, the Ideal Dipole Approximation (IDA) applies when the two coupled systems are small compared to their separation distance. Within this approximation, the coupling between two orthogonal electric dipoles is indeed not efficient. However, the IDA is known to perform poorly for finite-sized organic molecules at separation distances below 5 nm [196]. Furthermore, the most recent literature on STM-induced luminescence of single molecules is on flat-lying molecules that have in-plane transition dipole moments (see, e.g., Ref. [70]). In addition, at the nanometer scale, the STM tunneling junction cannot be described as a point-like oscillating dipole. The 2D geometry of the luminescent sample also makes the IDA inapplicable.

Finally, the observation of luminescence from the bright excitons in MoSe₂, which have an in-plane transition dipole moment, does not necessarily mean that a resonance energy transfer only occurs from the tunneling current to these bright excitons. A resonance energy transfer may also occur from the tunneling current to the dark excitons in MoSe₂, which have an out-of-plane transition dipole moment and an energy a few tens of meV above their bright counterparts. The dark excitons are expected to convert into the lower-energy bright excitons (through phonon coupling) before decaying radiatively.

Appendix E

STM-induced alteration of a TMD monolayer

As discussed in Section 2 we use a scanning tunneling microscope (STM) to excite excitons in a TMD monolayer. However, during the first experiments carried out on MoSe₂, we noted that the photoluminescence of the sample was impacted by the STM-induced electroluminescence measurements: see Fig. E.1. In this figure, the photoluminescence images of the sample before and after STM excitation are shown. The STM excitation position may be identified by a slight decrease in intensity in the after image. In the first case, shown in Fig. E.1-a and -b, a series of five STM excitations are carried out along a vertical line, 100 nm apart (bias voltage 4 V, $I_{Setpoint} = 10$ nA, acquisition time = 200 s). Comparing horizontal cross-sections from the before and after images at the STM excitation position show that there is a maximum decrease of the photoluminescence of 57% of the average photoluminescence in the same zone, with a FWHM of 800 nm. In the second case, a single STM excitation is performed (bias voltage 3 V, $I_{Setpoint} = 5$ nA, acquisition time = 200 s). Here, again comparing horizontal cross-sections from the before and after images, a maximum decrease of the photoluminescence of 13% of the average photoluminescence in the same zone is observed, with a FWHM of 320 nm. Thus, we note that the series of excitations (each carried out 100 nm apart on a vertical line) with a 10 nA tunneling current setpoint and a 4 V bias voltage appears to have a greater impact on the sample than an excitation with a 5 nA tunneling current setpoint and a 3 V bias voltage.

Several hypothesis are possible: a first possibility is that as we are working in air, the STM may be unstable due to ionic current in the water layer that covers our sample [48], thus leading to mechanical damage of the sample. However, during STM imaging (not shown here, see Fig. 2.12-a) we note that there are more instabilities or STM tip “jumps” when the STM tip is above the ITO layer than when the tip is above the TMD monolayer. This may be due to the roughness of the sample, as ITO has a granular structure, or it may be due to the hydrophobic nature of aged TMDs [197, 198], which may explain the stability of the tip on the TMD. The damage may also be due to heating from the tunneling current, which may directly damage the TMD or evaporate the water layer between the monolayer and the ITO substrate, thus changing the coupling to the ITO. It may also be an electrochemical reaction in the water layer, either above or below the monolayer.

In order to obtain results unaffected by this degradation we perform excitations with the STM tip scanning a small area (generally a 50 nm x 50 nm area unless stated otherwise). Thus we never perform an excitation on the exact same spot. We also change the excitation location for each new excitation, with the assumption that the monolayer properties are homogeneous.

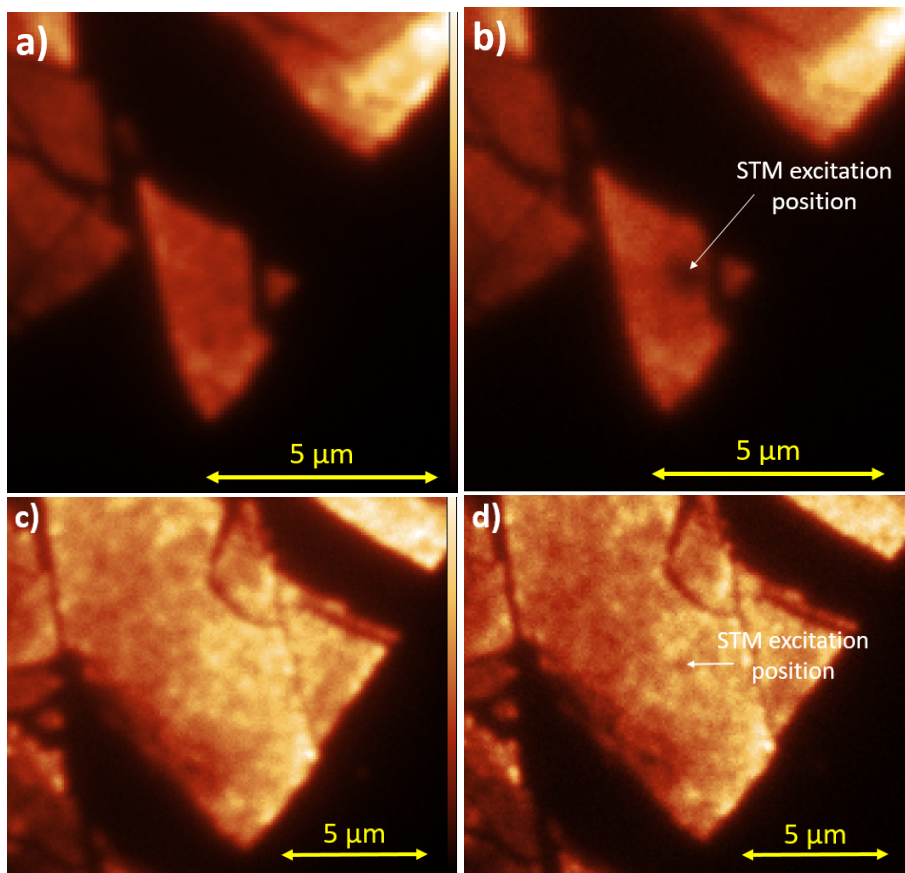


Figure E.1: Photoluminescence image of a MoSe₂ monolayer a) before and b) after a series of five STM excitations (carried out on a vertical line, 100 nm apart) at 4 V, $I_{Setpoint} = 10$ nA, acquisition time = 200 s, and c) before and d) after an STM excitation at 3 V, $I_{Setpoint} = 5$ nA, acquisition time = 200 s.

Appendix F

Parameter study for the non-destructive STM excitation of a nanoantenna

As seen in Fig. 3.14 of Chapter 3, when using an STM to excite surface plasmons on a nanoantenna for 200 seconds, at a 5 nA tunneling current setpoint and with a bias voltage of 2.5 V, the nanoantenna does not survive the excitation. We have two hypotheses to explain this problem: heating or mechanical damage. The first possibility may be due the fact that the energy of the tunneling electrons lost to phonons is sufficient to raise the heating rate above the cooling rate, leading to the melting of the gold. The second possibility is related to the fact that we are working with an STM in air. It is well known that samples in ordinary air are in general covered with a thin water layer, and that this water layer can affect the STM imaging dynamics when a high (> 2 V) potential is applied between the tip and sample [48, 50, 199]. The STM current may have an ionic component when a voltage higher than the water dissociation potential is applied between the tip and the sample when a water film covers the surface. The result of this ionic component is that the tip tends to oscillate vertically, which could put mechanical pressure on the gold sample: as tungsten is much “harder” than gold, the tip oscillation may result in a deformation of the gold surface or structure. (“Hardness” is roughly defined as the pressure necessary to indent the material, 3500 MPa for tungsten, and 200 MPa for gold [200]).

In order to avoid destroying our antennas, we investigate which parameters influence this phenomenon the most and how this damage may be limited: we perform STM excitations on a thin gold film and we observe the deformation of the gold surface after each excitation while varying each parameter so that we may understand its impact on the damage.

When the “after” image is the same as the “before” image, with the grains in the gold film unchanged and well-defined, we consider that no damage has occurred (Fig. F.1-a). When the “after” image is similar to the “before” image but the grains in the gold film have changed shape or are less defined (Fig. F.1-b), either because the STM tip has changed too much to be able to image them properly, or because the film was damaged by the excitation, we define such a result as a small deformation. In these two cases, the excitation parameters are suitable for an excitation on a nanoantenna since the impact on the antenna shape is not significant. When the “after” image presents a small hole, less than 10 nm in depth (Fig. F.1-c), we consider that there is sample damage, and that the excitation parameters are too dangerous for an excitation on a gold nanoantenna. Finally, we also differentiate between damage and extensive damage which we define as the case when the STM excitation leaves behind a hole deeper than 10 nm (Fig. F.1-d).

Thus, we need to determine the appropriate excitation parameters in order to minimize the damage. The feedback loop parameters were investigated previously by two former PhD students from our group, Benoit Rogez and Shuiyan Cao [50]. During these investigations, three different regimes in the measured tunneling current were observed:

- The stable regime, typically for low applied voltage (≤ 1.5 V), during which the measured tunneling current is stable and close to the tunneling current setpoint.
- The free oscillating regime, during which the tunneling current more or less follows the setpoint but is interrupted by pulses of $\sim 10 - 100$ nA during which the STM tip withdraws quickly, as expected due to

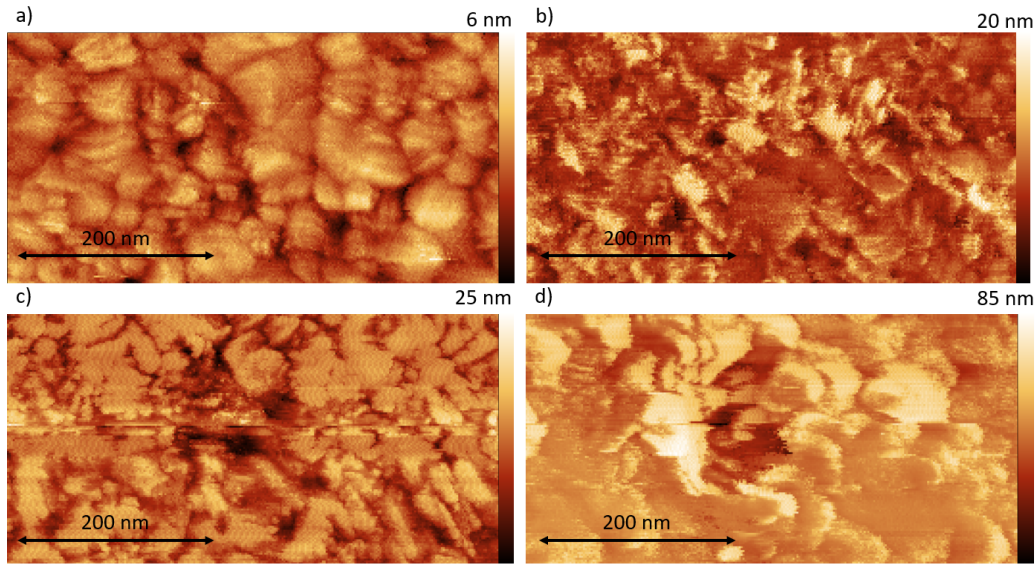


Figure F.1: Defining the extent of damage. STM image of the thin gold film after STM excitation with varying parameters, when there is a) *no damage* (the grains in the gold surface are well-defined and are of homogenous size, $I_{setpoint} = 0.1$ nA, voltage applied to the substrate $V_S = 2.5$ V, acquisition time = 50 s), b) there is a small change in the image, such as a *small deformation* in the grain shape, but no clear damage ($I_{setpoint} = 1$ nA, $V_S = 0.5$ V, acquisition time = 50 s). This change may be attributed either to a change in the film or to a change in the STM tip shape. c) We observe *damage*, in form of a hole less than 10 nm deep ($I_{setpoint} = 10$ nA, $V_S = 2.5$ V, acquisition time = 50 s) and d) *extensive damage* in form of a hole deeper than 10 nm ($I_{setpoint} = 5$ nA, $V_S = 2.8$ V, acquisition time = 150 s).

the feedback loop. This regime was observed for higher values of the bias voltage (typically ≥ 1.5 V) and low feedback loop gain values ($I_{gain} \geq 10$ Hz, $P_{gain} \simeq 10^{-4}$, JPK setup).

- The periodic oscillating regime, during which the STM tip oscillates regularly and the tunneling current varies from 0 nA to detector saturation ($\simeq 120$ nA). This was observed for higher values of the bias voltage (also typically ≥ 1.5 V) and high feedback loop gain values ($I_{gain} \geq 100$ Hz, $P_{gain} > 10^{-4}$).

In Fig. F.2, we present an example of the free oscillating regime (a- in which the tunneling current remains close to the setpoint value, but some small current peaks are visible) and the periodic oscillating regime (b- in which the tunneling current oscillates periodically between 0 nA and the detector saturation value).

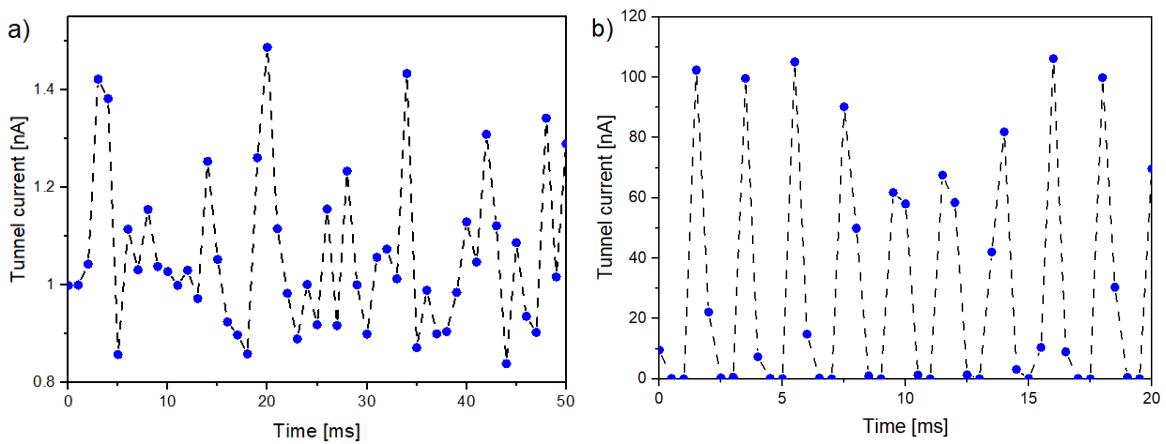


Figure F.2: Tunneling current as a function of time for a) a relatively stable tunneling current, with only some small peaks in the tunneling current ($V_S = 0.5$ V, $I_{setpoint} = 1$ nA, $I_{gain} = 10$ Hz, $P_{gain} = 2 \times 10^{-4}$), b) an unstable tunneling current with a periodic oscillation ($V_S = 1$ V, $I_{setpoint} = 1$ nA, $I_{gain} = 150$ Hz, $P_{gain} = 5 \times 10^{-4}$).

In order to test the effect of each parameter, we first choose a set of “baseline” parameters as follows:

- Excitation time 50 seconds
- Tunneling current setpoint 1 nA
- Bias voltage 0.5 V

- Feedback loop parameters $I_{gain} = 20$ Hz and $P_{gain} = 10^{-4}$ (JPK Nanowizard III)

Then we vary the tunneling current setpoint, the bias voltage and the excitation time independently (with the other parameters fixed as stated above) in order to understand their impact on the extent of the damage.

◇ Influence of the excitation time:

We study the influence of the excitation time by varying the excitation duration from 50 to 150 s. A longer excitation time leads to more deformation: we notice no damage for 50-second excitations, but the surface is destroyed for 150-second long excitations. A longer excitation time means a higher temperature if the cooling rate is lower than the heating rate. As the tunneling current is stable for these parameters, the mechanical damage is expected to be minimal.

◇ Influence of the tunneling current setpoint:

Varying the tunneling current setpoint from 100 pA to 10 nA shows that a higher tunneling current setpoint causes more damage: excitations at 100 pA inflict no damage, at most a deformation, but excitations with a 10-nA setpoint cause extensive damage. This suggests that heating may be the source of the problem since an increase in tunneling current means an increased electrical power ($P = IV_S$).

◇ Influence of the bias voltage:

Varying the bias voltage applied between the STM tip and the sample from 0.5 V to 2.8 V does not have a significant impact on the nanoantenna shape as we see only some deformation for 2.5 V and no damage. We only vary the bias voltage up to 2.8 V as we do not require higher voltages to excite surface plasmons in the visible. An increased bias voltage should lead to more damage for both hypotheses: increasing the electrical power means increasing the heating, however we only increase the bias voltage by a factor 5. On the other hand, increasing the bias voltage above the water dissociation potential means an unstable feedback loop [50], and thus more chance for mechanical damage. There was no damage measured for the maximum value of bias voltage in our range of interest, thus, this result only shows that even for a bias voltage high enough to excite plasmons in the visible (2.5 V), we measure no damage. This suggests then that mechanical stress is not the main source of the damage.

Parameters	Influence	Heating hypothesis?	Mechanical stress?
Integration time	✓	✓	–
Tunneling current setpoint	✓	✓	–
Voltage applied	✗	≈	–

Table F.1: Summary of the investigated parameters: we summarize whether the different parameters have an influence on the damage of the sample, and if this dependence validates a hypothesis.

The feedback loop gains, which affect the STM tip stability, have a low impact on the damage inflicted as long as the tip is stable, but may lock the feedback loop in an unstable periodic regime. Thus, we chose low gain values to stay in a stable regime. The main factors that lead to destruction appear to be long excitation times and high tunneling current, with the bias voltage having a low impact on the extent of the damage (in the bias voltage range of interest). As a bias voltage higher than the water dissociation potential causes an instability of the tip but does not lead to a destruction of the sample, we propose that the main source of damage during the excitation is heating.

To conclude, these measurements determine the best parameters for exciting propagating surface plasmons without destroying the nanoantennas. First, we have to use low feedback loop gain values ($I_{gain} \simeq 20$ Hz, $P_{gain} \simeq 10^{-4}$, in order to keep the tunneling current stable), decrease the excitation time and decrease the tunneling current setpoint. However, decreasing the excitation time and tunneling current setpoint leads to fewer collected photons and as the excitation is already inefficient, the noise would quickly mask our signal. We compromise by using an excitation time of 100 s and a tunneling current of 1 nA, and verify the nanoantenna shape before and after each STM excitation. The applied voltage is 2.5 V in order to excite plasmons in the visible range (500 nm – 900 nm = 1.38 eV – 2.48 eV).

Appendix G

CAFM tip comparison

G.1 AFM tips with a conducting layer

In order to choose the best conducting AFM (CAFM) tip for our experiment, we compare several CAFM tips by testing them with the same protocol on a thin gold film:

◇ First we measure at what deflection setpoint an electrical contact may be achieved in contact mode (called here the contact setpoint, in V). The electrical contact is defined as the smallest deflection setpoint for which the contact resistance is the lowest possible: increasing the deflection setpoint further does not change the measured tunneling current.

◇ Then we measure the total electrical resistance of the CAFM tip when approached in contact mode at the contact setpoint by performing an $I(V)$ curve. So as not to damage the tip by having a high current pass through the conductive layer, we add a $\simeq 1$ M Ω resistor in series. We subtract this value from the measured resistance to obtain the total electrical resistance (that is, tip resistance plus contact resistance).

◇ Lastly, we compare the mechanical resistance of the different CAFM tips to abrasion by performing a contact scan $1 \mu\text{m}$ large with 1024×1024 pixels at a scanning frequency of 0.2 Hz, and with an applied voltage of 1 V. The deflection setpoint we use is the contact setpoint, and we observe how the intensity of the current evolves during the image. If the conductive layer of the tip is damaged, the measured current will fall to zero. The following table summarizes the results obtained for the tips with different conducting layers.

The gold-coated CAFM tips are too delicate and cannot withstand the mechanical wear. The most mechanically resistant tips are the p-doped diamond-coated ones, however their electrical resistance is high and they are costly. The platinum silicide tips seem to be the best compromise as the electrical resistance is low and the mechanical resistance is quite high.

Once the best coating is determined, the choice of cantilever spring constant must be made. Recall that we use the same AFM tip to image the sample in tapping mode, and to contact the nanoantenna electrically in contact mode. Imaging in tapping mode using contact mode probes is very difficult to do as the cantilever is very flexible (spring constant ~ 0.2 N/m) and the oscillation frequency is low: the image often becomes unstable after a few lines. The stiffness of tapping mode cantilevers is higher (on the order of $\sim 10 - 100$ N/m), but this means that a higher mechanical force will be applied when in contact mode for an excitation. Thus we choose to use, with caution, cantilevers with intermediate spring constant values ($\sim 1 - 10$ N/m).

G.2 AFM tips made entirely of a conducting material

For the sample in Section 4.3, we need CAFM tips able to withstand long scans in tapping mode without losing their conducting properties. The tips presented in the previous section are useful in an experiment where the antennas are easy to locate thanks to markers (Section 3.3). However, in the sample of Section 4.3, the

Brand & Model	Layer type	Electrical resistance [k Ω]	Mechanical resistance	Stiffness [N/m]	Contact setpoint [V]	Applied force [a.u.]
CSC18 / CrAu	Gold	22	Very low: the electrical contact is lost after a few pixels	2.8	1.15	3.22
CSC17 / Pt	Platinum	18	Medium: the extremity of the tip seems to be non-conductive, but the electrical contact is good on the sides	0.18	1.1	0.198
DPE - XSC11	Platinum	7	Low: the electrical contact is lost after a few lines, except for some places on the sample, which means most but not all the conductive layer was destroyed	0.2	0.9	0.18
CDT - CONTR	P-Doped diamond	308	High: the extremity of the tip seems to be less conductive, but there is no loss of contact	0.5	0.57	0.285
PtSi - FM	Platinum-Silicide	15.6	Medium: the electrical contact is lost at the end of the scan	2.8	0.83	2.324
PtSi - CONT	Platinum-Silicide	15.5	Very high: no loss of electrical contact	0.2	0.9	0.18
PPP - CONTPt	Platinum-Iridium	15.2	Medium: the electrical contact lasts for one image	0.2	0.6	0.12

Table G.1: CAFM tip test results for tips with a conducting layer. The tips in orange are from μ Masch and the tips in green are from Nanosensors.

nanoantennas are nanocubes dispersed on the sample with a 0.12 particles per μm^2 density, thus we have to scan large regions in order to find the cubes. We quickly noticed that the CAFM tips with a conducting layer were losing their conducting properties after long scans, to the point that we had to use two tips a day. Our hypothesis is that the conducting layer was eroded by the scanning, even in tapping mode.

Thus a better alternative for the experiment of Section 4.3 is a CAFM tip made entirely of a conductive material. These tips are fabricated by Rocky Mountain Nanotechnology (see <https://rmnano.com/>). Tapping mode tips, the best choice for imaging the topography in tapping mode, have a spring constant (or stiffness) that is too high for contacting the nanocubes in contact mode (over 250 N/m): even with the smallest detectable setpoint (0.02 V), the AFM tip indents the surface: see Fig. G.1.

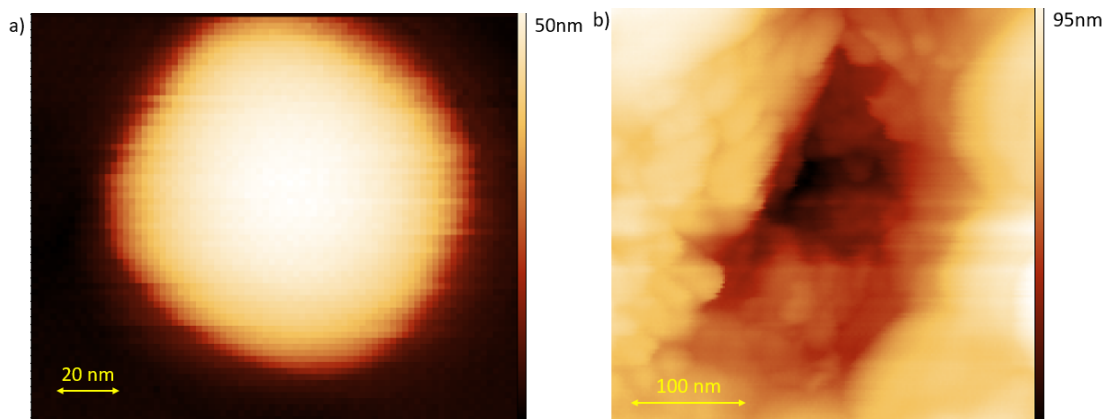


Figure G.1: AFM image of a nanocube a) before attempting to make an electrical contact using a tapping mode CAFM tip with a 250 N/m spring constant and a 0.1 V deflection setpoint, and b) after contact: the tip has indented the surface.

Thus we can only use contact tips or tips with intermediate spring constants in our experiment (≤ 10 N/m). In the table below, we compare the different tips available using three different criteria: (i) if the tip can

electrically contact the nanocubes without destroying them, (ii) the suitability of the tips for imaging in tapping mode and (iii) the suitability of the tips for making a good electrical contact. For all tips for which we could make an electrical contact, the electrical resistance was of the order of magnitude of 1 k Ω , which is negligible compared to that for the tunneling junction with a bias voltage around 2.5 V. Thus when taking into account the conducting properties, we only consider whether the conductivity of the tip decreases after a 10 μm x 10 μm scan. For repeatability purposes, these measurements are carried for two different tips of each type.

Model	Stiffness [N/m]	Material	Imaging properties in tapping mode	Conducting properties	Impact of excitations on nanocubes
12Pt400	0.3	Platinum	It was possible to image the surface, although the image was not of good quality	No electrical contact could be achieved with the two tips we tried	x
12PtIr400	0.6	Platinum-Iridium	Very difficult to properly image the surface	No electrical contact could be achieved	x
25Pt400	8	Platinum	Good	Good electrical contact, no loss of conductivity after a large scan	No destruction
12Pt300	0.8	Platinum	It was possible to image the surface but the imaging was very unstable	One of the tips was not conducting, good electrical contact and no loss of conductivity for the second tip after a large scan	No destruction

Table G.2: Rocky Mountain Nanotechnology CAFM tip test results.

We choose to use the 25Pt400 CAFM tip, made entirely of platinum and with a spring constant of 8 N/m, since the conductivity is good even after a large scan in tapping mode. Imaging in tapping mode with this tip can be challenging, but less so than with other tips, with more flexible cantilevers. Electrical contact made using a 0.1 V deflection setpoint has no noticeable impact on the nanocube shape.

Appendix H

Gold nanoantennas on aluminum

In this appendix, we study a sample similar to the one in Chapter 4, but which uses a different material system. The sample is an integrated tunneling junction with a gold nanoantenna on an oxidized aluminum film, with the thin alumina layer serving as the tunneling junction.

H.1 Tunneling junction in an alumina layer, with a top-down fabricated gold nanoantenna, contacted via CAFM

Sample

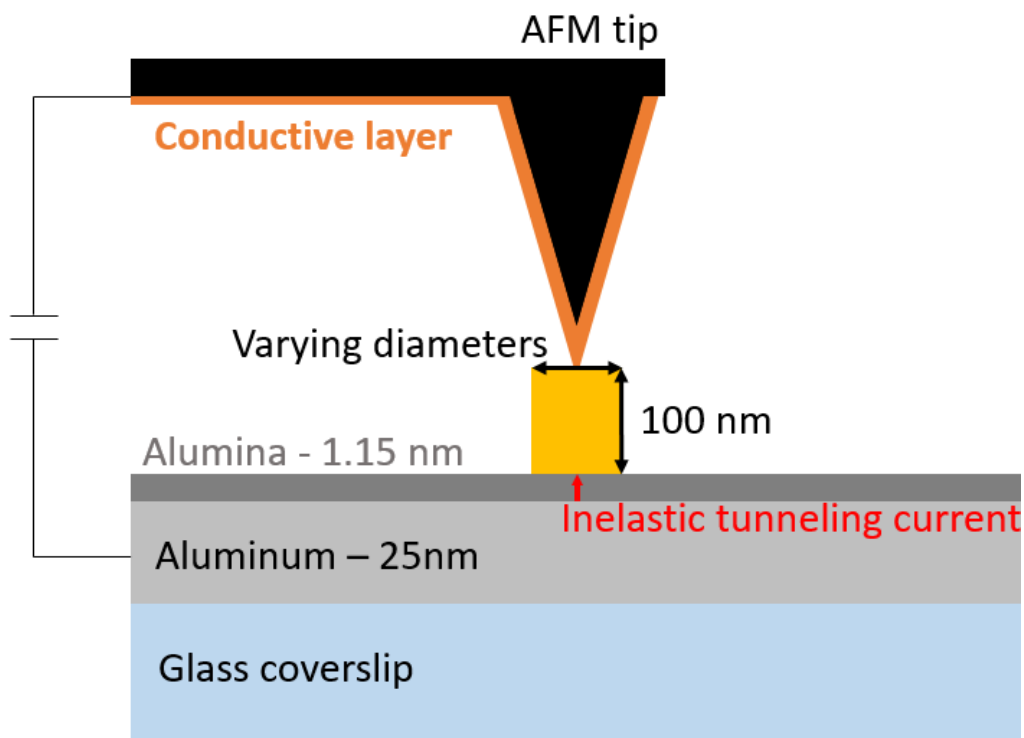


Figure H.1: Schematic of the experiment.

The nanoantennas are fabricated using e-beam lithography as was the case for the nanoantennas on a thin gold film in Chapter 3. We are thus again limited by the minimum possible size of the nanoantennas. The

samples we use are fabricated by Cheng Zhang using the method described in Fig. H.2. The nanoantennas have different target diameters, from 70 nm to 140 nm, so that the impact of the nanoantenna diameter on the resonance may be measured. Around two thousand nanoantennas are fabricated for each target diameter.

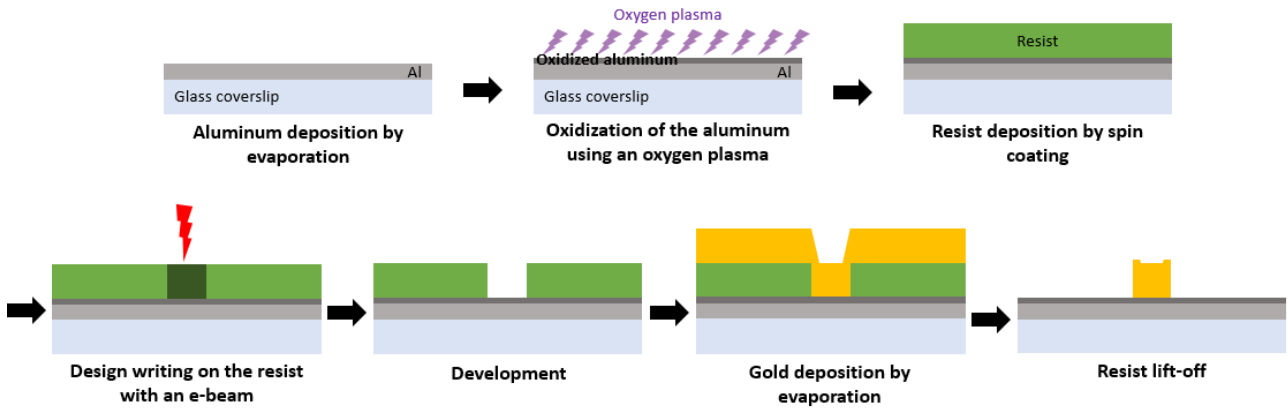


Figure H.2: Sample fabrication process.

Once the nanoantennas are fabricated, we want to image them and determine their dimensions. However, we quickly realized that the fabrication process was not very successful: we had two samples in total, one of which had no nanoantennas at all (while the markers were perfectly deposited), and on the other we counted less than 600 nanoantennas, and only for target diameters above 90 nm (thus we had less than 8 % of the expected nanoantennas). In Section 3.3.2, we were able to fabricate gold nanoantennas with the same method and with smaller diameters, so this problem may be because gold will adhere less on alumina than on gold, which leads to nanoantennas disappearing during liftoff.

In the absence of the nanoantennas, we test the quality of the junction by applying a bias voltage and measuring the tunneling current on one of the markers deposited at the same time as the nanoantennas. These markers are used to navigate the sample more easily. In Fig. H.3, we fit the experimental $I(V)$ curve with a simulated $I(V)$ curve using Simmons' model [175] and a 1.145 nm thick junction (± 0.005 nm, which is the thickness increase step in our simulation). This barrier thickness is thinner than what was found in our test sample (see Fig. 4.2). This thin barrier is an advantage as the tunneling current decays exponentially with the barrier thickness, so we may expect more signal. However, it also means that the junction may be more fragile than in our test sample.

The quality of the junction seems to be poor almost all the markers have the $I(V)$ curve characteristic of an ohmic contact (with an electrical resistance of $R = 18.2\text{k}\Omega \pm 1.5\text{k}\Omega$, likely a short-circuit through the junction), but as we could find a marker with a tunneling current $I(V)$ characteristic, it means that we may find a $25\ \mu\text{m}^2$ area with no defects in the alumina insulating layer.

Results

We then excite propagating surface plasmons by connecting the nanoantenna with the conducting AFM and applying a voltage between the antenna and the aluminum film as described in Section 4.2.1. However, for over 300 nanoantennas tested, only 6 antennas had a working tunneling junction resistant enough to withstand an excitation.

Because of our low number of data points, we cannot give a meaningful mean experimental efficiency value with any satisfactory precision. We still consider the measured efficiencies and the spectrum of a plasmonic excitation using this system, which are presented in Fig. H.4.

We present the efficiencies we measured on the different nanoantennas with a functioning tunneling junction in this figure. We also measured on some nanoantennas tunneling currents high enough to saturate our detector (saturation limit at 120 nA, see Section 1.2). This saturated current prevents us from estimating the actual experimental efficiency but also shows that when the tunneling junction does not have any defects, a high tunneling current may be achieved without destroying the junction.

Unlike our experiment in Chapter 3.3 using an STM on nanoantennas, in this experiment we do not have a reference system to compare with in order to estimate the surface plasmon experimental efficiency improvement due to the nanoantenna. The experiment we use to obtain reference data is to use the conducting AFM tip in contact mode, with a low deflection, to excite surface plasmons with the inelastic tunneling current through

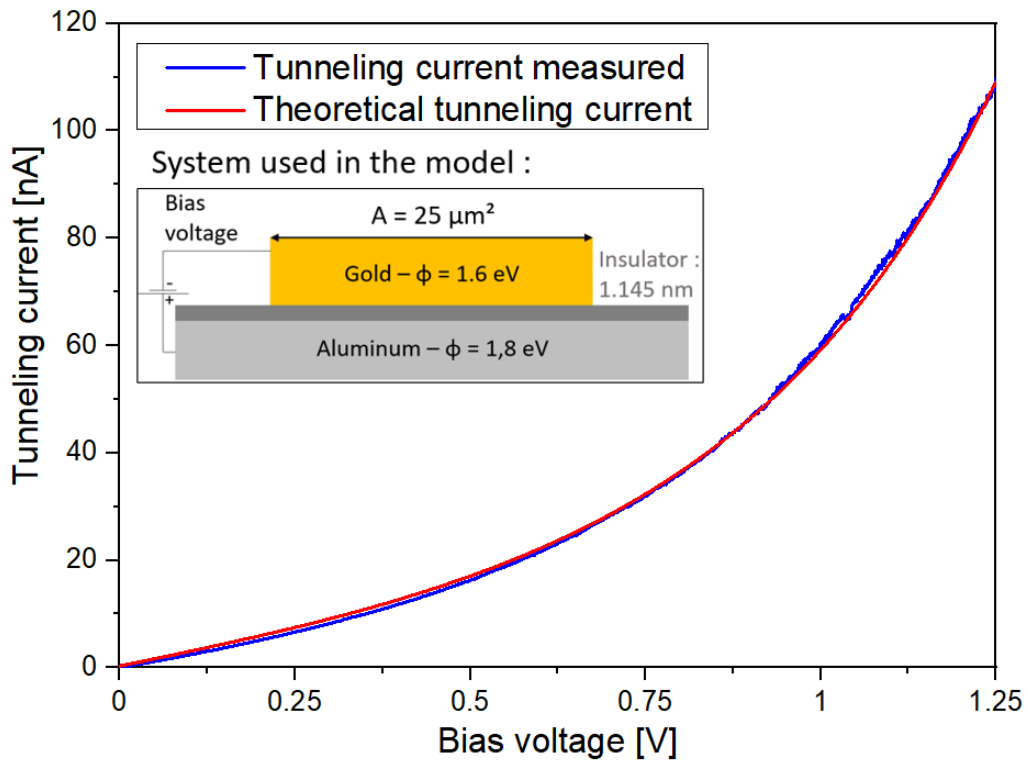


Figure H.3: Tunneling current measured experimentally on a triangular marker (blue curve) compared to a simulated tunneling current characteristic for a 1.145 nm thick junction of $25 \mu\text{m}^2$ area and with a gold work function of 1.6 eV and an aluminum work function of 1.8 eV, (determined using Simmons' model from [175]).

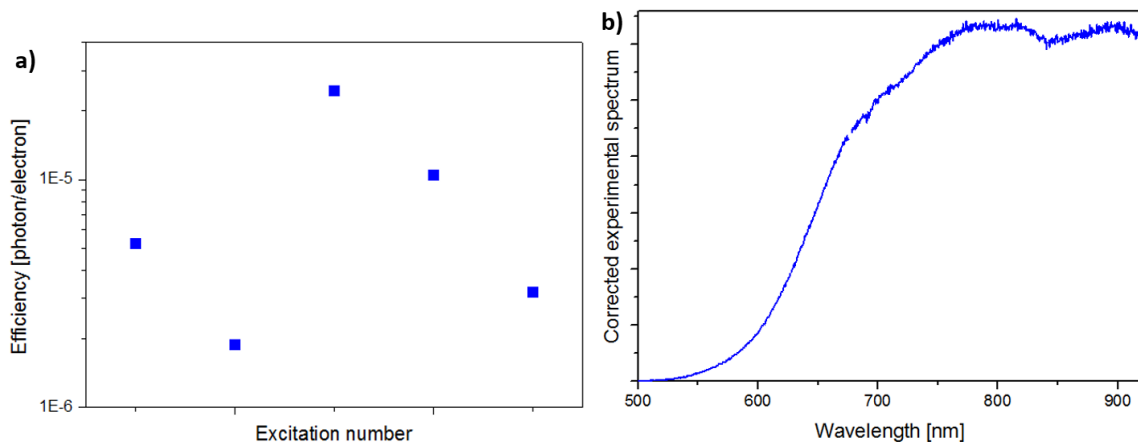


Figure H.4: a) Surface plasmon experimental efficiency (in photons detected per electron passing through the junction), and b) surface plasmon emission spectrum, for excitations with a 2.5 V bias voltage and a 100 second acquisition time.

the alumina barrier, between the aluminum and the conducting AFM. However, the alumina barrier was too delicate, and the tip would be either too distant from the surface (no electrical contact, no current measured) or go through the tunneling junction (current measured with a $U_{bias} = IR$ curve with $R = 16.7\text{k}\Omega \pm 8.8\text{ k}\Omega$, no tunneling), even using a soft contact CAFM tip (lowest stiffness used: 0.2 N/m). Thus, no experimental efficiency improvement factor could be determined.

H.2 Simulation results for a gold nanoantenna on aluminum

Simulations are also carried out for this system, an integrated tunneling junction comprised of a gold nanoantenna on an oxidized aluminum film, with the thin alumina layer serving as the tunneling junction. Similarly to Fig. 4.11 of Chapter 4, to better understand the surface plasmon emission, we plot the spectrum of the power emitted into surface plasmons (P_{SPP}) as a function of the nanoantenna height for a nanoantenna with a diameter of 40 nm (see Fig. H.6-a)¹. As before, in order to better understand the different modes at play in this system, we also plot the spatial distribution of the imaginary part of the perpendicular magnetic field ($imag(Hy)$) for the different bright spots.

From Fig. H.5-b and -c we identify the wavelengths of the S_{02} and S_{04} gap modes in this system. On Fig. H.5-a, we propose that the blue dashed line follows the resonance of an antenna mode, which red shifts with the increasing nanoantenna height, and that the red lines follow the resonance of the gap modes, which are not impacted by the increasing nanoantenna height.

Figure H.6 shows the same trend for different antenna diameters. We propose that an antenna mode (which red shifts as the height increases) couples to several gap modes (which may be identified by the fact that the resonance wavelength is not impacted by the antenna height increase). When the dimensions increase, we observe an overall decrease of the power emitted into the surface plasmon mode in the wavelength range of interest, and a red shift of the modes (red shift of the antenna mode resonance wavelength with the nanoantenna height, and red shift of the gap mode resonance wavelength with the nanoantenna diameter).

Finally, Fig. H.7 compares the surface plasmon excitation efficiency ($\eta_{NA-SPP} = P_{SPP}/P_{tot}$) for a vertical dipole excitation of the system with and without the gold nanoantenna. The nanoantenna is 40 nm large and 50 nm high and is seen to have a peak in the surface plasmon emission around 650 nm . As shown in Fig. H.6, we see that with this geometry, the antenna mode L_{01} and the second order gap mode S_{04} couple at 650 nm : although P_{SPP} appears to be less intense with these dimensions than with an antenna that is 95 nm high and 40 nm large, we chose these dimensions as the resonance wavelength is in the wavelength range of interest, whereas the coupling between S_{02} and L_{01} happens for a wavelength larger than 900 nm . The chosen system gives us a total surface plasmon excitation efficiency enhancement of a factor 55 when compared to a system with no nanoantenna (when comparing the integrated spectra averaged over the whole wavelength range of interest).

¹It has been experimentally demonstrated [201] that a gap of around $8\text{-}10\text{ nm}$ yields a good photon excitation efficiency, while once the gap's thickness is under 2 nm , quenching is considered to be dominant. However, in our case since this gap is used as the tunneling current excitation source, and as the tunneling current decreases exponentially when the gap thickness increases, we use a gap with a thickness of 1 nm to increase the total number of electrons, and thus, the number of electrons tunneling inelastically through the junction and exciting surface plasmons

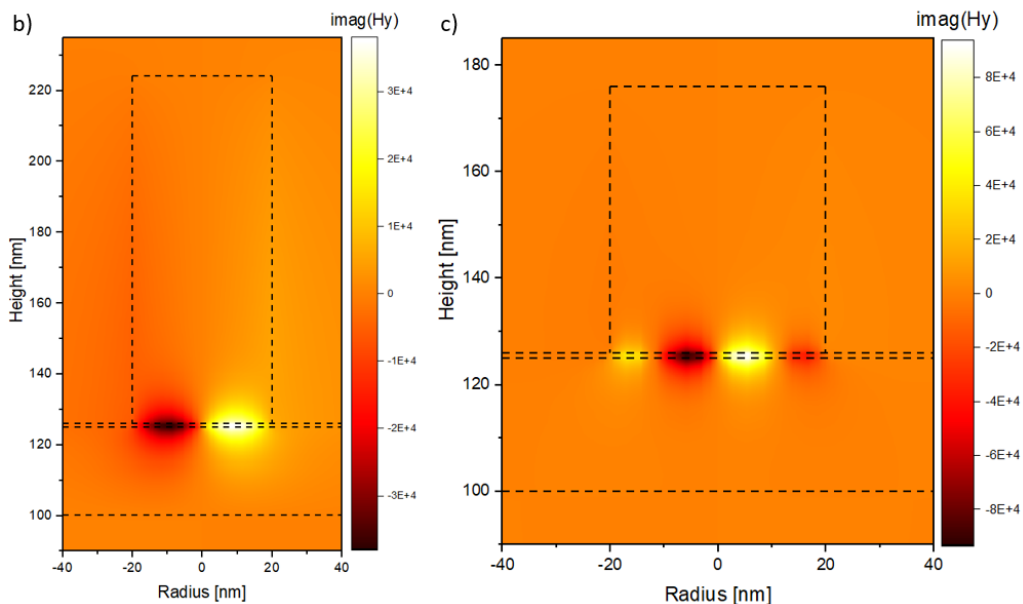
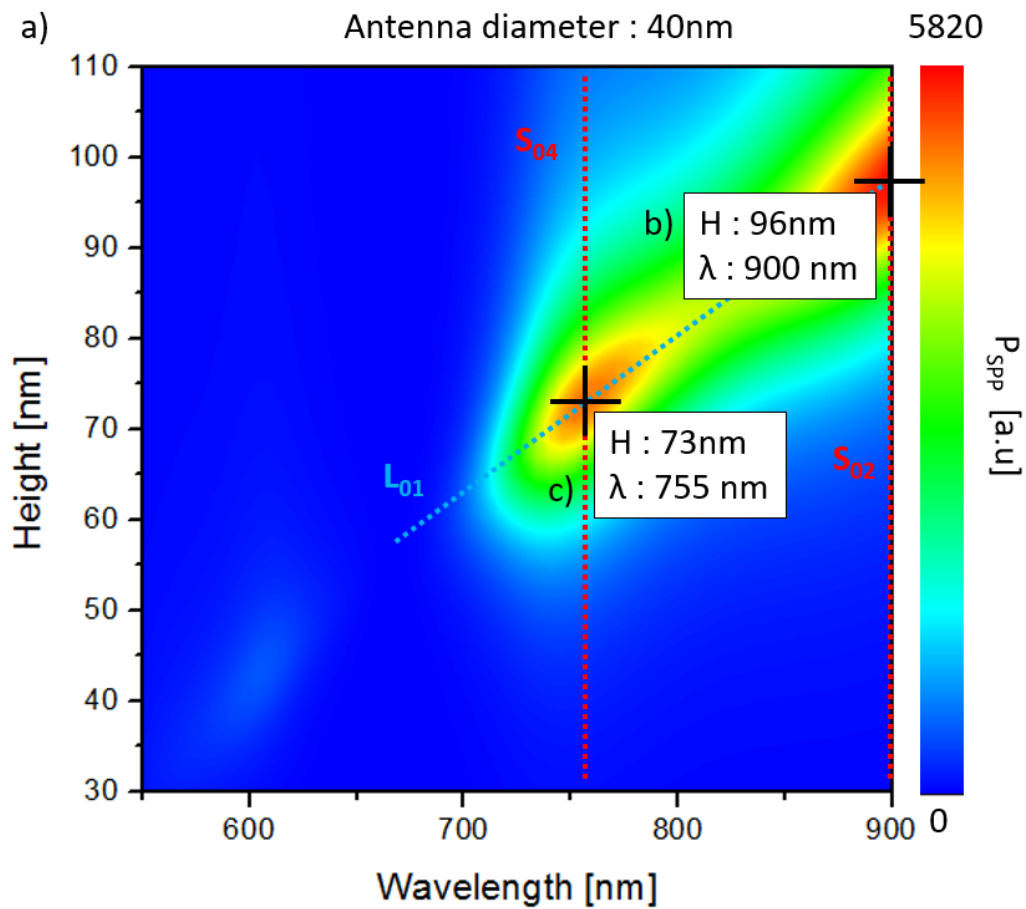


Figure H.5: a) Spectrum of the power emitted into surface plasmons (P_{SPP}) as a function of nanoantenna height for a nanoantenna of diameter 40 nm, with a gap thickness of 1 nm. b) and c) Spatial distribution of the imaginary part of the transverse magnetic field plotted for the dimensions and wavelengths noted in a), which correspond to b) the gap mode S_{02} and c) the gap mode S_{04} .

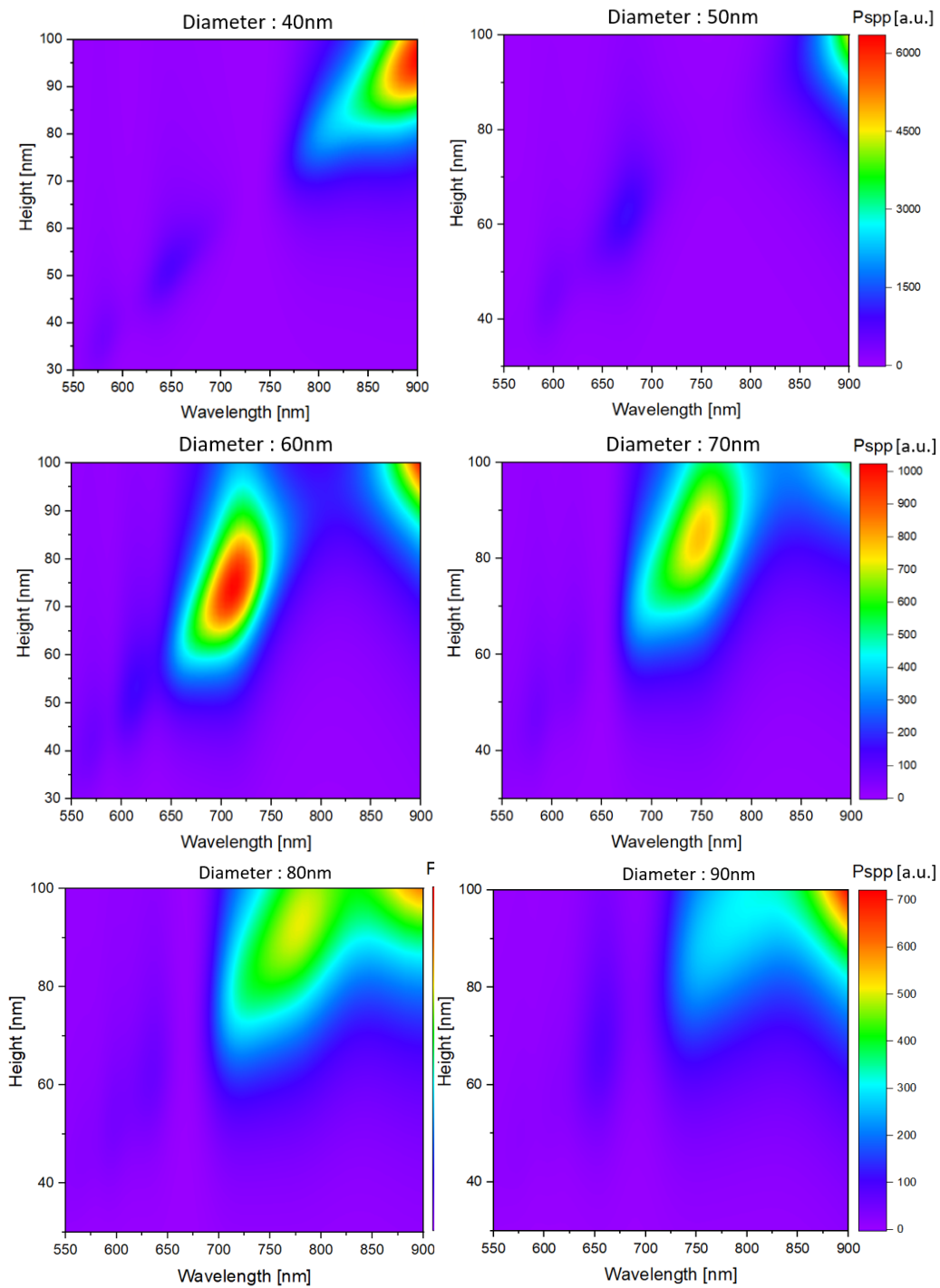


Figure H.6: Surface plasmon mode power spectrum (P_{SPP}) as a function of the nanoantenna height for different nanoantenna diameters, from 40 nm to 90nm, with a gap thickness of 1.145 nm, as was measured in Fig. H.3. For better visibility purposes, the scale is different for each line, but identical for the two maps on the same line.

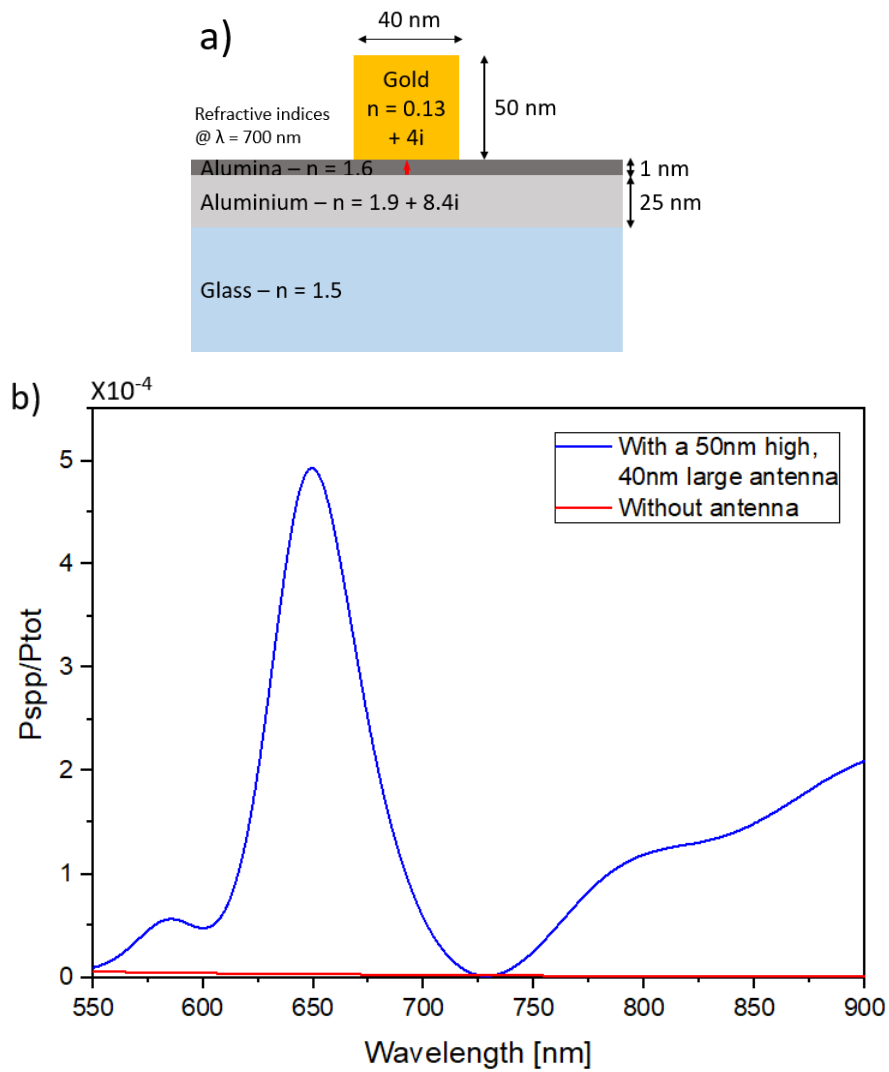


Figure H.7: a) Simulation conditions to compute b) the surface plasmon excitation efficiency ($\eta_{NA-SPP} = P_{SPP}/P_{tot}$) for an nanoantenna for this system (blue curve) and for the same system without the nanoantenna (red curve) (gap thickness of 1.145 nm). The refractive indices were from Ref. [16] for the gold and Ref. [17] for the aluminium (Lorentz-Drude model).

Appendix I

Correction factors for the comparison of the experimental efficiency values measured with different detectors

In Section 4.3.7, in order to estimate the experimental efficiency of the excitation of surface plasmons using a “nanocube-on-a-mirror” system, we wish to exploit the maximum amount of data available. To do so, we use the results obtained from three different kinds of measurements, using the different detectors that were presented in Section 1.2.5 (see Fig. 1.13). As we wish to compare the measurements obtained with different detection systems, we need to take into account the transmission and the detector quantum efficiencies for each type of measurement. These measurements are:

- Real plane images obtained using the Andor CCD camera, which require taking into account the system transmission factor and the quantum efficiency of the Andor CCD camera.
- Real plane images obtained using the camera of the HORIBA spectrometer, which require taking into account the system transmission factor and the quantum efficiency of the spectrometer CCD camera.
- Spectra obtained using the HORIBA spectrometer, which require taking into account the system transmission factor, the grating transmission factor and the quantum efficiency of the spectrometer CCD camera.

The total detection efficiency (transmission factor \times quantum efficiency of the detector) for all detectors is shown in Fig. 1.14 in Section 1.2.5. When comparing spectra, we directly correct the spectra using the total detection efficiency spectra for each detector. However, when comparing the experimental efficiency estimated from real plane measurements (i.e., number of photons detected per number of electrons passing through the tunneling junction), this is not as simple as we do not have the spectrum of the emitted light.

In order to correct the measured experimental efficiencies for the total detection efficiency (T_{det}) for each detection system, we make the hypothesis that the spectrum of the emitted light (S) has the same spectral distribution as an average spectrum as determined from our experimental results (S_{mean}). Thus we may approximate the spectrum of the emitted light S from the detected spectrum (S_{det}):

$$\sum_{\lambda} S = \sum_{\lambda} S_{det} \times \frac{\sum_{\lambda} S_{mean}}{\sum_{\lambda} (S_{mean} \times T_{det})} = \sum_{\lambda} S_{det} \times R \quad (I.1)$$

Thus, in order to correct the experimental results for the total detection efficiency of each detector, we multiply the number of detected photons by a correction factor R . We have $R = 1.5863$ for the Andor CCD camera, $R = 1.1067$ for the spectrometer CCD camera and $R = 2.8591$ for the spectrometer grating and CCD camera.